

Carnegie Mellon University
MELLON COLLEGE OF SCIENCE

THESIS

SUBMITTED IN PARTIAL FULFILLMENT OF THE REQUIREMENTS
FOR THE DEGREE OF

DOCTOR OF PHILOSOPHY IN THE FIELD OF PHYSICS

TITLE: "Systematic effects in realistic image simulations for future Weak Lensing surveys"

PRESENTED BY: Arun Kannawadi

ACCEPTED BY THE DEPARTMENT OF PHYSICS

RACHEL MANDELBAUM 9/27/16
RACHEL MANDELBAUM, CHAIR PROFESSOR DATE

STEPHEN GAROFF 9/27/16
STEPHEN GAROFF, DEPT HEAD DATE

APPROVED BY THE COLLEGE COUNCIL

REBECCA DOERGE 9/27/16
REBECCA DOERGE, DEAN DATE

Systematic effects in realistic image simulations for future Weak Lensing surveys

by

Arun Kannawadi Jayaraman

Submitted in partial fulfillment of the
requirements for the degree of
Doctor of Philosophy

at

Carnegie Mellon University
Department of Physics
Pittsburgh, Pennsylvania

Advised by Professor Rachel Mandelbaum

September 16, 2016

Abstract

Weak gravitational lensing measurements from the large-scale structure of the Universe probe the growth of structures at different epochs, thereby providing information about the mysterious dark energy component. Wide-field redshift surveys such as WFIRST, Euclid and LSST will image the sky and collect an unprecedented amount of data. The decrease in the statistical errors must necessarily be accompanied by an increase in our understanding of systematic errors. The sources of the systematic errors could be i) astrophysical, such as intrinsic alignments, failure to account for the complex morphology of the galaxies when estimating lensing distortions, or could be ii) foreground effects such as the Point Spread Function (PSF) or imperfections from the detectors etc. The systematic errors are estimated by testing the shear estimation pipeline on mock galaxy images that are forward-simulated from first principles. The simulated galaxy images must have realistic properties for the estimates of the systematic biases to be accurate. In this thesis, I describe in detail the work done towards incorporating in the image simulations some of the detector effects relevant for WFIRST and understanding the limitations of using images from narrow surveys, such as COSMOS, as input into image simulations for wide field surveys.

Acknowledgments

As my research advisor, Prof. Rachel Mandelbaum played a major role in the development of this thesis. I thank her for introducing me to the exciting field of observational cosmology, about which I had no idea prior to working with her. For someone like me with only a minor background in Physics and almost no exposure to Astronomy/Astrophysics, Prof. Mandelbaum has been helpful and understanding while I was making my transition to be a cosmologist. I owe her for carefully looking at my many intermediate results and help me figure out what was going wrong in my analysis, which helped me progressed in my research. I thank her for being accommodative and understanding when I hit roadblocks and pushing me when I was falling behind. She has provided me guidance in various technical aspects of the research projects and has helped in my presentation and writing skills. Finally, Prof. Mandelbaum has also been a source of inspiration, showing how one can excel in one's career while paying due attention to one's family as well.

My parents, Jayaraman and Bhama, have been two supporting pillars throughout my life and continue to be so. I cannot possibly describe the efforts they have put in in making my life effortless. They have been very kind and encouraging for the various life decisions made so far. I thank them whole heartedly, especially for being with me during the last few months of my graduate school.

I thank my one special friend, Preeti Ravindra. She has been with me and help me pick up myself during many many physical and emotional breakdowns. She is my well-wisher and has made feel better about myself in multiple occasions. The two gifts that Pittsburgh has given me, which I would cherish for life, is the Doctorate degree that I get by submitting this thesis and her.

I am indebted to the members of my thesis committee - Prof. Tiziana Di Matteo, Prof. Matthew Walker and Prof. Peter Freeman for their guidance and ensuring that that the progress towards my Ph.D. is on track. I appreciate the constructive criticisms of various people in my research group - Ananth Tanneti, Sukhdeep Singh, Hung-Jin Huang, Melanie Simet, Ying Zu, Wentao Luo. I thank all my officemates, Shadab Alam, Siddharth Satpathy, Tanmay Mudholkar, Zongge Liu, Mao Sheng Liu, Xianglin Liu. I enjoyed the many discussions with the post-doctoral researchers Alex Geringer-Sameth, François Lanuesse, Layne Price, Sebastien Fromenteau, Elena

Guisarma.

Graduate courses were a key aspect in improving the understanding of various physics and developing an apt attitude towards research. I have learnt a lot from Prof. Mike Widom, Prof. James Russ, Dr. Hael Collins, Prof. Richard Holman, Prof. Robert Griffiths, Prof. Ira Rothstein, Prof. Robert Swendsen, Prof. Shirley Ho and Prof. Rachel Mandelbaum. I am grateful to my fellow batchmates, Paul La Plante, Sergio de la Barrera, David Menasche, Amy Stetten, Tereza Vardanyan, Bai-Cian Ke, Xin Wang, Ian Laflotte, Daniel Fleischer and Marcus Thomas for their company during the early courses. I would like to make a special mention for Prof. Kunal Ghosh, under whom I served as a Teaching Assistant (TA) for 3 regular semesters and an intense summer semester, for educating me about the undergraduate education. I enjoyed the second part of my first summer working as a TA for Prof. Jefferson Peterson who keeping alive the Electrical Engineer in me. I thank my fellow TAs Melih Ozbek, Patrick Diggins, Stephan Piotrowski for being supportive throughout the courses.

I thank Prof. Manfred Paulini for being the to-go person for all of the administrative concerns right and as a moral support from the time of my admission into CMU until this day. I would also like to thank the Physics department staff members Maria Wilkin, Mary Jane, Hilary Homer, Heather Cororan, Charles Gitzen and Amanda Bodnar for ensuring that all the mandatory paperwork is done smoothly.

I could not have sustained 5 years of my graduate school without the generous financial support from various grants. I acknowledge the support of NASA ROSES 12-EUCLID12-0004, and program HST-AR-12857.01-A, provided by NASA through a grant from the Space Telescope Science Institute, which is operated by the Association of Universities for Research in Astronomy, Incorporated, under NASA contract NAS5-26555. I am also indebted to the WFIRST study office

Outside of my rigorous academic life at Carnegie Mellon, the Indian Graduate Student Association (IGSA) has been very engaging, making me miss home lesser. Many of the friends that I made in Pittsburgh were through IGSA, and I thank the organization for that. I am also obliged to mention some of good friends - Kaushik Vaidyanathan, Lavanya Subramaniam, Varoon Shankar, Anusha Srinivasan, Divya Hariharan, Ashwathi Krishnan, Siddharth Swaminathan, Sreekanth Rajagopalan, Shivram Kashyap,

Anusha Rangarajan, Pratiti Mandal, Sudipto Mandal, Utsav Drolia, Amit Datta and the list goes on.

I have tried my best to acknowledge everyone whose help I have sought in the last 5 years. Despite my efforts, if I might have missed some names in the list, it is only because of my oversight.

Contents

1	Introduction	1
1.1	Cosmic history	2
1.2	Outline	6
2	Cosmological background	7
2.1	Λ CDM - the standard model of Cosmology	7
2.1.1	Smooth Universe	8
2.1.2	Structure formation	13
2.2	Weak lensing	16
2.2.1	Basic formalism	16
2.2.2	Systematic effects	24
3	The impact of cosmic variance on simulating weak lensing surveys	28
3.1	Introduction	30
3.2	Data	32
3.3	Methods	34
3.3.1	Finding overdensities	34
3.3.2	Volume-limiting	38
3.3.3	Describing galaxy morphology and shape	45
3.4	Results	48
3.4.1	Axis ratios	48
3.4.2	Morphological parameters	56
3.4.3	Mitigating the effects of line of sight fluctuations	60
3.5	Implications for future surveys	66
3.5.1	Magnitude of shear calibration bias	66
3.5.2	Effective impact on current and future surveys	69

3.6	Conclusions	70
4	The Impact of Interpixel Capacitance in CMOS Detectors on PSF shapes and Implications for WFIRST	74
4.1	Introduction	75
4.2	Interpixel Capacitance	78
4.2.1	Detector model	78
4.2.2	Parametrizing IPC	79
4.2.3	Implications of IPC	82
4.3	Definitions of sizes and shapes	84
4.3.1	Based on quadrupole moments	84
4.3.2	Other size definitions	87
4.4	Methods	89
4.4.1	WFIRST module description	89
4.4.2	Simulation	93
4.4.3	Overcoming undersampling	93
4.5	Results	96
4.5.1	Increase in PSF sizes	96
4.5.2	Error in PSF shapes from uncertainty in IPC parameters	100
4.5.3	Effects on PSF due to anisotropy of IPC	105
4.6	IPC in the context of WFIRST requirements	106
4.7	Conclusion and future work	107
5	The impact of interpixel capacitance (IPC) on shear calibration biases for WFIRST from realistic galaxy image simulations	110
5.1	Introduction	110
5.2	Lensing basics	113
5.3	Interpixel capacitance	117
5.3.1	Detector model	117
5.4	Data	119
5.5	Methods	121
5.5.1	WFIRST PSF simulation	121
5.5.2	Galaxy simulation	122
5.5.3	Shape measurements	124
5.6	Results	126

5.6.1	Noiseless case	126
5.7	Discussion	127
A	Unweighted moments	132

List of Tables

3.1	List of different redshift bins, their environmental classification and the number of galaxies per redshift bin for volume-limited samples constructed in three different ways: using a hard luminosity cut ($\mathcal{S}1$), using a redshift-dependent luminosity cut ($\mathcal{S}2$) and using stellar-mass cuts ($\mathcal{S}3$).	42
3.2	p -values from the Kolmogorov-Smirnov (top) and Anderson-Darling (bottom) tests obtained by comparing the distributions of axis ratios for three cases: <i>all</i> overdense (OD) vs. <i>all</i> underdense (UD), two overdense bins that are not very separated in redshift, and a pair of adjacent overdense and underdense bins. $\mathcal{S}1$, $\mathcal{S}2$, $\mathcal{S}3$ refer to the three different types of volume-limited samples. The Anderson-Darling p -values are computed only up to 5 decimal places, so values that were given as zero are denoted $< 1 \times 10^{-5}$	50
3.3	p -values from the Kolmogorov-Smirnov (top) and Anderson-Darling (bottom) obtained by comparing the second moments-based distortion for the same three cases as in Table 3.2. The Anderson-Darling p -values are computed only up to 5 decimal places.	50
4.1	Table of minimum, maximum and effective wavelengths in nanometers for each of the six bandpasses.	91
4.2	Table of PSF sizes and ellipticity. Adaptive sizes and half-light radii in milliarcseconds (mas) and magnitude of ellipticities are tabulated for the PSFs of the J129, H158 and F184 bandpasses. Size and ellipticity measurements for the PSFs without including the diffraction spikes are also tabulated, so as to be able to relate to the values in WFIRST documents [1, 2].	96

4.3	List of the six coefficients given in Eqns. 4.30 for the J129, H158 and F184 bandpasses. The coefficients represent the ‘instantaneous rate’ of change in PSF size and ellipticity with respect to the change in one of the IPC parameters about the nominal values for the case of isotropic kernel (Eq. 4.8).	104
4.4	List of the six coefficients given in Eqns. 4.31 for the J129, H158 and F184 bandpasses. The coefficients represent the ‘instantaneous rate’ of change in PSF size and ellipticity with respect to the change in one of the nearest neighbor coupling parameters about the nominal values for the case of anisotropic kernel (Eq. 5.16).	105

List of Figures

1.1	The Cosmic Uroboros	5
2.1	Left Top: $\gamma_+ > 0, \gamma_\times = 0$ Right Top: $\gamma_+ < 0, \gamma_\times = 0$ Left Bottom: $\gamma_\times < 0, \gamma_+ = 0$ Right Bottom: $\gamma_\times > 0, \gamma_+ = 0$ Source: [3]	21
3.1	Upper panel: Redshift distribution of flux-limited ($m_{\text{F814W}} \leq 23.5$) sample with photometric redshift bins that are 0.05 wide. The vertical line at $z = 0.3$ indicates the delineation between lower redshifts that we do not use for our analysis, and higher redshifts that are used. Fits to two analytical functions, $p_1(z)$ and $p_2(z)$, defined in Eqs. 3.2 and 3.3, are also shown, with best-fitting parameters $a = 2.53 \pm 0.98$, $z_1 = 0.32 \pm 0.16$, $b = 1.70 \pm 0.50$ and $z_2 = 0.63 \pm 0.13$. We also show the distributions from [4] from Eqs. 3.4 and 3.5. Lower panel: Plot of $\delta_{g,1D} = N/N_{\text{mod}} - 1$ with each functional form as the model for each redshift bin.	35
3.2	Distribution of absolute magnitude M_I for various flux-limited samples in the redshift range $[0.80, 0.85]$ are plotted together. The vertical line corresponds to our luminosity cut of -20.8 , brighter than which the $m_{\text{F814W}} < 23.5$ sample includes > 95.3 per cent of the galaxies in the $m_{\text{F814W}} < 25.2$ sample.	39

3.3	Stellar mass distribution for various flux-limited samples are shown in three redshift ranges as separate panels. The redshift bins have been chosen to facilitate the comparison with a study of the SMF in [5]. At high mass, the distributions are the same for various flux limits, indicating that the samples are complete in that mass range. The curves begin to deviate at low masses due to incompleteness coming from the flux limit. The point at which the deviation exceeds our threshold determines where the mass cutoff should be to volume-limit the sample.	42
3.4	Upper panel: Redshift distribution of volume-limited ($M_I < -22$) sample with photometric redshift bins that are 0.05 wide. Two analytical functions with best fit parameters are plotted over it, as discussed in the text. Lower panel: Plot of $(1 + \delta_{g,1D}) = N/N_{\text{mod}}$ with each functional form as the model for each redshift bin.	44
3.5	The distributions of the morphological parameters of interest, namely the distortion (top left, from Sérsic fits, and top right, from re-Gaussianization), Sérsic index (bottom left) and bulge-to-total ratio (bottom right) are presented. The shapes of these distributions depend on the way the volume-limiting process is carried out. $\mathcal{S}0$ refers to the flux-limited ($m_{F814} \leq 23.5$) sample and $\mathcal{S}1$, $\mathcal{S}2$ and $\mathcal{S}3$ refer to the volume-limited samples, as discussed in Sec. 3.3.2.	45
3.6	The distributions of axis ratios of galaxies in <i>all</i> overdense (OD) and <i>all</i> underdense (UD) regions in the case of the luminosity-selected sample $\mathcal{S}1$ (left), luminosity-selected sample with B -band evolution taken into account $\mathcal{S}2$ (center), and the stellar-mass-selected sample $\mathcal{S}3$ (right). The upper panels show the histograms, and the bottom panels show the cumulative distribution functions (CDF). The p -values computed using these CDFs are shown in Table. 3.2.	49
3.7	Galaxy axis ratio distributions in two overdense redshift bins, $z = 0.65 - 0.75$ (blue, dotted) and $z = 0.80 - 0.85$ (red, solid), to check for consistency in the case that the environment is the same even if the redshift differs. The p -values from the KS and AD tests are given in Table. 3.2.	49

3.8	Galaxy axis ratio distributions in a single underdense redshift slice, $z = 0.55 - 0.65$ (blue, dotted), and a single overdense redshift slice, $z = 0.65 - 0.75$ (red, solid). The p -values from the KS and AD tests are given in Table. 3.2.	50
3.9	RMS distortions as a function of redshift. The horizontal errorbars indicate the width of the redshift bin, while the vertical ones are 1σ errorbars obtained by bootstrapping. The colours and shapes of the points indicate their environmental classification, as shown in the legend. Points with open centers and thick errorbars correspond to the stellar-mass selected sample $\mathcal{S}3$ and points with filled centers and thin errorbars correspond to the luminosity-selected samples $\mathcal{S}1$ and $\mathcal{S}2$	53
3.10	RMS distortions as a function of redshift, with points defined in a similar way as in Fig. 3.9. In this case, the distortions from moments-based shape estimates, rather than from the Sérsic fits.	54
3.11	Median values of the Sérsic indices for volume-limited samples $\mathcal{S}1$ and $\mathcal{S}2$ are plotted (filled centers and thin errorbars) in top and bottom panels, respectively, for each redshift bin. Median values for the $\mathcal{S}3$ sample are plotted in both the panels (open centers and thick errorbars) in both the panels.	58
3.12	Median values of the bulge-to-total ratios for volume-limited samples $\mathcal{S}1$ and $\mathcal{S}2$ are plotted (filled centers and thin errorbars) in left and right panels respectively for each redshift bin. Median values for the $\mathcal{S}3$ sample are plotted in both the panels (open centers and thick errorbars). The horizontal errorbars simply correspond to the binwidth while the vertical ones are 1σ errorbars obtained by bootstrapping.	59
3.13	Plot of $\delta_{g,1D} = N/N_{\text{mod}} - 1$ with each functional form as the model for each of our new wide redshift bins discussed in Sec. 3.4.3, for flux-limited (top) and volume-limited (bottom) samples.	61

3.14	Median values of Sérsic index, as a function of redshift for our wider redshift ranges used in Sec. 3.4.3. The horizontal errorbars indicate the width of the redshift bin, while the vertical ones are 1σ errorbars obtained by bootstrapping. Points with open centers and thick errorbars correspond to the stellar-mass selected sample $\mathcal{S}3$ and points with filled centers and thin errorbars correspond to the luminosity-selected samples $\mathcal{S}1$ and $\mathcal{S}2$	62
3.15	The fraction of galaxies in $\mathcal{S}1$ (solid symbols) and $\mathcal{S}3$ (open symbols) that are classified as bulge-dominated as a function of redshift, including the correlation with redshift slices classified as overdense or underdense as indicated by the symbol shape and colour.	64
3.16	The RMS distortion as a function of redshift for the full volume-limited galaxy sample $\mathcal{S}3$ (partially-full symbols), the disk-dominated galaxy sample (open symbols), and the bulge-dominated galaxy sample (full symbols). The fact that the bulge-dominated sample has a lower RMS distortion than the disk-dominated sample is consistent with expectations.	65
4.1	<i>Left:</i> WFIRST pupil plane configuration for long wavelength bands W149, H158, and F184. <i>Right:</i> WFIRST pupil plane configuration for short wavelength bands Z087, Y106, and J129. The simulations in this work use the pupil plane image on the left for all wavelengths.	91
4.2	Simulated PSF images using the WFIRST module in GalSim for different filters, in logarithmic intensity scale, relative to the brightest pixel at the center. The PSFs are evaluated at the effective wavelength of the bandpass filters listed in Table. 4.2. The images correspond to an area of $1.76'' \times 1.76''$ or 16×16 pixels, drawn at a scale that is 32 times smaller than the native pixel scale, thus giving images of 512×512 pixels. The filters are arranged in increasing wavelengths from left to right, top to bottom, i.e., the top row corresponds to Z087, Y106, and J129 (from left to right) and the bottom row corresponds to W149, H158, and F184 bands (from left to right).	92

4.3 Contour plot of the relative increase in the adaptive size (expressed as a percent) as a function of the α and α' parameters in the IPC kernel in Eq. (4.8) for the relevant WFIRST PSFs. The black \times represents a nominal value of the IPC parameters in H4RG detectors. For each filter, the adaptive size in milliarcseconds (mas) and ellipticity (e_1, e_2) without IPC is noted above the subplots. 97

4.4 Contour plot of the relative increase in the half-light radius EE50 (expressed as a percent) as a function of the α and α' parameters in the IPC kernel in Eq. (4.8) for the relevant WFIRST PSFs. The black \times represents a nominal value of the IPC parameters in H4RG detectors. For each filter, the EE50 in milliarcseconds (mas) and ellipticity (e_1, e_2) without IPC is noted above the subplots. The black cross marker represents a nominal value of the IPC parameters in the H4RG detectors. 98

4.5 Contour plot of the change in the ellipticity component e_1 as a function of the α and α' parameters in the IPC kernel in Eq. (4.8) for the relevant WFIRST PSFs. The black \times represents a nominal value of the IPC parameters in H4RG detectors. For each filter, the adaptive size in milliarcseconds (mas) and ellipticity (e_1, e_2) without IPC is noted above the subplots. 98

4.6 Contour plot of the change in the ellipticity component e_2 as a function of the α and α' parameters in the IPC kernel in Eq. (4.8) for the relevant WFIRST PSFs. The black \times represents a nominal value of the IPC parameters in H4RG detectors. For each filter, the adaptive size in milliarcseconds (mas) and ellipticity (e_1, e_2) without IPC is noted above the subplots. 99

4.7 Contour plot of the change in the ellipticity component e_1 as a function of the α and α_+ parameters in the IPC kernel in Eq. (5.16) with $\alpha' = 0.002$ for the relevant WFIRST PSFs. The black \times represents a nominal value of the IPC parameters in H4RG detectors. For each filter, the adaptive size in milliarcseconds (mas) and ellipticity (e_1, e_2) without IPC is noted above the subplots. 100

4.8	Contour plot of the change in the ellipticity component e_2 as a function of the α and α_+ parameters in the IPC kernel in Eq. (5.16) with $\alpha' = 0.002$ for the relevant WFIRST PSFs. The black \times represents a nominal value of the IPC parameters in H4RG detectors. For each filter, the adaptive size in milliarcseconds (mas) and ellipticity (e_1, e_2) without IPC is noted above the subplots.	101
4.9	Contour plot of the relative change in the adaptive size (expressed as a percent) as a function of $\delta\alpha$ and $\delta\alpha'$, the deviation from their nominal values ($\alpha_0 = 0.02$ and $\alpha'_0 = 0.002$) of the parameters in the IPC kernel in Eq. (4.8) for the relevant WFIRST PSFs. The black \times corresponds to no deviation from the chosen nominal values of the IPC parameters in H4RG detectors. For each filter, the adaptive size in milliarcseconds (mas) and ellipticity (e_1, e_2) without IPC is noted above the subplots.	103
4.10	Contour plot of the absolute change (after multiplication by 10^3) in the ellipticity component e_1 as a function of $\delta\alpha$ and $\delta\alpha'$, the deviation from their nominal values ($\alpha_0 = 0.02$ and $\alpha'_0 = 0.002$) of the parameters in the IPC kernel in Eq. (4.8) for the relevant WFIRST PSFs. The black \times corresponds to no deviation from the chosen nominal values of the IPC parameters in H4RG detectors. For each filter, the adaptive size in milliarcseconds (mas) and ellipticity (e_1, e_2) without IPC is noted above the subplots.	103
4.11	Contour plot of the absolute change (after multiplication by 10^3) in the ellipticity component e_2 as a function of $\delta\alpha$ and $\delta\alpha'$, the deviation from their nominal values ($\alpha_0 = 0.02$ and $\alpha'_0 = 0.002$) of the parameters in the IPC kernel in Eq. (4.8) for the relevant WFIRST PSFs. The black \times corresponds to no deviation from the chosen nominal values of the IPC parameters in H4RG detectors. For each filter, the adaptive size in milliarcseconds (mas) and ellipticity (e_1, e_2) without IPC is noted above the subplots.	104
5.1	Plot of difference between the estimated shear when IPC is present and the estimate shear in the absence of IPC for the three passbands.	126

- 5.2 Changes in the shear calibration bias as a function of the IPC parameter α for J129 passband in the absence of random noise (non quantization noise). The errorbars obtained by computing the bias values of 10 equal subsets of the galaxies with 2000 galaxy pairs and taking the standar error of the mean value. The shaded region corresponds to the allowed uncertainties in the bias values for Euclid (not very different from WFIRST). The vertical line corresponds to the nominal value of α .128
- 5.3 Changes in the shear calibration bias as a function of the IPC parameter α for H158 passband in the absence of random noise (non quantization noise). The errorbars obtained by computing the bias values of 10 equal subsets of the galaxies with 2000 galaxy pairs and taking the standar error of the mean value. The shaded region corresponds to the allowed uncertainties in the bias values for Euclid (not very different from WFIRST). The vertical line corresponds to the nominal value of α .129
- 5.4 Changes in the shear calibration bias as a function of the IPC parameter α for F184 passband in the absence of random noise (non quantization noise). The errorbars obtained by computing the bias values of 10 equal subsets of the galaxies with 2000 galaxy pairs and taking the standar error of the mean value. The shaded region corresponds to the allowed uncertainties in the bias values for Euclid (not very different from WFIRST). The vertical line corresponds to the nominal value of α .130

Chapter 1

Introduction

“We’re made of star stuff. We
are a way for the cosmos to
know itself”

Carl Sagan

Cosmology is broadly defined in modern terms as the study of origin, evolution and the destiny of the Universe. It attempts to explain one of the most fundamental concepts - existence.

How did everything in the Universe came into being and what is our place in it?

Are we alone in this Universe?

Is the Universe really infinite?

These are some of the intriguing questions that the mankind has asked itself since the early days.

The subject of Cosmology belonged to the philosophers and the religious. It was a matter of speculation, with arbitrary ideas of ideals and perfections were imposed upon the structure of the Universe. Observing the motion of the stars (and plan-

ets) and predicting their positions in the future - astronomy - became one of the first science disciplines. Physics, the study of natural phenomena, and astronomy combined together to give rise to the branch called astrophysics. This enabled the understanding of the nature of the heavenly bodies rather than just their angular positions on the sky. We could understand stellar dynamics and their evolution, the temperature at the core and at the surface of the stars, the composition of atmosphere in distant planets and so on. Powerful telescopes enabled Edwin Hubble and others to see galaxies other than Milky Way and realize that the Universe is much bigger than what it was thought to be. With the realization that gravity is the result of curved spacetime from Albert Einstein's General Theory of Relativity, the pieces to build testable cosmological models were in place.

Today, Cosmology is a predictive science with precise agreement between theory and observations. Since the beginning of the last decade in the 20th century, the term *concordance cosmology* is used to denote the agreement of the results from independent methods of observations.

1.1 Cosmic history

According to our current understanding, the Universe started with a singularity (commonly referred to as the *Big Bang*) $t_0 = 13.8$ years ago and began expanding. In the first few fraction of the seconds after the big bang, the Universe experienced an exponential expansion - a phase known as *inflation* - in which quantum fluctuations were stretched beyond the horizon, freezing the fluctuations, and stretching any possible curvature. After the first few minutes of the birth of the Universe, there were photons and relativistic neutrinos and a hot dense plasma of baryonic matter containing protons and electrons and dark matter particles. The mean free path of the photons in the early stages of the Universe was small, thus keeping the baryon components in thermal equilibrium with each other and with the radiation.

Until about 75,000 years after Big Bang, the dominant contributor to the total energy of the Universe were photons. As the Universe expands, the energy density of the photons gets 'diluted' faster than the energy density of the matter particles and non-relativistic matter became the dominate the energy budget. The era where the energy

in the form of photons and matter were equal is denoted as the era of matter-radiation equality. In the matter-dominated phase of the Universe, the tiny fluctuations imprinted during the inflation act as seeds for structure growth. Dark matter particles begin to accumulate at the overdense regions, making it more overdense with time. However, the photon number density is 10 orders magnitude higher than the number density of the baryonic particles. As a result, the baryons did not quite trace the gravitational potential initially due to the overdensities; instead they were constantly bombarded by the photons. As the Universe continued to expand, it cooled down further and the protons and electrons combined to form Hydrogen atoms when the cosmic age was around 200,000 years - a phenomenon known as the *recombination* (a misnomer). However, the high energy photons were dissociating the H atoms back to p^+ and e^- . After about 380,000 since the initial singularity, the photons almost completely decoupled from the baryons and began free-streaming through the space. Today, we observe these photons as the Cosmic Microwave Background (CMB).

After the decoupling, the baryons are now free to fall into the dark matter structures or *halos* that have formed. As the baryonic matter fell into the potential wells, they got heated up and radiate (unlike the dark matter particles) to cool and continued to fall into the deepest parts of the halo, where they formed stars. Stars are organized into galaxies; galaxies are grouped together as groups, clusters (largest bound structures) and even larger superclusters. These superclusters form the largest structures known, such as *filaments*, *walls* or *sheets*, which are separated by large underdense regions called *voids*. Under the cold dark matter (CDM) model, structure grows from bottom to top, i.e., small objects aggregate to form larger structures. This hierarchical model of organization is known as the large-scale structure (LSS) of the Universe. On length scales larger than 100 Mpc, this hierarchy ends and the Universe begins to appear homogenous and isotropic, in accordance with the Copernican principle.

The expansion rate of the Universe had been slowing down after inflation, until about 9.5 billion years since Big Bang, where the dominant energy contribution appeared to come from a mysterious component that we call the *dark energy*, which appears to have constant energy density. This is consistent with the notion that the accelerated expansion is due to a non-zero cosmological constant, denoted as Λ . Cosmological constant can be interpreted as the energy or cost of having empty space. Experiments show that the observed value of Λ is 120 orders of magnitude smaller than the value

calculated from quantum field theories! This is often jokingly mentioned as the worst prediction in physics ever. Moreover, it is not clear if the standard model of particle physics is complete, and if not, the calculated value for Λ would change. An active area of research in cosmology is to find the real reason for the accelerated expansion of the Universe - is it the cosmological constant Λ , or is it *dark energy*, which is regarded as an exotic form of matter (sometimes referred to as *quintessence*) that is fueling the expansion? With the data currently available, it is impossible to determine what dark energy really is.

Despite the conclusive evidence for the existence of dark energy, little is known about its properties. The lack of persuasive theoretical explanation for the existence and magnitude of the dark energy highlights the vast holes in our understanding of the nature. In fact, dark energy featured in the list of top ten science problems of our time in *Science* magazine. This is because dark energy is not just of interest for cosmology but also has profound implications towards gaining a better understanding of high-energy particle physics and quantum gravity. Fig. 1.1 is a depiction of this idea by means of the cosmic uroboros - a snake's tail in its head - with different points along its body representing different length scales. Probably the strongest support of this idea is the fact that the tightest constraints on the masses of the neutrinos are obtained from cosmological observations and not high-energy particle accelerator experiments.

In the absence of theoretical guidance, it is common to rely on exploration by observation. With that spirit, several surveys, both ground-based and space-based, have been employed or are construction for operations in the near future, with the hope of invalidating various alternative theories about the evolution of the Universe.

The growth of the large-scale structure has now come to a halt almost and the Universe once again has begun to accelerate since inflation. Eventually, in another few billion years, structures that are not gravitationally bounded, will cross our event horizon and the observable Universe would consist only one galaxy cluster. We now live in the era where the structure has grown as much as it could, when the CMB radiation is still measurable and when we could still observe some of the first formed galaxies and thus an ideal era for large sky surveys.

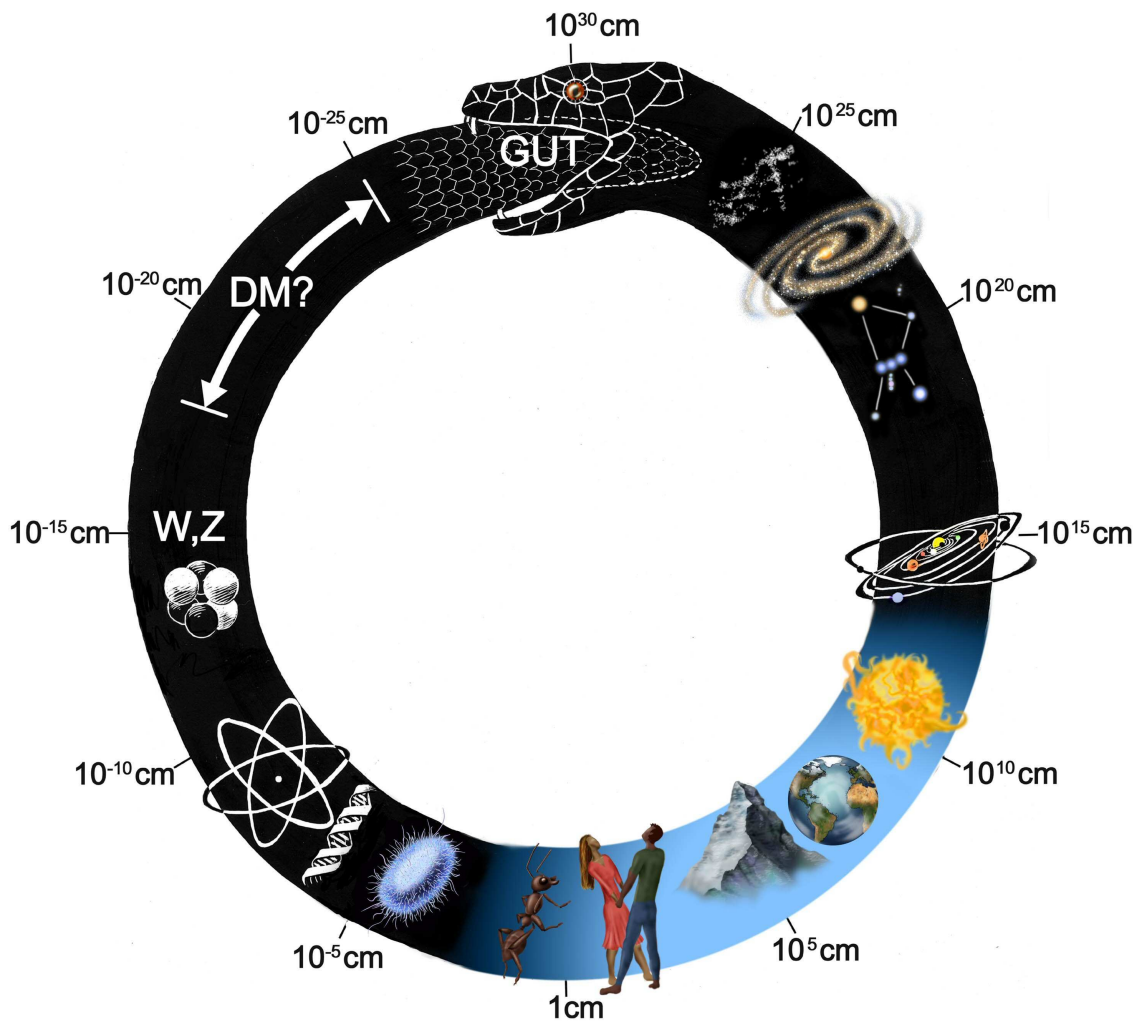


Figure 1.1: The cosmic uroboros represents the smallest size (the Planck length) at the tip of its tail, depicting progressively increasing sizes along its body, with its head representing the size of the entire observable Universe. The cosmic urboros is a symbolic representation that the physics at the largest scales is intimately related with the physics at the smallest scales. Image source: <http://new-universe.org/zenphoto/Chapter2/Illustrations/Abrams22.jpg.php>

1.2 Outline

This thesis contains 5 chapters. The main focus of Chapter 2 is the standard paradigm of Cosmology and a brief review of the formalism of weak gravitational lensing and how systematics affects the measurement. Chapters 3 to 5 focus on various systematic effects involved in the measurement of weak lensing. The goal of the introduction chapter is to layout the scientific background that provides the context for the rest of the chapters. Chapter 3 discusses the effect of using galaxy images from a narrow pencil-beam survey, such as COSMOS, as a training set for image simulations from which the systematic biases would be measured. Chapters 4 study the impact of a detector effects, called the interpixel capacitance (IPC), on the telescope PSF in the context of detector requirements for the WFIRST survey. Chapter 5 analyzes the impact of IPC on shear calibration bias in somewhat simplified settings. With the exception of Chapters 1 and 2, all other chapters are already public or will be made available publicly soon. Chapters 3 and 4 are published works, for which I am the lead author. Chapter 5 is a draft that is expected to be submitted in the near future. Chapter 3 and 5 consists of words written according to the British spelling rules, while the other chapters are written according to the American English spelling rules. This thesis covers only those projects that are relevant for weak gravitational lensing and for which I was the main contributor in both research and in writing.

Chapter 2

Cosmological background

The study of the life of the Universe is necessarily accompanied by a study of the contents in the Universe and their properties. The interaction between the components of the Universe is dominant by gravity, which is the only unshielded long range force. General Theory of Relativity by Albert Einstein is currently the best classical theory of gravity we know. The standard model of Cosmology assumed the theory of General Relativity to be true, which of course has stood the tests of time, with the two detections of gravitational waves [6, 7] being the last piece of missing evidence in favor of the theory. However, in many cases, Newtonian formulation of gravity suffices to study the evolution of the Universe.

This chapter contains two sections. In Sec. 2.1, I discuss the basic concepts of standard model of the Cosmology without rigorous derivations. In Sec. 2.2, I review the basic concepts of weak gravitational lensing, how it provides cosmological information and how systematics affect the measurement.

2.1 Λ CDM - the standard model of Cosmology

The standard paradigm of cosmology today is the six parameter flat Λ CDM cosmological model. In this section, we review the Λ CDM model, the equivalent of the standard model in particle physics for Cosmology. Most modern textbooks on Cosmology, for example [8, 9, 10, 11, 12, 13] cover the topics in great detail. In Sec. 1.1,

I described the cosmic history in a few paragraphs without any mathematical details. In Sec. 2.1.1, I discuss the Universe on large scales and in Sec. 2.1.2, I discuss how the tiny initial perturbations in a uniform background matter density grows to form into massive structures that we observe in the Universe today.

2.1.1 Smooth Universe

The early Universe was highly homogenous and isotropic, thus described the Friedmann-Robertson-Walker (FRW) metric:

$$ds^2 = -c^2 dt^2 + a(t)^2 [dX^2 + dY^2 + dZ^2] \quad (2.1)$$

$$= -c^2 dt^2 + a(t)^2 \left[\frac{1}{1 - Kr^2} dr^2 + r^2 (d\theta^2 + \sin^2 \theta d\phi^2) \right] \quad (2.2)$$

$$= -c^2 dt^2 + a(t)^2 [d\chi^2 + d_A^2(\chi)(d\theta^2 + \sin^2 \theta d\phi^2)], \quad (2.3)$$

where K is the global curvature (see later), t is the time coordinate and c refers to the speed of light in vacuum. In Cartesian coordinates, the physical (spatial) coordinates (x, y, z) are related to the *comoving* (spatial) coordinates (X, Y, Z) via the scale factor $a(t)$ as $(x, y, z) = (aX, aY, aZ)$ (the time dependence in a is suppressed). θ, ϕ are the polar and azimuthal coordinates and r and χ are called radial and line-of-sight coordinates. If $K = 0$, $r \equiv \chi$. Otherwise, $r \equiv d_A(\chi)$ and is known as the angular diameter distance given by

$$d_A(\chi) = \begin{cases} \chi & \text{if } K = 0 \quad (\text{flat}) \\ \frac{1}{\sqrt{K}} \sin \sqrt{K} \chi & \text{if } K > 0 \quad (\text{closed}) \\ \frac{1}{\sqrt{K}} \sinh \sqrt{K} \chi & \text{if } K < 0 \quad (\text{open}) \end{cases} \quad (2.4)$$

$K = 0$ corresponds to the simplest case of the Universe being flat, where Euclidean geometry holds true. $K < 0$ refers to the Universe being *open* and $K > 0$ corresponds to a *closed* which is bounded and has a finite volume. In a closed Universe, two light rays originating from a single point in different directions will eventually meet. In an open Universe, two light rays originating from the same point travelling in different directions will diverge, with the separation given by the angular diameter distance increasing at a faster rate than in a flat Universe.

Note that the scale factor $a(t)$ cannot be determined uniquely since it has a scalar degree of freedom, i.e., $a(t) \rightarrow \lambda a(t)$ along with $X \rightarrow \frac{1}{\lambda} X$, for arbitrary $\lambda \neq 0$, leaves the physical coordinates unchanged. Thus, the physical quantities that govern the evolution of the scale factor must necessarily be expressed as $\frac{a(t_1)}{a(t_2)}$ or $\frac{\dot{a}}{a}$ or $\frac{\ddot{a}}{a}$. As an example, the redshift of the wavelength of a photon, as a result of the expansion of the space, is given as

$$\text{Redshift } z \equiv \frac{\lambda_{obs} - \lambda_e}{\lambda_e} = \frac{\lambda_{obs}}{\lambda_e} - 1 = \frac{a(t_{obs})}{a(t_e)} - 1, \quad (2.5)$$

where λ_{obs} and λ_e are the observed and emitted (true) wavelengths, t_e is the cosmic time of emission and t_{obs} is the cosmic time of observation. It is conventional to define the scale factor today $a(t_0) \equiv 1$ for convenience. Thus, we obtain the redshift-scale factor relation

$$a(t) = \frac{1}{1+z}. \quad (2.6)$$

If $a(t)$ happens to be a *monotonic* function of time t (which it is, see later in this section), then redshift, which is an observable, can be used to refer to distances and cosmic times. Since light travels along null geodesics ($ds^2 = 0$) and for radially inward light $d\theta = d\phi = 0$, we get

$$c dt = a(t)d\chi \quad \implies \quad \frac{d\chi}{c} = \frac{dt}{a(t)} = \frac{da}{a^2(t)H(t)} = \frac{dz}{H(z)}, \quad (2.7)$$

where $H(t) \equiv \dot{a}(t)/a(t)$ is the Hubble parameter. The Hubble parameter evaluated today at $t = t_0$ is referred to as the Hubble constant, denoted by H_0 . We will denote the value of various quantities at the present epoch by a subscript 0. The Hubble constant is commonly expressed as $H_0 = 100h$ km/s/Mpc, where h is the unitless Hubble constant and is of order unity.

Evolution in a smooth Universe

The expansion scale factor $a(t)$, and the evolution of the Universe, is determined by ratio of densities of the different components. Plugging in the FRW metric in Einstein's field equations with homogenous matter gives the Friedmann equations:

$$\left(\frac{\dot{a}}{a}\right)^2 = \frac{8\pi G}{3}\rho - \frac{Kc^2}{a^2} + \frac{\Lambda}{3} \quad (2.8a)$$

$$\frac{\ddot{a}}{a} = -\frac{4\pi G}{3}\left(\rho + \frac{3p}{c^2}\right) + \frac{\Lambda}{3} \quad (2.8b)$$

Evaluating Eq. 2.8a at the present epoch, we get

$$\frac{3H_0^2}{8\pi G} = \rho_0 + \frac{3c^2}{8\pi G}\frac{K}{a^2} + \frac{\Lambda}{8\pi G} \quad (2.9)$$

The left hand side of the above equation is defined to be the *critical density* of the Universe, often denoted by ρ_{cr} . Defining the different density parameters

$$\Omega_0 = \frac{\rho_0}{\rho_{\text{cr}}} \quad \Omega_{K,0} = \frac{c^2}{H_0^2}\frac{K}{a_0^2} \quad \Omega_{\Lambda,0} = \frac{\Lambda}{3H_0^2}, \quad (2.10)$$

$$\Omega_0 + \Omega_{K,0} + \Omega_{\Lambda,0} = 1. \quad (2.11)$$

The contributions to the stress-energy tensor comes from radiation or relativistic components (photons, neutrinos etc.) and from non-relativistic matter components (baryons, dark matter). Thus, $\rho_0 = \rho_{\text{rad}} + \rho_{\text{m}}$ and hence $\Omega_0 = \Omega_{\text{m},0} + \Omega_{\text{rad},0}$.

At a generic epoch, $\rho(a) = \rho_{\text{m}}(a) + \rho_{\text{rad}}(a)$. The matter density in a region with constant number of particle scales as the inverse of the volume containing those particles, which itself grows as the 3rd power of the scale factor. For photons and other relativistic particles, in addition to the above mentioned effect, the energy of the individual particles scale as the inverse of the scale factor. Thus, the components scale differently with a :

$$\rho_{\text{rad}} \propto a^{-4} \quad \rho_{\text{m}} \propto a^{-3} \quad (2.12)$$

This allows us to related the density parameters at an earlier (and later) epoch to those at the present epoch.

$$\Omega_{\text{m}} = \Omega_{\text{m},0}a^{-3} \quad \Omega_{\text{rad}} = \Omega_{\text{rad},0}a^{-4} \quad \Omega_K = \Omega_{K,0}a^{-2} \quad \Omega_{\Lambda} = \Omega_{\Lambda,0} \quad (2.13)$$

Therefore,

$$\frac{H^2(t)}{H_0^2} = \Omega_{\text{rad},0}a^{-4} + \Omega_{\text{m},0}a^{-3} + \Omega_{K,0}a^{-2} + \Omega_{\Lambda,0} \quad (2.14)$$

By specifying the density parameters today and the Hubble constant, we can obtain the cosmic time t as a function of the scale a ,

$$t(a) = \int_0^a \frac{da'}{a'H_0} \frac{1}{\sqrt{\Omega_{\text{rad},0}a'^{-4} + \Omega_{\text{m},0}a'^{-3} + \Omega_{K,0}a'^{-2} + \Omega_{\Lambda,0}}} \quad (2.15)$$

which can then be inverted to obtain $a(t)$. The present epoch can be obtained by evaluating $t(a = 1)$, which by definition is t_0 .

There is no analytical solution for $a(t)$ in general. However, for hypothetical single-component universe, i.e., if all except one of the density parameters are zero, then we have simple analytical solutions.

$$a(t) = \begin{cases} (t/t_0) & \text{if } \Omega_{K,0} = 1 (\text{curvature dominated}) \\ (t/t_0)^{1/2} & \text{if } \Omega_{\text{rad},0} = 1 (\text{radiation dominated}) \\ (t/t_0)^{2/3} & \text{if } \Omega_{\text{m},0} = 1 (\text{matter dominated}) \\ e^{H_0 t} & \text{if } \Omega_{\Lambda} = 1 (\Lambda \text{ dominated}) \end{cases} \quad (2.16)$$

Despite Eq. 2.15 not be amenable to analytical solutions, we can make a few useful inferences by analyzing the behaviour of the terms in these equations. First, from Eq. 2.14, one can see that for $H(t) = 0$, one needs to have at least one of Ω_K or Ω_{Λ} to be negative. However, the measured values of the density parameters suggest that the RHS of Eq. 2.14 can never vanish and hence $a(t)$ is a monotonically increasing function of t . It is this property that makes the redshift a useful observable as z can be related to the scale factor a using Eq. 2.6 which, for a given cosmology, can be related to the time t . Second, the measurements suggest $|\Omega_{\Lambda}| \gg |\Omega_{\text{m},0}| \gg |\Omega_{\text{rad},0}|$, with $|\Omega_K| \approx 0$. Hence, as a increases from 0 to 1, the Universe goes through a radiation dominated phase, followed by the matter dominated phase and finally a Λ dominated phase (present epoch). This idea is crucial in formulating the ideas of the structure growth, which is the subject matter of discussion in Sec. 2.1.2

Note on Dark Energy

Eq. 2.16 implies that the second derivative of the scale factor, \ddot{a} is negative in a matter dominated or in a curvature dominated or in a radiation dominated Universe and naturally, a Universe that contains only these three energy parameters in some proportions will experience a decelerating expansion. However, the accelerating expansion of the Universe was proven, thus requiring Ω_Λ to be the dominant component. While a positive cosmological constant Λ can explain the acceleration, it poses several other problems. The energy density due to the cosmological constant, $\rho_\Lambda = \Omega_\Lambda \rho_{cr}$ is thought of to be the intrinsic energy density of the vacuum, ρ_{vac} . Calculations using quantum field theories predict a value for ρ_{vac} that is greater than ρ_Λ by 120 orders of magnitude! Moreover, some supersymmetric theories require $\Lambda = 0$. To circumvent these issues, a mysterious component called the *Dark Energy* was proposed to explain the accelerated expansion.

Dark Energy is speculated to be homogenous fluid, with negative pressure. It is hypothesized to not interact with the matter in any way, but affect the cosmology by contributing towards the expansion of the Universe. The equation of state for the dark energy (or any other component) is expressed as

$$P = w\rho c^2. \quad (2.17)$$

For pressure-less matter (dark matter), $w_m = 0$, for radiation, $w_{rad} = 1/3$ and for Λ , $w_\Lambda = -1$. Several ground-based and space-based surveys are in progress and are being planned to measure the equation of state parameter w_{DE} of the dark energy. $w_{DE} = -1$ implies that dark energy is indistinguishable from cosmological constant.

$$\rho_{DE}(a) = \rho_{DE,0} \exp \left[-3 \int \frac{da}{a} (1 + w_{DE}(a)) \right]. \quad (2.18)$$

Deviations of w_{DE} from -1 will give us hints about the nature and the evolution of the dark energy. A commonly used parametrization for w_{DE} is $w_{DE}(a) = w_0 + w_a(1 - a)$.

2.1.2 Structure formation

While the Universe is indeed homogenous and isotropic at very large length scales (e.g., [14]), it is obviously not so at smaller length scales. A perfectly homogenous Universe would never be able to give rise to the structures that we see today. It is hypothesized that the Universe in the first few fraction of the seconds experienced a rapid phase of acceleration known as the *inflation*. The tiny quantum fluctuations in the primordial fields were stretched beyond the horizon and frozen even after the end of the inflationary epoch, leading to tiny ‘seed’ density perturbations that is responsible for the large scale structure (LSS) in the Universe.

The local density $\rho(\vec{x})$ at a comoving position \vec{x} differs from the mean density $\bar{\rho}$. One defines the matter *overdensity* field as

$$\delta(\vec{x}, a) = \frac{\rho(\vec{x}, a) - \bar{\rho}(a)}{\bar{\rho}(a)} = \frac{\rho(\vec{x}, a)}{\bar{\rho}(a)} - 1 \quad (2.19)$$

The scale factor a is included to denote the time dependence of the density field.

During the intermediate matter dominated phase, the amplitude of the density contrast grows due to self-gravity as $\delta \propto a$, with overdense regions becoming more overdense and underdense regions becoming further underdense. The initial perturbation is small ($\delta(a \ll 1) \ll 1$) and its evolution is given by a linear differential equation. It is helpful to consider the Fourier transform of the overdensity field -

$$\tilde{\delta}(\vec{k}, a) = \int d^3k e^{-i\vec{k}\cdot\vec{x}} \delta(\vec{x}, a) \quad (2.20)$$

as different \vec{k} modes evolve independently.

By definition, the average of the overdensity field over a sufficiently large volume, $\langle \delta \rangle = 0$ in real space and in Fourier space. Hence one needs to consider two-point statistics or higher to characterize the fluctuations. The power spectrum of the fluctuations $P_\delta(k)$ is given as

$$\langle \tilde{\delta}(\vec{k}) \tilde{\delta}^*(\vec{k}') \rangle = (2\pi)^3 \delta_D(\vec{k} - \vec{k}') P_\delta(k), \quad (2.21)$$

where * denotes complex conjugation. P_δ depends only on the magnitude $k = |\vec{k}|$ and

not its direction due to isotropy. The primordial density fluctuations are assumed to come from a Gaussian field, i.e., they are completely characterized by their power spectrum (this assumption is constantly tested and not found to be violated so far). All the higher order statistics can be expressed in terms of its second order statistics. The power spectrum at later times is obtained from the primordial power spectrum by an application of the transfer function $T(k)$ defined as.

$$T(k, a) = \frac{\tilde{\delta}(k, a = 1)/\tilde{\delta}(k = 0, a = 1)}{\tilde{\delta}(k, a_i)/\tilde{\delta}(k = 0, a_i)}$$

At large scales, $T(k \rightarrow 0) \rightarrow 1$ by virtue of its normalization and at small scales, $T(k) \propto k^{-2}$. The exact details of the transfer function depends on the matter content and their equations of state 2.17 [15, 16, 17].

Inflationary models predict the form of the primordial power spectrum to be

$$P_\delta(k) = A_s k^{n_s}, \quad (2.22)$$

which is nearly scale-invariant with $n_s \approx 1$ [18, 19], where n_s is called the spectral index.

The power spectrum is also the Fourier transform of the correlation function

$$\xi(\vec{r}) = \int d^3x \delta(\vec{x})\delta(\vec{x} + \vec{r}) \quad P_\delta(k) = \int d^3r e^{-i\vec{k}\cdot\vec{x}}\xi(\vec{r})$$

In practice, it is impossible to measure the density perturbation $\delta(\vec{x})$ at every point \vec{x} . Moreover, it is regions of some finite volume with average density different from the mean density that are physically interesting, as they lead to structures that can be detected at cosmological length scales. Thus, we define a smoothed density fluctuation field $\delta_R(\vec{x}, a)$ as

$$\delta_R(\vec{x}, a) = \int d^3r W_R(\vec{r})\delta(\vec{x} + \vec{r}), \quad (2.23)$$

where $W_R(\vec{r})$ can be an arbitrary weight function normalized to unity. $W_R(\vec{r})$ sometimes called as the window function and R is a characteristic length scale of the weight function. The most commonly used window function is the spherical top-hat function: $W(r) = 3/(4\pi R^3)$ for $r < R$ and $W(r) = 0$ for $r \geq R$. whose Fourier transform

is $W(k) = 3j_1(kR)/kR$, where j_1 is a spherical Bessel function. The variance of the smoothed density fluctuations within spheres of radius R is given by

$$\sigma_R^2 = \frac{1}{2\pi^2} \int dk k^2 P(k) |W(k)|^2 = \int d \ln k \Delta^2(k) \left(\frac{3j_1(kR)}{kR} \right)^2, \quad (2.24)$$

where $\Delta^2(k) = k^3 P(k)/2\pi^2$ is called the reduced power spectrum. It is common to choose $R = 8h^{-1}\text{Mpc}$. It turns out that $\sigma_8 \sim 1$, with recent measurements indicating σ_8 close to being 0.8 [20].

Galaxy bias

Galaxy surveys with spectroscopic redshifts such as the Baryonic Oscillation Spectroscopic Survey of SDSS-III [BOSS; 21] provide a 3-dimensional mapping of galaxies from which the galaxy-galaxy correlation function $\xi_{gg}(r)$ can be computed. On large length scales, galaxies are considered to be a biased tracer of the matter density field [22].

$$\xi_{gg}(r) = b^2 \xi_{\delta\delta}(r) \quad P_g(k) = b^2 P_\delta(k), \quad (2.25)$$

where b is called as the galaxy bias. Galaxy bias encodes the physics of galaxy formation. One of the ways to estimate the bias parameter from the clustering data is by comparing the three-point correlation function (whose Fourier transform is known as *bi-spectrum*) $\langle ggg \rangle = b^3 \langle \delta\delta\delta \rangle$ to the two-point correlation function $\langle gg \rangle = b^2 \langle \delta\delta \rangle$. The two-point and three-point correlation functions of δ are calculated from perturbation theory by assuming that the initial perturbations were Gaussian. However, estimating the three-point correlation function requires large areas in the sky and the bias estimates have found to be noisy. Another way to estimate the bias parameter is by combining lensing and clustering measurements, since they have different powers of b .

The bias parameter can also be estimated from cosmological simulations with both dark matter and baryonic particles, bu studying the relative clustering of baryonic particles and dark matter particles. Uncertainty in the bias parameter arises from our lack of understanding of baryonic physics at small scales such as star formation, gas cooling, feedback processes etc. Thus, our understanding of the distribution of

the dark matter on small scales from the distribution of the galaxies is limited by our understanding of the galaxy formation processes.

Since dark matter does not interact electromagnetically, we cannot directly see or observe its distribution. However, since dark matter interacts gravitationally, we can infer its distribution by looking at how it affects the light from the background galaxies. This phenomenon is known as *gravitational lensing* and it provides us the ability to probe the matter power spectrum directly.

2.2 Weak lensing

This section is intended to give an extremely brief overview of weak gravitational lensing or simply referred to as *Weak Lensing* (WL). For a detailed review, refer to [3, 23, 24, 25, 26, 27, 28]

2.2.1 Basic formalism

The images of distant galaxies (sources) appear distorted in their shapes and sizes as a result of the action of the tidal gravitational field (foreground) on light bundles that travel from the sources to us (observers). The conservation of the number of photons in their journey towards us (*cf.* Liouville's theorem) implies that the surface brightness is conserved. Thus, if $I^{(\text{int})}(\boldsymbol{\beta})$ is the surface brightness distribution in the source plane (or sphere), then the observed surface brightness distribution is given as

$$I^{(\text{obs})}(\boldsymbol{\theta}) = I^{(\text{int})}(\mathcal{A}\boldsymbol{\theta}), \quad (2.26)$$

where \mathcal{A} is the mapping from the image coordinates to the source coordinates, i.e. $\mathcal{A} : \boldsymbol{\theta} \rightarrow \boldsymbol{\beta}(\boldsymbol{\theta})$. Here, $\boldsymbol{\theta}$ ($\boldsymbol{\beta}$) refers to the two-dimensional vector, denoting the image (intrinsic) position of the source in the sky. If the angular size of the source is small compared to the angular scale in which the properties of the foreground lens change, then the mapping \mathcal{A} can be locally linearized. This linearized mapping is

commonly expressed as

$$\mathcal{A}_{ij} \equiv \frac{\partial(\delta\theta_i)}{\partial\theta_j} = \begin{pmatrix} 1 - \kappa - \gamma_1 & -\gamma_2 \\ -\gamma_2 & 1 - \kappa + \gamma_1 \end{pmatrix} \quad (2.27)$$

$$= (1 - \kappa) \begin{pmatrix} 1 - g_1 & -g_2 \\ -g_2 & 1 + g_1 \end{pmatrix}, \quad (2.28)$$

The $(1 - \kappa)$ term is a scalar multiplicative factor affecting only in the magnification. The g_1 and the g_2 terms, in addition to affecting the magnification, are responsible for the distortion in the shape. The subscripts 1 and 2 correspond to the axes of an arbitrary Cartesian reference frame in the tangent plane at the position of the image. \mathcal{A} has only 3 free parameters and not 4, because there is a rotational degree of freedom in choosing the alignment of the axes. The parameters of \mathcal{A} , κ is called the *convergence* and γ_1 and γ_2 are the two components of a complex quantity called the *shear*, defined as $\gamma = \gamma_1 + i\gamma_2$. $g_i := \gamma_i/(1 - \kappa)$ for $i = 1, 2$ are the components of another complex quantity called the *reduced shear*, defined similarly as $g = g_1 + ig_2$.

\mathcal{A} maps circles to ellipses, with their axis ratios given by the magnitude of the reduced shear g , with the major axis making an angle $\phi = \frac{1}{2}\angle g = \frac{1}{2}\tan^{-1}(g_2/g_1)$. Thus,

$$g = g_1 + ig_2 = |g|e^{i2\phi} \quad \gamma = \gamma_1 + i\gamma_2 = |\gamma|e^{i2\phi} \quad (2.29)$$

The factor of 2 in the phase leaves g and hence the ellipse invariant under a 180° rotation, i.e., $\phi \rightarrow \phi \pm \pi \implies g \rightarrow g$. κ , being related to the magnification, is isotropic and hence a scalar.

The parameters of \mathcal{A} can be related to each other through a scalar potential $\psi(\boldsymbol{\theta})$, which is often referred to as *lensing potential* or *deflection potential* as

$$\kappa(\boldsymbol{\theta}) = \frac{1}{2}(\psi_{,11}(\boldsymbol{\theta}) + \psi_{,22}(\boldsymbol{\theta})) \quad (2.30)$$

$$\approx \frac{1}{2}\nabla^2\psi(\boldsymbol{\theta}), \quad (2.31)$$

where $\psi_{,ij} \equiv \partial^2\psi/\partial\theta_i\partial\theta_j$ and $\nabla^2 \equiv \partial^2/\partial\boldsymbol{\theta}^2$ in the flat-sky approximation.

$$\gamma_1 = \frac{1}{2}(\psi_{,11} - \psi_{,22}) \quad \gamma_2 = \psi_{,12}. \quad (2.32)$$

Note that the rotational properties of the parameters are still preserved. For a linear map with 3 degrees of freedom, such as \mathcal{A} , it is always possible to write the parameters in this fashion as it simply corresponds to using the degrees of freedom to choose the 3 second derivatives of a scalar function in 2 dimensions as required.

As an illustrative example, consider a typical gravitational lensing system, such as the lensing of background galaxies by galaxy clusters, where the extent of the sources and lenses is much smaller than their distances from the observers and between themselves. The derivation of these expressions can be found **elsewhere**; only the key results are given below. Using the *thin lens approximation* or Born approximation, we can obtain the deflection angle $\boldsymbol{\alpha}$ as

$$\boldsymbol{\alpha} = \nabla\psi(\boldsymbol{\theta}) \quad (2.33)$$

The lensing potential in this case is given by

$$\psi(\boldsymbol{\theta}) = \frac{1}{\pi} \int d^2\theta' \kappa(\boldsymbol{\theta}') \ln |\boldsymbol{\theta} - \boldsymbol{\theta}'|, \quad (2.34)$$

where

$$\kappa(\boldsymbol{\theta}) = \frac{\Sigma(d_d\boldsymbol{\theta})}{\Sigma_{\text{cr}}}, \quad \text{with } \Sigma(d_d\boldsymbol{\theta}) = \int dr_3 \rho(d_d\boldsymbol{\theta}, r_3) \text{ and } \Sigma_{\text{cr}} = \frac{c^2}{4\pi G} \frac{d_s}{d_d d_{ds}} \quad (2.35)$$

where d_d , d_s are the angular-diameter distance to the lens and the source respectively from the observer and d_{ds} is the angular-diameter distance between the lens and the source. Note that if $K \neq 0$, $d_{ds} \neq d_s - d_d$.

A significant detection of shear can be expected around massive objects, such as galaxy clusters. The tangential shear around a central spherical lens object is constant at constant radius. By estimating the average of the constant shear within an annulus around such objects and by comparing the average shears in multiple annuli to prediction from the parametric models of dark matter distribution, a great deal about the relationship between the baryonic matter and the dark matter can be learnt.

The statistical properties of the shear field, specified in terms of n -point correlation functions, can be predicted for a given model of the Universe. *Cosmic shear* refers to the gravitational lensing by the large scale structure (LSS) of the Universe. It measures the clustering of the LSS from the highly non-linear ($< \text{Mpc}$) regime to

very large scales, well within the linear regime. Cosmic shear measurements are weak lensing measurements made without the knowledge of the foreground (lens) structures. The distortions in the galaxy images introduced by the LSS is very weak and therefore very difficult to measure. However, measuring cosmic shear is of immense interest as it probes the matter power spectrum directly. In addition to measuring the geometry of the Universe, cosmic shear has the ability to study the growth of structure and distinguish between dark energy and modified gravity theories.

It differs from the formalism explained in Sec. 2.2.1 in several aspects. The deflection does not happen at a single lens plane but continuously by the 3-D matter distribution.

As mentioned in Sec. 2.2.1, if the angular size of the source galaxy is small, then the mapping \mathcal{A} between the observed angular position and the true position can be locally linearized. The lensing potential from which the parameters κ and γ can be derived using Eqs. 2.31 and 2.32 is given by

$$\psi(\boldsymbol{\theta}, \chi) \approx \frac{2}{c^2} \int_0^\chi d\chi' \frac{d_A(\chi - \chi')}{d_A(\chi)d_A(\chi')} \Phi(d_A(\chi')\boldsymbol{\theta}, \chi') \quad (2.36)$$

to the first order in the Newtonian gravitational potential Φ . The potential Φ is related to the density fluctuation via the Poisson equation

$$\nabla_{\vec{x}}^2 \Phi = 4\pi G \rho \quad \nabla_{\vec{x}'}^2 \Phi = 4\pi G \bar{\rho} a^2 \delta, \quad (2.37)$$

where $\nabla_{\vec{x}}^2$ and $\nabla_{\vec{x}'}^2$ are the Laplacian operators in physical and comoving coordinates respectively. Note that $\bar{\rho} = \Omega_m \rho_{\text{cr}}$ where $\rho_{\text{cr}} = 3H_0^2/8\pi G$. Substituting,

$$\nabla^2 \Phi(d_A(\chi)\boldsymbol{\theta}, \chi) = \frac{3H_0^2 \Omega_m}{2} \frac{\delta(d_A(\chi)\boldsymbol{\theta}, \chi)}{a(\chi/c)} \quad (2.38)$$

Lensing is sensitive to the geometry of the Universe by the fact that angular diameter distances appear in the definition of the lensing potential. However, better constraints are Ω_K are obtained from CMB experiments, which suggest that the geometry of the Universe is consistent with being flat. We will assume that the geometry of the Universe is flat for the rest of this document. In a flat universe, $d_A(\chi) = \chi$.

Since $\kappa = \frac{1}{2}\nabla^2\psi$, we get

$$\kappa(\boldsymbol{\theta}) = \int d\chi W(\chi)\delta(\chi, \chi\boldsymbol{\theta}) \quad (2.39)$$

where the lensing efficiency W is defined as

$$W(\chi) = \frac{3}{2}\Omega_{m0}H_0^2a^{-1}(\chi)\chi q(\chi) \quad (2.40)$$

with q referred to as the lens efficiency given by

$$q(\chi) = \int_{\chi_s=\chi}^{\chi_s=\chi_{lim}} d\chi_s n_s(\chi_s) \frac{\chi_s - \chi}{\chi_s} \quad (2.41)$$

The Fourier transform of the convergence and shear are given by

$$\tilde{\kappa}(\boldsymbol{\ell}) = \int d^2\theta e^{i\boldsymbol{\ell}\cdot\boldsymbol{\theta}} \kappa(\boldsymbol{\theta}) \quad \tilde{\gamma}(\boldsymbol{\ell}) = \int d^2\theta e^{i\boldsymbol{\ell}\cdot\boldsymbol{\theta}} \gamma(\boldsymbol{\theta}) \quad (2.42)$$

When averaged over large areas in the sky, $\langle\gamma\rangle = 0$ due to isotropy. Thus, one needs to look at a two-point statistics or higher order statistics. Similar to Eq. 2.21, we define the convergence and shear power spectrum as

$$\langle\tilde{\gamma}(\boldsymbol{\ell})\tilde{\gamma}^*(\boldsymbol{\ell}')\rangle = (2\pi)^2\delta_D(\boldsymbol{\ell} - \boldsymbol{\ell}')P_\gamma(\ell) \quad (2.43a)$$

$$\langle\tilde{\kappa}(\boldsymbol{\ell})\tilde{\kappa}^*(\boldsymbol{\ell}')\rangle = (2\pi)^2\delta_D(\boldsymbol{\ell} - \boldsymbol{\ell}')P_\kappa(\ell) \quad (2.43b)$$

The shear and the convergence in Fourier space are related to each other as

$$\tilde{\gamma}(\boldsymbol{\ell}) = \frac{(\ell_1 + i\ell_2)^2}{\ell^2}\tilde{\kappa}(\boldsymbol{\ell}) = e^{2i\beta}\tilde{\kappa}(\boldsymbol{\ell}) \quad (2.44)$$

Since the two quantities differ only by a phase factor, the convergence and shear power spectrum are same, i.e., $P_\gamma = P_\kappa$ and can simply be referred to as the lensing power spectrum. In practice, one computes the lensing power spectrum from a shear field. However, the lensing power spectrum is easy to analyze when viewed as convergence power spectrum, owing to the scalar nature of κ .

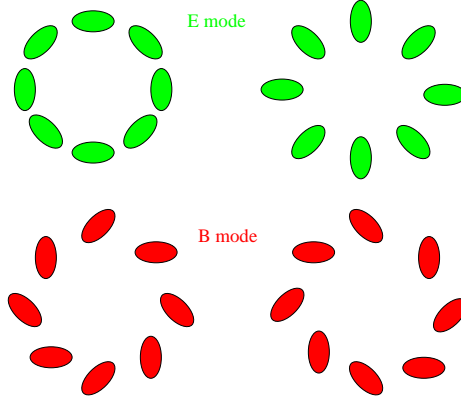


Figure 2.1: Left Top: $\gamma_+ > 0, \gamma_\times = 0$ Right Top: $\gamma_+ < 0, \gamma_\times = 0$ Left Bottom: $\gamma_\times < 0, \gamma_+ = 0$ Right Bottom: $\gamma_\times > 0, \gamma_+ = 0$ Source: [3]

The lensing power spectrum is related to the matter power spectrum P_δ as

$$P_\kappa(\ell) = \frac{9}{4} \Omega_{m0}^2 H_0^4 \int d\chi \frac{q^2(\chi)}{a^2(\chi)} P_\delta \left(k = \frac{\ell}{\chi}, \chi \right) \quad (2.45)$$

$$= \int d\chi \frac{W^2(\chi)}{\chi^2} P_\delta \left(k = \frac{\ell}{\chi}, \chi \right) \quad (2.46)$$

$$= \int dz \frac{W^2(z)}{\chi^2(z) H(z)} P_\delta \left(k = \frac{\ell}{\chi}, \chi \right) \quad (2.47)$$

While it is possible to obtain the lensing power spectrum directly from a catalog of shape estimates, most weak lensing analyses are done in real space using angular correlation functions.

Given a direction φ (polar angle on the ‘plane’ of the sky), we define the tangential and cross components of the shear *relative* to the given direction as

$$\gamma_+ = -\mathcal{R}e(\gamma e^{-i2\varphi}) \quad \gamma_\times = -\mathcal{I}m(\gamma e^{-i2\varphi}) \quad (2.48)$$

Fig. 2.1 shows the orientation of the galaxies when one of the tangential or cross components vanishes. The elongation for circular sources depends on the magnitude of the shear. Using these two shear components, we can define two autocorrelation functions $\langle \gamma_+ \gamma_+ \rangle$ and $\langle \gamma_\times \gamma_\times \rangle$ and a cross-correlation function $\langle \gamma_+ \gamma_\times \rangle$. However, it is

more convenient to define the autocorrelation functions as

$$\xi_{\pm}(\theta) = \langle \gamma_+ \gamma_+ \rangle(\theta) \pm \langle \gamma_{\times} \gamma_{\times} \rangle(\theta) \quad (2.49a)$$

$$\xi_{\times}(\theta) = \langle \gamma_+ \gamma_{\times} \rangle(\theta). \quad (2.49b)$$

Under a parity transformation, $\gamma_+ \rightarrow \gamma_+$ but $\gamma_{\times} \rightarrow -\gamma_{\times}$. Assuming that the population of the galaxies is invariant under parity, $\langle \gamma_+ \gamma_{\times} \rangle = 0$. The ξ_+ and ξ_- have even and odd parity. The correlation functions are related to the lensing power spectrum via the relations

$$\xi_+(\theta) = \frac{1}{2\pi} \int d\ell \ell J_0(\ell\theta) P_{\kappa}(\ell) \quad (2.50a)$$

$$\xi_-(\theta) = \frac{1}{2\pi} \int d\ell \ell J_4(\ell\theta) P_{\kappa}(\ell) \quad (2.50b)$$

where $J_n(x)$ is the n -th order Bessel function of the first kind.

The inverse relations are given as

$$P_{\kappa}(\ell) = 2\pi \int_0^{\infty} d\theta \theta J_0(\ell\theta) \xi_+(\theta) = 2\pi \int_0^{\infty} d\theta \theta J_4(\ell\theta) \xi_-(\theta) \quad (2.51)$$

Although this is *not* used to construct the lensing power spectrum from the correlation functions, the second equality is useful to see how ξ_+ and ξ_- are not independent but related to each other. This is not surprising since κ and the γ are obtained from a scalar lensing potential ψ .

Thus, a shear produced by gravitational lensing must obey the above equality. However, in practice, the measured shear correlation functions need not obey the constraint. The violation of the equality is usually a sign of a persisting systematic in the data analysis pipeline. To quantify this violation, we define an *aperture mass* statistic which is obtained from linear combinations of the correlation functions. They have the advantage that they can be separated into the so-called *E*-mode and *B*-mode components.

$$M_E(\theta) = \frac{1}{4\pi} \int d^2\theta' \left[\xi_+(\theta') T_+ \left(\frac{\theta'}{\theta} \right) + \xi_-(\theta') T_- \left(\frac{\theta'}{\theta} \right) \right] \quad (2.52a)$$

$$M_B(\theta) = \frac{1}{4\pi} \int d^2\theta' \left[\xi_+(\theta') T_+ \left(\frac{\theta'}{\theta} \right) - \xi_-(\theta') T_- \left(\frac{\theta'}{\theta} \right) \right] \quad (2.52b)$$

where

$$T_+(x) = \frac{x^4 - 16x^2 + 32}{128} \exp\left(-\frac{x^2}{4}\right) \quad (2.53a)$$

$$T_-(x) = \frac{x^4}{128} \exp\left(-\frac{x^2}{4}\right) \quad (2.53b)$$

In the absence of systematic effects, $M_B(\theta) \ll M_E(\theta)$.

Tomography

The lensing formalism explained above is essentially two-dimensional as the lensing power spectrum involves an integral over the line-of-sight coordinate. By separating the source galaxies according to their redshifts and assigning them to one of the many, say N_z redshift bins, we can obtain multiple lensing fields. Since the lensing efficiency of a given overdensity is different for different redshifts, with the maximum occurring at $\chi = \chi_s/2$ (in a flat Universe), we can probe different epochs in the growth history of the Universe differently. This method, which goes by the name Shear Tomography, allows us to reconstruct the three-dimensional view of the Universe.

One can compute N_z auto correlation functions and $N_z(N_z - 1)/2$ cross correlation functions. For $i, j \in \{1, 2, \dots, N_z\}$, we define

$$C_{\gamma\gamma}^{ij}(\ell) = C_{\kappa\kappa}^{ij}(\ell) = \int_0^\infty dz \frac{W_i(z)W_j(z)}{\chi^2(z)H(z)} P_\delta \left(k = \frac{\ell}{\chi(z)}, z \right) \quad (2.54)$$

One can also define a cross correlation between two different fields, such as between the shear and the convergence as

$$C_{g\kappa}^{ij}(\ell) = \int_0^\infty dz \frac{W_{g,i}(z)W_j(z)}{\chi(z)H(z)} P_{g\delta} \left(k = \frac{\ell}{\chi(z)}, z \right) \quad (2.55)$$

and galaxy-galaxy power spectrum $C_{gg}^{ij}(\ell)$. Tomography is an approximate method of 3D lensing [29] and was applied to CFHTLenS Lensing data [30] to find the cosmological parameters.

Practical estimates of shear

Galaxies have a wide distribution of their observed brightness. In a given area of the sky, the faint galaxies outnumber the bright galaxies. However, faint galaxies have a lower signal-to-noise (SNR) ratio compared to the brighter ones. Thus, practical estimates of the shear must account for the difference in their SNR by giving higher weights to the brighter ones and low weights to the fainter ones.

$$\hat{g}_i = \frac{\sum w_a \hat{\epsilon}_i^a}{\sum w_a} \quad (2.56)$$

A commonly adopted weighting scheme is the inverse-variance weighting scheme with weights defined as

$$w_a = \frac{1}{\sigma_{\text{SN}}^2 + \sigma_\epsilon^2}, \quad (2.57)$$

where σ_{SN} is the shape noise and σ_ϵ is the measurement noise. For a given set of weights, the shear correlation function estimator is then given as

$$\hat{\xi}_{\pm}^{AB}(\theta) = \frac{\sum_{a \in A, b \in B} w_a w_b [\hat{\epsilon}_+^a \hat{\epsilon}_+^b \pm \epsilon_x^a \hat{\epsilon}_x^b]}{\sum_{a \in A, b \in B} w_a w_b} \quad (2.58)$$

2.2.2 Systematic effects

During the process of acquiring the image, the image of the galaxies are smeared by the atmosphere (known as ‘seeing’) and then by the optics of the telescope. The smearing varies spatially and also temporally. The galaxy is observed against the zodiacal background light in the sky, which is a significant contributor to the Poisson noise in the image. The light profile is then pixelated at the detectors of the telescope and then read out using electronics that have their own noise characteristics. In addition to noise, detectors can introduce minor artifacts in the images due to their non-ideal behavior. For a pedagogical review of systematic effects from instrumentation, see [31].

During the shape measurement process, multiple exposures are *co-added* to boost the signal-to-noise ratio. For space-based surveys, exposures which are offset from each other by a fraction of the pixels are combined to give an image with higher resolution.

From this science image, one identifies the source objects using an automated software such as SExtractor [32]. Identifying two or more objects that are overlapping with each other, a problem known as *deblending* continues to be one of the problem that is not completely solved yet.

Given a catalog of shapes for the galaxies, we can construct a shear field on the sky using the estimator in Eq. 2.56. However, we do not get to observe the shape of the lensed image of the galaxies directly. Generation of a shape catalog is preceded by an image processing pipeline with multiple steps, each of which could introduce uncertainty and error in the shapes of the galaxies.

The main effect of the PSF on galaxy images is that it makes an elliptical source rounder: a small source (small compared to the PSF size) with a large ellipticity will appear as a fairly round image. An anisotropic PSF makes round sources look elliptical, mimicking a shear. Often times, the PSF is not completely known. Even if the PSF is known completely, the PSF correction schemes are only approximate in one way or another, leading to some residual effects and hence biasing the shear estimates. Moreover, usage of biased weights leads to biased estimates as well. Thus, the estimate $\hat{g} \neq g^{(\text{true})}$ but some function of the true shear. If $|g^{(\text{true})}| \ll 1$, then we could ignore the higher order terms and express \hat{g} as a linear function of $g^{(\text{true})}$. Following the parametrization in [33], we relate the measured shear $\hat{\gamma}$ and the true shear $\gamma^{(\text{true})}$ by a linear relation as

$$\hat{\gamma}_i(z_s, \boldsymbol{\theta}) = (1 + m_i(z_s, \boldsymbol{\theta}))\gamma_i^{(\text{true})}(z_s, \boldsymbol{\theta}) + c_i(z_s, \boldsymbol{\theta}), \quad (2.59a)$$

$$\hat{g}_i(z_s, \boldsymbol{\theta}) = (1 + m_i(z_s, \boldsymbol{\theta}))g_i^{(\text{true})}(z_s, \boldsymbol{\theta}) + c_i(z_s, \boldsymbol{\theta}), \quad (2.59b)$$

where m s are the multiplicative calibration biases and c s the additive shear biases. If we knew the bias parameters exactly, we could subtract them off from our measurements or include them in our models. However, it is not possible to know them precisely since they have complex dependencies on various quantities. The shear calibration biases depend on the galaxy ellipticity, its size, brightness etc. and thus an indirect dependency on the source redshift z_s . Thus, one can estimate a distribution of the systematic bias values and hope that the residual errors are small.

For the linear model given in Eqs. 5.20,

$$\langle \hat{\gamma} \hat{\gamma} \rangle = (1 + m)^2 \langle \gamma^{(\text{true})} \gamma^{(\text{true})} \rangle + 2(1 + m) \langle c \gamma^{(\text{true})} \rangle + \langle cc \rangle \quad (2.60)$$

$$\langle g \hat{\gamma} \rangle = (1 + m) \langle g \gamma^{(\text{true})} \rangle + \langle gc \rangle \quad (2.61)$$

, where g refers to the galaxy position (and *not* the reduced shear). For large areas, assuming that the additive bias is uncorrelated with the local shear, $\langle gc \rangle = 0 = \langle c \gamma^{(\text{true})} \rangle$. Taking the Fourier transform the shear-shear correlation, we get (see [34] for details)

$$\hat{C}(\ell, z_i, z_j) = \sum_{\ell'} (1 + \mathcal{M}(\ell, \ell', z_i, z_j)) C(\ell', z_i, z_j) + \mathcal{A}(\ell, z_i, z_j) \quad (2.62)$$

Thus, \mathcal{M} mixes different scales as well as the true E -mode signals with unphysical B -modes. In terms of the mean multiplicative bias $\langle m \rangle$, $\mathcal{M} = 2 \langle m \rangle + \langle m^2 \rangle \approx 2 \langle m \rangle$. While it may be possible to estimate the mean values of m and c analytically, they hold true only for special cases, such as modelling galaxies Gaussian light profiles and using unweighted second moments to calculate the galaxy sizes and shapes. In practice, one way to estimate the bias parameters is from image simulations. By forward simulating the images of galaxy fields with some input lensing shear or lensing power spectrum that also incorporate realistic effects such as smearing due to a PSF, pixelization and inclusion of noise, we can compare the estimated shear from a given shape measurement algorithm to the true shear and estimate the calibration bias parameters. For an accurate estimation of the biases, it is important that the simulated images are as realistic as possible. Several community-wide blind image analysis challenges such as the Shear TESting Programme [STEP; 33, 35] and GRavitational IEnsing Accuracy Testing challenges [GREAT; 36, 37, 38] have been held in the past, testing different aspects of the shear estimation pipeline in different challenges.

Prior works such as [34, 39] discuss the effects of systematic bias in cosmic shear. using Fisher analysis and its extensions.

Following is a summary of the conclusions from [34]. For the Euclid ¹ mission, in order to ensure that the bias on the dark energy equation of state parameter w is less than

¹www.euclid-ec.org

31% of the statistical error for 95% of the random realizations, one requires

$$\overline{\mathcal{A}} \lesssim 1.8 \times 10^{-12} \qquad \overline{\mathcal{M}} \lesssim 4.0 \times 10^{-3} \qquad (2.63)$$

This translates to $m \lesssim 2.0 \times 10^{-3}$ and $c \lesssim 1.4 \times 10^{-6}$. Less stringent requirements are given in [40] which were used in the GREAT3 challenge [38].

Chapter 3

The impact of cosmic variance on simulating weak lensing surveys

Journal reference: Monthly Notices of the Royal Astronomical Society 449.4 (2015): 3597-3612

Original authors: Arun Kannawadi, Rachel Mandelbaum, Claire Lackner

Original abstract: Upcoming weak lensing surveys will survey large cosmological volumes to measure the growth of cosmological structure with time and thereby constrain dark energy. One major systematic uncertainty in this process is the calibration of the weak lensing shape distortions, or shears. Most upcoming surveys plan to test several aspects of their shear estimation algorithms using sophisticated image simulations that include realistic galaxy populations based on high-resolution data from the Hubble Space Telescope (*HST*). However, existing datasets from the *HST* cover very small cosmological volumes, so cosmic variance could cause the galaxy populations in them to be atypical. A narrow redshift slice from such surveys could be dominated by a single large overdensity or underdensity. In that case, the morphology-density relation could alter the local galaxy populations and yield an incorrect calibration of shear estimates as a function of redshift. We directly test this scenario using the COSMOS survey, the largest-area *HST* survey to date, and show how the statistical distributions of galaxy shapes and morphological parameters (e.g., Sérsic n) are influ-

enced by redshift-dependent cosmic variance. The typical variation in RMS ellipticity due to environmental effects is 5 per cent (absolute, not relative) for redshift bins of width $\Delta z = 0.05$, which could result in uncertain shear calibration at the 1 per cent level. We conclude that the cosmic variance effects are large enough to exceed the systematic error budget of future surveys, but can be mitigated with careful choice of training dataset and sufficiently large redshift binning.

3.1 Introduction

Weak gravitational lensing, the deflection of light by mass, is one of the cleanest ways to study the nature of dark energy by tracking the growth of structure in the Universe as a function of time [e.g., 41, 42, 43]. As light from background sources passes by matter (including dark matter) on its way to us, the apparent shapes of the background galaxies get distorted, and the galaxies get slightly magnified as well. Because of its sensitivity to dark matter and dark energy, major surveys such as the Hyper Suprime-Cam [HSC; 44], Dark Energy Survey [DES; 45], the Kilo-Degree Survey [KIDS; 46], the Panoramic Survey Telescope and Rapid Response System [PanSTARRS; 47], the Large Synoptic Survey Telescope [LSST; 48], Euclid¹ [49], and Wide-Field Infrared Survey Telescope [WFIRST; 50] the Large Synoptic Survey Telescope [LSST; 48], Euclid² [49], and Wide-Field Infrared Survey Telescope [WFIRST; 50] are planned for the next two decades to gather enormous quantities of weak lensing data that will lead to precise constraints on the growth of structure with time, and therefore cosmological parameters.

For the upcoming surveys to achieve their promise, their systematic error budgets must be below their statistical error budgets. Systematic error budgets for weak lensing surveys typically include astrophysical effects, such as intrinsic alignments of galaxy shapes with large scale density fields [e.g., 51] and the effect of baryons on the matter power spectrum [e.g., 52, 53], as well as observational uncertainties such as the ability to robustly infer shears from observed galaxy shapes or photometric redshifts from their observed colours. Given the expected sub-per cent statistical errors on upcoming surveys, systematic errors must be reduced from their typical level in the current state-of-the-art measurements that typically achieve ~ 5 per cent statistical errors at best [e.g., 54, 55, 56, 57].

Some types of information about and tests of shear estimation for ongoing and future weak lensing surveys will rely on data from the Hubble Space Telescope (*HST*). For example, data from *HST* can be used to derive basic statistics of galaxy light profiles, such as joint distributions of size and the morphology. It can be used to infer the intrinsic distribution of galaxy shapes, which enters the shear estimation process

¹<http://sci.esa.int/euclid/>, <http://www.euclid-ec.org>

²<http://sci.esa.int/euclid/>, <http://www.euclid-ec.org>

either implicitly or explicitly depending on the method used for shear estimation [see, e.g., 58]. Going beyond basic information about the light profile, *HST* can be used to quantify the detailed morphology of galaxies, due to its higher resolution compared to any current or planned weak lensing survey. Finally, it can be used to address systematics due to colour gradients within galaxies, which are particularly problematic when combined with a wavelength-dependent diffraction-limited PSF [e.g., 59, 60].

One method that is commonly used to test for the presence of systematic errors in the shear estimation process is image simulation, where we can cleanly test whether our methods of shear estimation recover the ground truth. This is a valuable test, considering the numerous sources of additive and multiplicative bias such as a mismatch between galaxy model assumptions and actual galaxy light profiles [e.g., 61, 62], biases due to the effects of pixel noise on the shear estimates [63, 64, 65], and ellipticity gradients [66]. These biases often differ for galaxies with different morphologies (e.g., disks vs. ellipticals), sizes, S/N , and shape [67, 68]. A general requirement for simulations used to test shear recovery is that they should be as realistic as possible.

Realistic simulations may use samples based on images from the (*HST*). Software packages like GALSIM³ [69] can generate images of galaxies from the *HST* as they would appear with an additional lensing shear and viewed by some lower resolution telescope. Examples of training samples from the *HST* include the COSMOS survey [used by the GREAT3 challenge, 38] or the Ultra Deep Field [UDF, used by 56]. These two examples serve as the extremes in the *HST* samples used as the basis for image simulation, with COSMOS being the widest contiguous area surveyed by the *HST* currently and hence representative, and the latter being extremely deep but narrow.

For a variety of physical reasons, some of which are still not fully understood, the shape and morphology of galaxies depends on their local environment [e.g., 70, 71]. Hence, local overdensities or underdensities along the line of sight observed in these *HST* fields may (given the small size of the field) cause the properties of the galaxy population in redshift slices to be atypical depending on the environment in that slice. This has the undesired consequence of including a variation in galaxy properties due to the COSMOS (or other) survey cosmic variance in the simulated galaxy sample

³<https://github.com/GalSim-developers/GalSim>

in that redshift slice, rather than only including ensemble effects that would appear in a large cosmological volume, such as true redshift evolution of galaxy properties. Our goal is to quantify the degree to which the morphology-density correlations in COSMOS cause noticeable changes in the galaxy populations in narrow redshift slices at a level that could result in difficulty using the sample to derive redshift-dependent shear calibrations. Upcoming surveys will study lensing as a function of redshift and therefore need to simulate galaxy samples at different redshifts in order to assess the shear calibration at each redshift.

The paper is structured as follows: in Sec. 3.2, we describe the data that we use for this study. In Sec. 3.3, we describe our methods for deriving the relevant galaxy properties like environment, morphology, and shape. Using these ingredients, we present our results in Sec. 3.4 and discuss their implications in Sec. 3.5, concluding in Sec. 3.6.

3.2 Data

The COSMOS survey [72, 73, 74] is a flux-limited, narrow deep field survey covering a contiguous area of 1.64 deg^2 of sky, with images taken using the Advanced Camera for Surveys (ACS) Wide Field Channel (WFC) in the Hubble Space Telescope (HST). We use the COSMOS survey to define a parent sample of galaxy images to be used for making image simulations, following the approach taken in [38, 75].

We apply the following set of initial cuts to the COSMOS data, the first two of which are motivated and explained in more detail by [74]:

1. **MU_CLASS=1**: This criterion uses a comparison between the peak surface brightness and the background level to achieve a robust star/galaxy separation, with galaxies having **MU_CLASS=1**.
2. **CLEAN=1**: Objects near bright stars or those containing saturated pixels were removed; the rest pass this cut on **CLEAN**.
3. **GOOD_ZPHOT_SOURCE =1**: This cut requires that photometric redshifts be reliable and good enough to draw conclusions about the population (see [75] for details).

High resolution images taken through the wide F814W filter (broad I) for all galaxies

passing the above cuts were used to create a collection of postage stamp images for the GREAT3 challenge [38], using the procedure described in [75]. Each galaxy postage stamp image has a corresponding PSF image that can be used by GALSIM or other software to remove the effects of the *HST* PSF before simulating the galaxy image as it would appear at lower resolution.

To better characterize the galaxy population, parametric models were fit to the light profiles of these galaxies. These were carried out using the method described in [76], and include Sérsic profile fits and 2 component bulge + disk fits described in detail in [38] and briefly in Sec. 3.3.3 of this work.

In addition to the ACS/WFC (F814W) imaging, the COSMOS field has also been imaged by Subaru Suprime-Cam, the Canada-French Hawaii Telescope (CFHT) and KPNO/CTIO, yielding many bands of imaging data used to determine high-fidelity photometric redshifts. Photometric redshifts were determined by [77]. The accuracy of photometric redshifts for $m_{\text{F814W}} \leq 22.5$ is $\sigma_{\Delta z} = 0.007(1 + z)$; for $m_{\text{F814W}} \leq 24$, $\sigma_{\Delta z} = 0.012(1 + z)$. The photometric redshift values become noisier beyond $z \sim 1.2$, and the fits to the galaxy light profiles are also somewhat noisy once we go beyond $m_{\text{F814W}} \sim 23.5$. For this reason, we will exclude all galaxies that have F814W magnitude fainter than 23.5. However, we will use the $m_{\text{F814W}} \leq 25.2$ sample that was generated for the GREAT3 challenge to estimate the completeness, which is useful when generating a volume-limited sample (Sec. 3.3.2). We first use the $z \leq 1.25$ flux-limited sample to fit parametric redshift distribution models (Sec. 3.3.1), and then restrict ourselves to $z \leq 1$ sample for all further analysis.

Stellar mass estimates were obtained [78] using the Bayesian code described in [79]. This process involves constructing a grid of models that vary in age, star formation history, dust content and metallicity (always assuming a Chabrier IMF; [80]), to which the observed galaxy spectral energy distributions (SEDs) and photometric redshift are compared. At each grid point, the probability that the SED fits the model is calculated, and by marginalizing over the nuisance parameters in the grid, the stellar mass probability distribution is obtained. The median of this distribution is taken as the stellar mass estimate.

3.3 Methods

In order to study the variation in the intrinsic ellipticity distribution and various morphological indicators with the galaxy environment, there are three main steps to be carried out:

1. Identify overdense and underdense environments along the line of sight in our survey from the redshift distribution of galaxies (Sec. 3.3.1);
2. volume-limit the sample such that Malmquist bias is minimized before comparing galaxies in different redshift slices (Sec. 3.3.2); and
3. estimate the galaxy axis ratios and other morphological indicators such as Sérsic index and bulge-to-total ratios (Sec. 3.3.3).

In this section we will describe how these steps were carried out.

3.3.1 Finding overdensities

It is important to keep in mind when considering the environment estimation that our goal is not to create a full 3D mapping of the density field within the COSMOS region (a task that was already addressed by [81] using the zCOSMOS spectroscopic sample). Instead, we make a coarse, 1-dimensional, line of sight division of the COSMOS survey into redshift slices, just as would be done when making galaxy redshift slices as input to a weak lensing survey simulation. For each redshift slice, we can then check whether the environment is overdense or underdense on average. Our approach will tend to wash out some real trends from a 3D study, but is appropriate given our scientific goal of testing effects of the environment on weak lensing simulations based on the COSMOS survey.

For our (flux-limited) sample of galaxies, up to $z = 1.25$, we fit parametric models to the histograms of photometric redshifts in order to assign values of overdensity. We choose our bins to be 0.05 wide starting from $z = 0.3$, where the bin width is selected to be somewhat larger than the photometric redshift error but narrow enough that we can still identify rather than averaging over real cosmological structures. We neglect the lowest redshifts which have negligible cosmological volume and where the galaxy

Flux-limited sample S_0

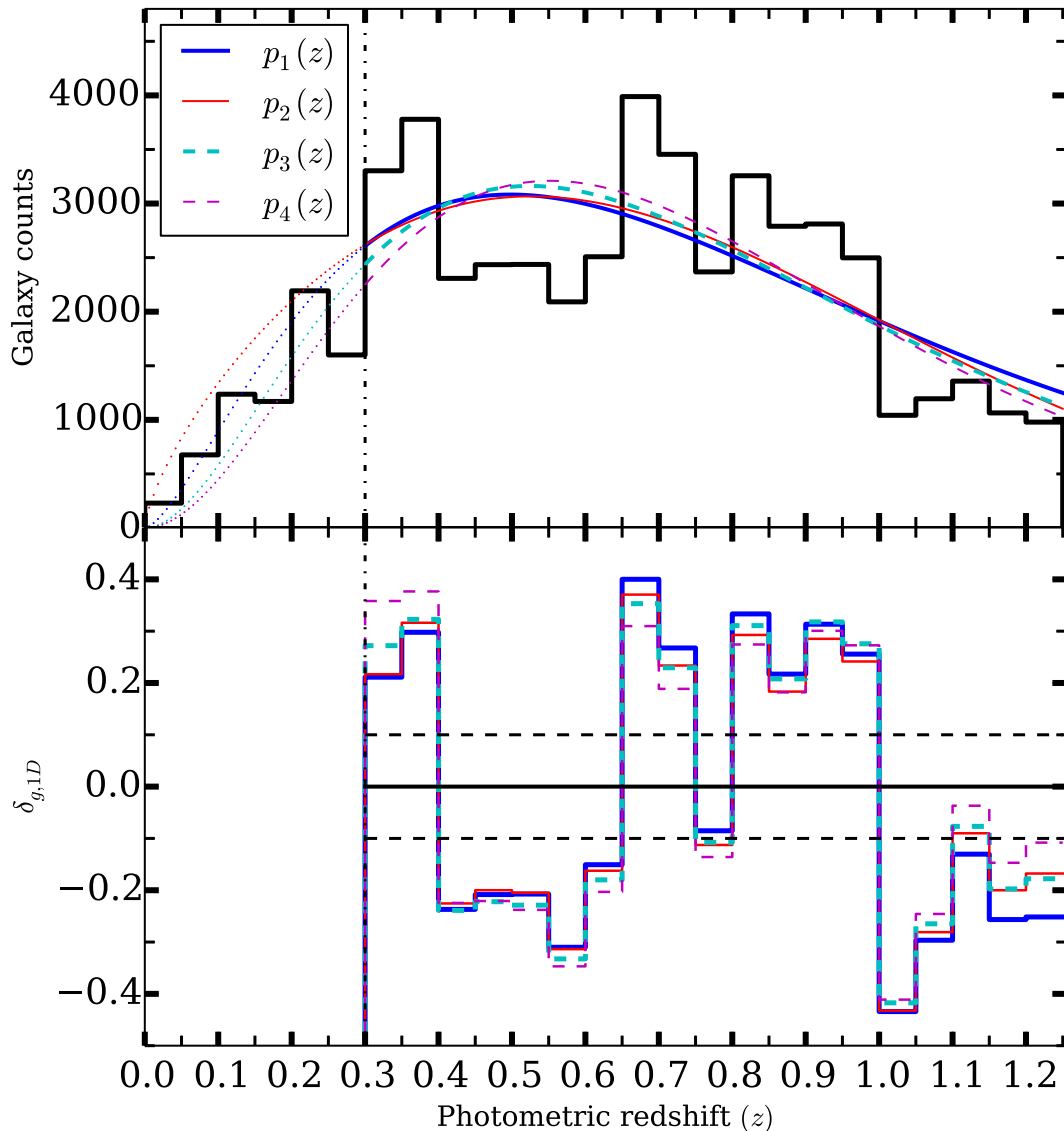


Figure 3.1: Upper panel: Redshift distribution of flux-limited ($m_{F814W} \leq 23.5$) sample with photometric redshift bins that are 0.05 wide. The vertical line at $z = 0.3$ indicates the delineation between lower redshifts that we do not use for our analysis, and higher redshifts that are used. Fits to two analytical functions, $p_1(z)$ and $p_2(z)$, defined in Eqs. 3.2 and 3.3, are also shown, with best-fitting parameters $a = 2.53 \pm 0.98$, $z_1 = 0.32 \pm 0.16$, $b = 1.70 \pm 0.50$ and $z_2 = 0.63 \pm 0.13$. We also show the distributions from [4] from Eqs. 3.4 and 3.5. Lower panel: Plot of $\delta_{g,1D} = N/N_{\text{mod}} - 1$ with each functional form as the model for each redshift bin.

population tends to be intrinsically bright and large enough that a non-negligible fraction is lost due to the cuts we impose (Sec. 3.2).

One of the most commonly used analytical expression for the redshift distribution in a magnitude-limited sample is

$$p(z) \propto \left(\frac{z}{z_0}\right)^\alpha \exp\left[-\frac{1}{2}\left(\frac{z}{z_0}\right)^\beta\right], \quad (3.1)$$

where α , β and z_0 are free parameters that are chosen to fit the data. While this functional form is convenient and is empirically seen to describe the data extremely well, the form could also be motivated from that of the Schechter function for the luminosity function. Intuitively, the power term captures the increase in the number of galaxies due to increase in the volume considered, while the exponential tail captures the decrease in the count due to the lack of bright enough galaxies.

The parametric redshift distributions that we use are

$$p_1(z) \propto z^{a-1} \exp[-z/z_1] \quad (3.2)$$

and

$$p_2(z) \propto z^{b-1} \exp\left[-\frac{1}{2}\left(\frac{z}{z_2}\right)^2\right] \quad (3.3)$$

Here a , b , z_1 and z_2 are free parameters that are to be determined. The normalization constants depend not only on the parameters but also on the lower and the upper limit of the redshifts considered, where we fix the normalization to ensure that the predicted number of galaxies in the range used ($0.3 < z < 1.25$) is equal to the actual number. Fig. 3.1 shows the photometric redshift histogram together with the best-fitting parametric distributions.

We compare our fits to the fits made by [4] using the DEEP2 galaxy redshift survey. Interpolating between their results for the $18 < I_{AB} < 23$ and $18 < I_{AB} < 24$ samples to our own limiting magnitude (and assuming equivalence of our I bands), we obtain the following redshift distributions:

$$p_3(z) \propto z^2 \exp[-z/0.262] \quad (3.4)$$

and

$$p_4(z) \propto z^2 \exp[-(z/0.361)^{1.2}] \quad (3.5)$$

which are also plotted in Fig. 3.1. Note that $p_3(z)$ is a special case of $p_1(z)$ with $a = 3$ and $z_1 = 0.262$; these parameter values are within the 1σ allowed regions for our fits to Eq. 3.2. Visually, these distributions appear quite similar to our own fits carried out here, which is reassuring given the use of different survey data and functional forms.

The estimated overdensity in a redshift bin is defined by comparing the observed galaxy counts in the bin with the counts that are predicted in that bin by one of the models in Eqs. (3.2) and (3.3):

$$\delta_{g,1D} = \frac{(N - N_{\text{mod}})}{N_{\text{mod}}}, \quad (3.6)$$

where

$$N_{\text{mod}} = \int_{z_{\text{min}}}^{z_{\text{max}}} p(z) dz \quad (3.7)$$

is determined by integrating the redshift distribution within the limits of that redshift slice. Note that $\delta_{g,1D}$ is dependent on our choice of model redshift distribution, and should have a mean value of 0 over the entire redshift range when weighted by the number fraction in each bin.

Our preliminary decision criterion for identifying overdense and underdense redshift slices involves leaving a 10 per cent margin around an overdensity of zero; i.e., if $|\delta_{g,1D}| < 0.1$, that is considered “neutral” (neither overdense nor underdense on average). We can then label each redshift slice as either overdense, underdense, or neutral as follows: We label a redshift bin as overdense if at least one model gives a value of $\delta_{g,1D} > 0.1$ while the other gives $\delta_{g,1D} > -0.1$ (neutral or overdense), and vice versa for the underdense regions. We label a redshift bin as neutral if both models give $\delta_{g,1D}$ within the neutral region, *or* if use of one model redshift distribution results in the conclusion that the bin is overdense while the other leads to the conclusion that it is underdense.

Once we volume-limit our sample (explained in Sec. 3.3.2), we again compare the histogram to the models. If there is no qualitative change in the overdensities, we stick with the preliminary decision. If the overdensity values flip in sign or become too

small, then we classify the redshift bin as ‘neutral’. The naive Poisson uncertainty of the counts in each bin is much less than the difference between the actual number of galaxies present and the number predicted by the models. For this reason, errorbars have been completely ignored.

We thus identify the regions $z = 0.30 - 0.40$, $0.65 - 0.75$, and $0.80 - 0.85$ as overdense; $z = 0.55 - 0.65$ and $0.75 - 0.80$ as underdense; and we defer classification of the somewhat ambiguous range from $z = 0.40 - 0.55$ until Sec. 3.3.2.

We have adopted this purely 1D environment classification for reasons explained at the beginning of this section. However, as a sanity check we can compare it with a more rigorous study that includes information about structure in the plane of the sky. [81] used a sample of $\sim 10\,000$ zCOSMOS spectroscopic galaxies with $I_{AB} < 22.5$ to reconstruct the three dimensional overdensity field up to $z \sim 1$. We find that our classification of overdensities and underdensities agrees with this work, except for our two highest redshift bins. We believe that this disagreement is due to the errors in our photometric redshifts, with the overdensity reported by [81] in the $z = 0.875 - 1$ range leaking into our $z = 0.80 - 0.85$ slice.

3.3.2 Volume-limiting

COSMOS is a flux-limited survey and is therefore affected by Malmquist bias, with the galaxy samples at higher redshifts being intrinsically brighter on average. Our analysis involves comparing galaxies in different redshift slices to identify significant differences in morphology that arise due to morphology-density correlations. Such an analysis would be very difficult with a flux-limited sample because there would be some variation in morphology with redshift just due to the intrinsic change in the sample properties. For a fair comparison, we must restrict ourselves to galaxies that are bright enough that they would be observed at all redshifts that we consider, which is achieved by volume-limiting the sample. We consider three different ways of carrying out this process, which results in three different galaxy sample selections, all of which we will use in the remainder of the analysis.

Call the flux-limited ($m_{F814W} \leq 23.5$) sample $\mathcal{S}0$. Our first approach is to generate a volume-limited sample that is complete up to $z = 1$, by applying a cut on luminosity

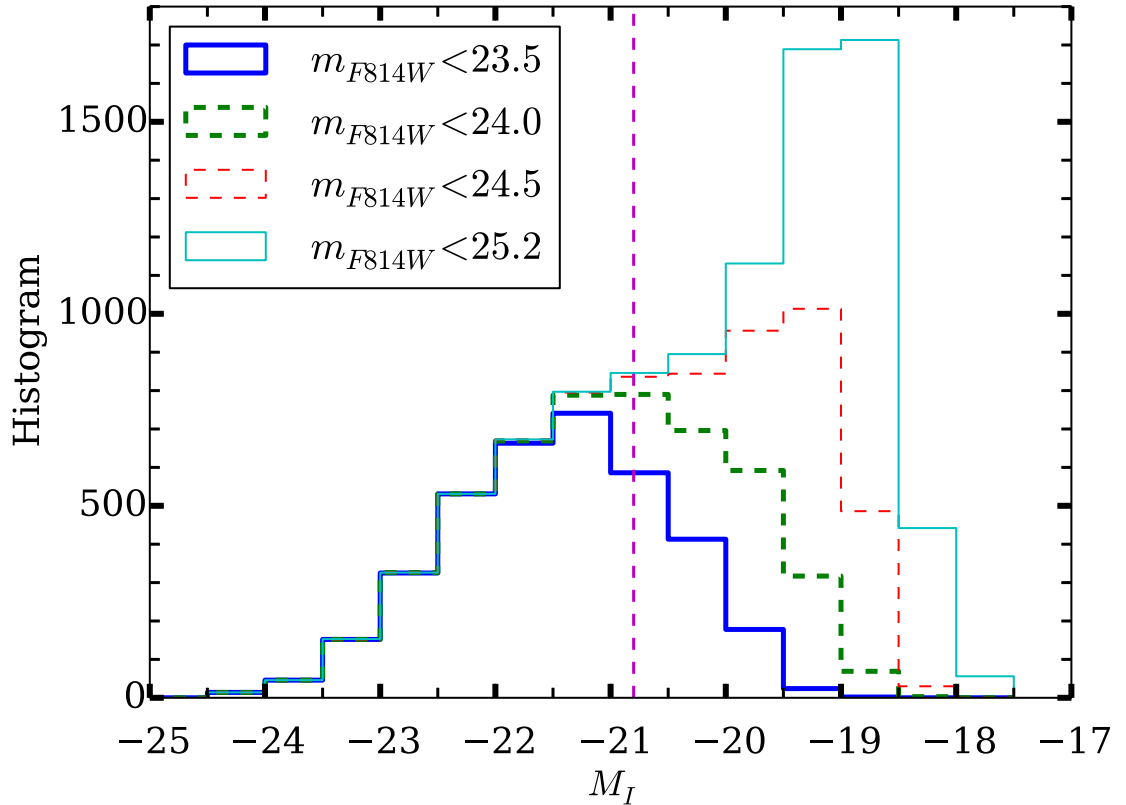


Figure 3.2: Distribution of absolute magnitude M_I for various flux-limited samples in the redshift range $[0.80, 0.85]$ are plotted together. The vertical line corresponds to our luminosity cut of -20.8 , brighter than which the $m_{F814W} < 23.5$ sample includes > 95.3 per cent of the galaxies in the $m_{F814W} < 25.2$ sample.

such that only galaxies intrinsically brighter than a certain threshold (determined in detail below) are considered. This threshold is set on the k -corrected I -band absolute magnitudes (M_I) from the COSMOS PSF-matched photometry catalog. Since the parent sample contains fainter galaxies and is quite complete to $m_{F814W} = 25.2$, we compare the M_I distribution of the $m_{F814W} = 23.5$ sample with flux-limited samples that have fainter flux limits, to see where the $m_{F814W} < 23.5$ sample that we want to use for our tests is no longer complete. At $M_I \sim -22.0$, the $m_{F814W} < 23.5$ sample is beginning to lose galaxies in the $0.9 < z < 1.0$ redshift bin due to the flux limit. However, the $0.85 < z < 1$ redshift bin was found to be only moderately overdense, so we choose to disregard this region for the rest of the analysis, and instead restrict to $z < 0.85$, which is advantageous because it allows us to choose a somewhat fainter intrinsic luminosity limit for the analysis. We relax our luminosity cut so that the sample is volume-limited *not* until $z = 1$ but until $z = 0.85$. We impose the cut at $M_I = -20.8$, which gives 95.3 per cent completeness in the $0.8 < z \leq 0.85$ bin (see Fig. 3.2). The resulting sample, which has 13 567 galaxies, will be called sample $\mathcal{S}1$ in the remainder of this work.

However, previous studies [e.g., 82, 83, 84, 85] have shown that galaxy intrinsic luminosities evolve with redshift. Thus, we should also let the luminosity cut that we apply to volume-limit the sample evolve with redshift. Unfortunately, the majority of the published work on evolution of the luminosity function uses B and V band data, and it is not apparent that the results should be the same in a redder passband like I . We use the results from [85] for the evolution of B -band magnitudes from the DEEP2 and COMBO-17 surveys, which is $\Delta M_B^* \sim -1.23$ mag per unit redshift (with the sign indicating that galaxies were intrinsically brighter in the past), for a combined sample of blue and red galaxies. Typically, estimates of evolution in the redder bands are less than the estimates of evolution in bluer bands [86, 87]. Assuming that the evolution is a smooth function of the wavelength, the evolution in I -band should be in between B and K band. Therefore, by considering no evolution (a lower limit) as in our $\mathcal{S}1$, and a second sample $\mathcal{S}2$ constructed using the B -band evolution (as an upper bound on the I -band evolution), we can assume that these two samples bracket reality.

Thus, $\mathcal{S}2$ is constructed by letting the luminosity cut evolve, starting from $M_I = -20.8$ (same as in $\mathcal{S}1$) for the $0.8 < z \leq 0.85$ bin. The cut values for the other bins are defined by allowing 1.23 magnitudes of evolution to fainter magnitudes as a

function of redshift (evaluated using the bin centers). Because of the sign of redshift evolution, $\mathcal{S}2$ includes more galaxies (15 903 galaxies).

One might wonder why we cannot use the luminosity function in F814W based on the COSMOS observations to directly determine the rate of evolution of the luminosity function for our sample, thus simplifying this exercise. However, this turns out to be highly non-trivial for two reasons. First, the F814W observations are relatively shallow compared to the deep ground-based observations used in many other works for determination of luminosity evolution. As a result, it is difficult to get a handle on the faint end of the luminosity function, and the unknown faint-end slope turns out to be degenerate with the evolution of the typical luminosity. Second, the photometric redshift error is a complicating factor that requires sophisticated techniques to remove. A derivation of the I -band luminosity evolution is therefore beyond the scope of this work.

Finally, we can circumvent the problem of redshift evolution of the luminosity by imposing cuts on stellar mass instead. In Fig. 3.3, we show the stellar mass function (SMF) of our sample for various F814W flux limits. The shapes of the SMF curves we obtain are consistent with those in [5] at the high stellar-mass end. [5] report the SMFs for the ZFOURGE survey, which includes COSMOS. They calculated stellar masses using the procedure and software described by [88], using a set of models with exponentially declining star formation history [89] assuming a Chabrier IMF [80]. As done for M_I , we compare the stellar mass function of the $m_{\text{F814W}} \leq 23.5$ sample with that of the $m_{\text{F814W}} \leq 25.2$ sample. The sample with $\log(M/M_\odot) > 10.15$ is ~ 95 per cent complete in the redshift bin $0.75 \leq z < 0.85$ and has 8953 galaxies in total across all redshifts. Thus, we construct a third volume-limited sample $\mathcal{S}3$ by imposing the stellar mass cut mentioned above.

The numbers of galaxies in redshift slices are tabulated in Table 3.1 for all three ways discussed in this section of obtaining a volume-limited sample. The stellar-mass limited sample is the smallest, most likely because when converting from flux to stellar mass, the stellar mass-to-light ratios vary strongly with galaxy type, so red galaxies with high M_*/L simply have too low a flux compared to the blue galaxies at the same M_* , and are not observed.

There is one subtlety in our method used for estimating completeness. We have used

Redshift	Environment	$\mathcal{S}1$	$\mathcal{S}2$	$\mathcal{S}3$
0.3-0.4	Overdense	1726	2505	1260
0.4-0.475	Neutral	988	1312	708
0.475-0.55	Neutral	1410	1793	904
0.55-0.65	Underdense	1797	2193	1183
0.65-0.7	Overdense	2096	2321	1354
0.7-0.75	Overdense	1963	2155	1239
0.75-0.8	Underdense	1159	1196	675
0.8-0.85	Overdense	2428	2428	1630

Table 3.1: List of different redshift bins, their environmental classification and the number of galaxies per redshift bin for volume-limited samples constructed in three different ways: using a hard luminosity cut ($\mathcal{S}1$), using a redshift-dependent luminosity cut ($\mathcal{S}2$) and using stellar-mass cuts ($\mathcal{S}3$).

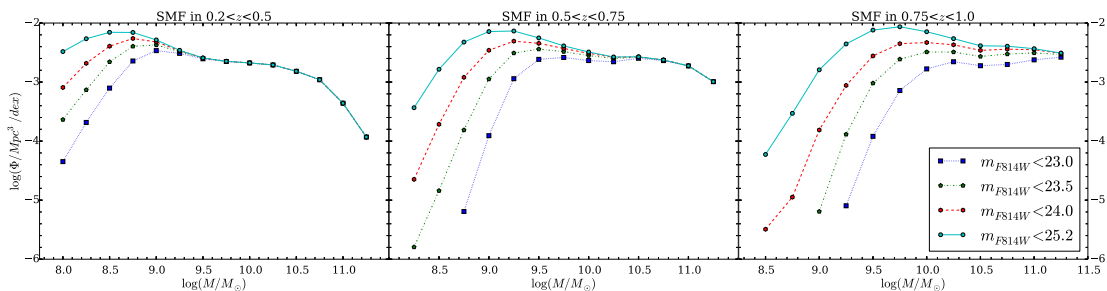


Figure 3.3: Stellar mass distribution for various flux-limited samples are shown in three redshift ranges as separate panels. The redshift bins have been chosen to facilitate the comparison with a study of the SMF in [5]. At high mass, the distributions are the same for various flux limits, indicating that the samples are complete in that mass range. The curves begin to deviate at low masses due to incompleteness coming from the flux limit. The point at which the deviation exceeds our threshold determines where the mass cutoff should be to volume-limit the sample.

the full $m_{\text{F814W}} \leq 23.5$ sample for identifying overdensities and for the completeness calculations that motivated our definitions of volume-limited samples. However, everywhere else in the paper, we consider only those galaxies for which there are postage stamp images used to create weak lensing simulations, in part because this is the sample for which fits to Sérsic profiles were carried out, which is a requirement for our morphology analysis. 12 per cent of the galaxies that pass our cuts do not have an associated postage stamp image. Postage stamps may not exist because, given the size of the galaxy, the size of the postage stamp we want to draw around it (including some blank space) intersects the edge of the CCD. If all galaxies were the same size, this would be a purely random effect, but in fact bigger galaxies are more likely to get excluded by this cut. It is commonly the case that galaxies that are nearby and intrinsically very bright do not have postage stamps associated with them, an effect that is dominant at lower redshifts (and is part of our reason for excluding $z < 0.3$). Our completeness calculation is done at high redshifts, and thus we believe that our conclusions are not affected by this bias.

The functional forms for the (flux-limited) redshift distribution that we used in Sec. 3.3.1 are not well-motivated for a volume-limited sample. If we fit them to the redshift distribution of the volume-limited sample ($M_I < -22$) that doesn't take into account the evolution of the luminosity function, then due to the absence of an exponential tail in the histogram, the parameters that set the scale for the redshift (z_1 and z_2) become very large. As a result, both $p_1(z)$ and $p_2(z)$ defined in Eqs. (3.2) and (3.3) essentially become the same power law. The best-fitting exponent is remarkably close to 2 ($a = 2.78 \pm 0.28$, giving an exponent 1.78 ± 0.28), suggesting that the comoving number density of galaxies is constant with redshift as we would expect for a volume-limited sample in a redshift range for which evolution is negligible. Fig. 3.4 shows that the values of $\delta_{g,1D}$ for the $z = 0.40 - 0.55$ bin increase and are within the $[-0.1, 0.1]$ range that we have defined as neutral. This is the reason that in Sec. 3.3.1 we classified them as neutral as opposed to underdense. We will see in Sec. 3.4 that they are more similar to overdense regions as opposed to underdense regions. The other redshift slices seem to exhibit a consistent behavior in Fig. 3.4 and Fig. 3.1.

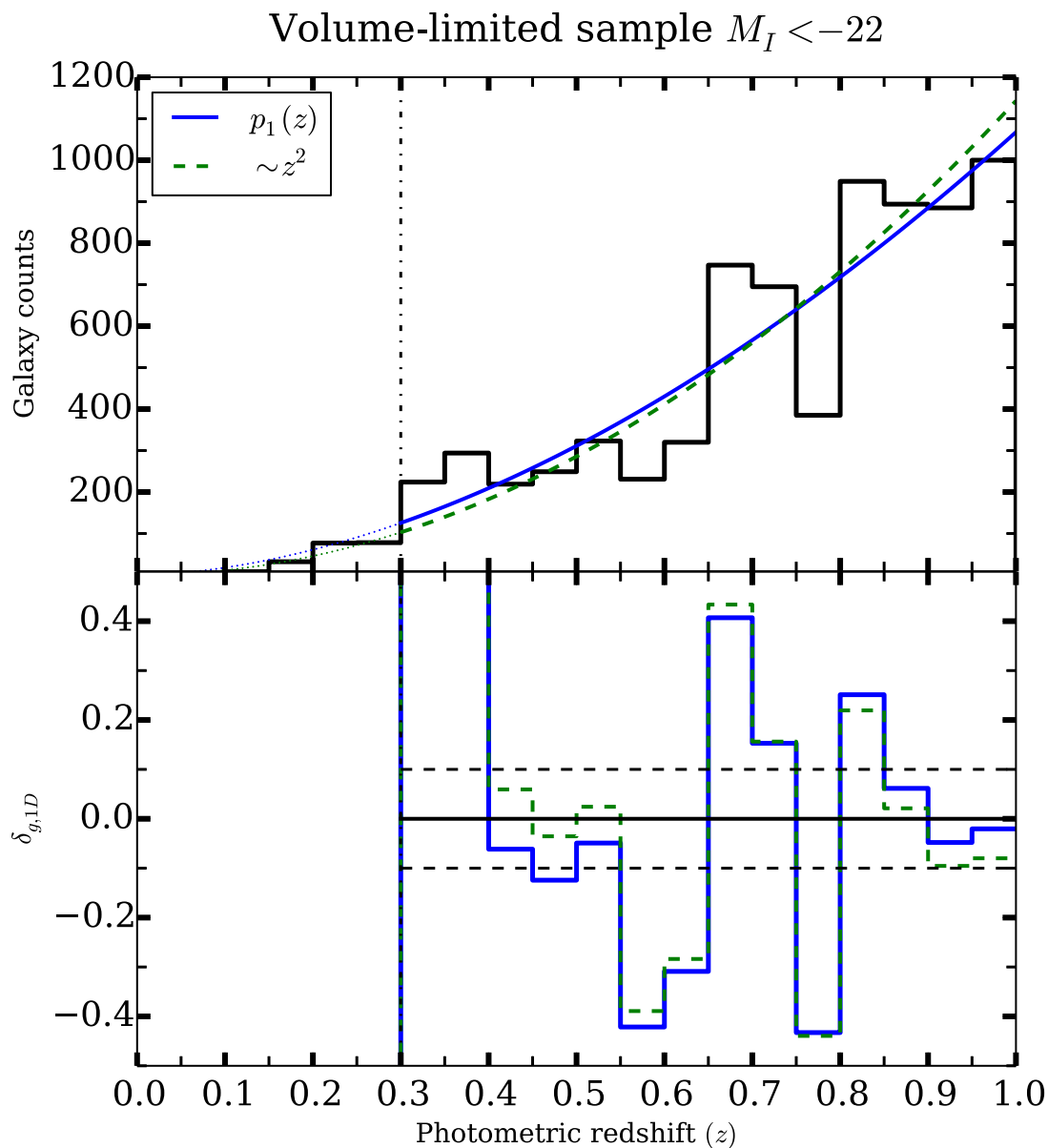


Figure 3.4: Upper panel: Redshift distribution of volume-limited ($M_I < -22$) sample with photometric redshift bins that are 0.05 wide. Two analytical functions with best fit parameters are plotted over it, as discussed in the text. Lower panel: Plot of $(1 + \delta_{g,1D}) = N/N_{\text{mod}}$ with each functional form as the model for each redshift bin.

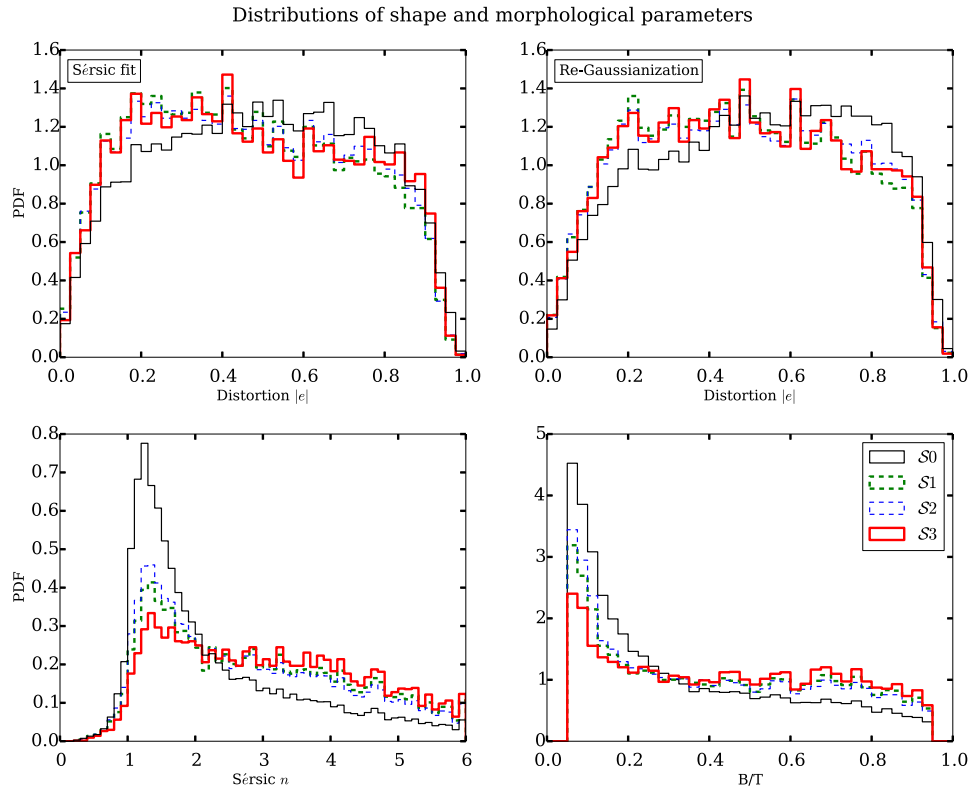


Figure 3.5: The distributions of the morphological parameters of interest, namely the distortion (top left, from Sérsic fits, and top right, from re-Gaussianization), Sérsic index (bottom left) and bulge-to-total ratio (bottom right) are presented. The shapes of these distributions depend on the way the volume-limiting process is carried out. $\mathcal{S}0$ refers to the flux-limited ($m_{F814} \leq 23.5$) sample and $\mathcal{S}1$, $\mathcal{S}2$ and $\mathcal{S}3$ refer to the volume-limited samples, as discussed in Sec. 3.3.2.

3.3.3 Describing galaxy morphology and shape

We choose simple and well-motivated ways to parametrize galaxy shapes and morphology based on existing methods in the literature. These methods have the advantage of being stable and well-defined in nearly all cases. However, for highly irregular galaxies the meaning of the structural parameters that we derive is not entirely clear. In all cases, our methods account for the effect of the *HST* PSF.

One method to estimate the galaxy ellipticities and other morphological parameters is to fit parametric models convolved with the PSF to the observed galaxy light profile.

We use the fits from [38], which used the methods and software from [76] to fit the images to the following profiles:

1. A Sérsic profile given by the expression

$$I_S(x, y) = I_{1/2} \exp \left[-k(R(x, y)/R_{\text{eff}})^{1/n} - 1 \right], \quad (3.8)$$

where

$$R^2(x, y) = ((x - x_0) \cos \Phi + (y - y_0) \sin \Phi)^2 + ((y - y_0) \cos \Phi - (x - x_0) \sin \Phi)^2 / q^2,$$

R_{eff} is the half-light radius of the profile defined along the major axis, $I_{1/2}$ is the surface brightness at $R = R_{\text{eff}}$, (x_0, y_0) is the centroid of the image, Φ is the position angle, n is the Sérsic index, k is a n -dependent normalization factor required to ensure that half the light is enclosed within the half-light radius, and q is the axis ratio of the elliptical isophotes. Thus, the Sérsic profile has 7 free parameters.

2. A sum of two Sérsic component fits: a de Vaucouleurs bulge ($n = 4$) plus an exponential disc profile ($n = 1$). In this case, there are 10 free parameters, because the Sérsic indices are fixed, and the two components are constrained to have the same centroid.

More details about the fitting algorithm can be found in [76].

To quantify galaxy morphology and shape, we will use several quantities from the above fits. First, from the single Sérsic profile fits, we use the Sérsic index and the axis ratio. The axis ratio can also be used to derive a distortion,

$$e = \frac{1 - q^2}{1 + q^2} \quad (3.9)$$

or an ellipticity,

$$\varepsilon = \frac{1 - q}{1 + q}. \quad (3.10)$$

As an alternative morphological indicator (instead of Sérsic index) we use a bulge-to-total ratio derived from the double Sérsic profile fits. This ratio is defined in terms

of bulge and disk fluxes as

$$\frac{B}{T} = \frac{F_{\text{bulge}}}{F_{\text{bulge}} + F_{\text{disk}}}. \quad (3.11)$$

The bulge-to-total flux ratio can be used as a proxy for colour gradients, since the bulge and disk will tend to have different spectral energy distributions, and hence any galaxy with $B/T \neq 0$ or 1 will have some level of colour gradients. If two galaxy samples have different values for the typical B/T , this is likely to indicate not only differences in morphology, but also in the level of colour gradients.

We also consider an alternative method for estimating the galaxy ellipticity or distortion. This method is based on using the observed weighted moments of the galaxy and PSF, and correcting those of the galaxy for those of the PSF. This PSF correction scheme is the re-Gaussianization method described in section 2.4 of [90] as implemented in the GALSIM software package (with implementation details described in [69]). This method models the true PSF $g(\mathbf{x})$ as a Gaussian $G(\mathbf{x})$ and the residual $\epsilon(\mathbf{x}) = g(\mathbf{x}) - G(\mathbf{x})$ is assumed to be small. Thus, the Gaussian-convolved intrinsic image, f , can be modeled as $I' = G \otimes f = I - \epsilon \otimes f$, where I is the observed image. The crucial idea here is that, when ϵ is small, we get a reasonably accurate estimate of I' even if we use an approximate form for f . The form assumed for f is that of a Gaussian with covariance $M_f^{(0)} = M_{(I)} - M_{(g)}$, where $M_{(I)}$ and $M_{(g)}$ are the elliptical Gaussian-weighted adaptive covariances of the measured object and PSF respectively, described in section 2.1 of [90] and [91]. We refer to the re-Gaussianization estimates of the PSF-corrected distortion as “moments-based shape estimates”. The value in including them in this analysis is that they have quite different radial weighting from the Sérsic profile fits, with the outer regions being quite downweighted when calculating adaptive moments. Thus, if ellipticity gradients are important, we could get different results using these two shape estimators.

Fig. 3.5 shows the distribution of these morphological and shape parameters for the flux-limited sample $\mathcal{S}0$ and the three volume-limited samples - $\mathcal{S}1$, $\mathcal{S}2$ and $\mathcal{S}3$. In addition to the basic value in characterizing these distributions for our sample overall, it is also useful to understand how the samples change when we vary our method of volume-limiting the sample. For instance, galaxies with lower Sérsic indices are preferentially selected in $\mathcal{S}2$ compared to $\mathcal{S}1$ and $\mathcal{S}3$. Similarly, galaxies with low ellipticity/distortion values are rejected in generating $\mathcal{S}2$ (despite the lack of any

explicit cut on shapes) while they are retained in $\mathcal{S}1$ and $\mathcal{S}3$. A simple explanation is that the cuts in $\mathcal{S}2$ are preferentially removing early-type populations, which have higher Sérsic indices and lower ellipticities. For example, if the luminosity evolution that was adopted is too strong particularly for early type populations, that could give rise to the effect shown in Fig. 3.5.

3.4 Results

Having identified the overdense and underdense regions in a volume-limited sample (Secs. 3.3.1 and 3.3.2), we will now see whether the morphological parameters of the galaxies described in Sec. 3.3.3 depend noticeably on the environment of the redshift slice in which they reside. Note that for true 3D overdensities there is already substantial evidence in the literature that we should see variation of properties with the environment. Our test is necessary to see whether such morphology-density correlations are evident in the kind of 1D redshift slices that would be used for constructing weak lensing simulations, or whether our use of an area as large as the size of COSMOS will wash out these trends (which would be good news for weak lensing simulations based on that dataset).

As described in Sec. 3.3.2, we have three different ways of volume-limiting our sample:

1. no redshift evolution of luminosity cut ($\mathcal{S}1$),
2. using B -band luminosity evolution applied to the I -band luminosities ($\mathcal{S}2$), and
3. impose stellar mass cuts instead of luminosity ($\mathcal{S}3$).

We will present our results in all three cases to check for their robustness to how the sample is selected.

3.4.1 Axis ratios

We can test the influence of environment on the galaxy shapes by comparing the distributions of the axis ratios for the overdense and underdense redshift slices, or by

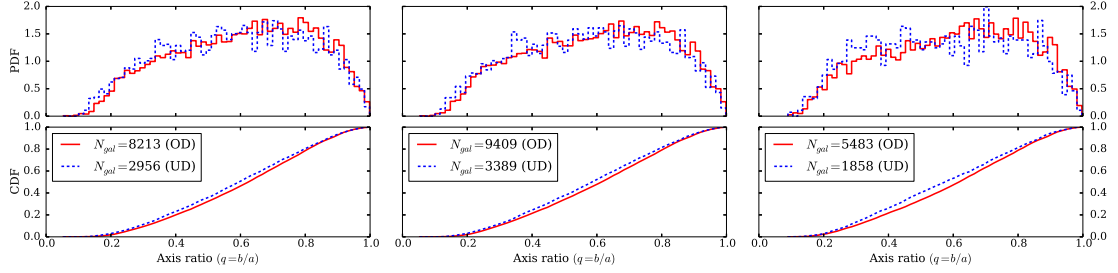


Figure 3.6: The distributions of axis ratios of galaxies in *all* overdense (OD) and *all* underdense (UD) regions in the case of the luminosity-selected sample $\mathcal{S}1$ (left), luminosity-selected sample with B -band evolution taken into account $\mathcal{S}2$ (center), and the stellar-mass-selected sample $\mathcal{S}3$ (right). The upper panels show the histograms, and the bottom panels show the cumulative distribution functions (CDF). The p -values computed using these CDFs are shown in Table. 3.2.

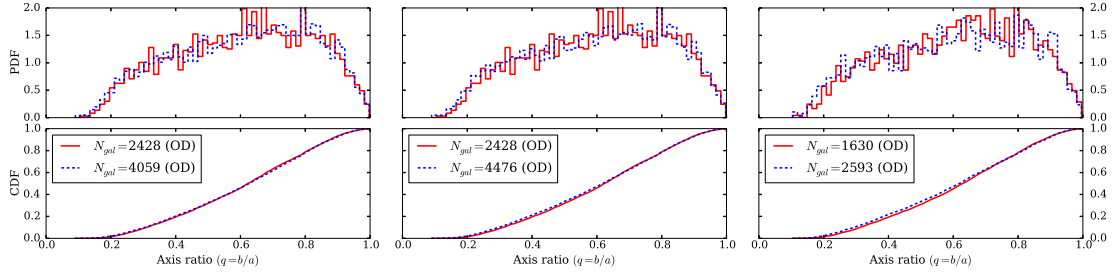


Figure 3.7: Galaxy axis ratio distributions in two overdense redshift bins, $z = 0.65 - 0.75$ (blue, dotted) and $z = 0.80 - 0.85$ (red, solid), to check for consistency in the case that the environment is the same even if the redshift differs. The p -values from the KS and AD tests are given in Table. 3.2.

encapsulating that distribution as a single number, the RMS (root mean squared) ellipticity or distortion. By volume-limiting the sample, we have avoided issues wherein the flux limit leads to artificial changes in the sample as a function of redshift. We will also carry out tests to differentiate between environmental effects versus evolution of the population with redshift (at fixed mass).

Comparing distributions

We begin by comparing the entire axis ratio distributions $p(q)$ between pairs of redshift slices. Unless otherwise mentioned, the axis ratios refer to the values obtained using the method of [76] to fit single Sérsic profiles to each galaxy image. To compare

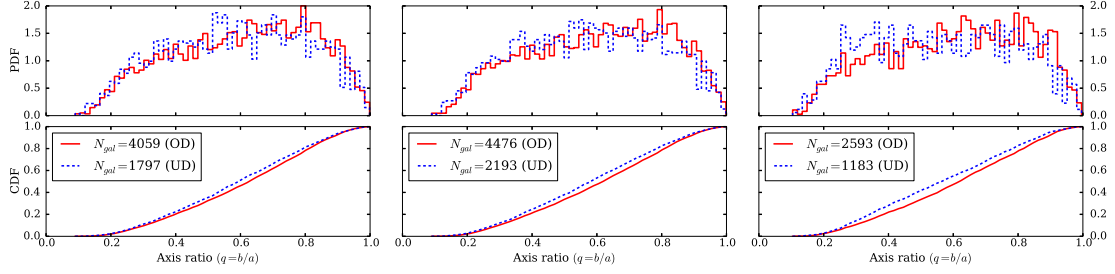


Figure 3.8: Galaxy axis ratio distributions in a single underdense redshift slice, $z = 0.55 - 0.65$ (blue, dotted), and a single overdense redshift slice, $z = 0.65 - 0.75$ (red, solid). The p -values from the KS and AD tests are given in Table. 3.2.

Redshift bins	$\mathcal{S}1$	$\mathcal{S}2$	$\mathcal{S}3$
All overdense vs. All underdense	1.1×10^{-4} 1×10^{-5}	2.6×10^{-5} $< 1 \times 10^{-5}$	1.9×10^{-6} $< 1 \times 10^{-5}$
[0.65, 0.75] (OD) vs. [0.80, 0.85] (OD)	0.61 0.49	0.43 0.24	0.23 0.13
[0.65, 0.75] (OD) vs. [0.55, 0.65] (UD)	5.8×10^{-4} 9.8×10^{-4}	1.5×10^{-5} $< 1 \times 10^{-5}$	3.5×10^{-6} $< 1 \times 10^{-5}$

Table 3.2: p -values from the Kolmogorov-Smirnov (top) and Anderson-Darling (bottom) tests obtained by comparing the distributions of axis ratios for three cases: *all* overdense (OD) vs. *all* underdense (UD), two overdense bins that are not very separated in redshift, and a pair of adjacent overdense and underdense bins. $\mathcal{S}1$, $\mathcal{S}2$, $\mathcal{S}3$ refer to the three different types of volume-limited samples. The Anderson-Darling p -values are computed only up to 5 decimal places, so values that were given as zero are denoted $< 1 \times 10^{-5}$.

Redshift bins	$\mathcal{S}1$	$\mathcal{S}2$	$\mathcal{S}3$
All overdense vs. All underdense	5.6×10^{-4} 3×10^{-5}	1.0×10^{-4} 1×10^{-5}	3.3×10^{-6} $< 1 \times 10^{-5}$
[0.65, 0.75] (OD) vs. [0.80, 0.85] (OD)	0.96 0.52	0.75 0.34	0.54 0.23
[0.65, 0.75] (OD) vs. [0.55, 0.65] (UD)	6.0×10^{-3} 1.2×10^{-2}	2.5×10^{-4} 2.5×10^{-4}	2.4×10^{-4} 5×10^{-5}

Table 3.3: p -values from the Kolmogorov-Smirnov (top) and Anderson-Darling (bottom) obtained by comparing the second moments-based distortion for the same three cases as in Table 3.2. The Anderson-Darling p -values are computed only up to 5 decimal places.

the distributions and make statistical statements about their consistency, we use two statistical tests, the Kolmogorov-Smirnov (KS) test and Anderson-Darling (AD) test, the latter of which is carried out using the `adk` package in R.

We first compare the distribution of galaxy axis ratios in *all* overdense bins against that for *all* underdense bins in Fig. 3.6, with different panels showing the comparison for $\mathcal{S}1$, $\mathcal{S}2$, and $\mathcal{S}3$. The cumulative distribution functions are also shown, since they form the basis for our statistical statements about consistency using the KS and AD tests. The results of these tests are shown in the first two rows in Table 3.2. For all three ways of volume-limiting the sample, the p -values from both the KS and AD tests are well below 0.05 (a maximum of 1.1×10^{-4} , but often smaller than that). We can therefore reject the null hypothesis that the overdense and underdense regions have the same underlying axis ratio distributions at high significance.

One might imagine that the disagreement between the distributions is, at least partly, due to the fact that the overdense and underdense sample have different redshift distributions and there could be some evolution of ellipticity/distortion distributions with redshift. To show that this redshift evolution effect is subdominant to environmental effects, we will compare distributions between pairs of two overdense (or pairs of underdense) redshift slices, where we expect to find similarity even if the redshifts are different if the environmental effects dominate. We will also compare between overdense and underdense regions that are selected to be nearby in redshift, so that any redshift evolution effects should be minimal. Figures 3.7 shows that the axis ratio distributions are indeed consistent when the environments are similar but the redshifts are different. Likewise Fig. 3.8 shows that for adjacent redshift slices with different environments, the axis ratio distributions are inconsistent. The results of statistical tests for the distributions in these figures are given in Table 3.2, and support our statement that the morphology-density correlation is the dominant effect when comparing overdense and underdense redshift slices, with redshift evolution of the population being negligible. Comparing other pairs of redshift bins leads to similar conclusions.

Finally, we can check whether these findings are particular to the axis ratios from the Sérsic fits, or whether we reproduce this finding when we use the shapes from the centrally-weighted moments-based re-Gaussianization method, which estimates a distortion (Eq. 3.9) for each galaxy. After neglecting a small fraction (< 0.01 per cent)

of galaxies for which the method does not converge, we carry out the same statistical tests from Table 3.2, but using the moments-based shape estimates. The results of the KS and AD tests are tabulated in Table 3.3. We see that all of our findings with the Sérsic fit-based shapes carry over to shapes from a centrally-weighted moments-based shape estimate.

RMS distortions

We can also carry out tests on a single statistic of the galaxy shape distribution in each redshift slice, like the RMS distortion. While tests of a single quantity may seem less powerful than tests that use the entire shape distributions, the advantage is that instead of picking out pairs of redshift slices for our tests, we can easily compute our statistic of interest for every single redshift slice, and look for trends with both redshift and environment.

For the luminosity-selected samples ($\mathcal{S}1$, $\mathcal{S}2$), the RMS distortions (Eq. 3.9) of galaxies in each redshift bin are shown in Fig. 3.9. In each case, the RMS distortions from the mass-selected sample ($\mathcal{S}3$) are also plotted. When the B -band luminosity evolution is taken into account in selecting the sample, a systematic increase in the distortion values at lower redshifts can be observed (bottom panel). The stellar-mass selected sample exhibits a similar trend.

For figures up to Fig. 3.12, the colours of the points were selected to easily differentiate between galaxies in overdense, neutral, and underdense redshift slices. Points with unfilled centers and thicker errorbars correspond to the $\mathcal{S}3$ sample and points with filled centers and thinner errorbars correspond to the luminosity-selected samples ($\mathcal{S}1$ or $\mathcal{S}2$).

As shown in Fig. 3.9, the underdense regions have higher values for RMS distortions when compared to the overdense regions. The difference between the underdense and overdense regions for $z > 0.5$ is significantly larger than any redshift evolution across the $z > 0.5$ range. Our conclusions are very similar if we use the RMS ellipticity from Eq. (3.10) instead of the distortions.

The sign of the dependence on the local environment is reasonable when compared with previous work on the morphology-density relation [see, e.g. 92]. Overdense

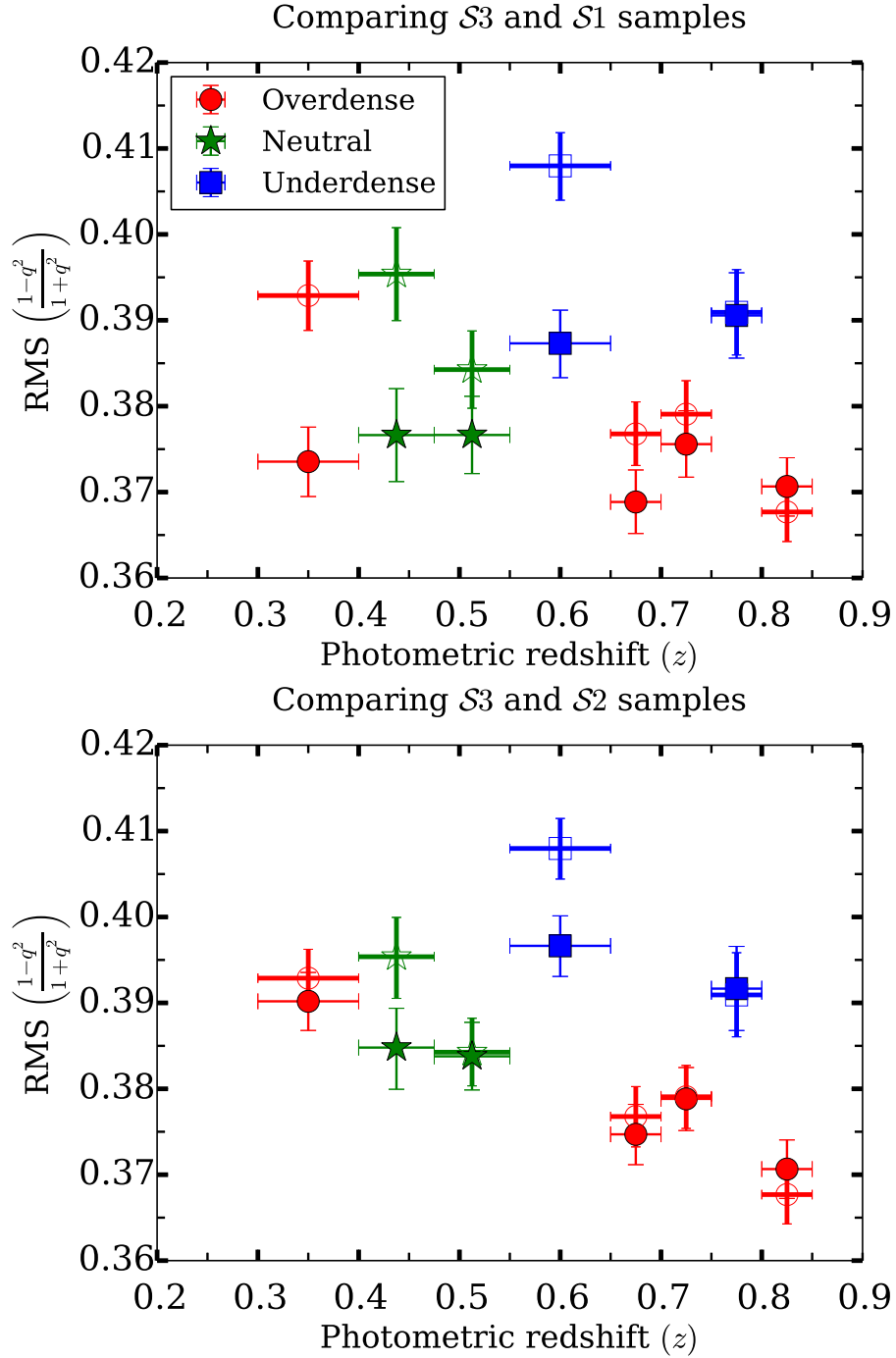


Figure 3.9: RMS distortions as a function of redshift. The horizontal errorbars indicate the width of the redshift bin, while the vertical ones are 1σ errorbars obtained by bootstrapping. The colours and shapes of the points indicate their environmental classification, as shown in the legend. Points with open centers and thick errorbars correspond to the stellar-mass selected sample $\mathcal{S}3$ and points with filled centers and thin errorbars correspond to the luminosity-selected samples $\mathcal{S}1$ and $\mathcal{S}2$.

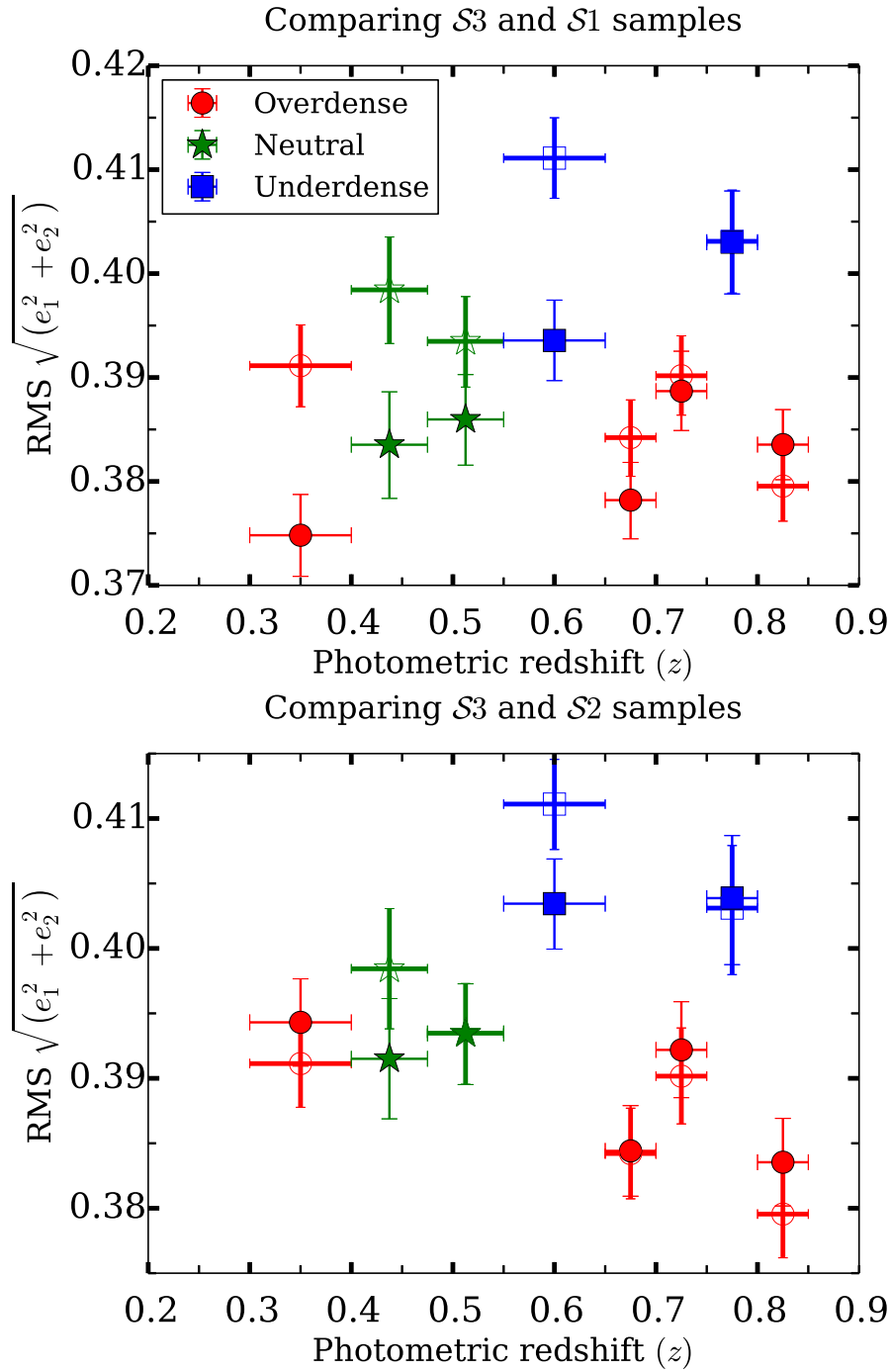


Figure 3.10: RMS distortions as a function of redshift, with points defined in a similar way as in Fig. 3.9. In this case, the distortions from moments-based shape estimates, rather than from the Sérsic fits.

regions typically contain many old, elliptical galaxies which are close to round (large axis ratio and low RMS ellipticity/distortion). In contrast, the underdense regions typically contain a larger population of younger, disk galaxies, which have lower axis ratios and higher RMS ellipticity/distortion.

From Figs. 3.1 and 3.4, the $0.4 \leq z < 0.55$ redshift range shows signs of being marginally underdense, but has low RMS ellipticity that agrees with the rest of the overdense regions.

Next, we show an analogous plot of RMS distortions for all three volume-limited sample using the moments-based shape estimates in Fig. 3.10. The conclusions are quite similar to those using the shapes from the Sérsic profile fits, with the underdense regions standing out in having larger RMS distortions than the other redshift slices, an effect that is substantially larger than any average redshift evolution of the RMS distortions.

However, the statistical significance of trends in this section using a single statistic of the shape distribution (the RMS) is less than the significance of the trends seen using the entire axis ratio distributions in Sec. 3.4.1.

Finally, we comment on whether the trends we have found could be caused by measurement noise rather than variations in the intrinsic shape distributions. Measurement error tends to cause an increase in the RMS ellipticity due to the broadening of the measured ellipticity distributions. However, this is one of the reasons we restricted the sample to a magnitude of 23.5. In this case, the S/N of the flux measured in the galaxy images is typically ≥ 50 . If we consider the worst case, i.e., assume all galaxies have $S/N = 50$ and use the Gaussian approximation from [91], the expected measurement error on the distortion is 0.08. If we add this in quadrature with an RMS of ~ 0.33 , then the new RMS becomes 0.34. However, we see variations in the RMS distortion in different environments that are as large as 0.05, or five times as large as this worst-case scenario due to measurement noise. Moreover, if measurement error were a significant issue, we would expect it to affect the comparison of (for example) low- and high-redshift samples in overdense regions. In a volume-limited sample, those will have different flux distributions and therefore different SNR distributions. However, there is little trend in the RMS distortion with redshift for overdense regions, which suggests empirically that measurement error is not a significant factor

in our results.

3.4.2 Morphological parameters

For the morphological parameters that we described in Sec. 3.3.3, the Sérsic index and bulge-to-total ratio, we do not compare the distributions directly. Doing so is relatively difficult because both distributions have hard cutoffs that are enforced in the fitting process (Sérsic n in the range $[0.25, 6]$ and $0.05 < B/T < 0.95$), as can be seen in Fig. 3.5. The KS statistical test is sensitive to exactly what happens at these hard boundaries in the distributions. So, instead of using the full distributions, we will study the dependence of these quantities on environment by computing the median values in different redshift slices. Median values are preferred over the full distributions or even the sample means since the medians are more robust to what happens at the edges of the distributions.

Fig. 3.11 shows the median value of the Sérsic index in each redshift slice, with and without taking into account of luminosity evolution when volume-limiting the samples ($\mathcal{S}1$ and $\mathcal{S}2$). Both panels also show the results with stellar mass-selected samples ($\mathcal{S}3$) for reference. When using the stellar mass-selected sample, we observe that the overdense regions tend to have higher Sérsic index than the underdense ones, with the redshift evolution being mild and the results for the underdense regions particularly standing out. This trend is consistent with our previous explanation for trends in RMS ellipticities; the underdense regions have more spiral galaxies and therefore a lower median value of Sérsic n . However, this trend is less evident for the luminosity-selected samples, where there seems to be some evolution with redshift that dominates over the environmental effects.

We also note that in Fig. 3.11, the median Sérsic indices of the stellar mass-selected samples ($\mathcal{S}3$) are systematically greater than those of the luminosity selected samples ($\mathcal{S}1$, $\mathcal{S}2$). This is because $\mathcal{S}3$ is restricted to galaxies with masses above $\log(M/M_\odot) > 10.15$, whereas in $\mathcal{S}1$ and $\mathcal{S}2$, the mass distribution of galaxies extends to $\log(M/M_\odot) \sim 9.0$, with about 44 per cent of the galaxies in $\mathcal{S}2$ having a stellar mass below the cut for $\mathcal{S}3$. It is therefore not surprising that $\mathcal{S}3$ has a higher median Sérsic n . Finally, even for the stellar mass-selected sample there is some sign of redshift evolution. The sign of this evolution is as expected, with lower Sérsic n and B/T for higher redshift

samples, which should have a higher fraction of disk and irregular galaxies and fewer galaxies with bulge-like morphology.

Finally, Fig. 3.12 shows the variation of the median bulge-to-total ratio with redshift. The results are quite consistent with those of Fig. 3.11. Thus, our results in this section suggest that the environment can significantly affect the median morphological parameters of galaxies selected in thin redshift slices, assuming that the galaxies represent a stellar mass-selected sample. The trend is less evident when using luminosity to select the galaxies.

One might expect the points corresponding to neutral regions to lie in between the points for overdense and underdense regions. In Figs. 3.9–3.12, this does not always appear to be the case. It is possible that a redshift bin may have an overdensity in one part of the field and an underdense region in another. In such a scenario, the redshift slice might appear to be ‘neutral’ in our histogram-based method of finding overdensities, while still having significant large-scale structure affecting the morphological mix of galaxies that complicates the situation. This indeed turns out to be the case in the ‘neutral’ regions of the COSMOS field. Using X-ray information in the COSMOS field, [78] have detected several galaxy groups in the redshift range $z = 0.425 - 0.575$. [81] report structures that are large and extended (in RA-DEC) within this redshift range. It is a challenge to make definitive statements regarding the relationship between environment and morphology in neutral regions that are composed of mixtures of multiple overdense and underdense regions. In addition, the redshift evolution, albeit weak, can make the neutral bins look like overdense or underdense regions. For instance, the neutral bins look overdense-like in Figs. 3.9–3.11 but underdense-like in Fig. 3.12, partly due to redshift evolution. However, when the overdensity (or underdensity) is prominent, we observe that the environment in which a galaxy resides affects its morphology, so the appearance of the neutral bins does not undermine the main conclusions of this paper.

To test the possibility that our choice of bins starting at $z = 0.3$ with $\Delta z = 0.05$ is particularly unlucky in enhancing the effects we see, we carried out the same analysis using bins of the same width but shifted by $\Delta z/2$. We recomputed the overdensities keeping the parameters of the redshift distributions same as before. Shifting the bins enhances the overdensities and underdensities in some cases and in other cases, it mixes the overdense and underdense regions to make them more neutral-like. The

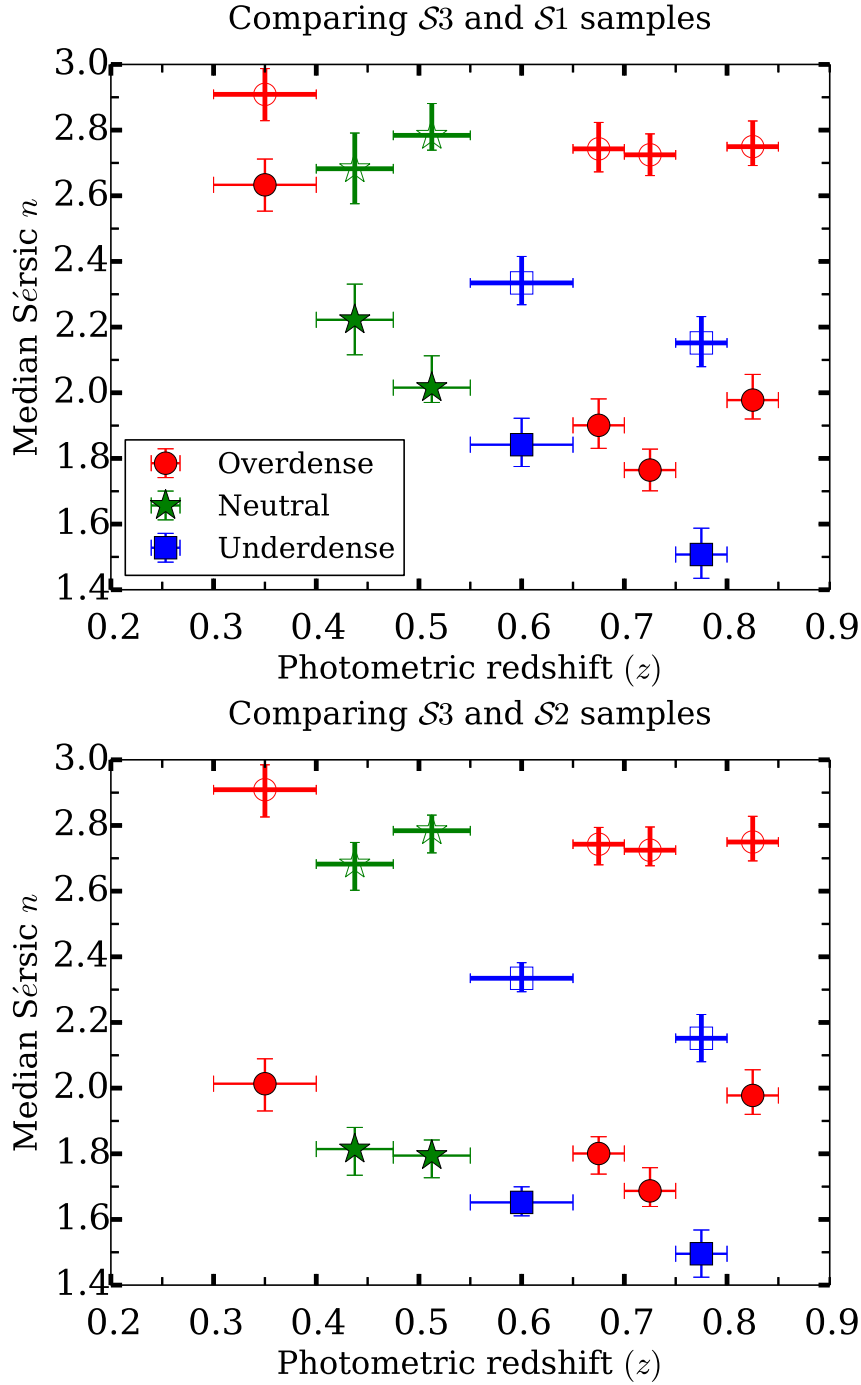


Figure 3.11: Median values of the Sérsic indices for volume-limited samples $\mathcal{S}1$ and $\mathcal{S}2$ are plotted (filled centers and thin errorbars) in top and bottom panels, respectively, for each redshift bin. Median values for the $\mathcal{S}3$ sample are plotted in both the panels (open centers and thick errorbars) in both the panels.

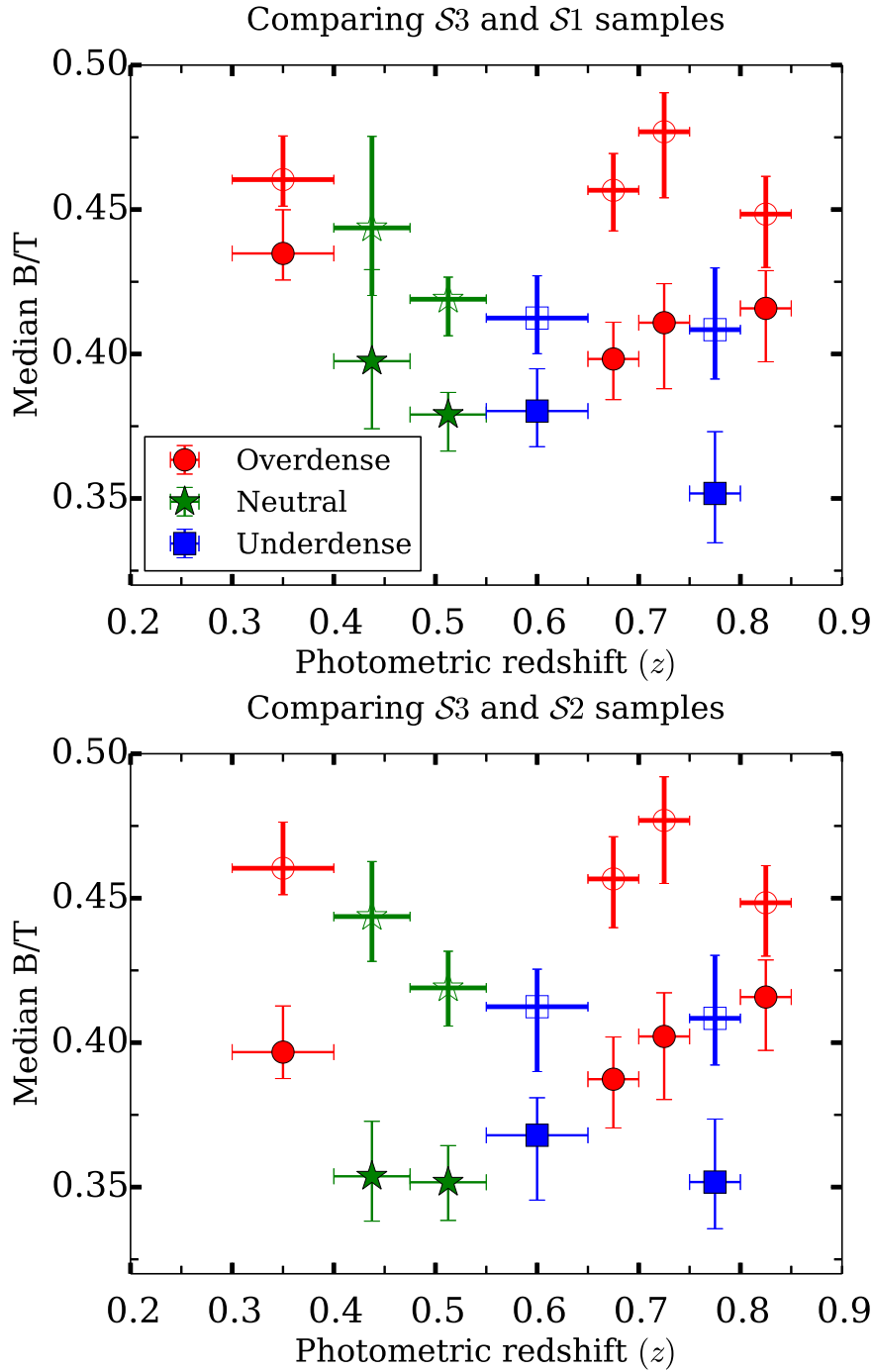


Figure 3.12: Median values of the bulge-to-total ratios for volume-limited samples $S1$ and $S2$ are plotted (filled centers and thin errorbars) in left and right panels respectively for each redshift bin. Median values for the $S3$ sample are plotted in both the panels (open centers and thick errorbars). The horizontal errorbars simply correspond to the binwidth while the vertical ones are 1σ errorbars obtained by bootstrapping.

environmental trends still are observed in the enhanced bins and hence our conclusions are still applicable.

The number of galaxies in overdense bins is typically higher than the number in underdense bins by about a factor of 2. (See Table 3.1). To eliminate the possibility (with great confidence) that this varying sample size is responsible for the trend observed, we repeated our analysis with only 50 per cent of overdense galaxies that were selected randomly. The vertical errorbars for overdense regions get bigger due to reduced sample size, but the statistical significance of our conclusions is still nearly as high as in the original analysis.

3.4.3 Mitigating the effects of line of sight fluctuations

Since we have argued that cosmic variance is giving rise to environmentally-based variations between galaxy populations in our redshift slices that are 0.05 wide, the natural question is how to mitigate this effect so that it will not affect attempts to simulate a realistic galaxy sample as a function of redshift. The most obvious approach is to repeat the analysis with wider redshift bins. Feigning ignorance of overdensities and underdensities along the line of sight, we choose the slices in redshift to be $[0.3 - 0.5]$, $[0.5 - 0.7]$ and $[0.7 - 0.85]$ (a nearly even division of our entire redshift range) and redo the analysis, beginning by checking the environmental classification for these wide bins.

Using the redshift distributions estimated earlier in this work (cf. Figs. 3.1 and 3.4), we obtain the overdensity estimates for the wider bins, $\delta_{g,1D}$. Although the $[0.7 - 0.85]$ bin seems to be overdense in the top panel of Fig. 3.13, it appears to be environmentally neutral when we volume-limit the sample using the methods from Sec. 3.3.2. Since the latter is what we use to study the galaxy morphology, we classify $[0.7 - 0.85]$ bin as ‘neutral’. What is surprising is the fact that the lowest and middle redshift slices still qualify as substantial overdensities and underdensities despite our use of $\Delta z = 0.2$.

As an example of what happens to morphological parameters, we show the median Sérsic index for three bins in Fig. 3.14. Comparing this with Fig. 3.11, we observe that the range of Sérsic n values has become smaller, as have the vertical errorbars,

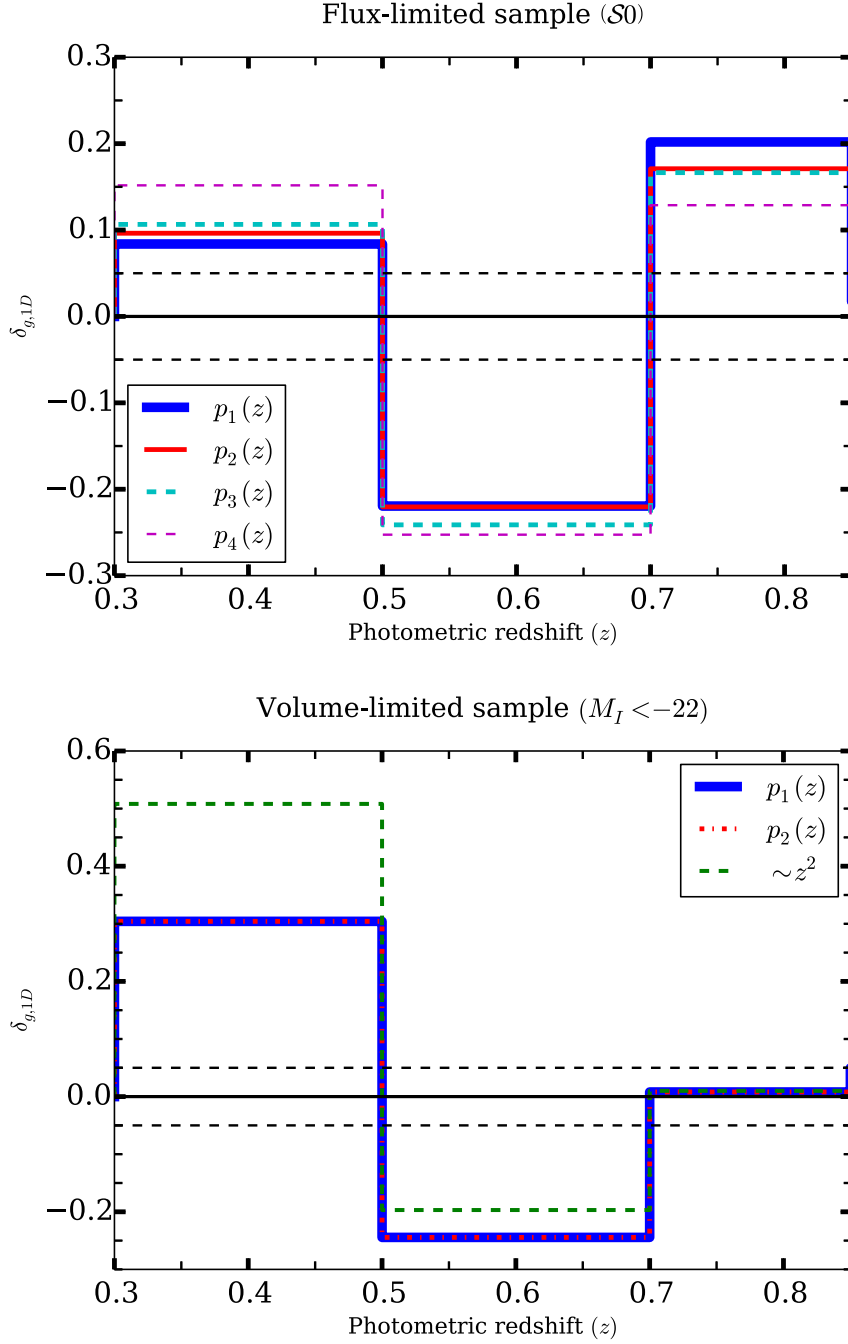


Figure 3.13: Plot of $\delta_{g,1D} = N/N_{\text{mod}} - 1$ with each functional form as the model for each of our new wide redshift bins discussed in Sec. 3.4.3, for flux-limited (top) and volume-limited (bottom) samples.

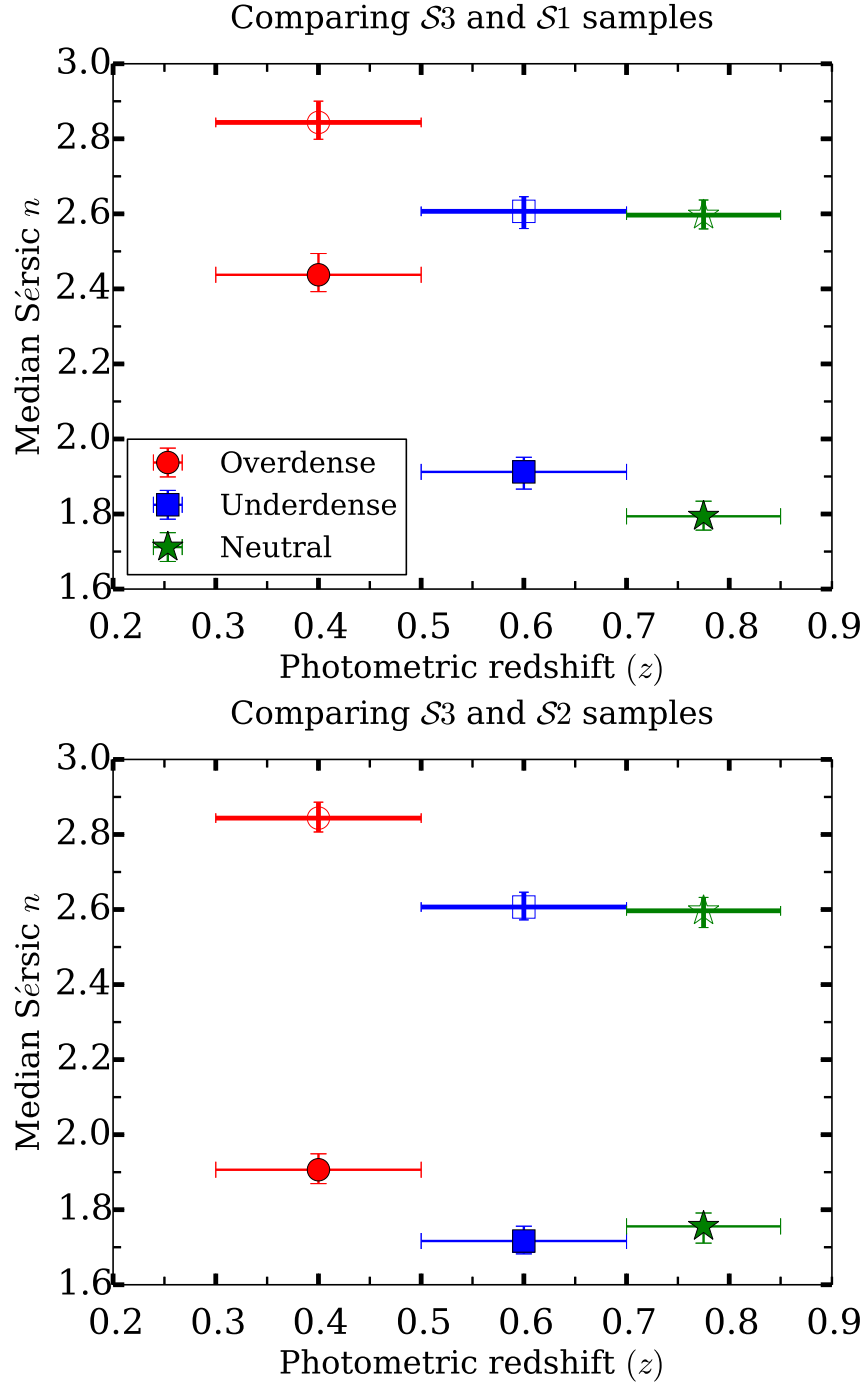


Figure 3.14: Median values of Sérsic index, as a function of redshift for our wider redshift ranges used in Sec. 3.4.3. The horizontal errorbars indicate the width of the redshift bin, while the vertical ones are 1σ errorbars obtained by bootstrapping. Points with open centers and thick errorbars correspond to the stellar-mass selected sample $S3$ and points with filled centers and thin errorbars correspond to the luminosity-selected samples $S1$ and $S2$.

mainly due to the increase in the number of galaxies in each redshift bin. The results do not suggest that the values are consistent across all redshift bins, and in particular, the disparity between overdense and underdense regions is still quite evident (with the same sign as before). However, in Fig. 3.11, the magnitude of that disparity between overdensities and underdensities was around 20 per cent, whereas here it is reduced to 7 per cent. This seems to suggest that when we choose wider redshift bins, some of the large-scale structure gets washed out, so the galaxy morphological parameters are less affected by cosmic variance. This is a promising result, which could be further improved by either (a) non-blind selection of the wide redshift bins with respect to known structure in the calibration fields, or (b) attempting some kind of reweighting of the galaxy populations in redshift slices affected by known structure.

As a test of the second option, we consider whether we can use some division of the galaxies by colour or B/T (as a proxy for colour) in order to determine the structural parameters of galaxies as a function of redshift for each of them separately. If the effects we are seeing can be cleanly described in terms of overdense (underdense) regions being dominated by bulge- (disk-)dominated galaxies, then division into samples based on B/T may help reduce the effects that we have described in previous subsections. We test this idea by dividing the sample into bulge- and disk-dominated galaxies based on requiring $B/T \geq$ or < 0.5 . The resulting bulge fraction f_{bulge} , shown as a function of redshift in Fig. 3.15, shows a mild effect from the large-scale structures in the COSMOS field.

Fig. 3.16 shows the RMS distortion as a function of redshift for the full $\mathcal{S}1$ sample (as shown previously) and for the separate bulge- and disk-dominated samples. As shown, the deviations in the values due to large-scale structure are clearly evident in all three cases, though slightly more prominent for the full sample and less so for the bulge-dominated sample. For comparison with the results for the full sample shown in Table 3.2, we compute the KS (AD) test p -values for consistency of axis ratios between overdense and underdense regions for bulge- and disk-dominated samples. For $\mathcal{S}1$, these p -values are 0.16 (0.08) for bulge-dominated galaxies and 0.005 (0.001) for disk-dominated galaxies. For $\mathcal{S}3$, these p -values are 0.03 (0.03) and 10^{-4} (3×10^{-4}), respectively. With the possible exception of bulge-dominated galaxies, it seems that separation into two morphological samples is not enough to remove the effect of the local environment on the ensemble properties like the intrinsic ellipticity distribution.

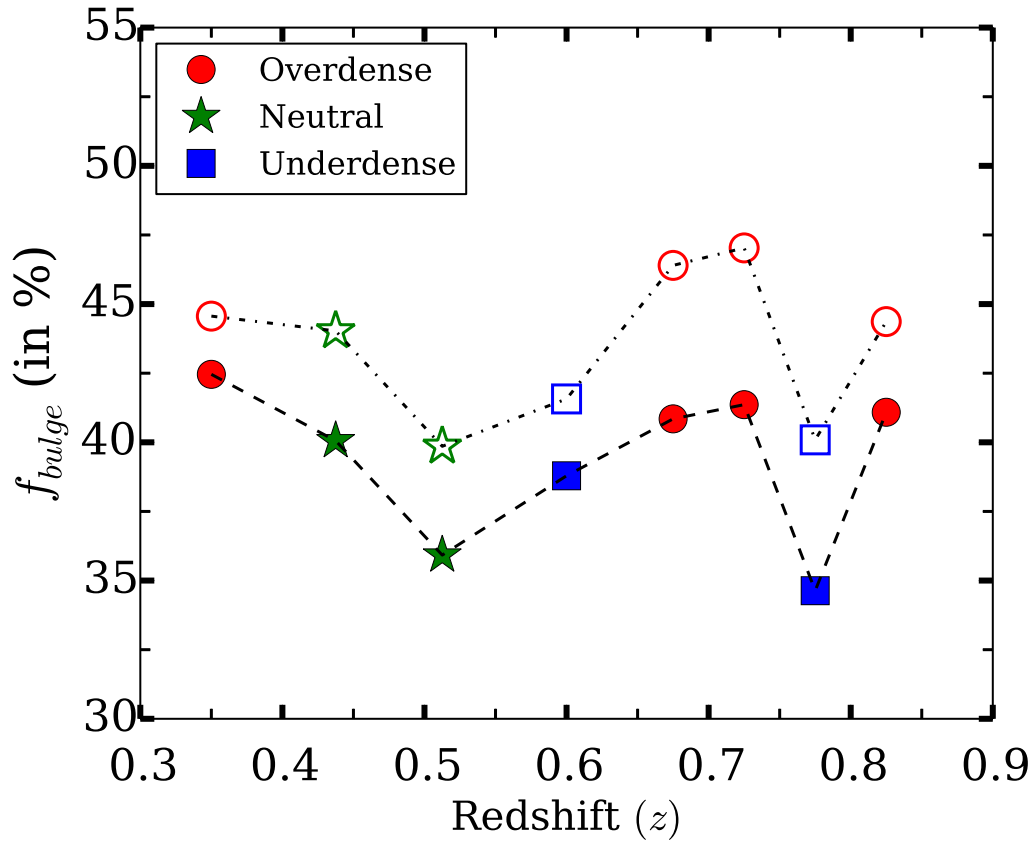


Figure 3.15: The fraction of galaxies in $\mathcal{S}1$ (solid symbols) and $\mathcal{S}3$ (open symbols) that are classified as bulge-dominated as a function of redshift, including the correlation with redshift slices classified as overdense or underdense as indicated by the symbol shape and colour.

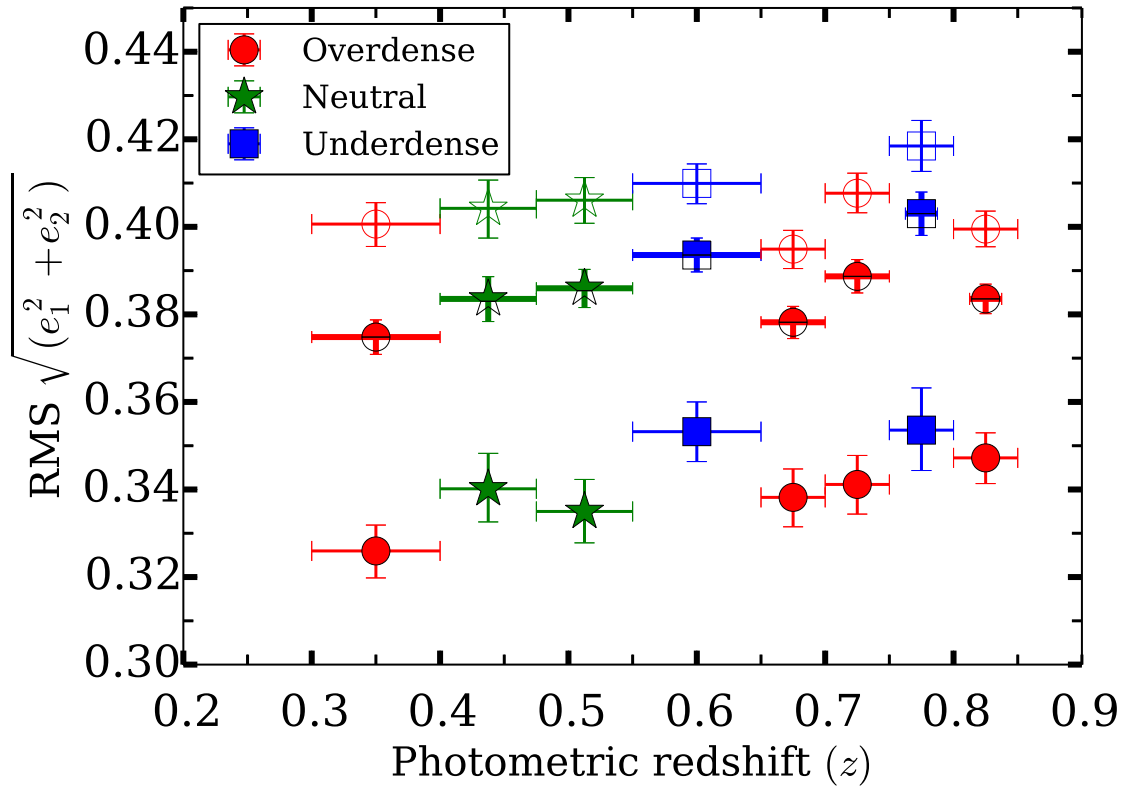


Figure 3.16: The RMS distortion as a function of redshift for the full volume-limited galaxy sample $\mathcal{S}3$ (partially-full symbols), the disk-dominated galaxy sample (open symbols), and the bulge-dominated galaxy sample (full symbols). The fact that the bulge-dominated sample has a lower RMS distortion than the disk-dominated sample is consistent with expectations.

Due to the limited sample size, we did not explore the possibility of an even finer morphological division of the sample, but with deeper *HST* datasets, this may be a promising path to pursue. However, if the nature of the bulges or disks themselves is altered by the local environment, then division purely into bulge- or disk-dominated sample will not be helpful in mitigating environmental effects.

3.5 Implications for future surveys

As mentioned previously, *HST* data will be used by current and future weak lensing surveys to characterize the galaxy population in several ways. In this section, we estimate how the results shown in Sec. 3.4 can affect estimates of shear calibration when using *HST* to characterize the galaxy population. We also discuss the situations in which this is likely to be important for current and future surveys from the space and ground.

3.5.1 Magnitude of shear calibration bias

Here we consider the impact of the findings in Sec. 3.4 on weak lensing shear calibration assuming that the COSMOS sample is used as a parent sample for simulations that are used to derive redshift-dependent shear calibrations. This could be done either directly using the galaxy images themselves, or by fitting for parametric distributions of Sérsic n , size, and shape in redshift slices, and then using those parametric distributions to make simulated images containing galaxies with Sérsic light profiles that match those distributions. We consider a few simple cases of how the above results affect shear calibration estimates. It is likely that the answer to this question varies quite significantly with the type of shear estimation method used. Some will be sensitive to the variations in morphology, others to the variation in the intrinsic ellipticity distribution, and many will be sensitive to both at some level. We consider both of these issues in turn.

The intrinsic ellipticity distribution plays a role in nearly all shear estimators. In some, the role is explicit: for example, LensFit [93, 94, 95] and the methods presented by [96] require accurate intrinsic ellipticity distributions as inputs, and uncertainty in the distribution was one source of systematic uncertainty in the CFHTLenS weak lensing results [55, 95]. The intrinsic ellipticity distribution enters the calculation for other methods in other ways. For example, the re-Gaussianization method and several other moment-based methods require calculation of a shear responsivity [90, 91] that describes how the galaxy population overall responds to a shear, based on its intrinsic ellipticity distribution. The responsivity can be calculated based on the observed shape distribution, assuming that the uncertainties in the shears are known

well enough that their contribution to that distribution can be removed. If a simulated sample in some redshift slice has a different intrinsic ellipticity distribution and therefore responsivity, it could lead to incorrect conclusions about shear calibration. The responsivity scales roughly like $1 - e_{\text{RMS}}^2$, which means that deviations in RMS distortion at the level of 0.01 due to local environments (Figs. 3.9 and 3.10) would become fractional shear errors of

$$\frac{\Delta\gamma}{\gamma} \approx \frac{2e_{\text{RMS}}\Delta e_{\text{RMS}}}{1 - e_{\text{RMS}}^2} \approx 0.01. \quad (3.12)$$

In the context of upcoming lensing surveys that seek to constrain shears to better than the per cent level, a systematic error of this magnitude in shear calibration is quite serious.

Regarding possible biases in the morphological mixtures of galaxies due to overdensities or underdensities in the training sample, there are results in the literature for several methods that show how shear biases vary with morphology. For example, for the maximum likelihood fitting code IM3SHAPE, figure 2 in [63] shows multiplicative biases for two-component Sérsic profile galaxies as a function of their bulge-to-total ratios (denoted there as $F_b/(F_b + F_d)$, which we will equate with our B/T). The shear calibration bias scales roughly like $0.04 - 0.05(B/T)$ as B/T goes from 0 to 1. Our results suggest that typical (median) B/T values may be influenced by cosmic variance in the COSMOS field, leading to fluctuations of order 0.05. The resulting variation in the shear calibration would therefore be $\sim 2.5 \times 10^{-3}$, or 0.25 per cent shear calibration uncertainty. For existing datasets this is not very problematic, but for surveys like LSST, Euclid, and WFIRST-AFTA, this would be a dominant part of the systematic error budget. As another example, for re-Gaussianization, figure 9 of [75] shows that as Sérsic n goes from 1 to 6, the shear calibration bias varies by 2 per cent. In this case, since we have shown that the median value of Sérsic n can vary by ~ 0.4 due to morphology-density correlations, this suggests that the shear calibration for re-Gaussianization could be misestimated by $\sim 2 \times 10^{-3}$, or 0.2 per cent. This too is acceptable in existing datasets, but not those that will be used for shear estimation in the next decade.

The estimates in this subsection are rough illustrations of the magnitudes of these effects. Other aspects of shear calibration that could be affected relate to the use of

HST data to estimate the impact of detailed galaxy morphology, or to calibrate the effect of colour gradients [59, 60]. In the latter case, what is most relevant in this work is our finding that B/T exhibits environmental dependence, which likely translates into environmental dependence of colour gradients. Unfortunately, we cannot directly test the strength of any colour gradient variations with environment using COSMOS data, due to the fact that there is only single-band coverage in much of its area. We note that our findings may seem to be at odds with the conclusions in [60] based on synthetic galaxy models that the existing area of *HST* coverage with ≥ 2 bands is sufficient for calibration of colour gradients⁴. This is particularly striking given that, as shown there, the dominant galaxy sample with 2-band coverage is the AEGIS dataset, which has substantially smaller area than COSMOS, and therefore should exhibit a stronger influence of cosmic variance. The presence of other fields besides AEGIS (e.g., GOODS) should help mitigate this effect given that the large-scale structure in the two fields will be completely uncorrelated, but the number of fields is still not large and the area is dominated by a small number of them⁵.

However, it is important to bear in mind that the method proposed in [60] involves determining not just a redshift-dependent correction but also a type-dependent colour gradient correction, which could partially mitigate the effects of the environment dependence seen here. Moreover, the colour gradient effect is higher order than the intrinsic ellipticity distribution, and thus may be less susceptible to systematics due to the environmental effects considered here. We showed in Sec. 3.4.3 that a simple type-dependent split does not remove the effects of environment on the intrinsic ellipticity distribution, but testing whether it (or a more complex type or colour split) is enough to remove the effects of colour gradients in Euclid is a more complicated analysis that is beyond the scope of this work. It seems that a future study using an *HST* field with more than one band would be warranted, to test whether or not our results suggest a discrepancy with those of [60]. It is possible that the connection between colour gradients and B/T is weak enough that our results do not imply a problem

⁴[59] showed that the fluctuations in colour gradients within the source galaxy sample in the Euclid weak lensing survey due to environmental effects will not be a significant source of uncertainty. However, the question addressed in that work is different from the question considered here, which is the impact of fluctuations in colour gradients in the training sample used to derive the corrections, rather than in the galaxy sample to which those corrections will be applied.

⁵For context, [97] showed that for tests of photometric redshift quality, the number of spectroscopic fields of this size that would be required for future surveys to avoid the influence of cosmic variance ranges from many tens to hundreds.

with colour gradient calibration, or that division into several galaxy types or colours is truly enough to remove the colour gradient effect due to its being a higher order effect, consistent with the findings of [60] using synthetic galaxy models.

3.5.2 Effective impact on current and future surveys

In addition to the order of magnitude of these effects presented in the previous subsection, it is important to bear in mind how current and future surveys plan to use *HST* data.

For example, before the Euclid survey begins, when carrying out tests of shear estimation methods, their simulated data will be based on *HST* in many ways: estimation of simple aspects of morphology (Sérsic n , bulge fraction), intrinsic ellipticity distribution, colour gradient calibration, and higher order moments (detailed morphology). Our results suggest that care should be taken to ensure that those simulations are not overly influenced by environment effects in the *HST* data, so that incorrect conclusions will not be drawn about the redshift-dependence of shear calibration for shear estimation methods to be used by the survey.

However, once the Euclid survey is underway, the derivation of simple galaxy morphology and the intrinsic ellipticity distribution will be based on the 40 deg² Euclid deep field, which goes two magnitudes fainter than the rest of the survey. With that data in hand, the Euclid weak lensing results will be less reliant on the much smaller and more cosmic variance-limited *HST* fields, using them only for colour gradient calibration and estimates of the impact of detailed galaxy morphology (since the *HST* resolution is higher than that of Euclid). The findings of [58] demonstrate that the area of this deep field is sufficient to accomplish the goal of determining the intrinsic ellipticity distribution at the accuracy required for shear calibration purposes for the Euclid survey.

In contrast, for ground-based surveys such as LSST, high-resolution space data will play a more important role in the understanding of the galaxy intrinsic ellipticity and morphology distributions, since even a deep field in a ground-based survey faces fundamental resolution limits that prevent the derivation of detailed information about the faint galaxy population. Galaxies that are near the resolution limit for a ground-

based survey are still very well-resolved in *HST*, making it the best resource for detailed information about them. Once the Euclid deep field is publicly available, the information from it will be beneficial to ground-based surveys as well.

Finally, our results for the effect on the intrinsic ellipticity distributions suggest that even current surveys should be careful to avoid this effect. While use of COSMOS without accounting for the effect that we have identified will cause a bias that is similar to the final requirements on the shear systematic errors for Stage III surveys, there are other elements in the systematic error budget, so ideally this effect should be mitigated somewhat using, for example, the wider redshift binning strategy that we tested in Sec. 3.4.3. Use of significantly smaller fields than COSMOS, while possibly helpful in building up a deeper galaxy sample, should naturally increase the impact of cosmic variance on the training dataset, which should be quantified as part of the systematic error budget.

3.6 Conclusions

In this study, we have shown that the shape distributions of galaxies (to a statistically significant degree) and morphological parameters like Sérsic n and bulge-to-total ratios (more marginally) depend on the local environments when dividing up the COSMOS sample into redshift slices along the line of sight. The redshift slices used for our primary analysis had a width of $\Delta z = 0.05$. Our findings are robust to the choice of shape estimator from Sérsic profile fits vs. using centrally weighted moments-based shear estimates.

These findings are relevant to attempts to use *HST*-based galaxy samples to calibrate shear estimates in weak lensing surveys. In general, the approach would be to define galaxy samples using all galaxies in redshift slices, and determine a redshift-dependent shear calibration. Our findings highlight the danger in such an approach: while we would like our simulations to include true evolution in galaxy properties with redshift, this approach also includes spurious variations in galaxy properties due to the large-scale structure within the COSMOS field. Since the fidelity of weak lensing shear estimates depends sensitively on the intrinsic shape distribution and galaxy morphological parameters, the conclusions for the redshift-dependent shear calibration would

be incorrect. As shown in Sec. 3.4.3, these errors are reduced as the redshift slices that are used become wider, so that the impact of local overdensities becomes washed out. However, our results suggest that even $\Delta z = 0.2$ may not be wide enough (and this is becoming dangerously close to the size of tomographic redshift bins to be used for weak lensing analysis in upcoming surveys). Thus, more complex schemes may become necessary to fully overcome this issue, depending on exactly how the *HST* data is to be used. As discussed in Sec. 3.5, particular care may be needed in ground-based surveys that will use the *HST* data to model many aspects of the galaxy population. In contrast, for Euclid, use of the relatively large area Euclid deep data to constrain many aspects of the galaxy population means that these issues with *HST* data are less important, though still not completely ignorable.

It is important to keep in mind the nature of COSMOS with respect to other possible *HST* training samples. COSMOS represents the largest contiguous field surveyed by the *HST*, with the sizes of other major *HST* fields such as GOODS and AEGIS lagging by at least a factor of 9 (for AEGIS, and more for GOODS). Combinations of CANDELS with existing datasets may ultimately be as large as 1/6 the COSMOS area. Hence, if cosmic variance due to structures along the line of sight in COSMOS are problematic for its use as a training sample for weak lensing simulations, studies that use even smaller area training samples are even more prone to errors, with the UDF serving as an extreme case. If the size of the *HST* survey is small enough, there is no reason *a priori* to suppose that the galaxy population is typical even when using all galaxies along the line of sight, without any division into redshift bins. Of course, future surveys are unlikely to pick just a single survey to serve as the basis for their image simulation training sample, but rather will combine as many as possible. Combining multiple surveys will reduce the cosmic variance and therefore the significance of the effects discussed in this work. However, as COSMOS is significantly larger than other *HST* surveys, combining COSMOS with smaller fields is unlikely to ameliorate this effect. Thus, it will be important to carefully choose the size of redshift slices used to derive properties of the galaxy population so as to be minimally affected by this issue.

A final consideration is the question of how applicable these results using volume-limited samples are to simulations of upcoming weak lensing surveys, which will exclusively use flux-limited samples. For our analysis, the volume-limiting sample

was necessary to avoid complications due to varying galaxy populations in each redshift slice, allowing us to isolate purely environmental effects. In principle, if the morphology-density correlations that we have identified turn out to not exist for intrinsically fainter galaxy populations, then at low redshift (where a flux limited sample will include galaxies that are intrinsically much fainter than at high redshift), the effects will be less serious for upcoming lensing surveys. However, we do not have any particular reason to believe that these effects will vanish for fainter galaxies. Moreover, at higher redshift where only intrinsically bright galaxies can be seen, the effect should be present at a level similar to what we have found here. Since higher redshift galaxies tend to dominate cosmological shear estimates (due to their higher shears), our findings will be important to take into account. It would also be advisable to carry out a future study of this effect at higher redshift (beyond 0.85), using for example the data from the CANDELS survey.

In conclusion, our results have serious implications for the plans to create realistic image simulations that will be used to derive redshift-dependent shear calibrations for upcoming weak lensing surveys. If care is not taken to mitigate this effect, then the cosmic variance in the training sample may bias the conclusions regarding shear calibration for redshift slices that represent significant overdensities or underdensities compared to the typical galaxy population. This is particularly a problem when using the smaller *HST* surveys, where a single galaxy cluster or a void could completely dominate the galaxy population in a given redshift slice. To mitigate this problem, it will be imperative to (a) collect training data from widely separated patches on the sky, and (b) take care to use redshift slices that are broad enough that these effects are reduced, so as to wash out the effect of any signal overdensity or underdensity on the simulated galaxy population. By employing these mitigation schemes, there is every reason to believe that the effect we have identified can be reduced to a small component of the systematic error budget of major upcoming lensing surveys.

Acknowledgments

The authors would like to thank Thomas Kitching, Henk Hoekstra, Tim Schrabback and the anonymous referee for their helpful comments on this work. AK and RM acknowledge the support of NASA ROSES 12-EUCLID12-0004, and program

HST-AR-12857.01-A, provided by NASA through a grant from the Space Telescope Science Institute, which is operated by the Association of Universities for Research in Astronomy, Incorporated, under NASA contract NAS5-26555. RM acknowledges the support of an Alfred P. Sloan Research Fellowship. Kavli IPMU is supported by World Premier International Research Center Initiative (WPI), MEXT, Japan. We thank Alexie Leauthaud for many useful discussions.

Chapter 4

The Impact of Interpixel Capacitance in CMOS Detectors on PSF shapes and Implications for WFIRST

Journal reference: Publications of the Astronomical Society of the Pacific (PASP) 2016, Vol. 128, Issue 967

Original authors: Arun Kannawadi, Charles A. Shapiro, Rachel Mandelbaum, Christopher M. Hirata, Jeffrey W. Kruk, Jason D. Rhodes

Original abstract: Unlike optical CCDs, near-infrared detectors, which are based on CMOS hybrid readout technology, typically suffer from electrical crosstalk between the pixels. The interpixel capacitance (IPC) responsible for the crosstalk affects the point-spread function (PSF) of the telescope, increasing the size and modifying the shape of all objects in the images while correlating the Poisson noise. Upcoming weak lensing surveys that use these detectors, such as WFIRST, place stringent requirements on the PSF size and shape (and the level at which these are known), which in turn must be translated into requirements on IPC. To facilitate this process, we

present a first study of the effect of IPC on WFIRST PSF sizes and shapes. Realistic PSFs are forward-simulated from physical principles for each WFIRST bandpass. We explore how the PSF size and shape depends on the range of IPC coupling with pixels that are connected along an edge or corner; for the expected level of IPC in WFIRST, IPC increases the PSF sizes by $\sim 5\%$. We present a linear fitting formula that describes the uncertainty in the PSF size or shape due to uncertainty in the IPC, which could arise for example due to unknown time evolution of IPC as the detectors age or due to spatial variation of IPC across the detector. We also study of the effect of a small anisotropy in the IPC, which further modifies the PSF shapes. Our results are a first, critical step in determining the hardware and characterization requirements for the detectors used in the WFIRST survey.

4.1 Introduction

A number of ongoing and future space telescopes will focus on the near-infrared (NIR) or infrared part of the electromagnetic spectrum, which provide a view through the gas and dust in nearby star-forming regions, and allow higher signal-to-noise imaging of high-redshift galaxies. Images in the NIR are currently being taken by the Wide Field Camera 3 [WFC3; 98] in the Hubble Space Telescope and the Wide-field Infrared Survey Explorer [WISE; 99]. Upcoming space telescope missions such as NASA’s James Webb Space Telescope [JWST; 100] and Wide Field InfraRed Space Telescope¹ [WFIRST; 1, 2, 50] will also focus on infrared imaging. WFIRST mission will provide high quality image data for weak gravitational lensing studies.

Weak gravitational lensing [for a review, see for example 24, 27, 41, 101] is the deflection of light rays from background sources such as galaxies by matter in the foreground, resulting in a small magnification and shape distortion. Weak lensing can be a powerful cosmological probe constraining cosmological parameters [e.g., 55, 56, 57, 102], test theory of gravity on large scales [e.g., 103, 104, 105] and on smaller scales relate the galaxies to their dark matter halos [e.g., 106, 107, 108, 109, 110, 111, 112]. Measuring the small but coherent distortions of the shapes of the galaxies, without the knowledge of their intrinsic shapes, is a challenging task that requires images with

¹<http://wfirst.gsfc.nasa.gov/>

high resolution and a statistical understanding of distances to the source galaxies [see 113, for recent tests on multiple methods]. Weak lensing measurements in surveys like WFIRST will require detailed (sub-percent level) knowledge of the point-spread function (PSF), from a combination of *a priori* modeling and empirical estimates using images of stars, in order to remove its effect on galaxy shapes.

While there are differences between the detectors for these missions, most notably the array size and cutoff wavelength, all of them use a hybrid CMOS readout architecture with mercury cadmium telluride ($\text{Hg}_{1-x}\text{Cd}_x\text{Te}$, often abbreviated HgCdTe) as the light-sensitive material. In particular, they use the HxRG² family of detectors manufactured by Teledyne Imaging Sensors. Extensive work on understanding and characterizing the impact of detector-based effects on astronomical imaging has been done for CCDs, which are used for optical imaging in many telescopes [see for e.g., 114, 115, 116, and references therein]. The use of HxRG detectors for astronomy is relatively recent, and understanding the systematic errors in astronomical measurements that result from HxRG detector effects is an active area of research.

Among the systematic effects in these detectors that will be relevant for WFIRST are non-linearity, reciprocity failure [117], interpixel capacitance (IPC), and persistence. Non-linearity refers to the small non-linearity in converting the charges in the pixel to the voltage read by the read-out assembly. Reciprocity failure usually implies that the response of a detector depends not only on the total number of incident photons, but also on how they are distributed in time (e.g., $2\times$ illumination for $1/2$ of the time leads to a different measurement of the total flux). This is typically a non-linear effect as well. Persistence is the phenomenon of retaining a small but non-negligible fraction of the flux in images from the previous exposures after a reset. Interpixel capacitance, the effect that we focus on in this study, is a form of electrical cross-talk between the pixels in the detectors. This is a linear effect and Sec. 5.3 of this paper presents a brief review of this effect.

Any realistic galaxy image simulations used for simulating PSFs and testing weak lensing shear estimation algorithms must include these effects in the images. To facilitate this simulation process, the authors have built a WFIRST module within

²HxRG stands for HAWAII $x \times x$ pixels with Reference pixels and Guide mode, and HAWAII stands for HgCdTe Astronomical Wide Area Infrared Imager.

GalSim³ [69], an open-source simulation package, that has the routines to include the above mentioned detector effects and reasonable values for the parameters involved. Additionally, values for other parameters such as the pixel scale, jitter, dark current, thermal backgrounds are also provided. The WFIRST module also takes into account of the telescope’s pupil plane configuration and forward simulates the PSF from physical principles. Throughout this paper, the term “PSF” refers to the *effective* PSF that is a convolution of the pixel response function (a 2-D top-hat function) and the optical PSF (distribution of flux at the focal plane from a point source).

The pixel scale for the WFIRST-AFTA telescope must strike a balance between the need for having a large field of view while achieving the sampling needed to resolve galaxy shapes. It is chosen to be 0.11'' [2] which causes the PSFs to be undersampled (more on this in Sec. 4.4.3). Better sampled images are expected to be achieved in post-processing by combining the images from a dither sequence.

The action of various detector effects cannot be expressed as a convolution for different reasons. Voltage non-linearity and reciprocity failure are intrinsically non-linear while convolution is a linear operation. Although IPC is specified by a convolution kernel, it cannot be considered as a part of the PSF (see Sec. 4.2.3 for details). Both the galaxy and PSF images must be corrected for the detector effects explicitly (in each exposure) before the galaxy image is corrected for the PSF (see, e.g., [90]) in order to perform shape measurement. Any imperfections in this correction, either due to the correction algorithm or due to insufficient knowledge of the detector effects themselves, can result in errors in PSF models that affect weak lensing shear estimation. To enable future studies of how detector effects and their uncertainties affect shear estimation, here we study the effect of IPC on the PSF images. Thus, the goal of this study is two-fold:

1. to understand how the observed PSF changes as a function of the level of coupling between pixels, and
2. to relate the errors in the coupling parameters to the errors in the reconstructed PSF.

Ultimately, these results will be useful for setting requirements on hardware and software for the upcoming WFIRST mission. For WFIRST, in addition to knowing

³<https://github.com/GalSim-developers/GalSim>

the overall size of PSFs, the ability to predict them is also of utmost interest.

This paper is organized as follows. We present the detector model and explain the origin of interpixel capacitance in Sec. 5.3. Sec. 4.3 summarizes the definitions of PSF sizes and shapes used in this paper. We present in Sec. 4.4 the details about how we simulate the WFIRST PSFs and how to overcome the problem of undersampling with IPC taken into account. In Sec. 4.5, we present our results for how the PSF size and shape is affected by IPC. Finally, our conclusions are summarized in Sec. 4.7.

4.2 Interpixel Capacitance

In this section, we present a brief review of interpixel capacitance, including its origins and its effect on astronomical images.

4.2.1 Detector model

The photodetector array is commonly modeled (see, for example, [118, 119]) as a rectangular array of capacitors indexed by i, j with node capacitance $C[i, j]$, each receiving a charge $Q[i, j]$ corresponding to the accumulated photocurrent entering the node over some integration time. In the ideal case of zero cross talk between the nodes, the detected voltage is

$$V[i, j] = \frac{Q[i, j]}{C[i, j]} \quad (4.1)$$

The node capacitances of all pixels are fabricated to be the same to a very high accuracy, i.e., $C[i, j] = C_{\text{node}}$, making the system invariant under shifts. If C_{node} is a constant independent of the signal, then the photodetector array is a linear system, in addition to being shift-invariant. This linear shift-invariant (LSI) system is characterized by a 2-dimensional impulse response function h . Thus, the voltage read out from a pixel (assuming no read noise) is given by

$$V[i, j] = (Q * h)[i, j] = \sum_m \sum_n Q[m, n] h[i - m, j - n]. \quad (4.2)$$

In the ideal case,

$$h_{\text{ideal}}[i - m, j - n] = \frac{\delta_{im}\delta_{jn}}{C_{\text{node}}}, \quad (4.3)$$

where δ_{im} and δ_{jn} are Kronecker delta functions. That is, the voltage in a pixel depends only on the charge accumulated in that pixel. $1/C_{\text{node}}$ is then the conversion gain. Factoring out the gain explicitly gives us

$$V[i, j] = \sum_m \sum_n \frac{1}{C_{\text{node}}} Q[m, n] K[i - m, j - n], \quad (4.4)$$

where K is called the *IPC kernel*.

However, in reality, fringing fields from the edges of the node capacitors cause the voltage readings in a pixel to depend on the charges in neighboring pixels. This effect is modeled by introducing a coupling capacitance C_c between pixels. This *interpixel capacitance* in principle couples every pixel to every other pixel. It is different from the phenomenon of charge diffusion, which involves actual physical movement of charge carriers to adjacent pixels; IPC is a deterministic effect arising through fringing fields without any actual movement of charge carriers. CCDs are not known to exhibit any IPC, although a crosstalk due to capacitive coupling between neighboring channels in the read-out electronics exists [120].

Pixels typically have some level of non-linear response, i.e., $C[i, j]$ varies with the charge. This variation of $C[i, j]$ from the nominal value of C_{node} is modeled separately as a non-linearity in the gain of the system, leaving IPC to be modeled as a strictly linear effect. Identical coupling capacitances between the nodes, by fabrication, ensure that the system is still shift-variant.⁴ Thus, the effect of interpixel capacitance can still be captured by a kernel K that is convolved with the image.

4.2.2 Parametrizing IPC

For any IPC kernel K , the entries, which refer to relative capacitance values, must satisfy $0 \leq K[i, j] \leq 1 \forall (i, j)$ [see 119]. Moreover, for unit nominal gain, the sum of all voltages is unity (in suitable units) for a unit charge (in suitable units) in some

⁴This is not strictly true. However, as long as the length scale over which the coupling changes significantly is more than a few pixels, all the arguments hold.

arbitrary node. This arbitrary node, which must be far from the edges, can be defined as the origin for convenience, i.e., if $Q[m, n] = \delta_{m,0}\delta_{n,0}$, then

$$C_{\text{node}} \sum_i \sum_j V[i, j] = 1, \quad (4.5)$$

implying

$$\sum_i \sum_j K[i, j] = 1. \quad (4.6)$$

This normalization for the IPC kernel ensures charge conservation in the case of a generic signal.

As mentioned in Sec. 4.2.1, a capacitive coupling exists between every pair of nodes, which decreases sharply with the distance between them. For small interpixel coupling, i.e., $C_c/C_{\text{node}} \ll 1$, we can consider only the coupling between pixels sharing an edge and ignore the rest, which are typically of second or higher order in α . In this limit, the kernel is described by a 3×3 matrix with 8 degrees of freedom (see Eq. 4.6). Symmetric coupling between the nodes is a reasonable assumption, i.e., $K[i, j] = K[j, i]$. The simplest, non-trivial IPC kernel is then given by

$$K_\alpha = \begin{pmatrix} 0 & \alpha & 0 \\ \alpha & 1 - 4\alpha & \alpha \\ 0 & \alpha & 0 \end{pmatrix}. \quad (4.7)$$

Note that we have assumed $\alpha \ll 1$, and thus $1 - 4\alpha$ is always positive.

Coupling between pixels that share a corner (diagonal coupling) can be stronger than second nearest neighbor (along one of the axes) due to proximity. Thus, we can introduce an additional level of complexity by introducing α' to represent the diagonal coupling, whose value can be independent of α .

$$K_{\alpha, \alpha'} = \begin{pmatrix} \alpha' & \alpha & \alpha' \\ \alpha & 1 - 4(\alpha + \alpha') & \alpha \\ \alpha' & \alpha & \alpha' \end{pmatrix}, \quad (4.8)$$

where typically $\alpha' < \alpha$. This is a reasonable assumption since in typical H2RG devices α and α' are typically of order 10^{-2} and 10^{-3} as we will show below. However, it is

important to confirm that the effect of α' on the PSF size and shape really is small compared to that of α , to justify that the kernel can indeed be truncated to 3×3 matrix.

There can exist a measurable asymmetry along the two axes of the detectors [121], i.e., the capacitive coupling along the rows can be different from that of the columns. Small anisotropies that arise because of this can have a significant effect on the ellipticity of objects we want to study. This leads us to a 3-parameter kernel given by

$$K_{\alpha, \alpha_+, \alpha'} = \begin{pmatrix} \alpha' & \alpha - \alpha_+ & \alpha' \\ \alpha + \alpha_+ & 1 - 4(\alpha + \alpha') & \alpha + \alpha_+ \\ \alpha' & \alpha - \alpha_+ & \alpha' \end{pmatrix}. \quad (4.9)$$

Care has to be taken at the edges since the above equation cannot possibly hold. Along the edges of the physical detector, the assumed IPC model is not valid. But along the edges of postage stamps, one can simply extend the sky image or simply truncate the edges.

For the IPC kernel K_α given in Eq. (5.15), to first order in α , the elements of the post-IPC image I_{obs} are related to those of the pre-IPC image I_{im} as

$$I_{\text{obs}}[i, j] = (1 - 4\alpha)I_{\text{im}}[i, j] + \alpha (I_{\text{im}}[i + 1, j] + I_{\text{im}}[i - 1, j] + I_{\text{im}}[i, j + 1] + I_{\text{im}}[i, j - 1]). \quad (4.10)$$

A similar equation with more terms can be written for the IPC kernels given in Eqs. (4.8) and (5.16). For the IR channel of WFC3, direct measurements of the IPC kernel made on-orbit [121] yield

$$K_{\text{WFC3}} = \begin{pmatrix} 0.0011 \pm 0.0006 & 0.0127 \pm 0.0009 & 0.0011 \pm 0.0006 \\ 0.0163 \pm 0.0014 & 0.936 \pm 0.0045 & 0.0164 \pm 0.0011 \\ 0.0011 \pm 0.0006 & 0.0127 \pm 0.0010 & 0.0011 \pm 0.0006 \end{pmatrix}, \quad (4.11)$$

which can be described by the 3-parameter model in Eq. (5.16). For H4RGs, the nominal values for the IPC parameters (given by a subscript 0) are $\alpha_0 = 0.02$, $\alpha'_0 = 0.002$ and $\alpha_{+,0} = 0$ (Content, D. personal communication, 2015-11-05).

4.2.3 Implications of IPC

Failure to account for IPC results in underestimation of conversion gain [119, 122, 123] and overestimation of various kinds of quantum efficiencies [DQE; 124]. Thus, IPC must be estimated and accounted for in order to understand the fundamental parameters of the detectors. In addition, one must account for the effect of IPC on image shapes, which is the focus of this paper.

If one were to obtain an image of the PSF by pointing the telescope at a star, the image of the star will include the effects of IPC. The effect of the IPC is to blur the image through a convolution. However, the IPC kernel may be considered as being distinct from the PSF for several reasons. Some of them are:

1. The PSF is an intrinsically continuous profile that is convolved with the image and is discretized only when the light hits the detector. The IPC kernel, on the other hand, is inherently discrete, with a pre-defined pixel scale.
2. The effects of IPC are centered on each pixel, independent of where the photons land.
3. The effect of IPC comes in later than that of the PSF, at the detector level, after the addition of dark current, Poisson noise and nonlinearity of the conversion gain. Thus the IPC introduces correlations in the signal and noise, whereas the PSF does not correlate the noise.

IPC corrections are therefore different from the PSF corrections, and could be applied as a deconvolution kernel (essentially the inverse of the IPC kernel) before the majority of the image processing. Moreover, they would be applied to each exposure, while PSF corrections to galaxy shape measurements would typically be made after obtaining an oversampled image from multiple exposures.

With a precisely known IPC kernel, and in the absence of detector noise, the original image at the focal plane can be recovered by direct deconvolution. However, read-out noise and quantization noise is added after IPC convolution occurs. Despite this fact, the straightforward deconvolution or division in Fourier space can be done [125], as it is stable to noise due to the absence of zeros in the Fourier representation of the IPC kernel. This deconvolution would now introduce additional correlations in the read noise and quantization noise. Thus an exact recovery of the noisy image,

removing just the effects of the IPC, is impossible. As an alternative to an exact correction scheme, which would have recovered the original noisy image in the absence of noise after IPC, an approximate, fast correction scheme suggested in [125] should be evaluated to see if it is sufficient. The approximate correction scheme suggests convolving the individual exposures with another kernel, with the sign of the IPC parameters reversed. For the 3-parameter kernel (Eq. 5.16), it involves convolving the image with another kernel

$$K'_{\alpha, \alpha_+, \alpha'} = K_{-\alpha, -\alpha_+, -\alpha'} = \begin{pmatrix} -\alpha' & -\alpha + \alpha_+ & -\alpha' \\ -\alpha - \alpha_+ & 1 + 4(\alpha + \alpha') & -\alpha - \alpha_+ \\ -\alpha' & -\alpha + \alpha_+ & -\alpha' \end{pmatrix} \quad (4.12)$$

to correct for IPC effects to first order in the coupling parameters. For the 1-parameter kernel (Eq. 5.15), $(K_\alpha \otimes K'_\alpha)_{ij} = \delta_{i0}\delta_{j0} + \mathcal{O}(\alpha^2)$. Here, the $(0, 0)$ element refers to the center element of the kernel. For $\alpha \sim 0.02$, which is roughly what H4RG detectors are anticipated to exhibit, $\alpha^2 \sim 0.0004$ which may be negligible. For kernels with more than one parameters, bi-linear correction terms may exist, which are also small in magnitude. If it turns out that $\mathcal{O}(\alpha^2)$ terms are not negligible for shape measurements for WL analysis, then one can always go for the direct deconvolution.

As stated in Sec. 5.1, one of the main goals of this study is to highlight the uncertainty in the PSF due to imperfect knowledge of the IPC parameters. In real detectors, the coupling between the pixels varies spatially [126], violating the assumption that IPC is a shift-invariant effect. However, as long as the scale on which the coupling varies is greater than a few pixels, we can treat IPC as approximately shift-invariant with kernel parameters that vary slowly with position. Thus, the IPC parameters cannot be known perfectly and come with errorbars, which would also be the case if there is some unknown time-dependence of the IPC. If $\delta\alpha$ denotes the difference between the actual parameters and their assumed (nominal) values, then $K_\alpha \otimes K'_{\alpha+\delta\alpha}$ will have terms that are of order $\delta\alpha$.

Throughout this work, we carefully distinguish ΔX from δX ; the former refers to the change in the quantity X due to the IPC and the latter refers to the change in a quantity X due to error in determining the IPC parameters or equivalently the change due to a small deviation of the IPC parameters from their nominal values. Thus, ΔX represents a systematic change that is correctable (at least, in principle),

while δX represents a systematic error.

4.3 Definitions of sizes and shapes

4.3.1 Based on quadrupole moments

A common way to define the sizes and shapes of objects in astronomical images (PSFs, galaxies) uses weighted second moments [91]. The first moments of an image I (in arbitrary units) are defined as

$$\mathbf{x}_0 = \frac{\int d^2\mathbf{x} \mathbf{x} w(\mathbf{x}) I(\mathbf{x})}{\int d^2\mathbf{x} w(\mathbf{x}) I(\mathbf{x})}, \quad (4.13a)$$

and the second moments as

$$\mathbf{M}_{ij} = \frac{\int d^2\mathbf{x} (\mathbf{x} - \mathbf{x}_0)_i (\mathbf{x} - \mathbf{x}_0)_j w(\mathbf{x}) I(\mathbf{x})}{\int d^2\mathbf{x} w(\mathbf{x}) I(\mathbf{x})} \quad (4.13b)$$

for some weight function $w(\mathbf{x})$. Here, \mathbf{x} and \mathbf{x}_0 are 2-vectors, i.e., $\mathbf{x} = (x_1, x_2) = (x, y)$.

For a given weight function, one possible definition of linear object size σ is given by $[\det(\mathbf{M})]^{1/4}$. Another is the square root of the trace of the moment matrix, $\text{tr}(\mathbf{M})^{1/2} = \sqrt{\mathbf{M}_{xx} + \mathbf{M}_{yy}}$. Both options have dimensions of length and are invariant under rotation; however, the determinant is less sensitive to the shear, so we use the determinant to define σ .

The ellipticity of the object can be expressed in terms of the second moments as

$$(e_1, e_2) = \left(\frac{\mathbf{M}_{xx} - \mathbf{M}_{yy}}{\mathbf{M}_{xx} + \mathbf{M}_{yy}}, \frac{2\mathbf{M}_{xy}}{\mathbf{M}_{xx} + \mathbf{M}_{yy}} \right). \quad (4.14)$$

Often, the ellipticity is expressed as a complex number $\mathbf{e} = e_1 + ie_2$. The complex ellipticity can also be specified by the magnitude of the ellipticity $|\mathbf{e}| = \sqrt{e_1^2 + e_2^2}$ and an angle β , where β is the position angle, as

$$(e_1, e_2) = |\mathbf{e}| (\cos 2\beta, \sin 2\beta). \quad (4.15)$$

The two linear sizes are related through the total ellipticity by the equation

$$\text{tr}(\mathbf{M}) = \frac{2\sigma^2}{\sqrt{1 - |\mathbf{e}|^2}}. \quad (4.16)$$

Choosing the weight function

When $w(\mathbf{x})$ is a constant, Eq. (4.13b) reduces to unweighted second moments, which are divergent in the presence of noise [127]. Moreover, diffraction-limited PSFs are Airy-like, with intensity decreasing with distance from the image center as $1/r^3$ for large r . Thus, the elements in the moment matrix for an Airy PSF diverge logarithmically and hence are formally infinite. In practice, due to the finite size of the detector, one would obtain finite values, but they would depend strongly on the number of pixels used to calculate the moments, which is undesirable. This is true independent of the exact form of the PSF when the pupil of the telescope has a sharp edge.

[127] introduced circular Gaussian weight functions in order to obtain finite values of higher order moments. [91] generalized the weight function to be an elliptical Gaussian that matches the shape of the object. This can be achieved in principle by finding the best-fit elliptical Gaussian to the image by minimising

$$E = \int d^2\mathbf{x} \left| I(\mathbf{x}) - A \exp \left[-\frac{1}{2}(\mathbf{x} - \mathbf{x}_0)^T \mathbf{M}^{-1}(\mathbf{x} - \mathbf{x}_0) \right] \right|^2 \quad (4.17)$$

over the six independent variables in $(A, \mathbf{x}_0, \mathbf{M})$. The optimal values of \mathbf{x}_0 and \mathbf{M} satisfy Eqs. (4.13a) and (4.13b) for the weight function

$$w(\mathbf{x}) = \exp \left[-\frac{1}{2}(\mathbf{x} - \mathbf{x}_0)^T \mathbf{M}^{-1}(\mathbf{x} - \mathbf{x}_0) \right]. \quad (4.18)$$

In practice, it is more common to determine this weight function via an iterative process than by minimising Eq. (4.17), resulting in the term ‘‘adaptive moments’’.

For Gaussian objects, the adaptive and unweighted moments are equivalent, while the adaptive size of a non-Gaussian PSF is typically smaller than its unweighted size since the former downweights the extended wings of the PSF.

Transformation properties

The image arising from the convolution of the IPC kernel with a given image can be seen as the sum of shifted and scaled versions of the original image (see Eq. 4.10). Eq. 4.10 is a particular case of a generic linear transformation of the image given as

$$I(\mathbf{x}) \rightarrow I_{\text{new}}(\mathbf{x}) = (K_{\text{IPC}} \otimes I)(\mathbf{x}) = \sum_{d\mathbf{x}} \lambda(d\mathbf{x})I(\mathbf{x} + d\mathbf{x}). \quad (4.19)$$

for some set of coefficients λ . The transformation of the best-fit Gaussian parameters (obtained in the form of adaptive moments) under the individual operations of rescaling and shifting are simple:

$$I(\mathbf{x}) \rightarrow I_{\text{new}}(\mathbf{x}) = \lambda I(\mathbf{x}) \implies (A, \mathbf{x}_0, \mathbf{M}) \rightarrow (\lambda A, \mathbf{x}_0, \mathbf{M}) \quad (4.20)$$

$$I(\mathbf{x}) \rightarrow I_{\text{new}}(\mathbf{x}) = I(\mathbf{x} + \Delta\mathbf{x}_0) \implies (A, \mathbf{x}_0, \mathbf{M}) \rightarrow (A, \mathbf{x}_0 + \Delta\mathbf{x}_0, \mathbf{M}) \quad (4.21)$$

A combined spatial translation and intensity rescaling of an image is trivial. However, the operation of finding the best-fit single Gaussian does not behave in any simple way under a general linear transformation, i.e., the best-fit Gaussian to an image $I_1(\mathbf{x})$ and the best-fit Gaussian to an image $I_2(\mathbf{x})$ do not determine the best-fit Gaussian to an image $I_3(\mathbf{x}) = I_1(\mathbf{x}) + I_2(\mathbf{x})$ in a straightforward manner.

Unlike the adaptive moments, the unweighted moments are amenable to analytical calculations. Since the unweighted moments of two images simply add to give the unweighted moments of the third image obtained by convolving the two images, we can write an expression for the unweighted size (if it exists) of *any* object as a function of the two IPC coupling parameters α and α' , including the pixel response as

$$\sigma_{\text{un,obs}}(\alpha, \alpha') = \sqrt{\sigma_{\text{un}}^2 + 2\alpha + 4\alpha'} = \sqrt{\sigma_{\text{un,int}}^2 + \frac{1}{12} + 2\alpha + 4\alpha'}, \quad (4.22)$$

where $\sigma_{\text{un,obs}}$ and σ_{un} are the unweighted sizes with and without the effects of IPC, and $\sigma_{\text{un,int}}$ is the intrinsic size of the object (without the broadening due to the pixel response) in pixels. We derive this relation in Appendix A.

The expression derived may not be useful for space-based PSFs, but for larger objects ($\sigma_{\text{un,int}} \gg \sqrt{1/12}$) that are approximately Gaussian (for which the adaptive and

unweighted moments agree), it can serve as a good approximation for the adaptive size if $\alpha' < \alpha \ll 1$. The conditions on α , α' , and $\sigma_{\text{un,int}}$ ensure that the non-Gaussianity in the final image is small. As an expression for the unweighted size, Eq. (4.22) holds true in all cases (if σ exists).

4.3.2 Other size definitions

There are other size definitions that are not based on second moments. The full width at half maximum (FWHM) is one common measure of the size of a PSF. For an Airy PSF corresponding to a wavelength λ ,

$$\text{FWHM (in pixels)} \approx \frac{1.03\lambda}{sD}, \quad (4.23)$$

where D is the telescope diameter and s is the pixel scale in units of radians/pix.

Another measure of size is the half-light radius, R_e , which is the radius of the circle centered at the object centroid that encloses 50% of the energy. It is sometimes denoted as *EE50*. For an Airy PSF,

$$R_e = \text{EE50 (in pixels)} \approx 0.535 \frac{\lambda}{sD}. \quad (4.24)$$

Note that the *EE50* is a radius and the FWHM is more like a diameter.

Diffraction-limited PSFs have large wings. The adaptive moments represent the core size of the PSF, while the unweighted moments and (to a lesser extent) the non-moment-based sizes also capture information about these wings. The WFIRST Science Definition Team report [SDT; 2] specifies the requirement of PSF sizes in terms of *EE50*. However, for weak lensing systematics, we focus on the PSF core size from the adaptive moments. For comparison, we present the half-light radius and adaptive size for the PSFs in Table 4.2, with and without diffraction spikes (which were neglected in the WFIRST SDT report).

Realistic PSFs have features such as diffraction spikes from the supporting struts, central obscuration, aberrations and pixelization and hence the resulting profile is not an Airy pattern (see Fig. 4.2). Thus, one cannot use Eq. 4.23 or Eq. 4.24 to estimate the PSF size. One way to define these quantities is to fit the image to a

profile with well-defined FWHM or $EE50$. However, as we will see in Sec. 4.4, the WFIRST PSFs have complex features that are not captured by simple PSF models. Thus, we will use an empirical measurement of $EE50$ directly from the images.

Measuring FWHM directly from the PSF image is a difficult task and is highly sensitive to noise in the image. Measuring the half-light radius is comparatively robust since we integrate (partially) the light profile instead of using the individual samples of the profile. The first task in measuring the half-light radius of a PSF is to identify the centroid of the image. Starting from that location, we find the radius of the smallest circle that contains at least 50% of the total flux. This is done by calculating the distance of every pixel from the center and determining empirically the azimuthally averaged radial profile. That is, given a center (x_0, y_0) and a separation from the centroid R , the fraction of light enclosed $f(R; x_0, y_0)$ is

$$f(R; x_0, y_0) = \sum_{i,j} I[i, j] \Theta(R^2 - (i - x_0)^2 - (j - y_0)^2), \quad (4.25)$$

where $\Theta()$ is the Heaviside step function. Here we have implicitly assumed that the PSF has unit flux. The half-light radius is calculated by solving for R such that $f(R; x_0, y_0) = 0.5$ for some x_0, y_0 .

The half-light radius can be fairly sensitive to the choice of the centroid. For Airy-like PSFs that exhibit circular symmetry, which would be the case if the supporting struts were radial (see Sec. 4.4.1 for details) and in the absence of aberrations, the center is unambiguously the peak of the profile. But the WFIRST PSFs do not exhibit any such symmetry and hence it is not evident where the centroid should be. In simulations, one can locate the ‘true’ center by identifying the center of the underlying Airy profile and treat aberrations as re-distribution the light around the ‘true’ center, thus affecting the half-light radius (but not the centroid itself). However, in real observations of stars to determine the PSF, it is impossible to know where the ‘true’ centroid would be and thus we need a prescription to calculate the centroid given a PSF image. One natural choice is to use the coordinates obtained from Eq. 4.13a as the centroid for calculating the half-light radius, which will not coincide with the ‘true’ center of the PSF in general.

4.4 Methods

4.4.1 WFIRST module description

Realistic WFIRST PSFs used in this work are simulated using GalSim [69]. GalSim is a commonly-used open-source tool for the weak lensing community to simulate realistic images of galaxies. The authors of this paper have built a WFIRST module within GalSim, which is now publicly available in GalSim v1.3. We provide a brief description of the WFIRST module below.

Filter responses for the six bandpasses - Z087, Y106, J129, W149, H158 and F184 - are available in this module, along with the blue and red wavelength limits for each of the filters and the corresponding effective wavelengths, which are the bandpass-weighted mean wavelength. This information, listed in Table 4.1, can be retrieved by calling the `getBandpasses` routine within the WFIRST module.

The focal plane assembly (FPA) of the WFIRST-AFTA telescope consists of 18 H4RG detectors. PSFs corresponding to one or more of these detectors can be generated by passing the detector numbers as parameters to the argument `SCAs` of `getPSF`. The variations of the PSFs within each detector were verified to be small and GalSim v1.3 does not account for this variation, though future releases of GalSim may include them.

Complex, aberrated wavefronts incident on a circular pupil can be approximated by a sum of Zernike polynomials. Following the convention in [128], the polynomials are labelled by an integer j . The low order Zernike polynomials map the low-order aberrations commonly found in telescopes, such as defocus ($j = 4$), astigmatism ($j = 5, 6$), coma ($j = 7, 8$), trefoil ($j = 9, 10$), and so on. Using these polynomials up to $j = 11$, corresponding to spherical aberration, the WFIRST PSFs corresponding to any of 18 detectors can be constructed from the `getPSF` routine.

By default, `getPSF` outputs instances of the `ChromaticOpticalPSF` class which can be convolved with a galaxy or star that has an SED to make a chromatic image. Alternatively, the user has an option to obtain instances of achromatic `OpticalPSF` class, which evaluates the chromatic WFIRST PSFs at a particular wavelength provided by the user. For the results described in this paper, PSFs for each of the

six bandpasses are obtained by evaluating the chromatic PSFs at the corresponding effective wavelengths.

The WFIRST-AFTA telescope has a central obscuration in the pupil plane and the supporting struts are not radial (see Fig. 4.1). The `getPSF` routine in the WFIRST module takes the pupil plane configuration into account and simulates the PSF images, with expected aberrations according to the latest design with chromatic effects if requested by the user, for each of the bandpasses and for each of the 18 H4RG detectors in the focal plane [129]. This process requires two inputs: the pupil plane configuration and the aberrations described by the Zernike coefficients, which are available publicly ⁵. The latter have been incorporated within the WFIRST module but in GalSim v1.3, only the circular pupil plane configuration, which is appropriate for the long-wavelength bands, is incorporated.

The PSFs can be drawn as a GalSim `Image` instance with the (approximate) native WFIRST pixel scale of 0.11" per pixel (`wfirst.pixel_scale`), which results in realistically undersampled images. The resolution of a PSF image can be increased by convolving the PSF profile with a top-hat profile corresponding to the pixel response and then drawing the image at a smaller scale. Fig. 4.2 shows higher-resolution images of the PSFs generated in such a manner in the absence of IPC or any other detector effects and noise. However, resampling the PSF image in the presence of IPC requires combining multiple dithered exposures containing IPC. We explain in Sec. 4.4.3 how to handle PSF images in the presence of IPC.

The WFIRST module also has routines to incorporate many detector non-idealities such as nonlinearity, reciprocity failure and IPC, and to model the detector configuration for an observation at a given position with a given orientation angle. Values for telescope parameters such as the pupil diameter and obscuration; detector parameters such as the pixel scale, dark current, and IPC coupling; and basic survey parameters like planned bandpasses and exposure times are also included. These values will be adjusted as the WFIRST design evolves.

⁵http://wfirst.gsfc.nasa.gov/science/sdt_public/wps/references/instrument/

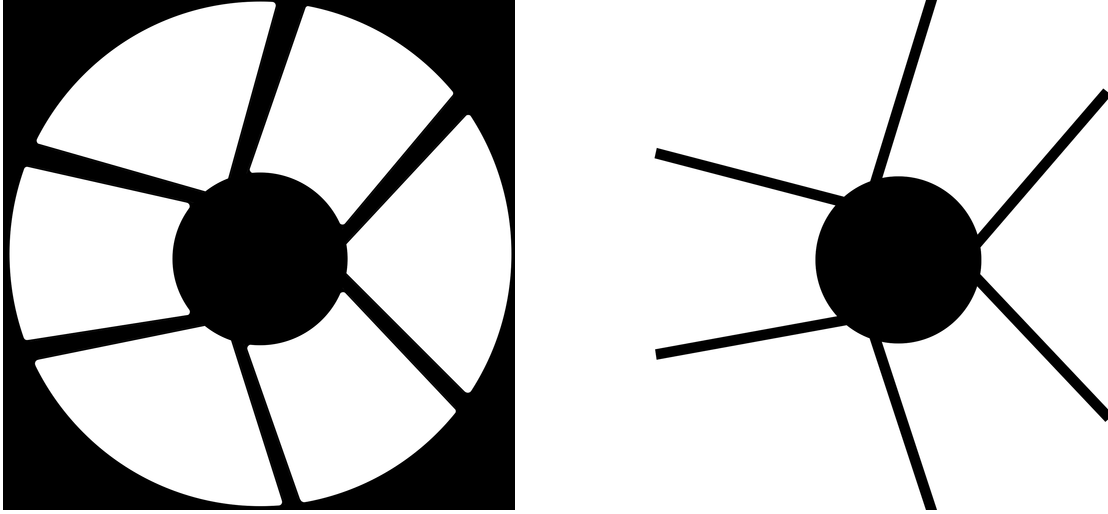


Figure 4.1: *Left:* WFIRST pupil plane configuration for long wavelength bands W149, H158, and F184. *Right:* WFIRST pupil plane configuration for short wavelength bands Z087, Y106, and J129. The simulations in this work use the pupil plane image on the left for all wavelengths.

Bandpass	Minimum λ	Maximum λ	Effective λ
Z087	735.0	1010.0	873.39
Y106	900.0	1230.0	1061.43
J129	1095.0	1500.0	1292.11
W149	905.0	2050.0	1458.01
H158	1340.0	1830.0	1577.05
F184	1630.0	2060.0	1837.3

Table 4.1: Table of minimum, maximum and effective wavelengths in nanometers for each of the six bandpasses.

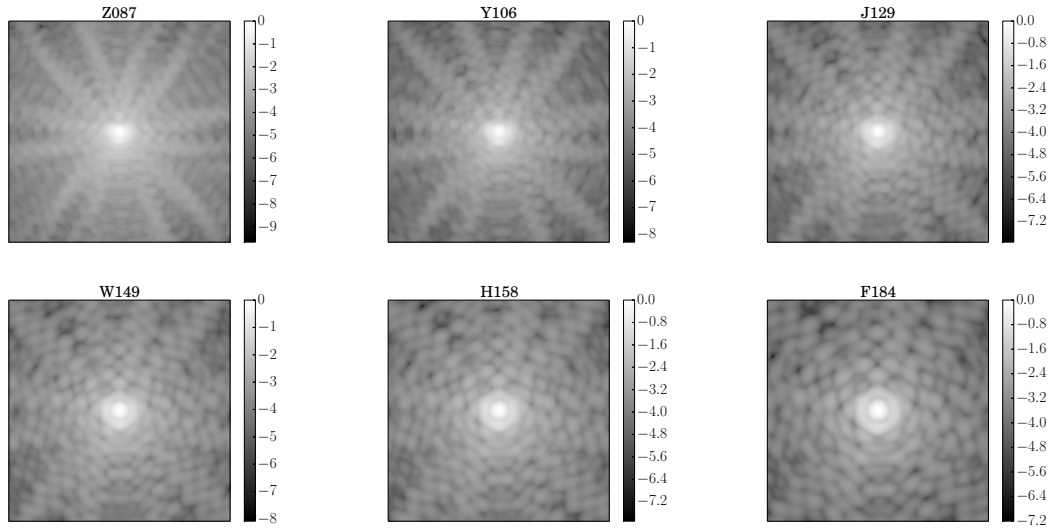


Figure 4.2: Simulated PSF images using the WFIRST module in GalSim for different filters, in logarithmic intensity scale, relative to the brightest pixel at the center. The PSFs are evaluated at the effective wavelength of the bandpass filters listed in Table. 4.2. The images correspond to an area of $1.76'' \times 1.76''$ or 16×16 pixels, drawn at a scale that is 32 times smaller than the native pixel scale, thus giving images of 512×512 pixels. The filters are arranged in increasing wavelengths from left to right, top to bottom, i.e., the top row corresponds to Z087, Y106, and J129 (from left to right) and the bottom row corresponds to W149, H158, and F184 bands (from left to right).

4.4.2 Simulation

To study the effects of IPC on PSFs in the simplest possible setting, we ignore all other detector effects (non-linearity, reciprocity, read noise etc.). Effects that are non-linear will lead to slightly different PSF images depending on the apparent magnitude of the star and the exposure time; ignoring them helps to understand the effects on PSFs independent of such quantities. We also add no noise in our simulations since that would require specification of a particular signal level.

Resampling the PSF profile (see Sec. 4.4.3) to obtain high resolution PSF images ensures that our results are less sensitive to where the centroid of the PSF falls within a pixel (center or edge or corner). We let the signal level of the PSF images be arbitrary since we do not include noise or any signal-dependent effects, and since IPC is linear it does not depend on the signal level. For all the reasons mentioned above, it suffices to simulate one PSF image per band for each of the detectors.

The results presented below are for the center of a randomly chosen detector, 7 [see 129, for numbering system]. We confirmed that our results are not significantly altered when using other detectors. The WFIRST reference weak lensing program requires shape measurements in only the J129, H158 and F184 bands. Thus, we present our results only for the PSFs of these 3 bands.

It is important to understand what features are included in our PSF simulations and what features are not. First, the PSFs include the diffraction spikes due to the supporting struts, while the WFIRST SDT report set requirements while masking out these spikes. The WFIRST requirements [2] also considered jitter and charge diffusion, which are not included in our simulations. Thus, while the simulated PSFs are fairly realistic, they differ in certain ways from the PSFs on which the requirements were set. Also, the short-wavelength bands - Z087, Y106 and J129 - do not use the appropriate pupil plane configuration shown in Fig. 4.1, but rather use that of the long-wavelength bands throughout this work.

4.4.3 Overcoming undersampling

Measurements of object sizes or shapes from undersampled images can significantly differ depending on where the object centroid falls within a pixel. The image sampling

rate must be at least the Nyquist rate for the band limit set by the optical response of the system in order to recover the full continuous image from discrete pixel values, and thereby avoid aliasing. We want to analyse only oversampled images to distinguish detector effects from aliasing artifacts.

WFIRST PSFs are not Nyquist sampled, by design. In order to measure the change in the PSF sizes due to interpixel capacitance, we must increase the resolution of the PSF image. In GalSim, the sampling rate of the PSF image can be increased when calling the `drawImage` routine with a scale parameter `scale=s/N` for some $N > 1$, with s being the native pixel scale. This will alter the pixel response as well and hence does not produce the correct PSF image. One must first convolve the PSF with the pixel response corresponding to the native pixel scale, then call `drawImage` with `method='no_pixel'`. For detector effects like voltage non-linearity and reciprocity failure [see, e.g., 117] for which the detector effect depends on the pixel value, the above method of obtaining Nyquist-sampled images is sufficient.

However, to include interpixel capacitance, for which the pixel correction depends on neighboring pixel values, images must be drawn at the native pixel scale. Higher-resolution images can be obtained from multiple lower-resolution images with sub-pixel offsets, also known as a dither sequence. Softwares like Drizzle [130], iDrizzle [131], and IMCOM [132] use algorithms to combine dither sequences. However, for uniform sub-pixel offsets, the resolution can be increased by simply interleaving the images - a technique that dates back to [133]. This technique is ideal for PSF images from simulations, where offsets can be precisely set, allowing higher sampling to be achieved without external (to GalSim) image combination software.

The basic interleaving concept is mathematically described as follows: Let $I_{n \times n}[\cdot, \cdot]$ denote some $n \times n$ image of some continuous light profile $I(x, y)$ hitting the detector. Thus

$$I_{n \times n}[i, j] = \int_{-\frac{p}{2}}^{\frac{p}{2}} dx' \int_{-\frac{p}{2}}^{\frac{p}{2}} dy' I(ip + x', jp + y') \quad (i, j \in \{1, 2, \dots, n\}), \quad (4.26)$$

where p is the pixel spacing or more appropriately, the length of the side of a pixel in the above equation. Consider a set of 3 images $I_{n \times n}^{(m)}[\cdot, \cdot]$ for $m = 1, 2, 3$, obtained by moving the detector by a distance $p/2$ along either of the axes or both, with

$I_{n \times n}^{(0)} = I_{n \times n}$. Therefore

$$I_{n \times n}^{(m)}[i, j] = \int_{-\frac{p}{2}}^{\frac{p}{2}} dx' \int_{-\frac{p}{2}}^{\frac{p}{2}} dy' I \left(\left(i + \frac{b_1}{2}\right)p + x', \left(j + \frac{b_2}{2}\right)p + y' \right), \quad (4.27)$$

with $b_1, b_2 \in \{0, 1\}$ and $m = 2b_1 + 2b_2$. Given these four images, one can obtain a $2n \times 2n$ image of $I(x, y)$ with twice the resolution than the original by simply interleaving these 4 images:

$$I_{2n \times 2n}[2i + b_1, 2j + b_2] = I_{n \times n}^{(m)}[i, j], \quad (4.28)$$

This image has an effective sampling interval of $p/2$ while the pixel response function is still p . Note that the interleaved image has a higher flux given by the sum of the fluxes of the individual images. Since we are interested in measuring only the second moments, the normalization does not matter.

$$I_{2n \times 2n}[i, j] = \int_{-\frac{p}{2}}^{\frac{p}{2}} dx' \int_{-\frac{p}{2}}^{\frac{p}{2}} dy' I(ip/2 + x', jp/2 + y') \quad (i, j \in \{1, 2, \dots, 2n\}) \quad (4.29)$$

One can interleave $N \times N$ ($N \geq 2$) images in either direction to generate an image with a sampling rate that is N times greater than the native one, without changing the pixel response. The `interleaveImages` routine in `galsim.utilities` carries out this process for GalSim users.

An oversampled image of the WFIRST PSF with detector effects included must be obtained by interleaving multiple undersampled PSF images that have these effects included. For band-limited PSFs, one can in principle reconstruct the Nyquist-sampled PSF from a ‘superimage’ of the PSF by choosing $N = \lceil (2p)/(\lambda_{\min} N_f) \rceil$, where λ_{\min} is the smallest wavelength in a given bandpass filter and N_f is the focal ratio or the f-number of the telescope. For the WFIRST-AFTA telescope, $p = 10\mu m$ and $N_f = 7.8$ [2]. This gives $N \geq 3$ for J129 and $N \geq 2$ for H158 and F184 bands. However, we choose to oversample the images by a large factor in order to additionally reduce the quantization error, the error due to discretizing, and to reduce the variance due to any sub-pixel offsets that PSFs may have. We find that setting $N = 32$ is sufficient for all our analysis by checking for convergence in our results as a function of N .

Bandpass	Adaptive size σ (in mas)		HLR R_e (in mas)		Ellipticity $ e $	
	w/ spikes	w/o spikes	w/ spikes	w/o spikes	w/ spikes	w/o spikes
J129	61.50	60.480	114.85	95.06	0.0646	0.0652
H158	66.16	65.884	123.72	103.85	0.0379	0.0417
F184	72.39	72.452	132.37	113.21	0.0246	0.0292

Table 4.2: Table of PSF sizes and ellipticity. Adaptive sizes and half-light radii in milliarcseconds (mas) and magnitude of ellipticities are tabulated for the PSFs of the J129, H158 and F184 bandpasses. Size and ellipticity measurements for the PSFs without including the diffraction spikes are also tabulated, so as to be able to relate to the values in WFIRST documents [1, 2].

The oversampled image is a special linear combination of the undersampled images, such as IMCOM would produce from a dither sequence. Oversampling images in this manner does not introduce any shape measurement error [134].

4.5 Results

4.5.1 Increase in PSF sizes

The High Latitude Imaging Survey Data Set requirements on the half-light radii of the PSFs are: $\leq 0.12''$ for the J129 band, $\leq 0.13''$ for the H158 band and $\leq 0.14''$ for the F184 band. These requirements were set using specific methodology, including the masking of diffraction spikes and inclusion of jitter and charge diffusion. We cannot compare our PSF sizes with those from [2] due to these methodology differences. However, since our goal is to determine how IPC affects PSF sizes, we provide our estimates of PSF sizes without IPC (computed various ways) in Table 4.2 as a baseline, then consider increases with respect to that baseline.

As mentioned in Sec. 4.3.2, the half-light radius depends on the choice of the centroid and the centroid computed from Eq. 4.13a will in general not agree with the ‘true’ center of the image. The centroid from the adaptive moments disagrees with the ‘true’ center of the image by at most half a pixel ($0.055''$) in either direction. Prior to the application of IPC, the half-light radius determined using Eq. 4.13a for the centroid is smaller compared to the one calculated using the ‘true’ center of the image by 2 – 4%.

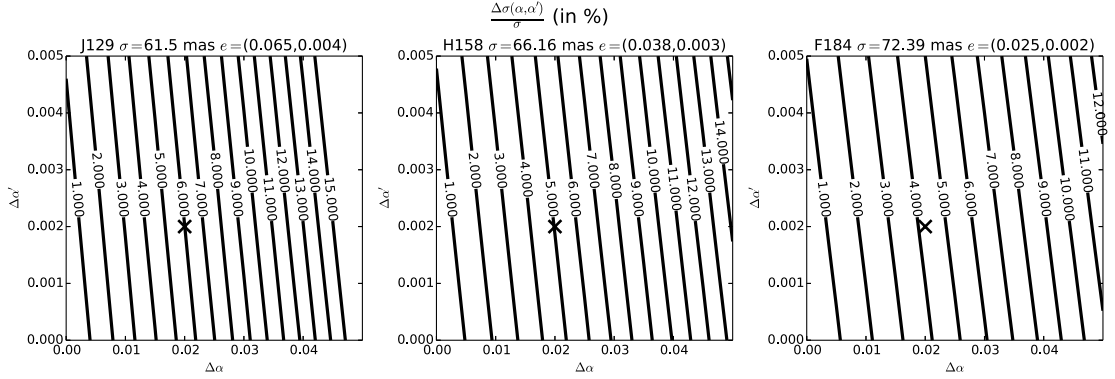


Figure 4.3: Contour plot of the relative increase in the adaptive size (expressed as a percent) as a function of the α and α' parameters in the IPC kernel in Eq. (4.8) for the relevant WFIRST PSFs. The black \times represents a nominal value of the IPC parameters in H4RG detectors. For each filter, the adaptive size in milliarcseconds (mas) and ellipticity (e_1, e_2) without IPC is noted above the subplots.

We present our results for two specific sub-classes of the 3-parameter IPC kernel (Eq. 5.16). The first of them is the 2-parameter isotropic IPC model (Eq. 4.8). We consider this case since the nominal value of α_+ is 0. Figures 4.3 and 4.4 show the increase in PSF size in all bands as a function of α and α' , using the adaptive size (Fig. 4.3) and the EE50 size (Fig. 4.4). As shown in Figs. 4.3- 4.4, the increase in PSF sizes is a few per cent in all bands for the nominal values ($\alpha_0 = 0.02$ and $\alpha'_0 = 0.002$) of the IPC parameters. More specifically, the relative change in the adaptive size is about 4 – 6% and the relative change in the half-light radius (with Eq. 4.13a as centroid) is about 5 – 6% depending on the bandpass. When the half-light radius is computed with the ‘true’ center as the centroid, the relative increase is smaller ($\sim 4.5\%$) and the variation is smaller across the bandpasses. We emphasize that it is impossible to know the location of the ‘true’ center in the real observations of PSF and thus results with ‘true’ center being the centroid are not relevant in practice. We nevertheless present these results to show that not knowing the ‘true’ center does not significantly affect our overall conclusions.

As expected, the size is affected more by the coupling between nearest neighbors than by diagonal coupling, owing to a higher coupling parameter. The same is true for the change in PSF ellipticity shown in Figs. 4.5 and 4.6 for the ellipticity components e_1 and e_2 , along and at 45° with respect to the pixel edges respectively. A typical value for Δe_1 (Δe_2) is $\sim 10^{-3}$ (10^{-4}). Thus, even if uncorrected, the contribution of IPC to

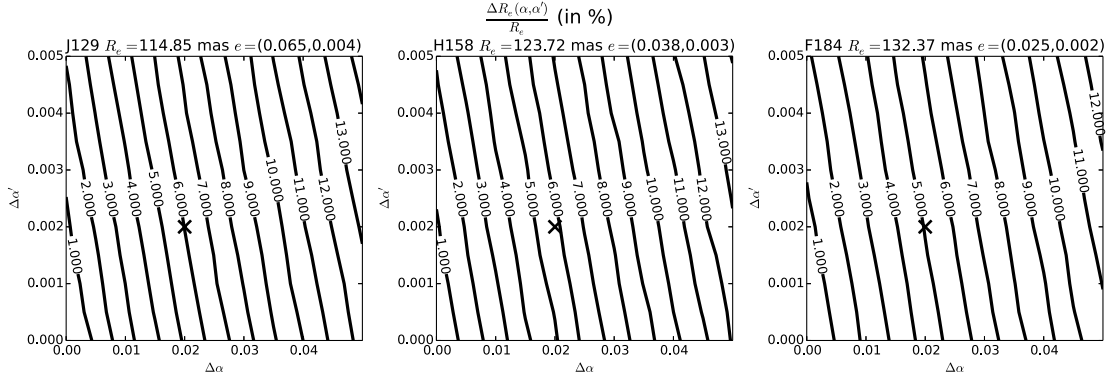


Figure 4.4: Contour plot of the relative increase in the half-light radius EE50 (expressed as a percent) as a function of the α and α' parameters in the IPC kernel in Eq. (4.8) for the relevant WFIRST PSFs. The black \times represents a nominal value of the IPC parameters in H4RG detectors. For each filter, the EE50 in milliarcseconds (mas) and ellipticity (e_1, e_2) without IPC is noted above the subplots. The black cross marker represents a nominal value of the IPC parameters in the H4RG detectors.

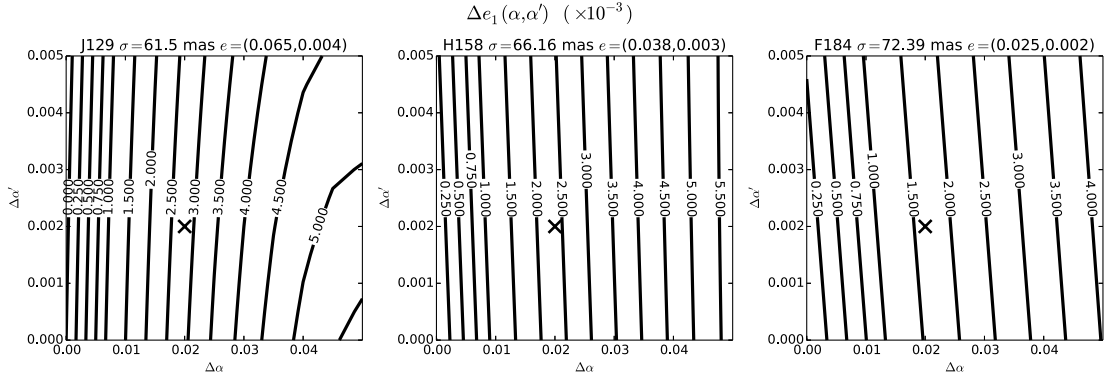


Figure 4.5: Contour plot of the change in the ellipticity component e_1 as a function of the α and α' parameters in the IPC kernel in Eq. (4.8) for the relevant WFIRST PSFs. The black \times represents a nominal value of the IPC parameters in H4RG detectors. For each filter, the adaptive size in milliarcseconds (mas) and ellipticity (e_1, e_2) without IPC is noted above the subplots.

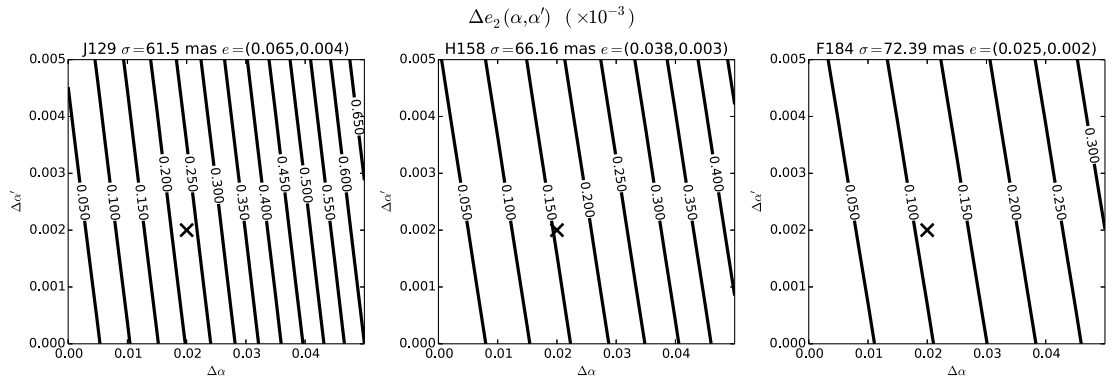


Figure 4.6: Contour plot of the change in the ellipticity component e_2 as a function of the α and α' parameters in the IPC kernel in Eq. (4.8) for the relevant WFIRST PSFs. The black \times represents a nominal value of the IPC parameters in H4RG detectors. For each filter, the adaptive size in milliarcseconds (mas) and ellipticity (e_1, e_2) without IPC is noted above the subplots.

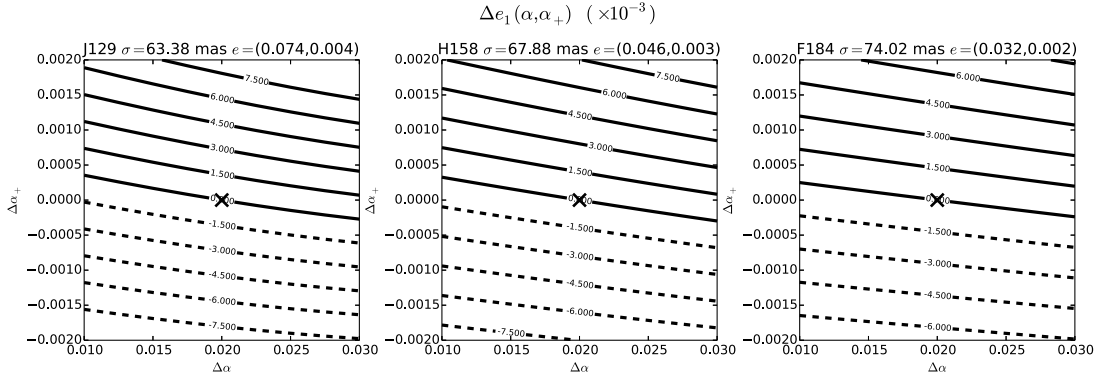


Figure 4.7: Contour plot of the change in the ellipticity component e_1 as a function of the α and α_+ parameters in the IPC kernel in Eq. (5.16) with $\alpha' = 0.002$ for the relevant WFIRST PSFs. The black \times represents a nominal value of the IPC parameters in H4RG detectors. For each filter, the adaptive size in milliarcseconds (mas) and ellipticity (e_1, e_2) without IPC is noted above the subplots.

the PSF anisotropy and hence to the additive bias in the shear estimate is expected to be small.

The second sub-class of IPC kernel allows for the anisotropy with a fixed value for the diagonal coupling α' , set equal its nominal value of 0.002. We consider this case since the PSF sizes and shapes are least sensitive to α' . Figs. 4.7- 4.8 show the change to the components of PSF ellipticity. The change in e_2 is about $\pm 5\%$ ($\sim 10^{-4}$) over the entire range of α_+ values we have considered whereas the change in e_1 is of the order 10^{-2} , much bigger than the original e_1 value itself. This is not surprising since both the anisotropy and the e_1 component are aligned along the axes. For a symmetric PSF with $e_2 = 0$, we expect the e_2 to remain 0 after the IPC. The small change in e_2 is attributed to e_2 not being zero to begin with. We verified that the relative increases in sizes have negligible dependence on the anisotropy (figure not shown).

4.5.2 Error in PSF shapes from uncertainty in IPC parameters

If the IPC kernel is known precisely, then the effect can, in principle, be perfectly corrected. However, errors in IPC parameters arise either because of measurement uncertainties or because of the parameters varying (slowly) across the pixels. In

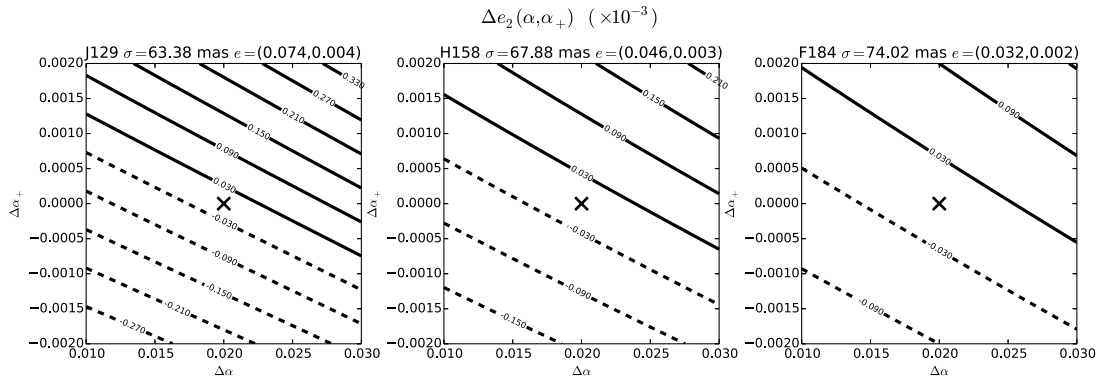


Figure 4.8: Contour plot of the change in the ellipticity component e_2 as a function of the α and α_+ parameters in the IPC kernel in Eq. (5.16) with $\alpha' = 0.002$ for the relevant WFIRST PSFs. The black \times represents a nominal value of the IPC parameters in H4RG detectors. For each filter, the adaptive size in milliarcseconds (mas) and ellipticity (e_1, e_2) without IPC is noted above the subplots.

addition, there is a possibility of error due to adopting an incorrect IPC model, the use of a 3×3 kernel. Even with a perfect IPC correction scheme, errors in the IPC kernel that is assumed and corrected for will propagate into errors in PSF sizes and ellipticities. In this section, we investigate the magnitude of this effect, in all cases assuming a perfect correction scheme.

We start by considering the 2-parameter isotropic IPC kernel (Eq. 4.8) assuming that the model is correct but its parameters have uncertainties. The issue at hand can be addressed by looking the change in the PSF sizes and shapes as a function of α and α' , as done in Sec. 4.5.1; but now on a finer grid over the range of values of the IPC parameters where we expect them to lie. In the ideal case of being able to correct for IPC exactly, the error in PSF size and shape will be due to $\delta\alpha$ and $\delta\alpha'$, the difference between the true values of α and α' and their assumed values, denoted by α_0 and α'_0 . For nominal values of $\alpha_0 = 0.02$ and $\alpha'_0 = 0.002$, Figs. 4.9–4.11 show the error in PSF size and ellipticity as a function of errors in the parameters, $\delta\alpha$ and $\delta\alpha'$. For a 10% error in α and fixed α' ($\delta\alpha' = 0$), the error in relative increase in size is $\sim (5 \pm 0.5)\%$. All the contour lines in these three figures are parallel and approximately equally spaced, which suggests that a linear fitting function could describe these results very well. Thus,

$$\sigma'(\alpha, \alpha') - \sigma'(\alpha_0, \alpha'_0) \approx \delta\alpha R_\alpha(\alpha_0, \alpha'_0) + \delta\alpha' R_{\alpha'}(\alpha_0, \alpha'_0) \quad (4.30a)$$

$$e'_k(\alpha, \alpha') - e'_k(\alpha_0, \alpha'_0) \approx \delta\alpha S_{k,\alpha}(\alpha_0, \alpha'_0) + \delta\alpha' S_{k,\alpha'}(\alpha_0, \alpha'_0), \quad \text{for } k = 1, 2 \quad (4.30b)$$

for some set of coefficients R_α , $R_{\alpha'}$, $S_{k,\alpha}$ and $S_{k,\alpha'}$ (for $k = 1, 2$), which are equivalent to appropriate partial derivatives evaluated at the chosen nominal values of the parameters.

The coefficients in Eqs. (4.30) were calculated by performing linear regression on an 11×11 grid of $\delta\alpha$ and $\delta\alpha'$, with $\delta\alpha$ varying uniformly from -0.005 to $+0.005$ and $\delta\alpha'$ varying uniformly from -5×10^{-4} to $+5 \times 10^{-4}$. The values of the coefficients for the PSFs of the J129, H158 and F184 bandpasses are given in Table 4.3. We find that the quantities on the left hand side of Eqs. (4.30) agree with the linear model prediction with at most a 1% error, for $\delta\alpha \approx 0.1\alpha_0$. Thus, the errors in PSF sizes and ellipticities can simply be specified by the six linear coefficients, R_α , $R_{\alpha'}$, $S_{1,\alpha}$, $S_{1,\alpha'}$, $S_{2,\alpha}$ and $S_{2,\alpha'}$, defined in Eq. 4.30.

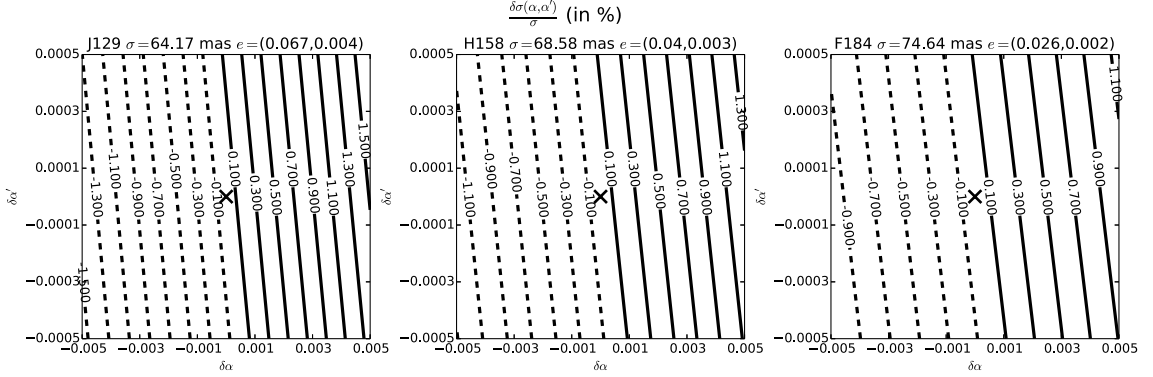


Figure 4.9: Contour plot of the relative change in the adaptive size (expressed as a percent) as a function of $\delta\alpha$ and $\delta\alpha'$, the deviation from their nominal values ($\alpha_0 = 0.02$ and $\alpha'_0 = 0.002$) of the parameters in the IPC kernel in Eq. (4.8) for the relevant WFIRST PSFs. The black \times corresponds to no deviation from the chosen nominal values of the IPC parameters in H4RG detectors. For each filter, the adaptive size in milliarcseconds (mas) and ellipticity (e_1, e_2) without IPC is noted above the subplots.

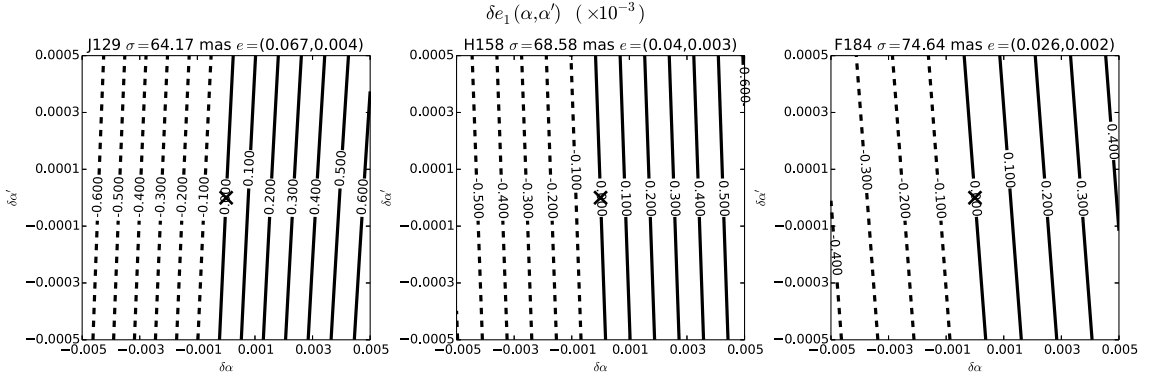


Figure 4.10: Contour plot of the absolute change (after multiplication by 10^3) in the ellipticity component e_1 as a function of $\delta\alpha$ and $\delta\alpha'$, the deviation from their nominal values ($\alpha_0 = 0.02$ and $\alpha'_0 = 0.002$) of the parameters in the IPC kernel in Eq. (4.8) for the relevant WFIRST PSFs. The black \times corresponds to no deviation from the chosen nominal values of the IPC parameters in H4RG detectors. For each filter, the adaptive size in milliarcseconds (mas) and ellipticity (e_1, e_2) without IPC is noted above the subplots.

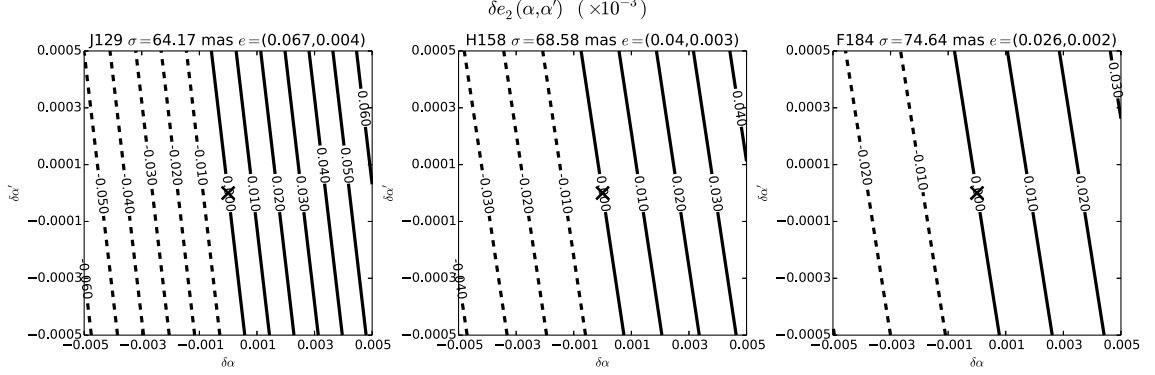


Figure 4.11: Contour plot of the absolute change (after multiplication by 10^3) in the ellipticity component e_2 as a function of $\delta\alpha$ and $\delta\alpha'$, the deviation from their nominal values ($\alpha_0 = 0.02$ and $\alpha'_0 = 0.002$) of the parameters in the IPC kernel in Eq. (4.8) for the relevant WFIRST PSFs. The black \times corresponds to no deviation from the chosen nominal values of the IPC parameters in H4RG detectors. For each filter, the adaptive size in milliarcseconds (mas) and ellipticity (e_1, e_2) without IPC is noted above the subplots.

Bandpass	$R_\alpha/\sigma(\alpha_0, \alpha'_0)$	$R_{\alpha'}/\sigma(\alpha_0, \alpha'_0)$	$S_{1,\alpha}$	$S_{1,\alpha'}$	$S_{2,\alpha}$	$S_{2,\alpha'}$
J129	2.9432	2.7691	0.1308	-0.063	0.0116	0.0134
H158	2.4457	2.5631	0.1171	0.0406	0.0076	0.0112
F184	2.0168	2.3741	0.0807	0.0604	0.0054	0.0084

Table 4.3: List of the six coefficients given in Eqns. 4.30 for the J129, H158 and F184 bandpasses. The coefficients represent the ‘instantaneous rate’ of change in PSF size and ellipticity with respect to the change in one of the IPC parameters about the nominal values for the case of isotropic kernel (Eq. 4.8).

Bandpass	$R_\alpha/\sigma(\alpha_0, \alpha'_0)$	$R_+/\sigma(\alpha_0, \alpha'_0)$	$S_{1,\alpha}$	$S_{1,+}$	$S_{2,\alpha}$	$S_{2,+}$
J129	2.9429	0.0383	0.1308	4.1516	0.0116	0.1165
H158	2.4454	0.0435	0.1171	3.7389	0.0075	0.0704
F184	2.0166	0.0336	0.0807	3.2975	0.0054	0.045

Table 4.4: List of the six coefficients given in Eqns. 4.31 for the J129, H158 and F184 bandpasses. The coefficients represent the ‘instantaneous rate’ of change in PSF size and ellipticity with respect to the change in one of the nearest neighbor coupling parameters about the nominal values for the case of anisotropic kernel (Eq. 5.16).

We computed the coefficients corresponding to the PSFs with no supporting struts (not shown in the figures or tables). When we do not include the struts (but do include obscuration and the expected level of aberrations), $R_\alpha/\sigma(\alpha_0, \alpha'_0)$ decreases by 10% from its original value when we include struts. This suggests that requirements on IPC may not depend very strongly on the choice to include or exclude struts in the simulations. The change in the S -type coefficients is comparable or even greater than the coefficients themselves by a factor of 2 in many cases (and hence a change of sign in some cases), indicating that the ellipticities are very sensitive to the diffraction spikes.

Instead of the adaptive size, if we consider the EE50 radius, the coefficient that is the analog of $R_\alpha/\sigma(\alpha_0, \alpha'_0)$ is either comparable or slightly smaller (by 33% or less) than the corresponding coefficient for the adaptive size. On the other hand, the coefficient that is the analog of $R_{\alpha'}/\sigma(\alpha_0, \alpha'_0)$ is consistently about 60% larger than the corresponding one for the adaptive size. Thus, the EE50 radius, like the unweighted moment (Sec. 4.3.1), is more sensitive to the diagonal coupling than the adaptive size is.

4.5.3 Effects on PSF due to anisotropy of IPC

We now address the effect of a slight anisotropy that is commonly observed in the IPC kernel on the PSF shapes. The difference between the nearest neighbor coupling along the axes of H4RG detectors is expected to be small, as in for WFC3 (Eq. 5.17). This lets us handle the anisotropy perturbatively as we handled the uncertainties in the coupling in Sec. 4.5.2. If we denote the average nearest neighbor coupling along both the directions as α , we consider the exact coupling along x and y axes as a small

deviation from α , which we denote as α_+ . Generalizing the Eqns. 4.30, we now write

$$\delta\sigma' = \delta\alpha R_\alpha + \delta\alpha_+ R_+, \quad (4.31a)$$

$$\delta e'_k = \delta\alpha S_{k,\alpha} + \delta\alpha_+ S_{k,+}, \quad \text{for } k = 1, 2. \quad (4.31b)$$

Naively, we expect the anisotropy to have only a weak effect on the PSF sizes and a relatively stronger effect on the ellipticity, compared to that from the isotropic term α . We verify this and quantify the effect from simulations. In our simulations to compute the coefficients in Eq. 4.31, we varied α_x defined as $\alpha + \alpha_+$ and α_y defined as $\alpha - \alpha_+$ uniformly on a 11×11 grid from $0.02 - 0.005$ to $0.02 + 0.005$. We held α' constant at its nominal value of 2×10^{-3} for simplicity. The best fit parameters for R_α , R_+ , $S_{k,\alpha}$ and $S_{k,+}$ in Eqns. 4.31 are found from linear regression. If the model is valid, then we should expect the R_α values to agree with their earlier values. Table 4.4 lists these coefficients for the J129, H158 and F184 bandpasses and indeed the R_α values agree for all of them.

4.6 IPC in the context of WFIRST requirements

It is informative to place the results of our analysis in Sec. 4.5 into context, comparing IPC-related shape measurement errors to the requirements for the WFIRST PSF as outlined in [2]. We highlight again that the PSFs used in our analysis do not include jitter and charge diffusion. These effects will tend to increase the size of the PSFs and somewhat reduce the relative effects of IPC. Thus, not including these effects would tend to push our bounds on the IPC parameters to the slightly pessimistic/conservative side.

While the maximum allowed PSF sizes are given in terms of the half-light radii, the maximum tolerable error on PSF sizes are given in terms of the second moments. Since the adaptive moments are sensitive mainly to the core of the PSF, our overall conclusions based on adaptive moments are fairly independent of the choice of including the diffraction spikes. This can be seen from Table 4.2, where the adaptive sizes change by $\lesssim 1.6\%$ whether or not we consider the diffraction spikes as a part of the

PSF.

Let us suppose that it is possible to measure the IPC parameters to within errors of $\delta\alpha = \delta\alpha' = \delta\alpha_+ = 10^{-4}$. These could be simple calibration errors or perhaps due to some spatial or temporal IPC variation that went uncharacterized. If we model the WFIRST PSF with these parameters, we see that the worst PSF shape errors are in the J band, with $\delta\sigma/\sigma \approx 5.75 \times 10^{-4}$ (and from Eq. 4.16, $\delta\text{tr}(\mathbf{M})/\text{tr}(\mathbf{M}) \lesssim 1.15 \times 10^{-3}$) and $\delta e_1 \approx 4.35 \times 10^{-4}$. These values are obtained from Eqs. 4.30 and 4.31, with values for the coefficients taken from Tables 4.3 and 4.4. For the High Latitude Imaging Survey, the tolerance on the relative error of trace of the second moments of the PSFs is set as 0.093%, and the required knowledge of PSF ellipticity is 4.7×10^{-4} per component [2]. These tolerances might evolve as the details of the survey are finalized. Thus, our model would have errors comparable to the tolerances for the entire survey. In practice, a PSF model will be fit to on-sky measurements, and shape errors caused by a misestimate of IPC parameters will be absorbed by other parameters in the PSF model. This freedom relaxes requirements for the IPC parameters. To set definitive IPC requirements for WFIRST, we need to consider the planned shape measurement strategy and other sources of shape measurement error, which are still being studied. However, we have shown that the effect of IPC on shape measurement is sufficiently large that our ability to calibrate it out should not be taken for granted.

4.7 Conclusion and future work

We have explored the impact of interpixel capacitance, an effect that will be relevant for surveys such as WFIRST that will use near-infrared detectors, on the point-spread function, including its size and shape. To carry out this work, we have created a new WFIRST module in the publicly-available GalSim software package. Using this software, we have determined linear fitting formulae that describe how the PSF size and shape change with the level of IPC, including the effects of changing different parts of a two-parameter IPC model. Our simulations show that the level of IPC that is present in state-of-the-art detector technology will increase the typical PSF sizes by $\sim 5\%$ for WFIRST. This is roughly the case irrespective of whether we include the supporting struts in simulating the PSFs or not.

The isotropic IPC kernel also changes the ellipticity of the PSFs. The changes in e_1 and e_2 are an order of magnitude smaller than the expected PSF e_1 and e_2 themselves. These results may be useful inputs into WFIRST hardware requirements.

There are schemes [125] for removing the effect of IPC from astronomical images. However, these schemes rely on knowledge of the IPC. Thus, we also consider the scenario where the IPC is assumed to be at the nominally expected level, but there are actually systematic deviations from that level, and derive linear fitting formulae for errors on PSF sizes and shapes in the different WFIRST passbands. Assuming a perfect IPC correction scheme, a 10% error in determining the nearest neighbor coupling results in relative errors that are of the order 5×10^{-3} in the PSF sizes. For the errors in PSF sizes and shapes to be within the allowed limits for WFIRST, the uncertainty in the parameters α , α' and α_+ must be much smaller than 10^{-4} .

Our results represent an important step towards placing requirements on hardware that affects the PSF for the WFIRST survey. Future work will use these to consider their impact on the scientific measurements of interest, such as weak lensing. The modifications of the PSFs due to imperfect knowledge of IPC can contribute towards shear calibration biases when carrying out the process of PSF correction to estimate weak lensing shears (Kannawadi et. al., in prep). Even if we had perfect knowledge of IPC, the correlation in the noise caused due to IPC will affect the shear calibration biases. We analyze these effects of IPC in the presence of noise in a future work (Kannawadi et. al., in prep).

Another interesting direction for future work would be to consider the interplay between different detector effects, such as IPC and read noise. Since the introduction of read noise happens at a later stage compared to IPC, any IPC correction scheme would correlate the read noise. We defer exploration of the impact of correlated read noise to future work.

Acknowledgement

The authors thank Roger Smith, Bernard Rauscher and Andrés Plazas Malagón for many useful discussions and Mike Jarvis and Joshua Meyers for their inputs in developing the GalSim WFIRST module. We thank Edward Cheng of Conceptual Analyt-

ics for his comments in improving the manuscript and the referee, David Spergel, for correcting a few minor errors in the original version of the manuscript. This work was carried out in part at the Jet Propulsion Laboratory (JPL), a NASA center run by California Institute of Technology. The authors acknowledge funding from WFIRST study office. C.M.H. is supported by the US Department of Energy, the Packard Foundation, and the Simons Foundation.

[Kannawadi et al.] Arun Kannawadi¹akannawa@andrew.cmu.edu, Rachel Mandelbaum¹, Charles Shapiro², Jason Rhodes^{2,3}

¹McWilliams Center for Cosmology, Carnegie Mellon University, Pittsburgh, PA 15217, USA

²Jet Propulsion Laboratory, California Institute of Technology, Pasadena, CA 91109

³California Institute of Technology, Pasadena, CA 91125

Chapter 5

The impact of interpixel capacitance (IPC) on shear calibration biases for WFIRST from realistic galaxy image simulations

5.1 Introduction

The standard model of cosmology today is the six-parameter Λ CDM model, which has been repeatedly found consistent with a number of independent observations and probes [see for e.g., 20, 135, 136]. This *concordance* model assumes that the theory of General Relativity (GR) is the correct theory of gravity on cosmological scales, according to which, light bends in response to a gravitational field - a phenomenon known as *gravitational lensing*. The observations listed above also suggest that about 27% of the energy in the Universe (or about 85% of the matter by mass) of the Universe is contributed by cold dark matter, which is thought to interact with the more familiar baryonic matter only via gravitation [for attempts of direct detection of dark matter, see for e.g., 137, 138]. While the properties and the distribution of the dark matter can be inferred from the growth of cosmic structure, gravitational

lensing provides us with a tool to probe them directly.

Weak gravitational lensing, or weak lensing (WL), is the most ubiquitous lensing phenomenon that is used. For a detailed review, see [24, 27, 28, 41, 101]. It refers to the small distortions in the shapes of distant galaxies due to massive structures between the observer and the source galaxies. The distortions are so small that they are not noticeable on per-galaxy basis and requires employing statistical techniques on a large number of galaxies to detect the coherent distortion due to lensing.

Several missions that are in operation currently such as the Dark Energy Survey [DES; 45], the Hyper Suprime-Cam [HSC; 139], the Kilo-Degree Survey [KiDS; 46], the Panoramic Survey Telescope and Rapid Response System [PanSTARRS; 47] and several missions in the near future such as the Large Synoptic Survey Telescope [LSST; 48], Euclid [49] and the Wide-Field Infrared Survey Telescope [WFIRST; 1, 2, 50] will image $10^8 - 10^9$ galaxies with the aim of gathering data to perform weak lensing analysis. Among these missions, Euclid and WFIRST¹ are space-based surveys, planned for launch during the early 2020s. Imaging surveys from space offer several advantages, most notably a stable seeing condition (in comparison with ground based surveys, where the seeing conditions depend on the atmosphere). However, another advantage is to be able to image the sky in the near-infrared (NIR) or infrared (IR) wavelengths as the water vapour in the earth's atmosphere is opaque to these wavelengths. Currently, the Wide Field Camera [WFC3; 98] in the Hubble Space Telescope and the Wide Infrared Survey Explorer [WISE; 99] are taking images in the NIR bands. The information obtained in the NIR regime is of interest scientifically, because a) it complements the images in the visible bands b) it helps improve the accuracy of the photometric redshifts and c) it provides higher quality imaging of the high-redshift galaxies.

The enormous quantity of data that would be provided by these surveys imply that the statistical error will become lower than the systematic errors if we adopt the shear estimation procedures that were used in the previous surveys, leading to erroneous conclusions. Thus, with a significant decrease in the statistical errors, the source of systematic errors need to be understood and corrected for.

Among the sources for systematic errors in the galaxy shapes are the non-ideal be-

¹<http://wfirst.gsfc.nasa.gov>

haviour of the telescope detectors. WFIRST will have detectors that use $\text{Hg}_{(1-x)}\text{Cd}_x\text{Te}$ (or simply HgCdTe), an alloy of mercury(Hg), cadmium(Cd) and tellurium(Te) as the photosensitive material with a hybrid CMOS readout architecture. Specifically, they use HxRG family of sensors manufactured by the Teledyne Imaging Sensors. These are very different from the CCD sensors that are sensitive to visible light and have been used in astronomical commonly. Contrastingly, the use of HgCdTe detectors are relatively new and the detector based effects are yet to be fully understood.

The WFIRST Science Investigation Team (SIT) and the detector working group have listed several effects that are of concern for weak lensing with WFIRST. Some of them are:

1. *Interpixel Capacitance*(IPC): IPC is the electrical cross-talk between the pixels of the detectors due to the CMOS readout integrated circuit (ROIC).
2. *Non-linearity*(NL): NL refers to the non-linearity in the conversion of charges in the pixels to voltage readings
3. *Reciprocity Failure*(RF): RF implies that the respond of the detector depends not only on the number of photons but also on their arrival rates
4. *Persistence*: Persistence is the retention of the charges from the previous exposures even after the pixels have been reset to zero.

CCD detectors in LSST also share some of these effects and are of concern for weak lensing. For a brief review on some of the systematic effects arising from the detectors, see [31]. This work focusses on the impact of IPC (devoid of other aforementioned detector effects) on the shear estimates.

This paper is organized as follows. In Sec. 5.2, we provide a background on the basics of weak gravitational lensing - about how shapes of the galaxies are defined and how the lensing shear can be inferred given a population of galaxies. In Sec. 5.3, we describe the detector model and obtain a simple model for interpixel capacitance. In Sec. 5.4, we discuss the cuts applied to the COSMOS catalog along with the parametric fits to the galaxy shapes.

5.2 Lensing basics

If the source galaxy is described a brightness distribution $I^{(\text{int})}(\mathbf{x})$, then the effect of WL is to map the unlensed coordinates to a lensed one while conserving the surface brightness. If the angular size size of the lensed image is much smaller than the characteristic angular scale on which the tidal gravitation field varies, the mapping can be described as a linear transformation between the coordinates as

$$I^{(\text{lensd})}(\mathbf{x}) = I^{(\text{int})}(\mathcal{A}\mathbf{x}) \quad (5.1)$$

The equations relating \mathcal{A} , the Jacobian of the transformation, to the gravitational potential can be found in the reviews mentioned in Sec. 5.1. In this work, we are interested in the measurement bias of the reduced shear and *not* how it affects the lens parameters or cosmological parameters.

The distortion matrix \mathcal{A} is expressed in terms of the convergence κ and the shear components γ_1 and γ_2 as

$$\mathcal{A} = \begin{pmatrix} 1 - \kappa - \gamma_1 & -\gamma_2 \\ -\gamma_2 & 1 - \kappa + \gamma_1 \end{pmatrix} \quad (5.2)$$

$$= (1 - \kappa) \begin{pmatrix} 1 - g_1 & -g_2 \\ -g_2 & 1 - g_1 \end{pmatrix}, \quad (5.3)$$

where $g_i = \gamma_i/(1 - \kappa)$ for $i \in \{1, 2\}$ are the components of the reduced shear. In the weak lensing limit, $\kappa \ll 1$ and therefore $g_i = \gamma_i/(1 - \kappa) \approx \gamma_i$ for $i \in \{1, 2\}$. It is convenient to express the two components of the (reduced) shear as the real and imaginary parts of a complex quantity $(g)\gamma$.

$$g = g_1 + ig_2 = |g|e^{i2\varphi}, \quad \gamma = \gamma_1 + i\gamma_2 = |\gamma|e^{i2\varphi}. \quad (5.4)$$

In the case of a spatially constant lensing shear, an intrinsically round object (a source with concentric circular isophotes or contours) appears as an ellipse (an image with concentric elliptical isophotes). The magnitude of the complex shear determines the *ellipticity* of the lensed image. The axis ratio of the ellipse, which is defined as the ratio of semi-minor axis to semi-major axis, is given by $q := b/a = (1 - |g|)/(1 + |g|)$, assuming $|g| < 1$ (which is indeed the case in WL). Inverting the relation, we get

$$|g| = (1 - q)/(1 + q).$$

$$q := b/a = \frac{1 - |g|}{1 + |g|} \quad \Leftrightarrow \quad |g| = \frac{1 - q}{1 + q} \quad (5.5)$$

The phase φ denotes the orientation angle of the ellipse - the direction of major axis. Since an ellipse has a two-fold rotation symmetry, the phase of the complex shear is 2φ , which is unchanged upon a rotation by 180° .

However, in reality, sources such as galaxies are not circular and at best, elliptical. Thus, the observed ellipticity is a combination of its intrinsic ellipticity (the dominant contribution) and a small shear. For sources with elliptical isophotes with axis ratio q , we define the ellipticity ϵ and distortion e as follows:

$$|\epsilon(q)| = \frac{1 - q}{1 + q} \quad |e(q)| = \frac{1 - q^2}{1 + q^2} \quad (5.6)$$

As in the case of the shear, we assign a phase factor of $e^{i2\phi}$, where ϕ is now the angle of orientation for the major axis, to obtain a complex ellipticity and a complex distortion. Note that the definition of ellipticity is very similar to the expression obtained for the magnitude of the reduced shear for circular sources. However, the former is a geometric property of the source whereas the latter refers to a transformation(!)

Unfortunately, the shapes of faint galaxies could be quite irregular and not described well enough by ellipses. One approach to estimate the ellipticity is to model the light from galaxies using a profile that does have a well-defined ellipticity. Another common approach is to specify the shapes of the galaxies by their (weighted) second moments. The first moments are used to define the centroid of the galaxy as follows:

$$\mathbf{x}_0 = \frac{\int d^2\mathbf{x} \mathbf{x} w(\mathbf{x}) I(\mathbf{x})}{\int d^2\mathbf{x} w(\mathbf{x}) I(\mathbf{x})}, \quad (5.7a)$$

which in turn are used to define the second moments as

$$M_{ij}(I; w) = \frac{\int d^2\mathbf{x} (\mathbf{x} - \mathbf{x}_0)_i (\mathbf{x} - \mathbf{x}_0)_j w(\mathbf{x}) I(\mathbf{x})}{\int d^2\mathbf{x} w(\mathbf{x}) I(\mathbf{x})} \quad (5.7b)$$

for some weight function $w(\mathbf{x})$ and where $i, j \in \{1, 2\}$. The simplest case of $w(\mathbf{x}) \equiv 1$ suffers from divergence in the presence of noise [127] and when trying to measure

the shape of diffraction-limited PSFs. [127] proposed using circular Gaussian weight functions in order to obtain finite values of the moments. [91] generalized the weight function to be an elliptical Gaussian to match the shape of the object in order to maximize the signal-to-noise ratio. The weight function $w(\mathbf{x})$ is obtained by an iterative procedure, and hence referred to as *adaptive* moments.

The ellipticity and distortion for a galaxy can be defined from the galaxy image as

$$\epsilon = \frac{M_{11} - M_{22} + 2iM_{12}}{M_{11} + M_{22} + 2(M_{11}M_{22} - M_{12}^2)^{1/2}}, \quad (5.8a)$$

and

$$e = \frac{M_{11} - M_{22} + 2iM_{12}}{M_{11} + M_{22}}. \quad (5.8b)$$

The values of the ellipticity and distortion depend on the choice of the weight function in general. For sources with elliptical isophotes, the definitions in Eqs. 5.8 reduce to the definitions in Eq. 5.6 irrespective of the weight function.

Since the second moments are rank-2 tensors, their transformation law is given by

$$M^{(\text{int})} = \mathcal{A}M^{(\text{linsd})}\mathcal{A}^T = \mathcal{A}M^{(\text{linsd})}\mathcal{A}. \quad (5.9)$$

Substituting them in Eqs. 5.6, we get

$$e^{(\text{linsd})} = \frac{e^{(\text{int})} + 2g + g^2 e^{(\text{int})^*}}{1 + |g|^2 + 2\text{Re}(ge^{(\text{int})^*})} \quad (5.10a)$$

$$\epsilon^{(\text{linsd})} = \frac{\epsilon^{(\text{int})} + g}{1 + g^* \epsilon^{(\text{int})}}, \quad \text{assuming } |g| \leq 1 \quad (5.10b)$$

In the case of WL, $|g| \ll 1$ and we can express the observed shape to linear order in g as

$$\epsilon^{(\text{linsd})} \approx \epsilon^{(\text{int})} + g \quad (5.11a)$$

$$\begin{aligned} e^{(\text{linsd})} &\approx e^{(\text{int})} + 2g - g|e^{(\text{int})}|^2 \\ &\quad - g^* e^{(\text{int})2} - 2g^2 e^{(\text{int})^*} - 2|g|^2 e^{(\text{int})} \end{aligned} \quad (5.11b)$$

Assuming that the intrinsic orientation of the galaxies are random, we expect $\langle \epsilon^{(\text{int})} \rangle =$

$0 = \langle e^{(\text{int})} \rangle = \langle e^{(\text{int})^2} \rangle$. Thus, by averaging over a large number of galaxies in a small enough field of view (with high number density of galaxies) such that the shear remains fairly constant we can now turn Eqs. 5.11 to estimates of shear

$$\hat{g} = \langle \epsilon^{(\text{lensd})} \rangle \quad (5.12a)$$

and

$$\hat{g} = \frac{\langle e^{(\text{lensd})} \rangle}{(2 - \langle |e^{(\text{int})}|^2 \rangle)} \approx \frac{\langle e^{(\text{lensd})} \rangle}{(2 - \langle |e^{(\text{lensd})}|^2 \rangle)}. \quad (5.12b)$$

The approximation in the last equality is valid since $\langle |e^{(\text{lensd})}|^2 \rangle = \langle |e^{(\text{int})}|^2 \rangle$ holds to first order in $|g|$.

However, the observed image is not the lensed image itself but $I^{(\text{lensd})}(\mathbf{x})$ blurred by the atmosphere (for ground-based telescopes), convolved with a point-spread function (PSF) of the telescope (another blurring stage) and finally pixelated at the detectors. Thus, $e^{(\text{lensd})}$ cannot be measured directly but have to be estimated from the galaxy image given the knowledge of the PSF.

In space telescopes, the primary contribution to the blurring comes from the PSF due to the optics of the telescope. By definition, the PSF is the image of a point source, assuming that the telescope is a linear system. To a first approximation, the optical PSF is given by an Airy function. The functional form of the PSF is more complicated due to the central obscuration, supporting struts of the telescope. In practice, PSFs are estimated at the location of the bright stars by looking at their images.

The pioneering method in PSF correction was developed by [127] with improvements from [140] and [141]. Large number of methods have been developed since then [see 113, for a summary of various methods and comparison of their performances]. Several blind community challenges such as the Shear Testing Programme(s) [STEP- I; 33], [STEP - II; 35] and Gravitational lensing Accuracy Testing challenges [GREAT08; 36], [GREAT10; 37] and [GREAT3; 38] have been conducted with the intention of improving shape measurement algorithms and minimizing their systematic biases. For a recent list of PSF correction methods and their performances, see [113].

To summarize, the light from distant galaxies deflect in response to the intervening

matter and shear the image of the galaxies. This shear is the signal we want to measure. The shapes of the galaxies are further modified by the PSF of the telescope (and the atmosphere for ground-based telescopes) before the photons get collected in the detectors. Estimating the lensing shear is then, broadly speaking, a two-step process: i) correcting for the effects of PSF to estimate the ellipticity of the galaxies. ii) estimating the shear from a galaxy shape catalogue. Bayesian methods that skip assigning an ellipticity of individual galaxies have been devised and tested [93, 96, 142]. However, in this work, we adopt the tradition two-step process of estimating the shear.

5.3 Interpixel capacitance

5.3.1 Detector model

A photodetector array is commonly modelled as a 2-dimensional array of capacitors $C[i, j]$ [see for e.g., 118, 119]. The capacitors accrue an electric charge $Q[i, j]$ by integrating $\bar{I}[i, j]$, the photocurrent entering the node (i, j) , over the exposure time t_{exp} . All the capacitors are assumed to be fabricated in an identical manner. The photosensor can be modelled as a linear system with a nominal gain given by $1/C_{\text{node}}$, where C_{node} is the nodal capacitance. The voltage response function for a given distribution of charge Q is given by

$$V[i, j] = \sum_m \sum_n \frac{1}{C_{\text{node}}} Q[m, n] K[i - m, j - n], \quad (5.13)$$

where K couples the voltage response in one pixel to the charges in the other pixels. We refer to K as the IPC kernel. The kernel is normalized such that $\sum_{m, n} K[m, n] = 1$. The coupling between the nodes is symmetric, i.e., $K[i - m, j - n] = K[m - i, n - j]$.

In an ideal detector, the voltage at node depends linearly only on the charge in that pixel and therefore, $K[i - m, j - n] = \delta_{i, m} \delta_{j, n}$ and $1/C_{\text{node}}$ is the gain of the system. However, in real detectors, a small coupling exists between nearby pixels. Neglecting any non-linearity in the readout circuit, the read-out voltage values are proportional

to the pixel values of the image. Hence,

$$I_{\text{obs}}[i, j] = \sum_{m, n} I_{\text{ideal}}[m, n] K[i - m, j - n] \quad (5.14)$$

IPC is different from charge diffusion since it does not involve the actual movement of the physical charge carriers from one pixel to another. IPC arises due to the fringe fields interfering with the neighbouring pixels. Although the effect of the IPC is a convolution by a smoothing kernel, it is not considered as a part of the PSF itself. One of the reasons for that is that the effects of IPC enter the image generation/simulation pipeline after other detector effects such as the addition of dark current, noise from the sky background and voltage nonlinearity. The IPC kernel contributes toward some correlation in the noise whereas the PSF does not correlate the noise. The effects of IPC and NL on the WFIRST PSFs are described in detail in [143] and in [144]. While, PSF corrections to an image can correct for most of the effects of IPC, it is not sufficient for WFIRST and the effects of IPC may needed to be corrected for explicitly.

The simplest IPC kernel is where there is a small non-zero coupling between adjacent pixels, parametrized by α as

$$K_{\alpha} = \begin{pmatrix} 0 & \alpha & 0 \\ \alpha & 1 - 4\alpha & \alpha \\ 0 & \alpha & 0 \end{pmatrix}. \quad (5.15)$$

A simple extension to the IPC kernel of Eq. 5.15 can be made by including α' , a coupling between second nearest neighbours and α_+ , an anisotropic part in the coupling between the horizontal and vertical directions:

$$K_{\alpha, \alpha_+, \alpha'} = \begin{pmatrix} \alpha' & \alpha - \alpha_+ & \alpha' \\ \alpha + \alpha_+ & 1 - 4(\alpha + \alpha') & \alpha + \alpha_+ \\ \alpha' & \alpha - \alpha_+ & \alpha' \end{pmatrix}. \quad (5.16)$$

The three parameter IPC kernel (Eq. 5.16) is a good model to describe the IPC kernel

of the IR channel in WFC3 determined from the on-orbit measurements [121]

$$\begin{pmatrix} 0.0011 \pm 0.0006 & 0.0127 \pm 0.0009 & 0.0011 \pm 0.0006 \\ 0.0163 \pm 0.0014 & 0.936 \pm 0.0045 & 0.0164 \pm 0.0011 \\ 0.0011 \pm 0.0006 & 0.0127 \pm 0.0010 & 0.0011 \pm 0.0006 \end{pmatrix}, \quad (5.17)$$

The IPC kernels given above have no zeros (in Fourier representation) and hence are invertible in principle. However, since the kernels have a finite support in real space, they will have an infinite support in the Fourier space, making the inversion a challenging task. Following the suggestion in [125], we obtain another 3×3 kernel K'_α such that when convolved with K_α , the first order terms in α cancel. It can be verified that $K'_\alpha = K_{-\alpha}$. In this work, we focus only on the 1-parameter kernel given in Eq. 5.15

5.4 Data

The galaxy population that we used in our simulation is obtained from the COSMOS survey. The COSMOS survey [72, 73, 74] is a flux-limited, narrow deep field survey covering a contiguous area of 1.64 deg^2 of sky. The galaxy images were taken through the F814W (Broad I) filter using the Advanced Camera for Surveys (ACS) Wide Field Channel (WFC) in the Hubble Space Telescope (HST). Multiple dithered exposures were combined using the multidrizzle algorithm [145] after the standard image processing steps such as geometric distortion, sky subtraction and cosmic ray rejection. The final co-added images are 7000×7000 pixels with a pixel scale of $0.03''/\text{pixel}$.

Source objects were detected using SExtractor [32] and were classified as stars or galaxies or neither using the peak surface brightness and half-light radius [see 74, for details]. Photometric redshifts for the galaxies in the COSMOS field were calculated by [77]. Accurate redshifts were computed with 30 broad, intermediate and narrowbands covering the ultra-violet, visible near-IR and mid-IR wavelengths from a number of surveys.

The COSMOSCatalog that is available in GalSim v1.4 is obtained after applying the

following cuts [75]:

- F814W < 25.2
- MU_CLASS=1:
- CLEAN=1:
- GOOD_ZPHOT_SOURCE=1:

Postage stamps were cut out around the position of each galaxy that passes the above cuts following the procedure described in [75]. The COSMOS PSFs were estimated from a modification of a ray-tracing program Tiny Tim² v6.3. Two parametric models were fitted to the galaxies using a 2-dimensional Levenberg-Marquardt minimization (`mpfit2dfun` in IDL; [146]) which minimizes the weighted sum of the squared differences between the galaxy image and PSF-convolved models. This χ^2 -minimization assumes no correlation among the pixel values, which is indeed not the case. [76] describe the fitting method in detail.

The first of the two parametric models was a single Sérsic profile with the radial surface brightness profile given by

$$I_S(x, y) = I_{1/2} \exp \left[-b_n \left(\left(\frac{R(x, y)}{R_{\text{eff}}} \right)^{1/n} - 1 \right) \right], \quad (5.18)$$

where

$$R^2(x, y) = ((x - x_0) \cos \phi + (y - y_0) \sin \phi)^2 + \frac{1}{q^2} ((y - y_0) \cos \phi - (x - x_0) \sin \phi)^2,$$

R_{eff} is the half-light radius of the profile defined along the major axis, $I_{1/2}$ is the surface brightness at $R = R_{\text{eff}}$, (x_0, y_0) is the centroid of the image, ϕ is the position angle, n is the Sérsic index, b_n is an n -dependent normalization factor required to ensure that half the light is enclosed within the half-light radius, and q is the axis ratio of the elliptical isophotes. The Sérsic profile has 7 free parameters and we place the following constraints on them: $I_{1/2} > 0$, $0.1 \leq n \leq 6$, $0.05 \leq q \leq 1$ and the size of the galaxy must be smaller than the size of the postage stamp.

²<http://www.stsci.edu/software/tinytim/>

The second parametric model, often referred to as the bulge+disk model, is a sum of a de Vaucouleurs (bulge component; Sérsic $n=4$) and an exponential (disk component; Sérsic $n=1$) profile. The two components are constrained to have the same centroid and thus the bulge+disk model has 10 free parameters. In addition, the half-light radius of the bulge component is required to be less than that of the disk.

While both the models are fit to each of the galaxies, the catalogue considers only one of the two model parameters to generate a galaxy. First, the bulge+disk model which has the higher number of free parameters is considered. The single Sérsic fit parameters are considered when the ratio of the flux in the bulge component to the total flux (denoted by B/T) is below 0.1 or exceeds 0.9 or when the bulge radius or the axis ratio converged to the fit limits (which happens for about 70% of the galaxies). Single Sérsic fits are also used when the median absolute deviation is higher for the 2-component fits.

5.5 Methods

We simulate the PSFs and the galaxy images using GalSim³. GalSim [69] is a publicly available galaxy image simulation package. It has a convenient Python interface while the core of the software is written in C++. Currently, GalSim (v1.4) can simulate a PSF from first principles corresponding to any pupil plane as long as the aperture is circular. GalSim also has the capability to apply lensing transformations (5.3) to light profiles, convolve two or more light profiles/PSFs and ‘draw’ an image of the profile. GalSim even has a module dedicated to the WFIRST mission that can generate WFIRST PSFs in the passbands and include effects that are specific to WFIRST.

5.5.1 WFIRST PSF simulation

The WFIRST telescope has a circular aperture that is 2.36m in diameter. It has a central obscuration and supporting struts that are not aligned radially. The pupil

³<https://github.com/GalSim-developers/GalSim>

plane configuration and the wavefront aberrations described in terms of the Zernike coefficients are available publicly ⁴.

Realistic (chromatic) WFIRST PSF profiles, that take into account of the central obscuration, supporting struts and aberrations in terms of Zernike coefficients, are simulated in the J129, H158 and F184 bands. For more details about the PSF simulation, refer to [143]. The simulated profiles are then convolved with a top-hat pixel response function and drawn onto an image by sampling at the native pixel scale of 0.11" per pixel. The IPC kernel (Eq. 5.15) is then applied. The PSFs are not Nyquist-sampled, by construction, and hence a single exposure image of a star cannot be used to determine the moments of the PSF accurately. 8 other such exposures are generated by shifting the PSF profile by a third of a pixel in either direction along at least one of the detector axes. All the 9 exposures are then interleaved to obtain a higher resolution image of the star.

In order to keep the analysis simple, we do not apply any of the nonlinear effects to the PSFs and leave the flux of the star unspecified. The PSF images are also rendered noiseless - a limiting approximation when the star is bright enough that the signal-to-noise ratio tends to infinity.

5.5.2 Galaxy simulation

We simulate galaxy images using the `COSMOSCatalog` within GalSim, which is generated using the method described in Sec. 5.4. Since the galaxy images in the catalogue were taken through a single bandpass filter in the optical wavelengths (F814W) and since we require to simulate images in the near-IR wavelengths, there is a need to make some assumptions about the spectral energy distribution (SED) of the galaxies.

SED templates for E, Sbc, Scd types of galaxies are tabulated from the observations of local Universe ($z \sim 0$) by [147] for wavelengths between 1400Å to 10000Å. The SEDs were extended to about 120Å on the bluer end and to 22050Å on the redder end using the Hyper-Z⁵ code [148, 149] that uses the stellar synthesis models described in [150]. For galaxies described by the two component bulge+disk model, the bulge

⁴http://wfirst.gsfc.nasa.gov/science/sdt_public/wps/references/instrument/

⁵<http://webast.ast.obs-mip.fr/hyperz/>

components are assigned an SED corresponding to the E type and the disk components are assigned an SED corresponding to the Scd type. Galaxies described by a single Sérsic profile are assigned an Scd type SED (disk SED) if Sérsic $n < 1.5$, E type SED (bulge SED) if Sérsic $n > 3$ and Sbc type SED for intermediate Sérsic n values. The SEDs are redshifted appropriately based on the photometric redshift values of the galaxies and are set to have magnitude values same as the observed F814W magnitudes in COSMOSCatalog.

For our simulations, the fluxes of the galaxies in the COSMOS catalogue are scaled to account for the differences in the aperture size and exposure time between HST and WFIRST. To reduce the shape noise in our measurements, we follow the standard procedure [35, 38] of rotating each galaxy by 90° and including it in our sample. All the galaxies in our sample are sheared by a constant lensing shear $g^{\text{true}} = g_1^{\text{true}} + ig_2^{\text{true}}$, with $g_1^{\text{true}} = g_2^{\text{true}}$. The values of the components of g^{true} are varied between -0.05 and 0.05. The sheared galaxy profiles are then convolved with the effective PSF (PSF convolved with the pixel response) and are rendered using DFT methods onto images through the J129, H158 and F184 bandpass filters. The “exposures” have a sampling rate of 0.11”/pixel, same as that of the native WFIRST pixel scale.

The dominant source of photon shot noise is the background sky level from zodiacal light. The exact amount of the background light would depend on the day and the time of the observation, the celestial coordinates of the pointing and the adopted model for zodiacal light. The photon density as a function of the position in sky is calculated using [151]⁶ Assuming that the sun is at the ecliptic coordinate (0,0) and that the telescope is pointing at (30,90), we compute the expected background sky level from zodiacal light through each of the filters. It is to be noted that these are uncertain at $\sim 10\%$ level. The stray light in the telescope is required to be less than 10% of the background due to zodiacal light, and we consider the worst case scenario of the stray light fraction being 0.1. The thermal backgrounds for each of the filters are calculated [151] based on the telescope temperature of 282K. The last contribution to the background is given by the dark current, which is caused to spontaneous electron-hole pair generation within the depletion region of the sensor due to its finite temperature. The high electric field at the junction of photodiode sweeps these charge carriers causing a leakage current of $0.015e^-/s$ per pixel. Poisson

⁶<http://www.tapir.caltech.edu/~chirata/web/software/space-etc/>

noise corresponding to the total sky background and dark current is added.

9 such exposures are generated⁷ with the sampling grid is offset by 1/3 of the pixel size along x and y in both positive and negative directions, as was done to the PSF images. To each of the exposures, images of the total sky background and dark current (along with the noise) are added. The IPC kernel given in Eq. 5.15 is applied to the exposures for a particular value of the IPC coupling parameter α . To these IPC convolved exposures, the read noise due to the on-chip amplifier is added. Read noise is modelled as a Gaussian noise with a standard deviation of $10e^-s$.

In this above image generation process, the ‘exposures’ are quantized, i.e., pixel values are rounded to the nearest integer in two stages. First, prior to the converting the photon counts to electron counts and then once at the analog-to-digital conversion stage, assuming that the gain of the readout system is unity. The PSF images are not quantized.

The effect of IPC is corrected for in each of the exposures by applying the corresponding corrective kernel. The original (uncorrected) and the corrected exposures are interleaved to give a higher resolution image of the galaxy. The mean value of the total background (quantized) is then subtracted.

5.5.3 Shape measurements

Having generated the galaxy images and PSF images, the intrinsic galaxy shapes are measured in 4 ways:

1. IPC in gal & PSF - uncorrected: The galaxy images and the PSF images contain the same amount of IPC , but the presence of IPC is ignored.
2. IPC in gal & PSF - corrected: The galaxy images and the PSF images contained the same amount of IPC and they were corrected for.
3. IPC in gal only: The galaxy images contain IPC but the PSF images do not.
4. IPC in PSF only: The PSF images contain IPC but the galaxy images do not.

⁷Higher resolution image is rendered first for computational efficiency and deinterleaved to generate the individual exposures.

The last two measurements, where IPC is present either in the galaxy image or in the PSF image, is to be considered as an extreme case of the scenario where due to a possible spatial variation of IPC across the detectors, the IPC parameters at the location of the galaxy and at the location of the PSF differ by α .

Shape measurements are done using the re-Gaussianization method [90]. An estimate of the shear is obtained from a large number of such shape measurements using the equation

$$\hat{g}_i = \frac{\langle \hat{e}_i \rangle}{2 - \langle \hat{e}_1^2 + \hat{e}_2^2 \rangle} \quad i = 1, 2, \quad (5.19)$$

where $\langle X \rangle$ stands for an ensemble average of X . We plot $\hat{g}_i(\alpha) - g_i^{\text{true}}$ vs g_i^{true} for different values of α to see the deviation of the shear estimate from its true value as a function of the IPC parameter.

We adopt the linear bias model from [35] and express

$$\hat{g}_i = (1 + m_i)g_i + c_i, \quad (5.20)$$

where m_i and c_i are known as multiplicative and additive biases respectively and $i \in \{1, 2\}$. The intuition behind this parametrization is fairly straightforward. An isotropic PSF would make the galaxy appear ‘rounder’ than it actually is, hence contributing towards the multiplicative bias. However, if the PSF has a small ellipticity, it would smear the galaxy images coherently along the direction of its ellipticity and would thus mimic a shear signal. The additive bias term quantifies this spurious shear.

We obtain the multiplicative and the additive bias values m_i and c_i through linear regression. By repeating this procedure for different values of the IPC coupling parameter α , we can obtain $m_i(\alpha)$ and $c_i(\alpha)$.

Cuts

In performing the above calculations, we require that for all values of g^{true} and for all values of α , the shape measurements of a galaxy and its rotated pair be available. Furthermore, we require them to have a resolution factor > 0.4 , where the resolution

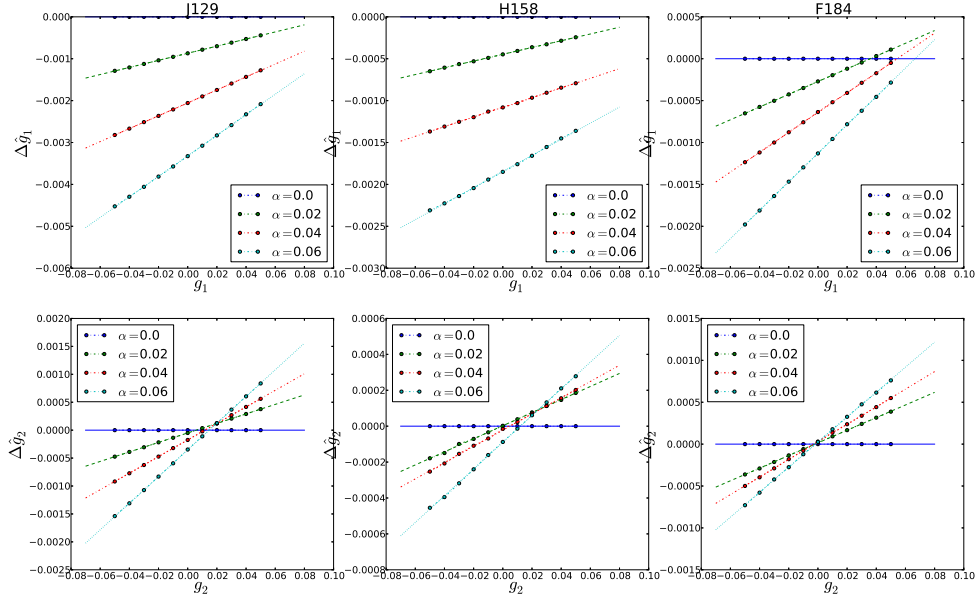


Figure 5.1: Plot of difference between the estimated shear when IPC is present and the estimate shear in the absence of IPC for the three passbands.

factor $R = 1 - \text{Tr}(M_{\text{gal}})/\text{Tr}(M_{\text{PSF}})$ after applying corrections for non-Gaussianity (see [90] for details). The former condition is required to not bias the shear calibration parameters and the latter is required to avoid any pseudo evolution in the IPC parameter due to differences in the galaxy sample.

5.6 Results

5.6.1 Noiseless case

If the shape measurement process were linear in the pixel values, then noise in the image would translate into noise in the estimate of shear calibration bias. But since the measurement process is non-linear, the noise in the image contributes towards the shear calibration bias as well. By generating noiseless images, we first study how the shear estimate varies with α and the shear calibration biases through it due to the change in the galaxy and the PSF images alone. ‘Quantization noise’ due to

rounding off of the pixel values is present, but no other source of random noise is included.

We simulate noiseless images for 20,000 galaxy pairs and apply the cuts mentioned earlier. In Fig. 5.1, we show how the estimated shear values differ from the true input shear for various values of the IPC parameter α . From the figures, the relationship between $\hat{g}(\alpha)$ and $g^{(\text{true})}$ can be seen to lie on a straight line extremely well, thus obeying the linear bias model (Eq. 5.20). In the absence of IPC, the bias values are characteristic of the shape measurement algorithm (in this case, re-Gaussianisation) for a given PSF and the galaxy images. Since we are interested in the change in the shear estimate, we plot $\hat{g}(\alpha) - \hat{g}(0)$ vs. $g^{(\text{true})}$ - whose best fit parameters will then correspond to $\Delta m_i(\alpha) \equiv m_i(\alpha) - m_i(0)$ and $\Delta c_i(\alpha) \equiv c_i(\alpha) - c_i(0)$. However, $\Delta m(\alpha)$ and $\Delta c(\alpha)$ are not independent of the shape measurement algorithm either - different algorithms could have different sensitivities to α . Shape measurements that employ wider weight functions are less sensitive to α than those that employ weight functions to describe the central core of the galaxies.

For $\Delta m_i(\alpha)$, there is little difference between the two cases where the IPC is explicitly corrected for and where the IPC correction is done by the PSF itself. In both of these cases, there are significant changes in the multiplicative bias values - about 0.01 for $\alpha = 0.02$, which is about a 5% change from its original value, i.e., when $\alpha=0$. This indicates that while using adaptive moments to measure shapes, neither the PSF deconvolution nor the IPC correction is completely able to remove the effects of IPC.

5.7 Discussion

In the case where only the PSF images have IPC, the observed galaxy image is over-corrected and the magnitude of the estimated shear is lowered, making the multiplicative bias terms more negative. The opposite effect happens where the galaxy images are under-compensated when the galaxy images have IPC, thus making the multiplicative bias terms less negative.

The behaviour of $c_i(\alpha)$ could be understood by the following argument. $c_1(\alpha)$ deviates the most from $c_1(0)$ (and approaches towards 0) when the PSF contains IPC. This

J129

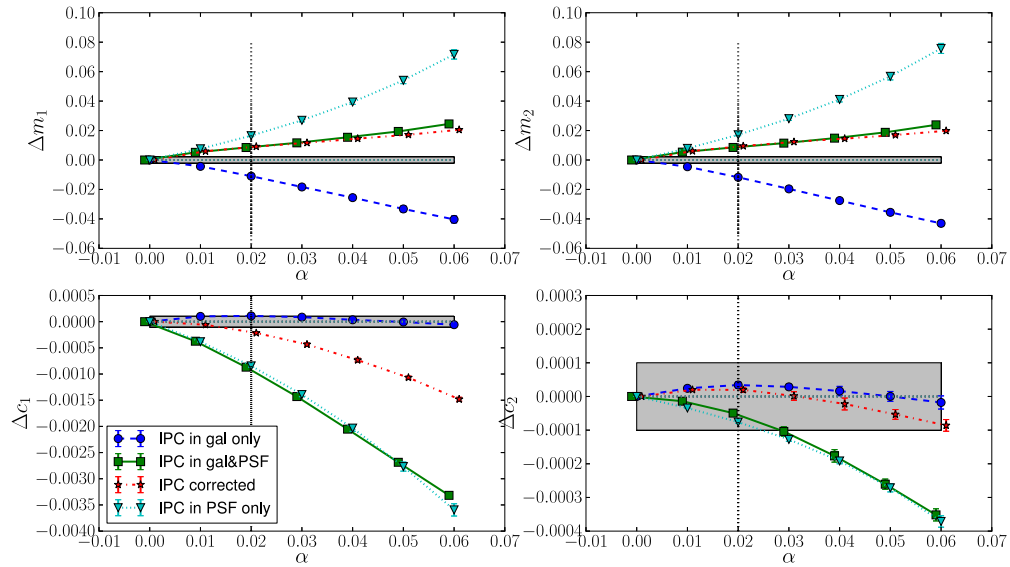


Figure 5.2: Changes in the shear calibration bias as a function of the IPC parameter α for J129 passband in the absence of random noise (non quantization noise). The errorbars obtained by computing the bias values of 10 equal subsets of the galaxies with 2000 galaxy pairs and taking the standard error of the mean value. The shaded region corresponds to the allowed uncertainties in the bias values for Euclid (not very different from WFIRST). The vertical line corresponds to the nominal value of α .

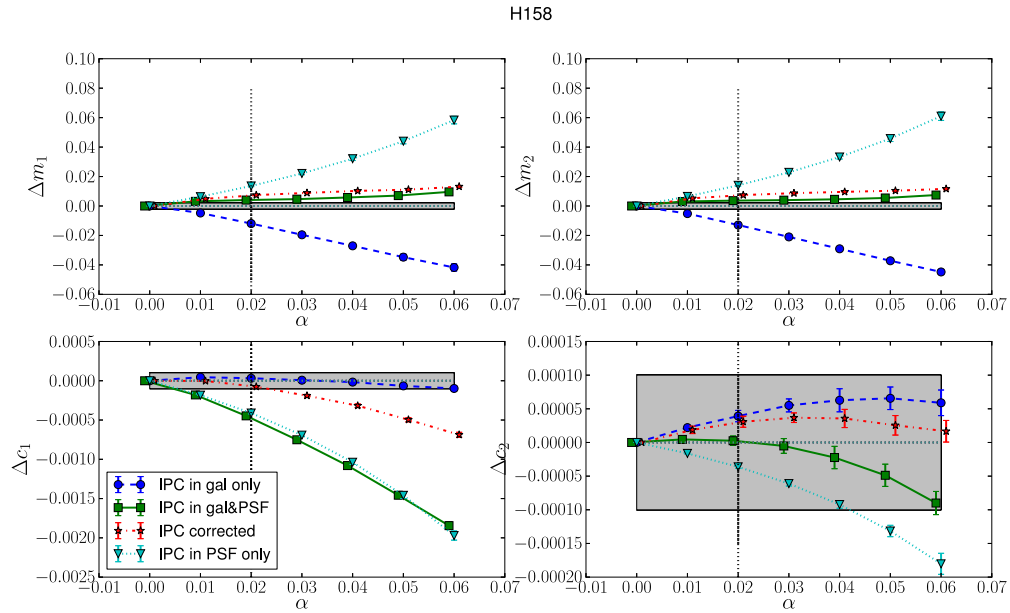


Figure 5.3: Changes in the shear calibration bias as a function of the IPC parameter α for H158 passband in the absence of random noise (non quantization noise). The errorbars obtained by computing the bias values of 10 equal subsets of the galaxies with 2000 galaxy pairs and taking the standar error of the mean value. The shaded region corresponds to the allowed uncertainties in the bias values for Euclid (not very different from WFIRST). The vertical line corresponds to the nominal value of α .

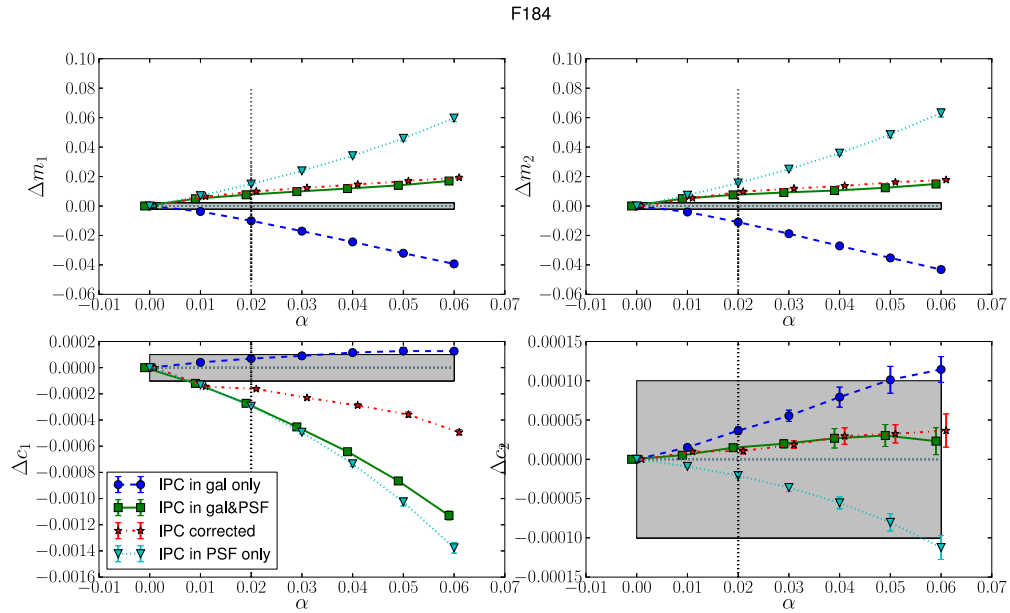


Figure 5.4: Changes in the shear calibration bias as a function of the IPC parameter α for F184 passband in the absence of random noise (non quantization noise). The errorbars obtained by computing the bias values of 10 equal subsets of the galaxies with 2000 galaxy pairs and taking the standard error of the mean value. The shaded region corresponds to the allowed uncertainties in the bias values for Euclid (not very different from WFIRST). The vertical line corresponds to the nominal value of α .

is because WFIRST PSF is not isotropic and the PSF images become effectively more ‘rounder’ in the presence of IPC. The difference in the behaviour of c_1 and c_2 components arise because the IPC kernel acts along the detector axes, affecting c_1 more than c_2 .

In the presence of random noise, IPC correlates the Poisson noise in the images and IPC correction introduces correlations in the read noise. Correlated noise impact the shape estimations differently than the uncorrelated noise ([see for e.g., 152]). In order to be able to observe the tiny change in the shear signal due to IPC in the presence of random noise, shape measurements from a larger set of galaxy images are required. This work is currently under progress.

*

Appendix A

Unweighted moments

If the unweighted moments of the PSFs did not diverge, then it is possible to obtain an expression for the sizes of the PSFs with and without the effect of interpixel capacitance. Eq. 4.22 shows how the effective size of any profile increases as a function of the isotropic IPC parameters, which we now derive. The crucial idea behind the derivation is the following: if we convolve two or more image profiles, their unweighted moments add, i.e.,

$$\mathbf{M}_h = \mathbf{M}_f + \mathbf{M}_g \quad (\text{A.1})$$

where $f(\vec{x})$ and $g(\vec{x})$ are two image profiles, $h(\vec{x}) = (f \otimes g)(\vec{x})$ and \mathbf{M}_f is the second moments of $f(\vec{x})$ and so on.

If the object we are measuring is circularly symmetric and has a finite size σ that can be defined from the unweighted moments, say like that of a Gaussian, then it's moment matrix would be $\sigma^2 \mathbf{1}_2$, where $\mathbf{1}_2$ is the 2×2 identity matrix. The pixel response is given by a top-hat profile, whose second moments matrix given by $\frac{1}{12} \mathbf{1}_2$. For the IPC kernel given in Eq. 4.8, the matrix of second moments is given by $(2\alpha + 4\alpha') \mathbf{1}_2$.

Thus, the moment matrix of the image would be $(\sigma^2 + 1/12 + 2\alpha + 4\alpha') \mathbf{1}_2$ and the measured size of the PSF, as a function of α would be

$$\sigma'(\alpha) = \sqrt{\sigma^2 + \frac{1}{12} + 2\alpha + 4\alpha'} \quad (\text{A.2})$$

If the moments of the object were given by a more generic 2×2 symmetric matrix, say,

$$M_G = \begin{pmatrix} \sigma_x^2 & \epsilon \\ \epsilon & \sigma_y^2 \end{pmatrix} \quad (\text{A.3})$$

then

$$\sigma'(\alpha) = \sqrt{\sqrt{\sigma_x^2 \sigma_y^2 - \epsilon^2} + \frac{1}{12} + 2\alpha + 4\alpha'} \quad (\text{A.4})$$

Note that this equation does not depend on the profile of the PSF but only on the fact that the second moments do not diverge. However, this expression is particularly useful only for Gaussian light profiles since this expression also matches the adaptive size of such objects. Moreover, the conditions that $\sigma \gg 1$ pixel and $\alpha, \alpha' \ll 1$ must be satisfied so that the non-Gaussianity introduced by the pixel response and the IPC kernel is not significant.

Bibliography

- [1] D Spergel, N Gehrels, J Breckinridge, M Donahue, A Dressler, B. S. Gaudi, T Greene, O Guyon, C Hirata, J Kalirai, N. J. Kasdin, W Moos, S Perlmutter, M Postman, B Rauscher, J Rhodes, Y Wang, D Weinberg, J Centrella, W Traub, C Baltay, J Colbert, D Bennett, A Kiessling, B Macintosh, J Merten, M Mortonson, M Penny, E Rozo, D Savransky, K Stapelfeldt, Y Zu, C Baker, E Cheng, D Content, J Dooley, M Foote, R Goullioud, K Grady, C Jackson, J Kruk, M Levine, M Melton, C Peddie, J Ruffa, and S Shaklan. Wide-Field InfraRed Survey Telescope-Astrophysics Focused Telescope Assets WFIRST-AFTA Final Report. *ArXiv e-prints*, may 2013.
- [2] D Spergel, N Gehrels, C Baltay, D Bennett, J Breckinridge, M Donahue, A Dressler, B. S. Gaudi, T Greene, O Guyon, C Hirata, J Kalirai, N. J. Kasdin, B Macintosh, W Moos, S Perlmutter, M Postman, B Rauscher, J Rhodes, Y Wang, D Weinberg, D Benford, M Hudson, W.-S. Jeong, Y Mellier, W Traub, T Yamada, P Capak, J Colbert, D Masters, M Penny, D Savransky, D Stern, N Zimmerman, R Barry, L Bartusek, K Carpenter, E Cheng, D Content, F Dekens, R Demers, K Grady, C Jackson, G Kuan, J Kruk, M Melton, B Nemati, B Parvin, I Poberezhskiy, C Peddie, J Ruffa, J. K. Wallace, A Whipple, E Wollack, and F Zhao. Wide-Field InfrarRed Survey Telescope-Astrophysics Focused Telescope Assets WFIRST-AFTA 2015 Report. *ArXiv e-prints*, mar 2015.
- [3] L. Van Waerbeke and Y. Mellier. Gravitational Lensing by Large Scale Structures: A Review. *ePrint arXiv*, page 48, 2003.
- [4] A. L. Coil, J. A. Newman, N Kaiser, M Davis, C.-P. Ma, D. D. Kocevski, and D. C. Koo. Evolution and Color Dependence of the Galaxy Angular Correlation

Function: 350,000 Galaxies in 5 Square Degrees. *The Astrophysical Journal*, 617:765–781, dec 2004.

- [5] A.~R. Tomczak, R.~F. Quadri, K.-V.~H. Tran, I Labbé, C.~M.~S. Straatman, C Papovich, K Glazebrook, R Allen, G.~B. Brammer, G.~G. Kacprzak, L Kawinwanichakij, D.~D. Kelson, P.~J. McCarthy, N Mehrrens, A.~J. Monson, S.~E. Persson, L.~R. Spitler, V Tilvi, and P van Dokkum. Galaxy Stellar Mass Functions from ZFOURGE/CANDELS: An Excess of Low-mass Galaxies since $z = 2$ and the Rapid Buildup of Quiescent Galaxies. *The Astrophysical Journal*, 783:85, mar 2014.
- [6] B. P. Abbott, R. Abbott, T. D. Abbott, M. R. Abernathy, F. Acernese, K. Ackley, C. Adams, T. Adams, P. Addesso, R. X. Adhikari, V. B. Adya, C. Affeldt, M. Agathos, K. Agatsuma, N. Aggarwal, O. D. Aguiar, L. Aiello, A. Ain, P. Ajith, B. Allen, A. Allocca, P. A. Altin, S. B. Anderson, W. G. Anderson, K. Arai, M. A. Arain, M. C. Araya, C. C. Arceneaux, J. S. Areeda, N. Arnaud, K. G. Arun, S. Ascenzi, G. Ashton, M. Ast, S. M. Aston, P. Astone, P. Aufmuth, C. Aulbert, S. Babak, P. Bacon, M. K M Bader, P. T. Baker, F. Baldaccini, G. Ballardin, S. W. Ballmer, J. C. Barayoga, S. E. Barclay, B. C. Barish, D. Barker, F. Barone, B. Barr, L. Barsotti, M. Barsuglia, D. Barta, J. Bartlett, M. A. Barton, I. Bartos, R. Bassiri, A. Basti, J. C. Batch, C. Baune, V. Bavigadda, M. Bazzan, B. Behnke, M. Bejger, C. Belczynski, A. S. Bell, C. J. Bell, B. K. Berger, J. Bergman, G. Bergmann, C. P L Berry, D. Bersanetti, A. Bertolini, J. Betzwieser, S. Bhagwat, R. Bhandare, I. A. Bilenko, G. Billingsley, J. Birch, R. Birney, O. Birnholtz, S. Biscans, A. Bisht, M. Bitossi, C. Biwer, M. A. Bizouard, J. K. Blackburn, C. D. Blair, D. G. Blair, R. M. Blair, S. Bloemen, O. Bock, T. P. Bodiya, M. Boer, G. Bogaert, C. Bogan, A. Bohe, P. Bojtos, C. Bond, F. Bondu, R. Bonnand, B. A. Boom, R. Bork, V. Boschi, S. Bose, Y. Bouffanais, A. Bozzi, C. Bradaschia, P. R. Brady, V. B. Braginsky, M. Branchesi, J. E. Brau, T. Briant, A. Brillet, M. Brinkmann, V. Brisson, P. Brockill, A. F. Brooks, D. A. Brown, D. D. Brown, N. M. Brown, C. C. Buchanan, A. Buikema, T. Bulik, H. J. Bulten, A. Buonanno, D. Buskulic, C. Buy, R. L. Byer, M. Cabero, L. Cadonati, G. Cagnoli, C. Cahillane, J. Calder??n Bustillo, T. Callister, E. Calloni, J. B. Camp, K. C. Cannon, J. Cao, C. D. Capano, E. Capocasa, F. Carbognani,

S. Caride, J. Casanueva Diaz, C. Casentini, S. Caudill, M. Cavagli??, F. Cavalier, R. Cavalieri, G. Cella, C. B. Cepeda, L. Cerboni Baiardi, G. Cerretani, E. Cesarini, R. Chakraborty, T. Chalermongsak, S. J. Chamberlin, M. Chan, S. Chao, P. Charlton, E. Chassande-Mottin, H. Y. Chen, Y. Chen, C. Cheng, A. Chincarini, A. Chiummo, H. S. Cho, M. Cho, J. H. Chow, N. Christensen, Q. Chu, S. Chua, S. Chung, G. Ciani, F. Clara, J. A. Clark, F. Cleva, E. Coccia, P. F. Cohadon, A. Colla, C. G. Collette, L. Cominsky, M. Constancio, A. Conte, L. Conti, D. Cook, T. R. Corbitt, N. Cornish, A. Corsi, S. Cortese, C. A. Costa, M. W. Coughlin, S. B. Coughlin, J. P. Coulon, S. T. Countryman, P. Couvares, E. E. Cowan, D. M. Coward, M. J. Cowart, D. C. Coyne, R. Coyne, K. Craig, J. D E Creighton, T. D. Creighton, J. Cripe, S. G. Crowder, A. M. Cruise, A. Cumming, L. Cunningham, E. Cuoco, T. Dal Canton, S. L. Danilishin, S. D'Antonio, K. Danzmann, N. S. Darman, C. F. Da Silva Costa, V. Dattilo, I. Dave, H. P. Daveloza, M. Davier, G. S. Davies, E. J. Daw, R. Day, S. De, D. Debra, G. Debreczeni, J. Degallaix, M. De Laurentis, S. Del??glise, W. Del Pozzo, T. Denker, T. Dent, H. Dereli, V. Dergachev, R. T. Derosa, R. De Rosa, R. Desalvo, S. Dhurandhar, M. C. D??az, L. Di Fiore, M. Di Giovanni, A. Di Lieto, S. Di Pace, I. Di Palma, A. Di Virgilio, G. Dojcinoski, V. Dolique, F. Donovan, K. L. Dooley, S. Doravari, R. Douglas, T. P. Downes, M. Drago, R. W P Drever, J. C. Driggers, Z. Du, M. Ducrot, S. E. Dwyer, T. B. Edo, M. C. Edwards, A. Effler, H. B. Eggenstein, P. Ehrens, J. Eichholz, S. S. Eikenberry, W. Engels, R. C. Essick, T. Etzel, M. Evans, T. M. Evans, R. Everett, M. Factourovich, V. Fafone, H. Fair, S. Fairhurst, X. Fan, Q. Fang, S. Farinon, B. Farr, W. M. Farr, M. Favata, M. Fays, H. Fehrmann, M. M. Fejer, D. Feldbaum, I. Ferrante, E. C. Ferreira, F. Ferrini, F. Fidecaro, L. S. Finn, I. Fiori, D. Fiorucci, R. P. Fisher, R. Flaminio, M. Fletcher, H. Fong, J. D. Fournier, S. Franco, S. Frasca, F. Frasconi, M. Frede, Z. Frei, A. Freise, R. Frey, V. Frey, T. T. Fricke, P. Fritschel, V. V. Frolov, P. Fulda, M. Fyffe, H. A G Gabbard, J. R. Gair, L. Gammaitoni, S. G. Gaonkar, F. Garufi, A. Gatto, G. Gaur, N. Gehrels, G. Gemme, B. Gendre, E. Genin, A. Genai, J. George, L. Gergely, V. Germain, Abhirup Ghosh, Archisman Ghosh, S. Ghosh, J. A. Giaime, K. D. Giardino, A. Giazotto, K. Gill, A. Glaefke, J. R. Gleason, E. Goetz, R. Goetz, L. Gondan, G. Gonz??lez, J. M Gonzalez Castro, A. Gopakumar, N. A. Gordon, M. L. Gorodetsky, S. E. Gossan, M. Gosselin,

R. Gouaty, C. Graef, P. B. Graff, M. Granata, A. Grant, S. Gras, C. Gray, G. Greco, A. C. Green, R. J S Greenhalgh, P. Groot, H. Grote, S. Grunewald, G. M. Guidi, X. Guo, A. Gupta, M. K. Gupta, K. E. Gushwa, E. K. Gustafson, R. Gustafson, J. J. Hacker, B. R. Hall, E. D. Hall, G. Hammond, M. Haney, M. M. Hanke, J. Hanks, C. Hanna, M. D. Hannam, J. Hanson, T. Hardwick, J. Harms, G. M. Harry, I. W. Harry, M. J. Hart, M. T. Hartman, C. J. Haster, K. Haughian, J. Healy, J. Heefner, A. Heidmann, M. C. Heintze, G. Heinzl, H. Heitmann, P. Hello, G. Hemming, M. Hendry, I. S. Heng, J. Hennig, A. W. Heptonstall, M. Heurs, S. Hild, D. Hoak, K. A. Hodge, D. Hofman, S. E. Hollitt, K. Holt, D. E. Holz, P. Hopkins, D. J. Hosken, J. Hough, E. A. Houston, E. J. Howell, Y. M. Hu, S. Huang, E. A. Huerta, D. Huet, B. Hughey, S. Husa, S. H. Huttner, T. Huynh-Dinh, A. Idrisy, N. Indik, D. R. Ingram, R. Inta, H. N. Isa, J. M. Isac, M. Isi, G. Islas, T. Isogai, B. R. Iyer, K. Izumi, M. B. Jacobson, T. Jacqmin, H. Jang, K. Jani, P. Jaranowski, S. Jawahar, F. Jimenez-Forteza, W. W. Johnson, N. K. Johnson-Mcdaniel, D. I. Jones, R. Jones, R. J G Jonker, L. Ju, K. Haris, C. V. Kalaghatgi, V. Kalogera, S. Kandhasamy, G. Kang, J. B. Kanner, S. Karki, M. Kasprzack, E. Katsavounidis, W. Katzman, S. Kaufer, T. Kaur, K. Kawabe, F. Kawazoe, F. Keffelian, M. S. Kehl, D. Keitel, D. B. Kelley, W. Kells, R. Kennedy, D. G. Keppel, J. S. Key, A. Khalaidovski, F. Y. Khalili, I. Khan, S. Khan, Z. Khan, E. A. Khazanov, N. Kijbunchoo, C. Kim, J. Kim, K. Kim, Nam Gyu Kim, Namjun Kim, Y. M. Kim, E. J. King, P. J. King, D. L. Kinzel, J. S. Kissel, L. Kleybolte, S. Klimenko, S. M. Koehlenbeck, K. Kokeyama, S. Koley, V. Kondrashov, A. Kontos, S. Koranda, M. Korobko, W. Z. Korth, I. Kowalska, D. B. Kozak, V. Kringel, B. Krishnan, A. Krulak, C. Krueger, G. Kuehn, P. Kumar, R. Kumar, L. Kuo, A. Kutynia, P. Kwee, B. D. Lackey, M. Landry, J. Lange, B. Lantz, P. D. Lasky, A. Lazzarini, C. Lazzaro, P. Leaci, S. Leavey, E. O. Lebigot, C. H. Lee, H. K. Lee, H. M. Lee, K. Lee, A. Lenon, M. Leonardi, J. R. Leong, N. Leroy, N. Letendre, Y. Levin, B. M. Levine, T. G F Li, A. Libson, T. B. Littenberg, N. A. Lockerbie, J. Logue, A. L. Lombardi, L. T. London, J. E. Lord, M. Lorenzini, V. Lorette, M. Lormand, G. Losurdo, J. D. Lough, C. O. Lousto, G. Lovelace, H. Lück, A. P. Lundgren, J. Luo, R. Lynch, Y. Ma, T. Macdonald, B. Machenschalk, M. Macinnis, D. M. Macleod, F. Magaña-Sandoval, R. M. Magee, M. Mageswaran, E. Majorana, I. Maksimovic, V. Malvezzi, N. Man, I. Mandel, V. Mandic, V. Mangano, G. L.

Mansell, M. Manske, M. Mantovani, F. Marchesoni, F. Marion, S. M??rka, Z. M??rka, A. S. Markosyan, E. Maros, F. Martelli, L. Martellini, I. W. Martin, R. M. Martin, D. V. Martynov, J. N. Marx, K. Mason, A. Masserot, T. J. Massinger, M. Masso-Reid, F. Matichard, L. Matone, N. Mavalvala, N. Mazumder, G. Mazzolo, R. McCarthy, D. E. McClelland, S. McCormick, S. C. McGuire, G. McIntyre, J. McIver, D. J. McManus, S. T. McWilliams, D. Meacher, G. D. Meadors, J. Meidam, A. Melatos, G. Mendell, D. Mendoza-Gandara, R. A. Mercer, E. Merilh, M. Merzougui, S. Meshkov, C. Messenger, C. Messick, P. M. Meyers, F. Mezzani, H. Miao, C. Michel, H. Middleton, E. E. Mikhailov, L. Milano, J. Miller, M. Millhouse, Y. Minenkov, J. Ming, S. Mirshekari, C. Mishra, S. Mitra, V. P. Mitrofanov, G. Mitselmakher, R. Mittleman, A. Moggi, M. Mohan, S. R P Mohapatra, M. Montani, B. C. Moore, C. J. Moore, D. Moraru, G. Moreno, S. R. Morriss, K. Mossavi, B. Mours, C. M. Mow-Lowry, C. L. Mueller, G. Mueller, A. W. Muir, Arunava Mukherjee, D. Mukherjee, S. Mukherjee, N. Mukund, A. Mullavey, J. Munch, D. J. Murphy, P. G. Murray, A. Mytidis, I. Nardecchia, L. Naticchioni, R. K. Nayak, V. Necula, K. Nedkova, G. Nelemans, M. Neri, A. Neunzert, G. Newton, T. T. Nguyen, A. B. Nielsen, S. Nissanke, A. Nitz, F. Nocera, D. Nolting, M. E N Normandin, L. K. Nuttall, J. Oberling, E. Ochsner, J. O'Dell, E. Oelker, G. H. Ogin, J. J. Oh, S. H. Oh, F. Ohme, M. Oliver, P. Oppermann, Richard J. Oram, B. O'Reilly, R. O'Shaughnessy, C. D. Ott, D. J. Ottaway, R. S. Ottens, H. Overmier, B. J. Owen, A. Pai, S. A. Pai, J. R. Palamos, O. Palashov, C. Palomba, A. Pal-Singh, H. Pan, Y. Pan, C. Pankow, F. Pannarale, B. C. Pant, F. Paoletti, A. Paoli, M. A. Papa, H. R. Paris, W. Parker, D. Pascucci, A. Pasqualetti, R. Passaquieti, D. Passuello, B. Patricelli, Z. Patrick, B. L. Pearlstone, M. Pedraza, R. Pedurand, L. Pekowsky, A. Pele, S. Penn, A. Perreca, H. P. Pfeiffer, M. Phelps, O. Piccinni, M. Pichot, M. Pickenpack, F. Piergiovanni, V. Pierro, G. Piliant, L. Pinard, I. M. Pinto, M. Pitkin, J. H. Poeld, R. Poggiani, P. Popolizio, A. Post, J. Powell, J. Prasad, V. Predoi, S. S. Premachandra, T. Prestegard, L. R. Price, M. Prijatelj, M. Principe, S. Privitera, R. Prix, G. A. Prodi, L. Prokhorov, O. Puncken, M. Punturo, P. Puppo, M. P??rrer, H. Qi, J. Qin, V. Quetschke, E. A. Quintero, R. Quitzow-James, F. J. Raab, D. S. Rabeling, H. Radkins, P. Raffai, S. Raja, M. Rakhmanov, C. R. Ramet, P. Rapagnani, V. Raymond, M. Razzano, V. Re, J. Read, C. M. Reed, T. Regimbau, L. Rei,

S. Reid, D. H. Reitze, H. Rew, S. D. Reyes, F. Ricci, K. Riles, N. A. Robertson, R. Robie, F. Robinet, A. Rocchi, L. Rolland, J. G. Rollins, V. J. Roma, J. D. Romano, R. Romano, G. Romanov, J. H. Romie, D. Rosi??ska, S. Rowan, A. R??diger, P. Ruggi, K. Ryan, S. Sachdev, T. Sadecki, L. Sadeghian, L. Salconi, M. Saleem, F. Salemi, A. Samajdar, L. Sammut, L. M. Sampson, E. J. Sanchez, V. Sandberg, B. Sandeen, G. H. Sanders, J. R. Sanders, B. Sassolas, B. S. Sathyaprakash, P. R. Saulson, O. Sauter, R. L. Savage, A. Sawadsky, P. Schale, R. Schilling, J. Schmidt, P. Schmidt, R. Schnabel, R. M S Schofield, A. Sch??nbeck, E. Schreiber, D. Schuette, B. F. Schutz, J. Scott, S. M. Scott, D. Sellers, A. S. Sengupta, D. Sentenac, V. Sequino, A. Sergeev, G. Serna, Y. Setyawati, A. Sevigny, D. A. Shaddock, T. Shaffer, S. Shah, M. S. Shahriar, M. Shaltev, Z. Shao, B. Shapiro, P. Shawhan, A. Sheperd, D. H. Shoemaker, D. M. Shoemaker, K. Siellez, X. Siemens, D. Sigg, A. D. Silva, D. Simakov, A. Singer, L. P. Singer, A. Singh, R. Singh, A. Singhal, A. M. Sintes, B. J J Slagmolen, J. R. Smith, M. R. Smith, N. D. Smith, R. J E Smith, E. J. Son, B. Sorazu, F. Sorrentino, T. Souradeep, A. K. Srivastava, A. Staley, M. Steinke, J. Steinlechner, S. Steinlechner, D. Steinmeyer, B. C. Stephens, S. P. Stevenson, R. Stone, K. A. Strain, N. Straniero, G. Stratta, N. A. Strauss, S. Sturigin, R. Sturani, A. L. Stuver, T. Z. Summerscales, L. Sun, P. J. Sutton, B. L. Swinkels, M. J. Szczepa??czyk, M. Tacca, D. Talukder, D. B. Tanner, M. T??pai, S. P. Tarabrin, A. Taracchini, R. Taylor, T. Theeg, M. P. Thirugnanasambandam, E. G. Thomas, M. Thomas, P. Thomas, K. A. Thorne, K. S. Thorne, E. Thrane, S. Tiwari, V. Tiwari, K. V. Tokmakov, C. Tomlinson, M. Tonelli, C. V. Torres, C. I. Torrie, D. T??yr??, F. Travasso, G. Traylor, D. Trifir??, M. C. Tringali, L. Trozzo, M. Tse, M. Turconi, D. Tuyenbayev, D. Ugolini, C. S. Unnikrishnan, A. L. Urban, S. A. Usman, H. Vahlbruch, G. Vajente, G. Valdes, M. Vallisneri, N. Van Bakel, M. Van Beuzekom, J. F J Van Den Brand, C. Van Den Broeck, D. C. Vander-Hyde, L. Van Der Schaaf, J. V. Van Heijningen, A. A. Van Veggel, M. Vardaro, S. Vass, M. Vas??th, R. Vaulin, A. Vecchio, G. Vedovato, J. Veitch, P. J. Veitch, K. Venkateswara, D. Verkindt, F. Vetrano, A. Vicer??, S. Vinciguerra, D. J. Vine, J. Y. Vinet, S. Vitale, T. Vo, H. Vocca, C. Vorvick, D. Voss, W. D. Vousden, S. P. Vyatchanin, A. R. Wade, L. E. Wade, M. Wade, S. J. Waldman, M. Walker, L. Wallace, S. Walsh, G. Wang, H. Wang, M. Wang, X. Wang, Y. Wang,

H. Ward, R. L. Ward, J. Warner, M. Was, B. Weaver, L. W. Wei, M. Weinert, A. J. Weinstein, R. Weiss, T. Welborn, L. Wen, P. Weßels, T. Westphal, K. Wette, J. T. Whelan, S. E. Whitcomb, D. J. White, B. F. Whiting, K. Wiesner, C. Wilkinson, P. A. Willems, L. Williams, R. D. Williams, A. R. Williamson, J. L. Willis, B. Willke, M. H. Wimmer, L. Winkelmann, W. Winkler, C. C. Wipf, A. G. Wiseman, H. Wittel, G. Woan, J. Worden, J. L. Wright, G. Wu, J. Yablon, I. Yakushin, W. Yam, H. Yamamoto, C. C. Yancey, M. J. Yap, H. Yu, M. Yvert, A. Zadrožny, L. Zangrando, M. Zanolin, J. P. Zenderi, M. Zevin, F. Zhang, L. Zhang, M. Zhang, Y. Zhang, C. Zhao, M. Zhou, Z. Zhou, X. J. Zhu, M. E. Zucker, S. E. Zuraw, and J. Zweizig. Observation of gravitational waves from a binary black hole merger. *Physical Review Letters*, 116(6):1–16, 2016.

- [7] B P Abbott, R Abbott, T D Abbott, M R Abernathy, F Acernese, K Ackley, C Adams, T Adams, P Addresso, R X Adhikari, V B Adya, C Affeldt, M Agathos, K Agatsuma, N Aggarwal, O D Aguiar, L Aiello, A Ain, P Ajith, B Allen, A Allocca, P A Altin, S B Anderson, W G Anderson, K Arai, M C Araya, C C Arceneaux, J S Areeda, N Arnaud, K G Arun, S Ascenzi, G Ashton, M Ast, S M Aston, P Astone, P Aufmuth, C Aulbert, S Babak, P Bacon, M K M Bader, P T Baker, F Baldaccini, G Ballardini, S W Ballmer, J C Barayoga, S E Barclay, B C Barish, D Barker, F Barone, B Barr, L Barsotti, M Barsuglia, D Barta, J Bartlett, I Bartos, R Bassiri, A Basti, J C Batch, C Baune, V Baviggadda, M Bazzan, M Bejger, A S Bell, B K Berger, G Bergmann, C P L Berry, D Bersanetti, A Bertolini, J Betzwieser, S Bhagwat, R Bhandare, I A Bilenko, G Billingsley, J Birch, R Birney, O Birnholtz, S Biscans, A Bisht, M Bitossi, C Biwer, M A Bizouard, J K Blackburn, C D Blair, D G Blair, R M Blair, S Bloemen, O Bock, M Boer, G Bogaert, C Bogan, A Bohe, C Bond, F Bondu, R Bonnand, B A Boom, R Bork, V Boschi, S Bose, Y Bouffanais, A Bozzi, C Bradaschia, P R Brady, V B Braginsky, M Branchesi, J E Brau, T Briant, A Brillet, M Brinkmann, V Brisson, P Brockill, J E Broida, A F Brooks, D A Brown, D D Brown, N M Brown, S Brunett, C C Buchanan, A Buikema, T Bulik, H J Bulten, A Buonanno, D Buskulic, C Buy, R L Byer, M Cabero, L Cadonati, G Cagnoli, C Cahillane, J Calderón Bustillo, T Callister, E Calloni, J B Camp, K C Cannon, J Cao, C D Capano, E Capocasa, F Carbognani, S Caride, J Casanueva Diaz, C Casentini, S Caudill, M Cavaglià, F Cavalier,

R Cavalieri, G Cella, C B Cepeda, L Cerboni Baiardi, G Cerretani, E Cesarini, S J Chamberlin, M Chan, S Chao, P Charlton, E Chassande-Mottin, B D Cheeseboro, H Y Chen, Y Chen, C Cheng, A Chincarini, A Chiummo, H S Cho, M Cho, J H Chow, N Christensen, Q Chu, S Chua, S Chung, G Ciani, F Clara, J A Clark, F Cleva, E Coccia, P.-F. Cohadon, A Colla, C G Collette, L Cominsky, M Constancio, A Conte, L Conti, D Cook, T R Corbitt, N Cornish, A Corsi, S Cortese, C A Costa, M W Coughlin, S B Coughlin, J.-P. Coulon, S T Countryman, P Couvares, E E Cowan, D M Coward, M J Cowart, D C Coyne, R Coyne, K Craig, J D E Creighton, J Cripe, S G Crowder, A Cumming, L Cunningham, E Cuoco, T Dal Canton, S L Danilishin, S D'Antonio, K Danzmann, N S Darman, A Dasgupta, C F Da Silva Costa, V Dattilo, I Dave, M Davier, G S Davies, E J Daw, R Day, S De, D DeBra, G Debreczeni, J Degallaix, M De Laurentis, S Deléglise, W Del Pozzo, T Denker, T Dent, V Dergachev, R De Rosa, R T DeRosa, R DeSalvo, R C Devine, S Dhurandhar, M C D'iaz, L Di Fiore, M Di Giovanni, T Di Girolamo, A Di Lieto, S Di Pace, I Di Palma, A Di Virgilio, V Dolique, F Donovan, K L Dooley, S Doravari, R Douglas, T P Downes, M Drago, R W P Drever, J C Driggers, M Ducrot, S E Dwyer, T B Edo, M C Edwards, A Effler, H.-B. Eggenstein, P Ehrens, J Eichholz, S S Eikenberry, W Engels, R C Essick, T Etzel, M Evans, T M Evans, R Everett, M Factourovich, V Fafone, H Fair, S Fairhurst, X Fan, Q Fang, S Farinon, B Farr, W M Farr, M Favata, M Fays, H Fehrmann, M M Fejer, E Fenyvesi, I Ferrante, E C Ferreira, F Ferrini, F Fidecaro, I Fiori, D Fiorucci, R P Fisher, R Flaminio, M Fletcher, H Fong, J.-D. Fournier, S Frasca, F Frasconi, Z Frei, A Freise, R Frey, V Frey, P Fritschel, V V Frolov, P Fulda, M Fyffe, H A G Gabbard, J R Gair, L Gammaitoni, S G Gaonkar, F Garufi, G Gaur, N Gehrels, G Gemme, P Geng, E Genin, A Gennai, J George, L Gergely, V Germain, Abhirup Ghosh, Archisman Ghosh, S Ghosh, J A Giaime, K D Giardino, A Gi-azotto, K Gill, A Glaefke, E Goetz, R Goetz, L Gondan, G González, J M Gonzalez Castro, A Gopakumar, N A Gordon, M L Gorodetsky, S E Gossan, M Gosselin, R Gouaty, A Grado, C Graef, P B Graff, M Granata, A Grant, S Gras, C Gray, G Greco, A C Green, P Groot, H Grote, S Grunewald, G M Guidi, X Guo, A Gupta, M K Gupta, K E Gushwa, E K Gustafson, R Gustafson, J J Hacker, B R Hall, E D Hall, H Hamilton, G Hammond, M Haney, M M Hanke, J Hanks, C Hanna, M D Hannam, J Hanson, T Hardwick, J Harms,

G M Harry, I W Harry, M J Hart, M T Hartman, C.-J. Haster, K Haughian, J Healy, A Heidmann, M C Heintze, H Heitmann, P Hello, G Hemming, M Hendry, I S Heng, J Hennig, J Henry, A W Heptonstall, M Heurs, S Hild, D Hoak, D Hofman, K Holt, D E Holz, P Hopkins, J Hough, E A Houston, E J Howell, Y M Hu, S Huang, E A Huerta, D Huet, B Hughey, S Husa, S H Huttner, T Huynh-Dinh, N Indik, D R Ingram, R Inta, H N Isa, J.-M. Isac, M Isi, T Isogai, B R Iyer, K Izumi, T Jacqmin, H Jang, K Jani, P Jaranowski, S Jawahar, L Jian, F Jiménez-Forteza, W W Johnson, N K Johnson-McDaniel, D I Jones, R Jones, R J G Jonker, L Ju, Haris K, C V Kalaghatgi, V Kalogera, S Kandhasamy, G Kang, J B Kanner, S J Kapadia, S Karki, K S Karvinen, M Kasprzack, E Katsavounidis, W Katzman, S Kaufer, T Kaur, K Kawabe, F Kéfélian, M S Kehl, D Keitel, D B Kelley, W Kells, R Kennedy, J S Key, F Y Khalili, I Khan, S Khan, Z Khan, E A Khazanov, N Kijbunchoo, Chi-Woong Kim, Chunglee Kim, J Kim, K Kim, N Kim, W Kim, Y.-M. Kim, S J Kimbrell, E J King, P J King, J S Kissel, B Klein, L Kleybolte, S Klimenko, S M Koehlenbeck, S Koley, V Kondrashov, A Kontos, M Korobko, W Z Korth, I Kowalska, D B Kozak, V Kringel, B Krishnan, A Królak, C Krueger, G Kuehn, P Kumar, R Kumar, L Kuo, A Kutynia, B D Lackey, M Landry, J Lange, B Lantz, P D Lasky, M Laxen, A Lazzarini, C Lazzaro, P Leaci, S Leavey, E O Lebigot, C H Lee, H K Lee, H M Lee, K Lee, A Lenon, M Leonardi, J R Leong, N Leroy, N Létendre, Y Levin, J B Lewis, T G F Li, A Libson, T B Littenberg, N A Lockerbie, A L Lombardi, L T London, J E Lord, M Lorenzini, V Loriette, M Lormand, G Losurdo, J D Lough, C O Lousto, H Lück, A P Lundgren, R Lynch, Y Ma, B Machenschalk, M MacInnis, D M Macleod, F Magaña-Sandoval, L Magaña Zertuche, R M Magee, E Majorana, I Maksimovic, V Malvezzi, N Man, I Mandel, V Mandic, V Mangano, G L Mansell, M Manske, M Mantovani, F Marchesoni, F Marion, S Márka, Z Márka, A S Markosyan, E Maros, F Martelli, L Martellini, I W Martin, D V Martynov, J N Marx, K Mason, A Masserot, T J Massinger, M Masso-Reid, S Mastrogiovanni, F Matichard, L Matone, N Mavalvala, N Mazumder, R McCarthy, D E McClelland, S McCormick, S C McGuire, G McIntyre, J McIver, D J McManus, T McRae, S T McWilliams, D Meacher, G D Meadors, J Meidam, A Melatos, G Mendell, R A Mercer, E L Merilh, M Merzougui, S Meshkov, C Messenger, C Messick, R Metzdorff, P M Meyers, F Mezzani, H Miao, C Michel, H Middleton, E E Mikhailov, L Milano,

A L Miller, A Miller, B B Miller, J Miller, M Millhouse, Y Minenkov, J Ming, S Mirshekari, C Mishra, S Mitra, V P Mitrofanov, G Mitselmakher, R Mittleman, A Moggi, M Mohan, S R P Mohapatra, M Montani, B C Moore, C J Moore, D Moraru, G Moreno, S R Morriss, K Mossavi, B Mours, C M Mow-Lowry, G Mueller, A W Muir, Arunava Mukherjee, D Mukherjee, S Mukherjee, N Mukund, A Mullavey, J Munch, D J Murphy, P G Murray, A Mytidis, I Nardecchia, L Naticchioni, R K Nayak, K Nedkova, G Nelemans, T J N Nelson, M Neri, A Neunzert, G Newton, T T Nguyen, A B Nielsen, S Nissanke, A Nitz, F Nocera, D Nolting, M E N Normandin, L K Nuttall, J Oberling, E Ochsner, J O'Dell, E Oelker, G H Ogini, J J Oh, S H Oh, F Ohme, M Oliver, P Oppermann, Richard J Oram, B O'Reilly, R O'Shaughnessy, D J Ottaway, H Overmier, B J Owen, A Pai, S A Pai, J R Palamos, O Palashov, C Palomba, A Pal-Singh, H Pan, C Pankow, F Pannarale, B C Pant, F Paoletti, A Paoli, M A Papa, H R Paris, W Parker, D Pascucci, A Pasqualetti, R Passaquieti, D Passuello, B Patricelli, Z Patrick, B L Pearlstone, M Pedraza, R Pedurand, L Pekowsky, A Pele, S Penn, A Perreca, L M Perri, H P Pfeiffer, M Phelps, O J Piccinni, M Pichot, F Piergiovanni, V Pierro, G Pillant, L Pinard, I M Pinto, M Pitkin, M Poe, R Poggiani, P Popolizio, A Post, J Powell, J Prasad, V Predoi, T Prestegard, L R Price, M Prijatelj, M Principe, S Privitera, R Prix, G A Prodi, L Prokhorov, O Puncken, M Punturo, P Puppo, M Pürerer, H Qi, J Qin, S Qiu, V Quetschke, E A Quintero, R Quitzow-James, F J Raab, D S Rabeling, H Radkins, P Raffai, S Raja, C Rajan, M Rakhmanov, P Rapagnani, V Raymond, M Razzano, V Re, J Read, C M Reed, T Regimbau, L Rei, S Reid, D H Reitze, H Rew, S D Reyes, F Ricci, K Riles, M Rizzo, N A Robertson, R Robie, F Robinet, A Rocchi, L Rolland, J G Rollins, V J Roma, J D Romano, R Romano, G Romanov, J H Romie, D Rosi, S Rowan, A Rüdiger, P Ruggi, K Ryan, S Sachdev, T Sadecki, L Sadeghian, M Sakellariadou, L Salconi, M Saleem, F Salemi, A Samajdar, L Sammut, E J Sanchez, V Sandberg, B Sandeen, J R Sanders, B Sassolas, B S Sathyaprakash, P R Saulson, O E S Sauter, R L Savage, A Sawadsky, P Schale, R Schilling, J Schmidt, P Schmidt, R Schnabel, R M S Schofield, A Schönbeck, E Schreiber, D Schuette, B F Schutz, J Scott, S M Scott, D Sellers, A S Sengupta, D Sentenac, V Sequino, A Sergeev, Y Setyawati, D A Shaddock, T Shaffer, M S Shahriar, M Shaltev, B Shapiro, P Shawhan, A Sheperd, D H Shoemaker, D M Shoemaker, K Siellez,

X Siemens, M Sieniawska, D Sigg, A D Silva, A Singer, L P Singer, A Singh, R Singh, A Singhal, A M Sintes, B J J Slagmolen, J R Smith, N D Smith, R J E Smith, E J Son, B Sorazu, F Sorrentino, T Souradeep, A K Srivastava, A Staley, M Steinke, J Steinlechner, S Steinlechner, D Steinmeyer, B C Stephens, S P Stevenson, R Stone, K A Strain, N Straniero, G Stratta, N A Strauss, S Strigin, R Sturani, A L Stuver, T Z Summerscales, L Sun, S Sunil, P J Sutton, B L Swinkels, M J Szczepa\ifmmode \acuten\else ´\ficzyk, M Tacca, D Talukder, D B Tanner, M Tápai, S P Tarabrin, A Taracchini, R Taylor, T Theeg, M P Thirugnanasambandam, E G Thomas, M Thomas, P Thomas, K A Thorne, E Thrane, S Tiwari, V Tiwari, K V Tokmakov, K Toland, C Tomlinson, M Tonelli, Z Tornasi, C V Torres, C I Torrie, D Töyrä, F Travasso, G Traylor, D Trifirò, M C Tringali, L Trozzo, M Tse, M Turconi, D Tuyenbayev, D Ugolini, C S Unnikrishnan, A L Urban, S A Usman, H Vahlbruch, G Vajente, G Valdes, M Vallisneri, N van Bakel, M van Beuzekom, J F J van den Brand, C Van Den Broeck, D C Vander-Hyde, L van der Schaaf, J V van Heijningen, A A van Veggel, M Vardaro, S Vass, M Vasúth, R Vaulin, A Vecchio, G Vedovato, J Veitch, P J Veitch, K Venkateswara, D Verkindt, F Vetrano, A Viceré, S Vinciguerra, D J Vine, J.-Y. Vinet, S Vitale, T Vo, H Vocca, C Vorvick, D V Voss, W D Voudsen, S P Vyatchanin, A R Wade, L E Wade, M Wade, M Walker, L Wallace, S Walsh, G Wang, H Wang, M Wang, X Wang, Y Wang, R L Ward, J Warner, M Was, B Weaver, L.-W. Wei, M Weinert, A J Weinstein, R Weiss, L Wen, P We\ssels, T Westphal, K Wette, J T Whelan, B F Whiting, R D Williams, A R Williamson, J L Willis, B Willke, M H Wimmer, W Winkler, C C Wipf, H Wittel, G Woan, J Woehler, J Worden, J L Wright, D S Wu, G Wu, J Yablon, W Yam, H Yamamoto, C C Yancey, H Yu, M Yvert, A Zadro\ifmmode \dotz\else ˙\fny, L Zangrando, M Zanolin, J.-P. Zendri, M Zevin, L Zhang, M Zhang, Y Zhang, C Zhao, M Zhou, Z Zhou, X J Zhu, M E Zucker, S E Zuraw, J Zweizig, M Boyle, D Hemberger, L E Kidder, G Lovelace, S Ossokine, M Scheel, B Szilagyi, and S Teukolsky. GW151226: Observation of Gravitational Waves from a 22-Solar-Mass Binary Black Hole Coalescence. *Phys. Rev. Lett.*, 116(24):241103, jun 2016.

[8] J. A. Peacock. *Cosmological Physics*. jan 1999.

[9] S Dodelson. *Modern cosmology*. 2003.

- [10] T Padmanabhan. *Theoretical Astrophysics - Volume 3, Galaxies and Cosmology*. dec 2002.
- [11] P. J. E. Peebles. *Principles of Physical Cosmology*. 1993.
- [12] S Weinberg. *Cosmology*. Oxford University Press, 2008.
- [13] E. W. Kolb and M. S. Turner. *The early universe*. 1990.
- [14] Jorge E. García-Farieta and Rigoberto A. Casas-Miranda. Effect of observational holes and borders on lacunarity and fractality measurements in a galaxy catalogue. page 10, apr 2016.
- [15] J. M. Bardeen, J. R. Bond, N. Kaiser, and a. S. Szalay. The statistics of peaks of Gaussian random fields. *The Astrophysical Journal*, 304:15 – 61, 1986.
- [16] Naoshi Sugiyama. Cosmic Background Anisotropies in Cold Dark Matter Cosmology. *The Astrophysical Journal Supplement Series*, 100:281, 1995.
- [17] Daniel J. Eisenstein and Wayne Hu. Baryonic Features in the Matter Transfer Function. *The Astrophysical Journal*, 496:605, 1998.
- [18] E. R. Harrison. Fluctuations at the threshold of classical cosmology. *Physical Review D*, 1(10):2726–2730, may 1970.
- [19] Ya. B. Zeldovich. A Hypothesis, Unifying the Structure and the Entropy of the Universe. *Monthly Notices of the Royal Astronomical Society*, 160(1):Short Communication, oct 1972.
- [20] Planck Collaboration, P. A. R. Ade, N Aghanim, M Arnaud, M Ashdown, J Aumont, C Baccigalupi, A. J. Banday, R. B. Barreiro, J. G. Bartlett, and Et al. Planck 2015 results. XIII. Cosmological parameters. *ArXiv e-prints*, feb 2015.
- [21] Kyle S. Dawson, David J. Schlegel, Christopher P. Ahn, Scott F. Anderson, Éric Aubourg, Stephen Bailey, Robert H. Barkhouser, Julian E. Bautista, Alessandra Beifiori, Andreas A. Berlind, Vaishali Bhardwaj, Dmitry Bizyaev, Cullen H. Blake, Michael R. Blanton, Michael Blomqvist, Adam S. Bolton, Arnaud Borde, Jo Bovy, W. N. Brandt, Howard Brewington, Jon Brinkmann, Peter J. Brown,

Joel R. Brownstein, Kevin Bundy, N. G. Busca, William Carithers, Aurelio R. Carnero, Michael A. Carr, Yanmei Chen, Johan Comparat, Natalia Connolly, Frances Cope, Rupert A. C. Croft, Antonio J. Cuesta, Luiz N. da Costa, James R. A. Davenport, Timothée Delubac, Roland de Putter, Saurav Dhital, Anne Ealet, Garrett L. Ebelke, Daniel J. Eisenstein, S. Escoffier, Xiaohui Fan, N. Filiz Ak, Hayley Finley, Andreu Font-Ribera, R. Génova-Santos, James E. Gunn, Hong Guo, Daryl Haggard, Patrick B. Hall, Jean-Christophe Hamilton, Ben Harris, David W. Harris, Shirley Ho, David W. Hogg, Diana Holder, Klaus Honscheid, Joe Huehnerhoff, Beatrice Jordan, Wendell P. Jordan, Guinevere Kauffmann, Eyal A. Kazin, David Kirkby, Mark A. Klaene, Jean-Paul Kneib, Jean-Marc Le Goff, Khee-Gan Lee, Daniel C. Long, Craig P. Loomis, Britt Lundgren, Robert H. Lupton, Marcio A. G. Maia, Martin Makler, Elena Malanushenko, Viktor Malanushenko, Rachel Mandelbaum, Marc Manera, Claudia Maraston, Daniel Margala, Karen L. Masters, Cameron K. McBride, Patrick McDonald, Ian D. McGreer, Richard G. McMahon, Olga Mena, Jordi Miralda-Escudé, Antonio D. Montero-Dorta, Francesco Montesano, Demitri Muna, Adam D. Myers, Tracy Naugle, Robert C. Nichol, Pasquier Noterdaeme, Sebastián E. Nuza, Matthew D. Olmstead, Audrey Oravetz, Daniel J. Oravetz, Russell Owen, Nikhil Padmanabhan, Nathalie Palanque-Delabrouille, Kaike Pan, John K. Parejko, Isabelle Pâris, Will J. Percival, Ismael Pérez-Fournon, Ignasi Pérez-Ràfols, Patrick Petitjean, Robert Pfaffenberger, Janine Pforr, Matthew M. Pieri, Francisco Prada, Adrian M. Price-Whelan, M. Jordan Raddick, Rafael Rebolo, James Rich, Gordon T. Richards, Constance M. Rockosi, Natalie A. Roe, Ashley J. Ross, Nicholas P. Ross, Graziano Rossi, J. A. Rubiño-Martin, Lado Samushia, Ariel G. Sánchez, Conor Sayres, Sarah J. Schmidt, Donald P. Schneider, C. G. Scóccola, Hee-Jong Seo, Alaina Sheldon, Erin Sheldon, Yue Shen, Yiping Shu, Anže Slosar, Stephen A. Smee, Stephanie A. Snedden, Fritz Stauffer, Oliver Steele, Michael A. Strauss, Alina Streblyanska, Nao Suzuki, Molly E. C. Swanson, Tomer Tal, Masayuki Tanaka, Daniel Thomas, Jeremy L. Tinker, Rita Tojeiro, Christy A. Tremonti, M. Vargas Magaña, Licia Verde, Matteo Viel, David A. Wake, Mike Watson, Benjamin A. Weaver, David H. Weinberg, Benjamin J. Weiner, Andrew A. West, Martin White, W. M. Wood-Vasey, Christophe Yèche, Idit Zehavi, Gong-Bo Zhao, and Zheng Zheng. the Baryon Oscillation Spectroscopic Survey of Sdss-Iii. *The Astronomical Journal*,

145(1):10, 2013.

- [22] N. Kaiser. On the spatial correlations of Abell clusters. *The Astrophysical Journal*, 284:L9, 1984.
- [23] Ramesh Narayan and Matthias Bartelmann. Lectures on Gravitational Lensing. *arXiv.org*, page 6001, 1996.
- [24] Matthias Bartelmann and Peter Schneider. Weak Gravitational Lensing. *Physics Reports*, 340(4-5):291–472, jan 1999.
- [25] Y. Mellier. Probing the Universe with Weak Lensing. *Annual Review of Astronomy and Astrophysics*, 37:54, 1999.
- [26] Peter Schneider, Christopher Kochanek, and Joachim Wambsganss. *Gravitational Lensing: Strong, Weak and Micro: Saas-Fee Advanced Course 33*, volume 33. Springer Science & Business Media, 2006.
- [27] Henk Hoekstra and Bhuvnesh Jain. Weak Gravitational Lensing and Its Cosmological Applications. *Annual Review of Nuclear and Particle Science*, 58(1):99–123, nov 2008.
- [28] Martin Kilbinger. Cosmology with cosmic shear observations: a review. *Reports on Progress in Physics*, 78(8):86901, jul 2015.
- [29] Alan Heavens. 3D weak lensing, 2003.
- [30] T. D. Kitching, A. F. Heavens, J. Alsing, T. Erben, C. Heymans, H. Hildebrandt, H. Hoekstra, A. Jaffe, A. Kiessling, Y. Mellier, L. Miller, L. van Waerbeke, J. Benjamin, J. Coupon, L. Fu, M. J. Hudson, M. Kilbinger, K. Kuijken, B. T P Rowe, T. Schrabback, E. Semboloni, and M. Velander. 3D cosmic shear: Cosmology from CFHTLenS. *Monthly Notices of the Royal Astronomical Society*, 442(2):1326–1349, 2014.
- [31] Rachel Mandelbaum. Instrumental systematics and weak gravitational lensing. *Journal of Instrumentation*, 10(05):C05017, may 2015.
- [32] Emmanuel Bertin and Stephane Arnouts. SExtractor: Software for source extraction. *Astronomy and Astrophysics Supplement Series*, 117(2):393–404, 1996.

- [33] Catherine Heymans, Ludovic Van Waerbeke, David Bacon, J. Berge, G.~M. Bernstein, E. Bertin, Sarah Bridle, M. L. Brown, Douglas Clowe, Håkon Dahle, Thomas Erben, M. Gray, M. Hetterscheidt, Henk Hoekstra, Patrick Hudelot, Mike Jarvis, Konrad Kuijken, Vera Margoniner, Richard Massey, Yannick Mellier, Reiko Nakajima, Alexandre Refregier, Jason Rhodes, Tim Schrabback, and D. Wittman. The Shear Testing Programme - I. Weak lensing analysis of simulated ground-based observations. *Monthly Notices of the Royal Astronomical Society*, 368(3):1323–1339, may 2006.
- [34] Richard Massey, Henk Hoekstra, Thomas Kitching, Jason Rhodes, Mark Cropper, J??r??me Amiaux, David Harvey, Yannick Mellier, Massimo Meneghetti, Lance Miller, St??phane Paulin-Henriksson, Sandrine Pires, Roberto Scaramella, and Tim Schrabback. Origins of weak lensing systematics, and requirements on future instrumentation (or knowledge of instrumentation). *Monthly Notices of the Royal Astronomical Society*, 429(1):661–678, feb 2013.
- [35] Richard Massey, Catherine Heymans, Joel Berg e, Gary Bernstein, Sarah Bridle, Douglas Clowe, Håkon Dahle, Richard Ellis, Thomas Erben, Marco Hetterscheidt, F. William High, Christopher Hirata, Henk Hoekstra, Patrick Hudelot, Mike Jarvis, David Johnston, Konrad Kuijken, Vera Margoniner, Rachel Mandelbaum, Yannick Mellier, Reiko Nakajima, Stephane Paulin-Henriksson, Molly Peeples, Chris Roat, Alexandre Refregier, Jason Rhodes, Tim Schrabback, Mischa Schirmer, Uroš Seljak, Elisabetta Semboloni, and Ludovic Van Waerbeke. The Shear Testing Programme 2: Factors affecting high-precision weak-lensing analyses. *Monthly Notices of the Royal Astronomical Society*, 376(1):13–38, mar 2007.
- [36] S Bridle, J Shawe-Taylor, A Amara, D Applegate, Joel S.~T. Balan Berge, G Bernstein, H Dahle, T Erben, M Gill, A Heavens, C Heymans, F.~W. High, H Hoekstra, M Jarvis, D Kirk, T Kitching, J.-P. Kneib, K Kuijken, D Lagatutta, R Mandelbaum, R Massey, Y Mellier, B Moghaddam, Y Moudde, R Nakajima, S Paulin-Henriksson, S Pires, A Rassat, A Refregier, J Rhodes, T Schrabback, E Semboloni, M Shmakova, L van Waerbeke, D Witherick, L Voigt, and D Wittman. Handbook for the GREAT08 Challenge: An image analysis competition for cosmological lensing. *Annals of Applied Statistics*, 3:6–37, 2009.

- [37] T Kitching, S Balan, G Bernstein, M Bethge, S Bridle, F Courbin, M Gentile, A Heavens, M Hirsch, R Hosseini, A Kiessling, A Amara, D Kirk, K Kuijken, R Mandelbaum, B Moghaddam, G Nurbaeva, S Paulin-Henriksson, A Rassat, J Rhodes, B Schölkopf, J Shawe-Taylor, M Gill, M Shmakova, A Taylor, M Velander, L van Waerbeke, D Witherick, D Wittman, S Harmeling, C Heymans, R Massey, B Rowe, T Schrabback, and L Voigt. Gravitational Lensing Accuracy Testing 2010 (GREAT10) Challenge Handbook. *ArXiv e-prints*, sep 2010.
- [38] Rachel Mandelbaum, Barnaby Rowe, James Bosch, Chihway Chang, Frederic Courbin, Mandeep Gill, Mike Jarvis, Arun Kannawadi, Tomasz Kacprzak, Claire Lackner, Alexie Leauthaud, Hironao Miyatake, Reiko Nakajima, Jason Rhodes, Melanie Simet, Joe Zuntz, Bob Armstrong, Sarah Bridle, Jean Coupon, Jörg P. Dietrich, Marc Gentile, Catherine Heymans, Alden S. Jurling, Stephen M. Kent, David Kirkby, Daniel Margala, Richard Massey, Peter Melchior, John Peterson, Aaron Roodman, and Tim Schrabback. The Third Gravitational Lensing Accuracy Testing (GREAT3) Challenge Handbook. *The Astrophysical Journal Supplement Series*, 212(1):5, may 2014.
- [39] A Amara and A Réfrégier. Systematic bias in cosmic shear: extending the Fisher matrix. *Monthly Notices of the Royal Astronomical Society*, 391:228–236, nov 2008.
- [40] M Cropper, H Hoekstra, T Kitching, R Massey, J Amiaux, L Miller, Y Mellier, J Rhodes, B Rowe, S Pires, C Saxton, and R Scaramella. Defining a weak lensing experiment in space. *Monthly Notices of the Royal Astronomical Society*, 431:3103–3126, jun 2013.
- [41] A Réfrégier. Weak Gravitational Lensing by Large-Scale Structure. *Annual Review of Astronomy and Astrophysics*, 41:645–668, 2003.
- [42] A Albrecht, G Bernstein, R Cahn, W.~L. Freedman, J Hewitt, W Hu, J Huth, M Kamionkowski, E.~W. Kolb, L Knox, J.~C. Mather, S Staggs, and N.~B. Suntzeff. Report of the Dark Energy Task Force. *preprint (arXiv:astro-ph/0609591)*, sep 2006.
- [43] D.~H. Weinberg, M.~J. Mortonson, D.~J. Eisenstein, C Hirata, A.~G. Riess,

and E Rozo. Observational probes of cosmic acceleration. *Physics Reports*, 530:87–255, sep 2013.

- [44] S Miyazaki, Y Komiyama, H Nakaya, Y Doi, H Furusawa, P Gillingham, Y Kamata, K Takeshi, and K Nariai. HyperSuprime: project overview. In *Society of Photo-Optical Instrumentation Engineers (SPIE) Conference Series*, volume 6269 of *Society of Photo-Optical Instrumentation Engineers (SPIE) Conference Series*, jun 2006.
- [45] The Dark Energy Survey Collaboration. The Dark Energy Survey. *preprint (arXiv:astro-ph/0510346)*, oct 2005.
- [46] J.~T.~A. de Jong, K Kuijken, D Applegate, K Begeman, A Belikov, C Blake, J Bout, D Boxhoorn, H Buddelmeijer, A Buddendiek, M Cacciato, M Capaccioli, A Choi, O Cordes, G Covone, M Dall’Ora, A Edge, T Erben, J Franse, F Getman, A Grado, J Harnois-Deraps, E Helmich, R Herbonnet, C Heymans, H Hildebrandt, H Hoekstra, Z Huang, N Irisarri, B Joachimi, F Köhlinger, T Kitching, F La Barbera, P Lacerda, J McFarland, L Miller, R Nakajima, N.~R. Napolitano, M Paolillo, J Peacock, B Pila-Diez, E Puddu, M Radovich, A Rifatto, P Schneider, T Schrabback, C Sifon, G Sikkema, P Simon, W Sutherland, A Tudorica, E Valentijn, R van der Burg, E van Uitert, L van Waerbeke, M Velander, G.~V. Kleijn, M Viola, and W.-J. Vriend. The Kilo-Degree Survey. *The Messenger*, 154:44–46, dec 2013.
- [47] N Kaiser, W Burgett, K Chambers, L Denneau, J Heasley, R Jedicke, E Magnier, J Morgan, P Onaka, and J Tonry. The Pan-STARRS wide-field optical/NIR imaging survey. In *Society of Photo-Optical Instrumentation Engineers (SPIE) Conference Series*, volume 7733 of *Society of Photo-Optical Instrumentation Engineers (SPIE) Conference Series*, jul 2010.
- [48] LSST Science Collaboration, P.~A. Abell, J Allison, S.~F. Anderson, J.~R. Andrew, J.~R.~P. Angel, L Armus, D Arnett, S.~J. Asztalos, T.~S. Axelrod, and Et al. LSST Science Book, Version 2.0. *preprint (arXiv:0912.0201)*, dec 2009.
- [49] R Laureijs, J Amiaux, S Arduini, J.~-. Auguères, J Brinchmann, R Cole,

M Cropper, C Dabin, L Duvet, A Ealet, and Et al. Euclid Definition Study Report. *preprint (arXiv:1110.3193)*, oct 2011.

- [50] J Green, P Schechter, C Baltay, R Bean, D Bennett, R Brown, C Conselice, M Donahue, X Fan, B.~S. Gaudi, C Hirata, J Kalirai, T Lauer, B Nichol, N Padmanabhan, S Perlmutter, B Rauscher, J Rhodes, T Roellig, D Stern, T Sumi, A Tanner, Y Wang, D Weinberg, E Wright, N Gehrels, R Sambruna, W Traub, J Anderson, K Cook, P Garnavich, L Hillenbrand, Z Ivezić, E Kerins, J Lunine, P McDonald, M Penny, M Phillips, G Rieke, A Riess, R van der Marel, R.~K. Barry, E Cheng, D Content, R Cutri, R Goullioud, K Grady, G Helou, C Jackson, J Kruk, M Melton, C Peddie, N Rioux, and M Seiffert. Wide-Field InfraRed Survey Telescope (WFIRST) Final Report. *ArXiv e-prints*, aug 2012.
- [51] M.~A. Troxel and M Ishak. The Intrinsic Alignment of Galaxies and its Impact on Weak Gravitational Lensing in an Era of Precision Cosmology. *preprint (arXiv:1407.6990)*, jul 2014.
- [52] M.~P. van Daalen, J Schaye, C.~M. Booth, and C Dalla Vecchia. The effects of galaxy formation on the matter power spectrum: a challenge for precision cosmology. *Monthly Notices of the Royal Astronomical Society*, 415:3649–3665, aug 2011.
- [53] E Semboloni, H Hoekstra, J Schaye, M.~P. van Daalen, and I.~G. McCarthy. Quantifying the effect of baryon physics on weak lensing tomography. *Monthly Notices of the Royal Astronomical Society*, 417:2020–2035, nov 2011.
- [54] T Schrabback, J Hartlap, B Joachimi, M Kilbinger, P Simon, K Benabed, M Bradač, T Eifler, T Erben, C.~D. Fassnacht, F.~W. High, S Hilbert, H Hildebrandt, H Hoekstra, K Kuijken, P.~J. Marshall, Y Mellier, E Morganson, P Schneider, E Semboloni, L van Waerbeke, and M Velander. Evidence of the accelerated expansion of the Universe from weak lensing tomography with COSMOS. *Astronomy and Astrophysics*, 516:A63, jun 2010.
- [55] Catherine Heymans, E Grocutt, A Heavens, M Kilbinger, T.~D. Kitching, F Simpson, J Benjamin, T Erben, H Hildebrandt, H Hoekstra, and Et~al. CFHTLenS tomographic weak lensing cosmological parameter constraints: Mit-

- igating the impact of intrinsic galaxy alignments. *Monthly Notices of the Royal Astronomical Society*, 432:2433–2453, jul 2013.
- [56] M. J. Jee, J. A. Tyson, M. D. Schneider, D Wittman, S Schmidt, and S Hilbert. Cosmic Shear Results from the Deep Lens Survey. I. Joint Constraints on $\{\Omega\}$ - $\{M\}$ and $\{\sigma\}$ - $\{8\}$ with a Two-dimensional Analysis. *The Astrophysical Journal*, 765:74, mar 2013.
- [57] Rachel Mandelbaum, Anze Slosar, Tobias Baldauf, Uroš Seljak, Christopher M. Hirata, Reiko Nakajima, Reinabelle Reyes, and Robert E. Smith. Cosmological parameter constraints from galaxy-galaxy lensing and galaxy clustering with the SDSS DR7. *Monthly Notices of the Royal Astronomical Society*, 432(2):1544–1575, jun 2013.
- [58] M Viola, T. D. Kitching, and B Joachimi. On the probability distributions of ellipticity. *Monthly Notices of the Royal Astronomical Society*, 439:1909–1932, apr 2014.
- [59] L. M. Voigt, S. L. Bridle, A Amara, M Cropper, T. D. Kitching, R Massey, J Rhodes, and T Schrabback. The impact of galaxy colour gradients on cosmic shear measurement. *Monthly Notices of the Royal Astronomical Society*, 421:1385–1398, apr 2012.
- [60] E Semboloni, H Hoekstra, Z Huang, V. F. Cardone, M Cropper, B Joachimi, T Kitching, K Kuijken, M Lombardi, R Maoli, Y Mellier, L Miller, J Rhodes, R Scaramella, T Schrabback, and M Velander. On the shear estimation bias induced by the spatial variation of colour across galaxy profiles. *Monthly Notices of the Royal Astronomical Society*, 432:2385–2401, jul 2013.
- [61] L. M. Voigt and S. L. Bridle. Limitations of model-fitting methods for lensing shear estimation. *Monthly Notices of the Royal Astronomical Society*, 404:458–467, may 2010.
- [62] P Melchior, A Böhnert, M Lombardi, and M Bartelmann. Limitations on shapelet-based weak-lensing measurements. *Astronomy and Astrophysics*, 510:A75, feb 2010.

- [63] Tomasz Kacprzak, Joe Zuntz, Barnaby Rowe, Sarah Bridle, Alexandre Refregier, Adam Amara, Lisa Voigt, and Michael Hirsch. Measurement and calibration of noise bias in weak lensing galaxy shape estimation. *Monthly Notices of the Royal Astronomical Society*, 427(4):2711–2722, 2012.
- [64] P Melchior and M Viola. Means of confusion: how pixel noise affects shear estimates for weak gravitational lensing. *Monthly Notices of the Royal Astronomical Society*, 424:2757–2769, aug 2012.
- [65] Alexandre Refregier, Tomasz Kacprzak, Adam Amara, Sarah Bridle, and Barnaby Rowe. Noise bias in weak lensing shape measurements. *Monthly Notices of the Royal Astronomical Society*, 425(3):1951–1957, sep 2012.
- [66] G.~M. Bernstein. Shape measurement biases from underfitting and ellipticity gradients. *Monthly Notices of the Royal Astronomical Society*, 406:2793–2804, aug 2010.
- [67] S Bridle, S.~T. Balan, M Bethge, M Gentile, S Harmeling, C Heymans, M Hirsch, R Hosseini, M Jarvis, D Kirk, T Kitching, K Kuijken, A Lewis, S Paulin-Henriksson, B Schölkopf, M Velander, L Voigt, D Witherick, A Amara, G Bernstein, F Courbin, M Gill, A Heavens, R Mandelbaum, R Massey, B Moghaddam, A Rassat, A Réfrégier, J Rhodes, T Schrabback, J Shawe-Taylor, M Shmakova, L van Waerbeke, and D Wittman. Results of the GREAT08 Challenge: an image analysis competition for cosmological lensing. *Monthly Notices of the Royal Astronomical Society*, 405:2044–2061, jul 2010.
- [68] T.~D. Kitching, S.~T. Balan, S Bridle, N Cantale, F Courbin, T Eifler, M Gentile, M.~S.~S. Gill, S Harmeling, C Heymans, M Hirsch, K Honscheid, T Kacprzak, D Kirkby, D Margala, R.~J. Massey, P Melchior, G Nurbaeva, K Patton, J Rhodes, B.~T.~P. Rowe, A.~N. Taylor, M Tewes, M Viola, D Witherick, L Voigt, J Young, and J Zuntz. Image analysis for cosmology: results from the GREAT10 Galaxy Challenge. *Monthly Notices of the Royal Astronomical Society*, 423:3163–3208, jul 2012.
- [69] Barnaby Rowe, Mike Jarvis, Rachel Mandelbaum, Gary M. Bernstein, James Bosch, Melanie Simet, Joshua Meyers, Tomasz Kacprzak, Reiko Nakajima, Joe Zuntz, Hironao Miyatake, Joerg Dietrich, Robert Armstrong, Peter Melchior,

and Mandeep S. Gill. GALSIM: The modular galaxy image simulation toolkit. *Astronomy and Computing*, 10:121–150, jul 2015.

- [70] C.~M. Carollo, A Cibinel, S.~J. Lilly, A Pipino, S Bonoli, A Finoguenov, F Miniati, P Norberg, and J.~D. Silverman. ZENS IV. Similar Morphological Changes associated with Mass- and Environment-Quenching, and the Relative importance of Bulge Growth versus the Fading of Disks. *preprint (arXiv:1402.1172)*, feb 2014.
- [71] R De Propris, I.~K. Baldry, J Bland-Hawthorn, S Brough, S.~P. Driver, A.~M. Hopkins, L Kelvin, J Loveday, S Phillipps, and A.~S.~G. Robotham. Galaxy and Mass Assembly (GAMA): merging galaxies and their properties. *Monthly Notices of the Royal Astronomical Society*, 444:2200–2211, nov 2014.
- [72] N Scoville, H Aussel, M Brusa, P Capak, C.~M. Carollo, M Elvis, M Giavalisco, L Guzzo, G Hasinger, C Impey, J.-P. Kneib, O LeFevre, S.~J. Lilly, B Mobasher, A Renzini, R.~M. Rich, D.~B. Sanders, E Schinnerer, D Schminovich, P Shopbell, Y Taniguchi, and N.~D. Tyson. The Cosmic Evolution Survey (COSMOS): Overview. *The Astrophysical Journal Supplement Series*, 172:1–8, sep 2007.
- [73] A.~M. Koekemoer, H Aussel, D Calzetti, P Capak, M Giavalisco, J.-P. Kneib, A Leauthaud, O Le Fèvre, H.~J. McCracken, R Massey, B Mobasher, J Rhodes, N Scoville, and P.~L. Shopbell. The COSMOS Survey: Hubble Space Telescope Advanced Camera for Surveys Observations and Data Processing. *The Astrophysical Journal Supplement Series*, 172:196–202, sep 2007.
- [74] A Leauthaud, R Massey, J.-P. Kneib, J Rhodes, D.~E. Johnston, P Capak, C Heymans, R.~S. Ellis, A.~M. Koekemoer, O Le Fèvre, Y Mellier, A Réfrégier, A.~C. Robin, N Scoville, L Tasca, J.~E. Taylor, and L Van Waerbeke. Weak Gravitational Lensing with COSMOS: Galaxy Selection and Shape Measurements. *The Astrophysical Journal Supplement Series*, 172:219–238, sep 2007.
- [75] Rachel Mandelbaum, Christopher Hirata, Alexie Leauthaud, Richard Massey, and Jason Rhodes. Precision simulation of ground-based lensing data using observations from space. *Monthly Notices of the Royal Astronomical Society*, 420:1518–1540, feb 2012.

- [76] C.~N. Lackner and J.~E. Gunn. Astrophysically motivated bulge-disc decompositions of Sloan Digital Sky Survey galaxies. *Monthly Notices of the Royal Astronomical Society*, 421:2277–2302, apr 2012.
- [77] O Ilbert, P Capak, M Salvato, H Aussel, H.~J. McCracken, D.~B. Sanders, N Scoville, J Kartaltepe, S Arnouts, E Le Floch, B Mobasher, Y Taniguchi, F Lamareille, A Leauthaud, S Sasaki, D Thompson, M Zamojski, G Zamorani, S Bardelli, M Bolzonella, A Bongiorno, M Brusa, K.~I. Caputi, C.~M. Carollo, T Contini, R Cook, G Coppa, O Cucciati, S de la Torre, L de Ravel, P Franzetti, B Garilli, G Hasinger, A Iovino, P Kampczyk, J.-P. Kneib, C Knobel, K Kovac, J.~F. Le Borgne, V Le Brun, O.~L. Fèvre, S Lilly, D Looper, C Maier, V Mainieri, Y Mellier, M Mignoli, T Murayama, R Pellò, Y Peng, E Pérez-Montero, A Renzini, E Ricciardelli, D Schiminovich, M Scodreggio, Y Shioya, J Silverman, J Surace, M Tanaka, L Tasca, L Tresse, D Vergani, and E Zucca. Cosmos Photometric Redshifts with 30-Bands for 2-deg². *The Astrophysical Journal*, 690:1236–1249, jan 2009.
- [78] A Leauthaud, A Finoguenov, J.-P. Kneib, J.~E. Taylor, R Massey, J Rhodes, O Ilbert, K Bundy, J Tinker, M.~R. George, P Capak, A.~M. Koekemoer, D.~E. Johnston, Y.-Y. Zhang, N Cappelluti, R.~S. Ellis, M Elvis, S Giodini, C Heymans, O Le Fèvre, S Lilly, H.~J. McCracken, Y Mellier, A Réfrégier, M Salvato, N Scoville, G Smoot, M Tanaka, L Van Waerbeke, and M Wolk. A Weak Lensing Study of X-ray Groups in the Cosmos Survey: Form and Evolution of the Mass-Luminosity Relation. *The Astrophysical Journal*, 709:97–114, jan 2010.
- [79] K Bundy, R.~S. Ellis, C.~J. Conselice, J.~E. Taylor, M.~C. Cooper, C.~N.~A. Willmer, B.~J. Weiner, A.~L. Coil, K.~G. Noeske, and P.~R.~M. Eisenhardt. The Mass Assembly History of Field Galaxies: Detection of an Evolving Mass Limit for Star-Forming Galaxies. *The Astrophysical Journal*, 651:120–141, nov 2006.
- [80] G Chabrier. Galactic Stellar and Substellar Initial Mass Function. *Publications of the Astronomical Society of the Pacific*, 115:763–795, jul 2003.
- [81] K Kovač, S.~J. Lilly, O Cucciati, C Porciani, A Iovino, G Zamorani, P Oesch, M Bolzonella, C Knobel, A Finoguenov, Y Peng, C.~M. Carollo, L Pozzetti,

- K Caputi, J.~D. Silverman, L.~A.~M. Tasca, M Scodreggio, D Vergani, N.~Z. Scoville, P Capak, T Contini, J.-P. Kneib, O Le Fèvre, V Mainieri, A Renzini, S Bardelli, A Bongiorno, G Coppa, S de la Torre, L de Ravel, P Franzetti, B Garilli, L Guzzo, P Kampczyk, F Lamareille, J.-F. Le Borgne, V Le Brun, C Maier, M Mignoli, R Pello, E Perez Montero, E Ricciardelli, M Tanaka, L Tresse, E Zucca, U Abbas, D Bottini, A Cappi, P Cassata, A Cimatti, M Fumana, A.~M. Koekemoer, D Maccagni, C Marinoni, H.~J. McCracken, P Memeo, B Meneux, and R Scaramella. The Density Field of the 10k zCOSMOS Galaxies. *The Astrophysical Journal*, 708:505–533, jan 2010.
- [82] C Wolf, K Meisenheimer, H.-W. Rix, A Borch, S Dye, and M Kleinheinrich. The COMBO-17 survey: Evolution of the galaxy luminosity function from 25 000 galaxies with $0.2 < z < 1.2$. *Astronomy and Astrophysics*, 401:73–98, apr 2003.
- [83] E Giallongo, S Salimbeni, N Menci, G Zamorani, A Fontana, M Dickinson, S Cristiani, and L Pozzetti. The B-Band Luminosity Function of Red and Blue Galaxies up to $z = 3.5$. *The Astrophysical Journal*, 622:116–128, mar 2005.
- [84] C.~N.~A. Willmer, S.~M. Faber, D.~C. Koo, B.~J. Weiner, J.~A. Newman, A.~L. Coil, A.~J. Connolly, C Conroy, M.~C. Cooper, M Davis, D.~P. Finkbeiner, B.~F. Gerke, P Guhathakurta, J Harker, N Kaiser, S Kassin, N.~P. Konidaris, L Lin, G Luppino, D.~S. Madgwick, K.~G. Noeske, A.~C. Phillips, and R Yan. The Deep Evolutionary Exploratory Probe 2 Galaxy Redshift Survey: The Galaxy Luminosity Function to $z \sim 1$. *The Astrophysical Journal*, 647:853–873, aug 2006.
- [85] S.~M. Faber, C.~N.~A. Willmer, C Wolf, D.~C. Koo, B.~J. Weiner, J.~A. Newman, M Im, A.~L. Coil, C Conroy, M.~C. Cooper, M Davis, D.~P. Finkbeiner, B.~F. Gerke, K Gebhardt, E.~J. Groth, P Guhathakurta, J Harker, N Kaiser, S Kassin, M Kleinheinrich, N.~P. Konidaris, R.~G. Kron, L Lin, G Luppino, D.~S. Madgwick, K Meisenheimer, K.~G. Noeske, A.~C. Phillips, V.~L. Sarajedini, R.~P. Schiavon, L Simard, A.~S. Szalay, N.~P. Vogt, and R Yan. Galaxy Luminosity Functions to $z \sim 1$ from DEEP2 and COMBO-17: Implications for Red Galaxy Formation. *The Astrophysical Journal*, 665:265–294, aug 2007.

- [86] H Lin, H.~K.~C. Yee, R.~G. Carlberg, S.~L. Morris, M Sawicki, D.~R. Patton, G Wirth, and C.~W. Shepherd. The CNOC2 Field Galaxy Luminosity Function. I. A Description of Luminosity Function Evolution. *The Astrophysical Journal*, 518:533–561, jun 1999.
- [87] M.~R. Blanton, D.~W. Hogg, N.~A. Bahcall, J Brinkmann, M Britton, A.~J. Connolly, I Csabai, M Fukugita, J Loveday, A Meiksin, J.~A. Munn, R.~C. Nichol, S Okamura, T Quinn, D.~P. Schneider, K Shimasaku, M.~A. Strauss, M Tegmark, M.~S. Vogeley, and D.~H. Weinberg. The Galaxy Luminosity Function and Luminosity Density at Redshift $z = 0.1$. *The Astrophysical Journal*, 592:819–838, aug 2003.
- [88] M Kriek, P.~G. van Dokkum, I Labbé, M Franx, G.~D. Illingworth, D Marchesini, and R.~F. Quadri. An Ultra-Deep Near-Infrared Spectrum of a Compact Quiescent Galaxy at $z = 2.2$. *The Astrophysical Journal*, 700:221–231, jul 2009.
- [89] G Bruzual and S Charlot. Stellar population synthesis at the resolution of 2003. *Monthly Notices of the Royal Astronomical Society*, 344:1000–1028, oct 2003.
- [90] Christopher Hirata and Uroš Seljak. Shear calibration biases in weak-lensing surveys. *Monthly Notices of the Royal Astronomical Society*, 343(2):459–480, aug 2003.
- [91] G.~M. Bernstein and M Jarvis. Shapes and Shears, Stars and Smears: Optimal Measurements for Weak Lensing. *The Astronomical Journal*, 123:583–618, feb 2002.
- [92] A van der Wel, E.~F. Bell, B.~P. Holden, R.~A. Skibba, and H.-W. Rix. The Physical Origins of the Morphology-Density Relation: Evidence for Gas Stripping from the Sloan Digital Sky Survey. *The Astrophysical Journal*, 714:1779–1788, may 2010.
- [93] L Miller, T.~D. Kitching, C Heymans, A.~F. Heavens, and L van Waerbeke. Bayesian galaxy shape measurement for weak lensing surveys - I. Methodology and a fast-fitting algorithm. *Monthly Notices of the Royal Astronomical Society*, 382:315–324, nov 2007.

- [94] T.~D. Kitching, L Miller, C.~E. Heymans, L van Waerbeke, and A.~F. Heavens. Bayesian galaxy shape measurement for weak lensing surveys - II. Application to simulations. *Monthly Notices of the Royal Astronomical Society*, 390:149–167, oct 2008.
- [95] L Miller, C Heymans, T.~D. Kitching, L van Waerbeke, T Erben, H Hildebrandt, H Hoekstra, Y Mellier, B.~T.~P. Rowe, J Coupon, J.~P. Dietrich, L Fu, J Harnois-Déraps, M.~J. Hudson, M Kilbinger, K Kuijken, T Schrabback, E Semboloni, S Vafaei, and M Velander. Bayesian galaxy shape measurement for weak lensing surveys - III. Application to the Canada-France-Hawaii Telescope Lensing Survey. *Monthly Notices of the Royal Astronomical Society*, 429:2858–2880, mar 2013.
- [96] G.~M. Bernstein and R Armstrong. Bayesian lensing shear measurement. *Monthly Notices of the Royal Astronomical Society*, 438:1880–1893, feb 2014.
- [97] J.~A. Newman, A Abate, F.~B. Abdalla, S Allam, S.~W. Allen, R Ansari, S Bailey, W.~A. Barkhouse, T.~C. Beers, M.~R. Blanton, M Brodwin, J.~R. Brownstein, R.~J. Brunner, M Carrasco Kind, J.~L. Cervantes-Cota, E Cheu, N.~E. Chisari, M Colless, J Comparat, J Coupon, C.~E. Cunha, A de la Macorra, I.~P. Dell’Antonio, B.~L. Frye, E.~J. Gawiser, N Gehrels, K Grady, A Hagen, P.~B. Hall, A.~P. Hearin, H Hildebrandt, C.~M. Hirata, S Ho, K Honscheid, D Huterer, Ž Ivezić, J.-P. Kneib, J.~W. Kruk, O Lahav, R Mandelbaum, J.~L. Marshall, D.~J. Matthews, B Ménard, R Miquel, M Moniez, H.~W. Moos, J Moustakas, A.~D. Myers, C Papovich, J.~A. Peacock, C Park, M Rahman, J Rhodes, J.-S. Ricol, I Sadeh, A Slozar, S.~J. Schmidt, D.~K. Stern, J Anthony Tyson, A von der Linden, R.~H. Wechsler, W.~M. Wood-Vasey, and A.~R. Zentner. Spectroscopic needs for imaging dark energy experiments. *Astroparticle Physics*, 63:81–100, mar 2015.
- [98] Randy A Kimble, John W MacKenty, Robert W O’Connell, and Jacqueline A Townsend. Wide Field Camera 3: a powerful new imager for the Hubble Space Telescope. *Proc. SPIE*, 7010:70101E–70101E–12, 2008.
- [99] E.~L. Wright, P.~R.~M. Eisenhardt, A.~K. Mainzer, M.~E. Ressler, R.~M. Cutri, T Jarrett, J.~D. Kirkpatrick, D Padgett, R.~S. McMillan, M Skrutskie, S.~A. Stanford, M Cohen, R.~G. Walker, J.~C. Mather, D Leisawitz,

- T.~N. Gautier III, I McLean, D Benford, C.~J. Lonsdale, A Blain, B Mendez, W.~R. Irace, V Duval, F Liu, D Royer, I Heinrichsen, J Howard, M Shannon, M Kendall, A.~L. Walsh, M Larsen, J.~G. Cardon, S Schick, M Schwalm, M Abid, B Fabinsky, L Naes, and C.-W. Tsai. The Wide-field Infrared Survey Explorer (WISE): Mission Description and Initial On-orbit Performance. *The Astronomical Journal*, 140:1868–1881, dec 2010.
- [100] J.~P. Gardner, J.~C. Mather, M Clampin, R Doyon, M.~A. Greenhouse, H.~B. Hammel, J.~B. Hutchings, P Jakobsen, S.~J. Lilly, K.~S. Long, J.~I. Lunine, M.~J. McCaughrean, M Mountain, J Nella, G.~H. Rieke, M.~J. Rieke, H.-W. Rix, E.~P. Smith, G Sonneborn, M Stiavelli, H.~S. Stockman, R.~A. Windhorst, and G.~S. Wright. The James Webb Space Telescope. *Space Science Reviews*, 123:485–606, apr 2006.
- [101] P Schneider. Part 3: Weak gravitational lensing. In G Meylan, P Jetzer, P North, P Schneider, C.~S. Kochanek, and J Wambsganss, editors, *Saas-Fee Advanced Course 33: Gravitational Lensing: Strong, Weak and Micro*, pages 269–451. Springer-Verlag Berlin Heidelberg, 2006.
- [102] M.~R. Becker, M.~A. Troxel, N MacCrann, E Krause, T.~F. Eifler, O Friedrich, A Nicola, A Refregier, A Amara, D Bacon, G.~M. Bernstein, C Bonnett, S.~L. Bridle, M.~T. Busha, C Chang, S Dodelson, B Erickson, A.~E. Evrard, J Frieman, E Gaztanaga, D Gruen, W Hartley, B Jain, M Jarvis, T Kacprzak, D Kirk, A Kravtsov, B Leistedt, E.~S. Rykoff, C Sabiu, C Sanchez, H Seo, E Sheldon, R.~H. Wechsler, J Zuntz, T Abbott, F.~B. Abdalla, S Allam, R Armstrong, M Banerji, A.~H. Bauer, A Benoit-Levy, E Bertin, D Brooks, E Buckley-Geer, D.~L. Burke, D Capozzi, A Carnero Rosell, M Carrasco Kind, J Carretero, F.~J. Castander, M Crocce, C.~E. Cunha, C.~B. D’Andrea, L.~N. da Costa, D.~L. DePoy, S Desai, H.~T. Diehl, J.~P. Dietrich, P Doel, A Fausti Neto, E Fernandez, D.~A. Finley, B Flaugher, P Fosalba, D.~W. Gerdes, R.~A. Gruendl, G Gutierrez, K Honscheid, D.~J. James, K Kuehn, N Kuropatkin, O Lahav, T.~S. Li, M Lima, M.~A.~G. Maia, M March, P Martini, P Melchior, C.~J. Miller, R Miquel, J.~J. Mohr, R.~C. Nichol, B Nord, R Ogando, A.~A. Plazas, K Reil, A.~K. Romer, A Roodman, M Sako, E Sanchez, V Scarpine, M Schubnell, I Sevilla-Noarbe, R.~C. Smith, M Soares-Santos, F Sobreira, E Suchyta, M.~E.~C. Swanson, G Tarle, J Thaler, D Thomas, V Vikram, A.~R. Walker,

and The DES Collaboration. Cosmic Shear Measurements with DES Science Verification Data. *ArXiv e-prints*, jul 2015.

- [103] A.~R. Pullen, S Alam, and S Ho. Probing gravity at large scales through CMB lensing. *Monthly Notices of the Royal Astronomical Society*, 449:4326–4335, jun 2015.
- [104] F Simpson, C Heymans, D Parkinson, C Blake, M Kilbinger, J Benjamin, T Erben, H Hildebrandt, H Hoekstra, T.~D. Kitching, Y Mellier, L Miller, L Van Waerbeke, J Coupon, L Fu, J Harnois-Déraps, M.~J. Hudson, K Kuijken, B Rowe, T Schrabback, E Semboloni, S Vafaei, and M Velander. CFHTLenS: testing the laws of gravity with tomographic weak lensing and redshift-space distortions. *Monthly Notices of the Royal Astronomical Society*, 429:2249–2263, mar 2013.
- [105] R Reyes, R Mandelbaum, U Seljak, T Baldauf, J.~E. Gunn, L Lombriser, and R.~E. Smith. Confirmation of general relativity on large scales from weak lensing and galaxy velocities. *\nat*, 464:256–258, mar 2010.
- [106] A Leauthaud, J Tinker, K Bundy, P.~S. Behroozi, R Massey, J Rhodes, M.~R. George, J.-P. Kneib, A Benson, R.~H. Wechsler, M.~T. Busha, P Capak, M Cortès, O Ilbert, A.~M. Koekemoer, O Le Fèvre, S Lilly, H.~J. McCracken, M Salvato, T Schrabback, N Scoville, T Smith, and J.~E. Taylor. New Constraints on the Evolution of the Stellar-to-dark Matter Connection: A Combined Analysis of Galaxy-Galaxy Lensing, Clustering, and Stellar Mass Functions from $z = 0.2$ to $z = 1$. *The Astrophysical Journal*, 744:159, jan 2012.
- [107] J.~L. Tinker, A Leauthaud, K Bundy, M.~R. George, P Behroozi, R Massey, J Rhodes, and R.~H. Wechsler. Evolution of the Stellar-to-dark Matter Relation: Separating Star-forming and Passive Galaxies from $z = 1$ to 0. *The Astrophysical Journal*, 778:93, dec 2013.
- [108] M Velander, E van Uitert, H Hoekstra, J Coupon, T Erben, C Heymans, H Hildebrandt, T.~D. Kitching, Y Mellier, L Miller, L Van Waerbeke, C Bonnett, L Fu, S Giodini, M.~J. Hudson, K Kuijken, B Rowe, T Schrabback, and E Semboloni. CFHTLenS: the relation between galaxy dark matter haloes and

- baryons from weak gravitational lensing. *Monthly Notices of the Royal Astronomical Society*, 437:2111–2136, jan 2014.
- [109] J Han, V.~R. Eke, C.~S. Frenk, R Mandelbaum, P Norberg, M.~D. Schneider, J.~A. Peacock, Y Jing, I Baldry, J Bland-Hawthorn, S Brough, M.~J.~I. Brown, J Liske, J Loveday, and A.~S.~G. Robotham. Galaxy And Mass Assembly (GAMA): the halo mass of galaxy groups from maximum-likelihood weak lensing. *Monthly Notices of the Royal Astronomical Society*, 446:1356–1379, jan 2015.
- [110] M.~J. Hudson, B.~R. Gillis, J Coupon, H Hildebrandt, T Erben, C Heymans, H Hoekstra, T.~D. Kitching, Y Mellier, L Miller, L Van Waerbeke, C Bonnett, L Fu, K Kuijken, B Rowe, T Schrabback, E Semboloni, E van Uitert, and M Velander. CFHTLenS: co-evolution of galaxies and their dark matter haloes. *Monthly Notices of the Royal Astronomical Society*, 447:298–314, feb 2015.
- [111] J Coupon, S Arnouts, L van Waerbeke, T Moutard, O Ilbert, E van Uitert, T Erben, B Garilli, L Guzzo, C Heymans, H Hildebrandt, H Hoekstra, M Kilbinger, T Kitching, Y Mellier, L Miller, M Scodreggio, C Bonnett, E Branchini, I Davidzon, G De Lucia, A Fritz, L Fu, P Hudelot, M.~J. Hudson, K Kuijken, A Leauthaud, O Le Fèvre, H.~J. McCracken, L Moscardini, B.~T.~P. Rowe, T Schrabback, E Semboloni, and M Velander. The galaxy-halo connection from a joint lensing, clustering and abundance analysis in the CFHTLenS/VIPERS field. *Monthly Notices of the Royal Astronomical Society*, 449:1352–1379, may 2015.
- [112] Y Zu and R Mandelbaum. Mapping stellar content to dark matter haloes using galaxy clustering and galaxy-galaxy lensing in the SDSS DR7. *Monthly Notices of the Royal Astronomical Society*, 454:1161–1191, dec 2015.
- [113] R Mandelbaum, B Rowe, R Armstrong, D Bard, E Bertin, J Bosch, D Boutigny, F Courbin, W.~A. Dawson, A Donnarumma, I Fenech Conti, R Gavazzi, M Gentile, M.~S.~S. Gill, D.~W. Hogg, E.~M. Huff, M.~J. Jee, T Kacprzak, M Kilbinger, T Kuntzer, D Lang, W Luo, M.~C. March, P.~J. Marshall, J.~E. Meyers, L Miller, H Miyatake, R Nakajima, F.~M. Ngólé Mboula, G Nurbaeva, Y Okura, S Paulin-Henriksson, J Rhodes, M.~D. Schneider, H Shan, E.~S.

- Sheldon, M Simet, J.-L. Starck, F Sureau, M Tewes, K Zarb Adami, J Zhang, and J Zuntz. GREAT3 results - I. Systematic errors in shear estimation and the impact of real galaxy morphology. *Monthly Notices of the Royal Astronomical Society*, 450(3):2963–3007, jul 2015.
- [114] J Estrada, T Abbott, B Angstadt, L Buckley-Geer, M Brown, J Campa, L Cardiel, H Cease, B Flaugher, K Dawson, G Derylo, H T Diehl, S Gruenendahl, I Karliner, W Merrit, P Moore, T C Moore, N Roe, V Scarpine, R Schmidt, M Schubnel, T Shaw, W Stuermer, and J Thaler. CCD testing and characterization for dark energy survey. *Proc. SPIE*, 6269:62693K–62693K–15, 2006.
- [115] C J Bebek, J H Emes, D E Groom, S Haque, S E Holland, A Karcher, W F Kolbe, J S Lee, N P Palαιο, and G Wang. CCD development for the Dark Energy Spectroscopic Instrument. *Journal of Instrumentation*, 10(05):C05026, 2015.
- [116] Y Okura, A A Plazas, M May, and T Tamagawa. Spurious shear induced by the tree rings of the LSST CCDs. *Journal of Instrumentation*, 10(08):C08010, 2015.
- [117] T Biesiadzinski, W Lorenzon, R Newman, M Schubnell, G Tarlé, and C Weaverdyck. Reciprocity Failure in HgCdTe Detectors: Measurements and Mitigation. *Publications of the Astronomical Society of the Pacific*, 123(906):958–963, 2011.
- [118] Andrew C Moore, Zoran Ninkov, and William J Forrest. Interpixel capacitance in nondestructive focal plane arrays. In *Optical Science and Technology, SPIE's 48th Annual Meeting*, pages 204–215. International Society for Optics and Photonics, 2004.
- [119] Andrew C Moore, Zoran Ninkov, and William J Forrest. Quantum efficiency overestimation and deterministic cross talk resulting from interpixel capacitance. *Optical Engineering*, 45(7):76402, 2006.
- [120] P O'Connor. Crosstalk in multi-output CCDs for LSST. *Journal of Instrumentation*, 10(05):C05010, 2015.

- [121] B Hilbert and P McCullough. Interpixel Capacitance in the IR Channel: Measurements Made On Orbit. 2011.
- [122] P-E. Crouzet, J ter Haar, F de Wit, T Beaufort, B Butler, H Smit, C van der Luijt, and D Martin. Characterization of HAWAII-2RG detector and SIDECAR ASIC for the Euclid mission at ESA. *Proc. SPIE*, 8453:84531R–84531R–15, 2012.
- [123] Ori Fox, Augustyn Waczynski, Yiting Wen, Roger D Foltz, Robert J Hill, Randy A Kimble, Eliot Malumuth, and Bernard J Rauscher. The 55Fe X-Ray Energy Response of Mercury Cadmium Telluride Near-Infrared Detector Arrays. *Publications of the Astronomical Society of the Pacific*, 121(881):743, 2009.
- [124] Peter R McCullough, M Regan, L Bergeron, and K Lindsay. Measurement of the Quantum efficiency of an HgCdTe Infrared sensor Array. *BULLETIN-AMERICAN ASTRONOMICAL SOCIETY*, 39(1):86, 2007.
- [125] P McCullough. Inter-pixel capacitance: prospects for deconvolution. *Instrument Science Report WFC3*, 26, 2008.
- [126] S Seshadri, D M Cole, B R Hancock, and R M Smith. Mapping electrical crosstalk in pixelated sensor arrays. *Proc. SPIE*, 7021:702104–702111, 2008.
- [127] Nick Kaiser, Gordon Squires, and Tom Broadhurst. A Method for Weak Lensing Observations. *Astrophysical Journal*, 449:449–460, aug 1995.
- [128] Robert J Noll. Zernike polynomials and atmospheric turbulence. *J. Opt. Soc. Am.*, 66(3):207–211, mar 1976.
- [129] Bert Pasquale, David Content, Jeffery Kruk, David Vaughnn, Qian Gong, Joseph Howard, Alden Jurling, Len Seals, Eric Mentzell, Nerses Armani, and Gary Kuan. Optical Design of the WFIRST-AFTA Wide-Field Instrument. *Proc. SPIE*, 9293:929305–929308, 2014.
- [130] A. S. Fruchter and R. N. Hook. Drizzle: A Method for the Linear Reconstruction of Undersampled Images. *Publications of the Astronomical Society of the Pacific*, 114(792):144–152, feb 2002.

- [131] A. S. Fruchter. A New Method for Band-limited Imaging with Undersampled Detectors. *Publications of the Astronomical Society of the Pacific*, 123:497–502, apr 2011.
- [132] Barnaby Rowe, Christopher Hirata, and Jason Rhodes. Optimal Linear Image Combination. *The Astrophysical Journal*, 741(1):46, nov 2011.
- [133] Tod R Lauer. Combining Undersampled Dithered Images. *Publications of the Astronomical Society of the Pacific*, 111(756):227–237, feb 1999.
- [134] C Shapiro, B. T. P. Rowe, T Goodsall, C Hirata, J Fucik, J Rhodes, S Seshadri, and R Smith. Weak Gravitational Lensing Systematics from Image Combination. *Publications of the Astronomical Society of the Pacific*, 125:1496–1513, dec 2013.
- [135] The Dark Energy Survey Collaboration, T Abbott, F. B. Abdalla, S Allam, A Amara, J Annis, R Armstrong, D Bacon, M Banerji, A. H. Bauer, E Baxter, M. R. Becker, A Benoit-Lévy, R. A. Bernstein, G. M. Bernstein, E Bertin, J Blazek, C Bonnett, S. L. Bridle, D Brooks, C Bruderer, E Buckley-Geer, D. L. Burke, M. T. Busha, D Capozzi, A Carnero Rosell, M Carrasco Kind, J Carretero, F. J. Castander, C Chang, J Clampitt, M Crocce, C. E. Cunha, C. B. D’Andrea, L. N. da Costa, R Das, D. L. DePoy, S Desai, H. T. Diehl, J. P. Dietrich, S Dodelson, P Doel, A Drlica-Wagner, G Efstathiou, T. F. Eifler, B Erickson, J Estrada, A. E. Evrard, A Fausti Neto, E Fernandez, D. A. Finley, B Flaugher, P Fosalba, O Friedrich, J Frieman, C Gangkofner, J Garcia-Bellido, E Gaztanaga, D. W. Gerdes, D Gruen, R. A. Gruendl, G Gutierrez, W Hartley, M Hirsch, K Honscheid, E. M. Huff, B Jain, D. J. James, M Jarvis, T Kacprzak, S Kent, D Kirk, E Krause, A Kravtsov, K Kuehn, N Kuropatkin, J Kwan, O Lahav, B Leistedt, T. S. Li, M Lima, H Lin, N MacCrann, M March, J. L. Marshall, P Martini, R. G. McMahon, P Melchior, C. J. Miller, R Miquel, J. J. Mohr, E Neilsen, R. C. Nichol, A Nicola, B Nord, R Ogando, A Palmese, H. V. Peiris, A. A. Plazas, A Refregier, N Roe, A. K. Romer, A Roodman, B Rowe, E. S. Rykoff, C Sabiu, I Sadeh, M Sako, S Samuroff, C Sánchez, E Sanchez, H Seo, I Sevilla-Noarbe, E Sheldon, R. C. Smith, M Soares-Santos, F Sobreira, E Suchyta, M. E. C. Swanson, G Tarle, J Thaler, D Thomas, M. A. Troxel, V Vikram, A. R. Walker, R. H. Wechsler, J Weller, Y Zhang,

and J Zuntz. Cosmology from Cosmic Shear with DES Science Verification Data. *ArXiv e-prints*, jul 2015.

- [136] T de Haan, B.~A. Benson, L.~E. Bleem, S.~W. Allen, D.~E. Applegate, M.~L.~N. Ashby, M Bautz, M Bayliss, S Bocquet, M Brodwin, J.~E. Carlstrom, C.~L. Chang, I Chiu, H Cho, A Clocchiatti, T.~M. Crawford, A.~T. Crites, S Desai, J.~P. Dietrich, M.~A. Dobbs, A.~N. Doucouliagos, R.~J. Foley, W.~R. Forman, G.~P. Garmire, E.~M. George, M.~D. Gladders, A.~H. Gonzalez, N Gupta, N.~W. Halverson, J Hlavacek-Larrondo, H Hoekstra, G.~P. Holder, W.~L. Holzappel, Z Hou, J.~D. Hrubes, N Huang, C Jones, R Keisler, L Knox, A.~T. Lee, E.~M. Leitch, A von der Linden, D Luong-Van, A Mantz, D.~P. Marrone, M McDonald, J.~J. McMahon, S.~S. Meyer, L.~M. Mocanu, J.~J. Mohr, S.~S. Murray, S Padin, C Pryke, D Rapetti, C.~L. Reichardt, A Rest, J Ruel, J.~E. Ruhl, B.~R. Saliwanchik, A Saro, J.~T. Sayre, K.~K. Schaffer, T Schrabback, E Shirokoff, J Song, H.~G. Spieler, B Stalder, S.~A. Stanford, Z Staniszewski, A.~A. Stark, K.~T. Story, C.~W. Stubbs, K Vanderlinde, J.~D. Vieira, A Vikhlinin, R Williamson, and A Zenteno. Cosmological Constraints from Galaxy Clusters in the 2500 square-degree SPT-SZ Survey. *ArXiv e-prints*, mar 2016.
- [137] The LZ Collaboration, D.~S. Akerib, C.~W. Akerlof, D.~Y. Akimov, S.~K. Alsum, H.~M. Araújo, X Bai, A.~J. Bailey, J Balajthy, S Balashov, M.~J. Barry, P Bauer, P Beltrame, E.~P. Bernard, A Bernstein, T.~P. Biesiadzinski, K.~E. Boast, A.~I. Bolozdynya, E.~M. Boulton, R Bramante, J.~H. Buckley, V.~V. Bugaev, R Bunker, S Burdin, J.~K. Busenitz, C Carels, D.~L. Carlsmith, B Carlson, M.~C. Carmona-Benitez, M Cascella, C Chan, J.~J. Cherwinka, A.~A. Chiller, C Chiller, W.~W. Craddock, A Currie, J.~E. Cutter, J.~P. da Cunha, C.~E. Dahl, S Dasu, T.~J.~R. Davison, L de Viveiros, A Dobi, J.~E.~Y. Dobson, E Druszkiewicz, T.~K. Edberg, B.~N. Edwards, W.~R. Edwards, M.~M. Elnimr, W.~T. Emmet, C.~H. Faham, S Fiorucci, P Ford, V.~B. Francis, C Fu, R.~J. Gaitskell, N.~J. Gantos, V.~M. Gehman, R.~M. Gerhard, C Ghag, M.~G.~D. Gilchriese, B Gomber, C.~R. Hall, A Harris, S.~J. Haselschwardt, S.~A. Hertel, M.~D. Hoff, B Holbrook, E Holtom, D.~Q. Huang, T.~W. Hurteau, C.~M. Ignarra, R.~G. Jacobsen, W Ji, X Ji, M Johnson, Y Ju, K Kamdin, K Kazkaz, D Khaitan, A Khazov, A.~V. Khromov,

A.~M. Konovalov, E.~V. Korolkova, H Kraus, H.~J. Krebs, V.~A. Kudryavtsev, A.~V. Kumpan, S Kyre, N.~A. Larsen, C Lee, B.~G. Lenardo, K.~T. Lesko, F.-T. Liao, J Lin, A Lindote, W.~H. Lippincott, J Liu, X Liu, M.~I. Lopes, W Lorenzon, S Luitz, P Majewski, D.~C. Malling, A.~G. Manalaysay, L Manenti, R.~L. Mannino, D.~J. Markley, T.~J. Martin, M.~F. Marzioni, D.~N. McKinsey, D.-M. Mei, Y Meng, E.~H. Miller, J Mock, M.~E. Monzani, J.~A. Morad, A.~S.~J. Murphy, H.~N. Nelson, F Neves, J.~A. Nikkel, F.~G. O'Neill, J O'Dell, K O'Sullivan, M.~A. Olevitch, K.~C. Oliver-Mallory, K.~J. Palladino, M Pangilinan, S.~J. Patton, E.~K. Pease, A Piepke, S Powell, R.~M. Preece, K Pushkin, B.~N. Ratcliff, J Reichenbacher, L Reichhart, C Rhyne, J.~P. Rodrigues, H.~J. Rose, R Rosero, J.~S. Saba, M Sarychev, R.~W. Schnee, M.~S.~G. Schubnell, P.~R. Scovell, S Shaw, T.~A. Shutt, C Silva, K Skarpaas, W Skulski, V.~N. Solovov, P Sorensen, V.~V. Sosnovtsev, I Stancu, M.~R. Stark, S Stephenson, T.~M. Stiegler, T.~J. Sumner, K Sundarnath, M Szydagis, D.~J. Taylor, W Taylor, B.~P. Tennyson, P.~A. Terman, K.~J. Thomas, J.~A. Thomson, D.~R. Tiedt, W.~H. To, A Tomás, M Tripathi, C.~E. Tull, L Tvrznikova, S Uvarov, J Va'vra, M.~G.~D. van der Grinten, J.~R. Verbus, C.~O. Vuosalo, W.~L. Waldron, L Wang, R.~C. Webb, W.-Z. Wei, M While, D.~T. White, T.~J. Whitis, W.~J. Wisniewski, M.~S. Witherell, F.~L.~H. Wolfs, E Woods, D Woodward, S.~D. Worm, M Yeh, J Yin, S.~K. Young, and C Zhang. LUX-ZEPLIN (LZ) Conceptual Design Report. *ArXiv e-prints*, sep 2015.

- [138] T Marrodán Undagoitia and L Rauch. Dark matter direct-detection experiments. *Journal of Physics G Nuclear Physics*, 43(1):13001, jan 2016.
- [139] S Miyazaki, Y Komiyama, H Nakaya, Y Kamata, Y Doi, T Hamana, H Karoji, H Furusawa, S Kawanomoto, T Morokuma, Y Ishizuka, K Nariai, Y Tanaka, F Uraguchi, Y Utsumi, Y Obuchi, Y Okura, M Oguri, T Takata, D Tomono, T Kurakami, K Namikawa, T Usuda, H Yamanoi, T Terai, H Uekiyo, Y Yamada, M Koike, H Aihara, Y Fujimori, S Mineo, H Miyatake, N Yasuda, J Nishizawa, T Saito, M Tanaka, T Uchida, N Katayama, S.-Y. Wang, H.-Y. Chen, R Lupton, C Loomis, S Bickerton, P Price, J Gunn, H Suzuki, Y Miyazaki, M Muramatsu, K Yamamoto, M Endo, Y Ezaki, N Itoh, Y Miwa, H Yokota, T Matsuda, R Ebinuma, and K Takeshi. Hyper Suprime-Cam. In

Ground-based and Airborne Instrumentation for Astronomy IV, volume 8446 of *\procspie*, page 84460Z, sep 2012.

- [140] G. A. Luppino and Nick Kaiser. Detection of Weak Lensing by a Cluster of Galaxies at $z = 0.83$. *The Astrophysical Journal*, 475(1):20, 1997.
- [141] H Hoekstra, M Franx, K Kuijken, and G Squires. Weak Lensing Analysis of CL 1358+62 Using Hubble Space Telescope Observations. *The Astrophysical Journal*, 504:636–660, sep 1998.
- [142] M. D. Schneider, D. W. Hogg, P. J. Marshall, W. A. Dawson, J Meyers, D. J. Bard, and D Lang. Hierarchical Probabilistic Inference of Cosmic Shear. *The Astrophysical Journal*, 807:87, jul 2015.
- [143] Arun Kannawadi, Charles A. Shapiro, Rachel Mandelbaum, Christopher M. Hirata, Jeffrey W. Kruk, and Jason D. Rhodes. The Impact of Interpixel Capacitance in CMOS Detectors on PSF Shapes and Implications for WFIRST. *Publications of the Astronomical Society of the Pacific*, 128(967):34, dec 2016.
- [144] Andrés. A. Plazas, Charles A. Shapiro, Arun Kannawadi, Rachel Mandelbaum, Jason D. Rhodes, and Roger Smith. The effect of detector nonlinearity on WFIRST PSF profiles for weak gravitational lensing measurements. page 19, may 2016.
- [145] A M Koekemoer, A S Fruchter, R N Hook, and W Hack. *the 2002 HST Calibration Workshop: Hubble after the Installation of the ACS and the NICMOS Cooling System*. PhD thesis, ed. S. Arribas, A. Koekemoer, & B. Whitmore (Baltimore, MD: STScI), 337, 2002.
- [146] C. B. Markwardt. Non-linear Least-squares Fitting in IDL with MPFIT. In D. A. Bohlender, D Durand, and P Dowler, editors, *Astronomical Data Analysis Software and Systems XVIII*, volume 411 of *Astronomical Society of the Pacific Conference Series*, page 251, sep 2009.
- [147] G. D. Coleman, C.-C. Wu, and D. W. Weedman. Colors and magnitudes predicted for high redshift galaxies. *Astrophysical Journal Supplement Series*, 43:393–416, jul 1980.

- [148] M Bolzonella, J.-M. Miralles, and R Pelló. Photometric redshifts based on standard SED fitting procedures. *Astronomy and Astrophysics*, 363:476–492, nov 2000.
- [149] M Bolzonella, J.-M. Miralles, and R Pelló. Hyperz: Photometric Redshift Code. Astrophysics Source Code Library, aug 2011.
- [150] A G Bruzual and S Charlot. Spectral evolution of stellar populations using isochrone synthesis. *The Astrophysical Journal*, 405:538–553, mar 1993.
- [151] C.~M. Hirata, N Gehrels, J.-P. Kneib, J Kruk, J Rhodes, Y Wang, and J Zoubian. The WFIRST Galaxy Survey Exposure Time Calculator. *ArXiv e-prints*, apr 2012.
- [152] Alex Gurvich and Rachel Mandelbaum. The impact of correlated noise on galaxy shape estimation for weak lensing. *Monthly Notices of the Royal Astronomical Society*, 457(4):3522–3534, feb 2016.